

**DESIGN, DEVELOPMENT AND ANALYSIS
OF CHIPLESS RFID TAGS USING PLANAR
MULTIRESONATORS**

A THESIS

submitted by

SUMI M

for the award of the degree

of

DOCTOR OF PHILOSOPHY



DIVISION OF ELECTRONICS ENGINEERING

SCHOOL OF ENGINEERING

COCHIN UNIVERSITY OF SCIENCE AND TECHNOLOGY

KOCHI - 682 022

December 2016

THESIS CERTIFICATE

This is to certify that the thesis entitled **DESIGN, DEVELOPMENT AND ANALYSIS OF CHIPLESS RFID TAGS USING PLANAR MULTIRESONATORS** submitted by **Sumi M** to the Cochin University of Science and Technology, Kochi for the award of the degree of Doctor of Philosophy is a bonafide record of research work carried out by her under my supervision and guidance at the Division of Electronics Engineering, School of Engineering, Cochin University of Science and Technology. The contents of this thesis, in full or in parts, have not been submitted to any other University or Institute for the award of any degree or diploma.

I further certify that the corrections and modifications suggested by the audience during the pre-synopsis seminar and recommended by the Doctoral committee of **Sumi M** are incorporated in the thesis.

Prof. (Dr) S. Mridula
Research Guide
Professor
Division of Electronics Engineering
School of Engineering
CUSAT, Kochi 682 022

Place: Kochi
Date : 14 - 12 - 2016

DECLARATION

I hereby declare that the work presented in the thesis entitled **DESIGN, DEVELOPMENT AND ANALYSIS OF CHIPLESS RFID TAGS USING PLANAR MULTIRESONATORS** is based on the original research work carried out by me under the supervision and guidance of Dr. S Mridula, Professor, Division of Electronics Engineering, School of Engineering, Cochin University of Science and Technology for the award of the degree of Doctor of Philosophy with Cochin University of Science and Technology. I further declare that the contents of this thesis in full or in parts have not been submitted to any other University or Institute for the award of any degree or diploma.

Kochi - 682 022

Sumi M

14 - 12 - 2016

ACKNOWLEDGEMENTS

I would like to thank my guide and mentor, Dr. S. Mridula, for her valuable guidance, encouragement and advice throughout my research work. I am deeply indebted to my supervisor who cared so much about my work, mentored me, and gave me right direction and responded to my questions and queries so promptly. I would like to convey my heartfelt gratitude for her commitment in correcting the thesis meticulously.

I would also like to thank Dr. P. Mohanan, UGC BSR Professor, Department of Electronics who has been a constant source of encouragement throughout my research. He has been always accessible for discussion and I am very thankful to him for his valuable suggestions. I extend my sincere thanks to him for extending excellent laboratory facilities for carrying out experimental work. I am grateful to Dr. K. Vasudevan, CSIR Emeritus Scientist, Department of Electronics, for his support. I also thank Dr. Binu Paul, HOD, Division of Electronics Engineering, School of Engineering and also the member of doctoral committee for her timely support and suggestions.

I am thankful to Dr. M. R. Radhakrishna Panicker, Principal, School of Engineering, and Dr. P. S. Sreejith, Dean, Faculty of Engineering, for providing the necessary facilities for research. Mere words are not enough to thank Dr. Nijas and Dr. Dinesh for all the timely help and valuable discussions. I gratefully acknowledge members of CREMA; Dr. Sujith R, Dr. Sarin P V, Mr. Deepak U, Mrs. Roshna T. K, Mrs. Sajitha V. R, Mr. Jayakrishnan and Mrs. Sumitha Mathew for the support given to me during the period of the work. I take this opportunity to thank my fellow research scholars at School of

Engineering; Dr. Anju Pradeep, Mrs. Mini P R, Mr. Rajesh Mohan, Mr. Basil J Paul and Dr. Jaya V L for being cordial to work with. Special thanks to Mr. Anjit T A for timely help. Technical support offered by Mr. Anil Kumar, Maintenance Engineer, Department of Electronics and Mrs. Gibi K Thomas, Division of Electronics Engineering, is also gratefully remembered.

I thank the support offered by Dr. Deepu V Nair, Technical Lead, Cambium Networks during the period of the work and Dr. R. Ratheesh, Scientist, C-MET, Thrissur for providing the low loss substrate. I am grateful to, Mr. Mahesh C, Mr. Unnikartha G, and Mrs. Parvathy R of FISAT for helping me with LaTeX related doubts. Words are not enough to thank Dr. Bindu C J and Mrs. Saira Joseph, for the support and care given to me in the entire period of my research work. We have complimented each other in many ways and this helped us to make the work more enjoyable and productive. I wish to thank the authorities of N S S College of Engineering, Palakkad for granting permission to do the research.

My father, Dr. K. S. M. Panicker and my mother, Dr. K. P. Saraswathy Amma, had spared no effort to provide the best possible environment for me to grow up and study. Thanks to my brother, Samoj M Panicker for being a supportive sibling and Sudeepa Nair, my sister in law for being a role model for me. I thank my grand mother, Smt. Padmini Amma for her boundless love. I take this opportunity to thank my mother-in-law Smt. S. Indiramma, my peramma Smt. Radhamoni Amma and my brother in laws Mr. Arun Sreekumar and Mr. Ajith Sreekumar for all the patient support and encouragement given to me. Above all, I thank my husband, Mr. Harikrishnan A.I for providing me with unfailing support and continuous encouragement throughout the period of research work. I appreciate my children Sandeep and Shreya, for their patience and understanding throughout the period of this work.

ABSTRACT

KEYWORDS: Absence or presence coding; bistatic measurement; chipless RFID tag; frequency shift coding; group delay; multiresonator

Radio frequency identification is a wireless data identification technology which utilizes radio waves to establish the communication link between RFID tag and RFID reader. Conventional RFID tags contain silicon chips and antennas. The thesis focuses on the design, development and analysis of spectral signature based chipless RFID tags using planar multiresonators with high data encoding capacity. Four novel multiresonator designs are presented in the thesis.

- ★ U slot multiresonator
- ★ Shorted stub multiresonator
- ★ Spurline multiresonator
- ★ E shaped multiresonator

Transmitting and receiving wide band antennas are connected to these multiresonators for range enhancement. The RFID reader setup comprises an Agilent PNA E8362B network analyser with transmitted power of 0 dBm along with two cross polarized medium gain horn antennas. The amplitude of the interrogating signal sent by the reader is modulated in the form of amplitude attenuations at the resonant frequencies of the multiresonator, thus revealing the identity of the tag. Chipless RFID tags using integrated antennas and coplanar spurline multiresonator are included in the appendix. The performance of these multiresonators was studied using CST microwave studio[®] and design equations

were developed using multivariable regression analysis. Agilent advanced design system was employed for deriving the equivalent circuit. Implementation of two different data encoding methods, namely absence or presence coding technique and frequency shift coding technique are presented. Improved bit encoding capacity is achieved using frequency shift coding technique.

TABLE OF CONTENTS

ACKNOWLEDGEMENTS	ii
ABSTRACT	iv
LIST OF FIGURES	xi
LIST OF TABLES	xxvi
ABBREVIATIONS	xxviii
NOTATIONS	xxix
1 RFID TECHNOLOGY	1
1.1 Introduction	1
1.2 RFID system	4
1.2.1 RFID tag	4
1.2.2 RFID reader	7
1.2.3 Host system	7
1.3 Chipless RFID tags	8
1.3.1 Time domain reflectometry based chipless RFID tags	8
1.3.2 Spectral signature based chipless RFID tags	10
1.4 Motivation for the present work	11
1.5 Potential applications	13
1.6 Methodology	13
1.6.1 Simulation and optimization	13
1.6.2 Fabrication	14
1.6.3 Measurement	14
1.6.4 Data encoding methods	15
1.7 Thesis outline	16

2	CHIPLESS RFID TAG USING U SLOT MULTIRESONATOR	20
2.1	Introduction	20
2.2	The U slot multiresonator	24
2.3	Evolution of U slot multiresonator	24
2.3.1	Analysis and design of U slot resonator	27
2.3.2	Equivalent circuit of U slot resonator	30
2.3.3	Experimental results of U slot multiresonator	32
2.4	Bistatic measurement for validation of the tag	34
2.5	Data encoding methods	38
2.5.1	Absence or presence coding technique	39
2.5.2	Experimental results of U slot multiresonator using absence or presence coding technique	43
2.5.3	Bistatic measurement results using absence or presence coding technique	44
2.5.4	Frequency shift coding technique for enhanced bit encoding capacity	44
2.5.5	Frequency shift coding applied to U slot resonator	47
2.5.6	Frequency shift coding applied to multiresonator with two U slots	48
2.5.7	Frequency shift coding applied to multiresonator with four U slots	51
2.5.8	Frequency shift coding applied to multiresonator with six U slots	59
2.6	Chapter summary	67
2.7	Inferences	67
3	CHIPLESS RFID TAG USING SHORTED STUB MULTIRESONATOR	69
3.1	Introduction	69
3.2	The shorted stub multiresonator	69
3.3	Evolution of shorted stub multiresonator	73
3.3.1	Analysis and design of shorted stub resonator	73
3.3.2	Equivalent circuit of shorted stub resonator	76
3.3.3	Experimental results of shorted stub multiresonator	78

3.4	Bistatic measurement for validation of the tag	80
3.5	Data encoding methods	82
3.5.1	Absence or presence coding technique	82
3.5.2	Experimental results of shorted stub multiresonator using absence or presence coding technique	84
3.5.3	Bistatic measurement results using absence or presence coding technique	87
3.5.4	Frequency shift coding technique for enhanced bit encoding capacity	88
3.5.5	Frequency shift coding applied to shorted stub resonator	88
3.5.6	Frequency shift coding applied to multiresonator with two shorted stubs	89
3.5.7	Frequency shift coding applied to multiresonator with four shorted stubs	95
3.5.8	Frequency shift coding applied to multiresonator with eight shorted stubs	100
3.6	Chapter summary	110
3.7	Inferences	111
4	CHIPLESS RFID TAG USING SPURLINE MULTIRESONATOR	112
4.1	Introduction	112
4.2	The spurline multiresonator	112
4.3	Evolution of spurline multiresonator	115
4.3.1	Analysis and design of spurline resonator	115
4.3.2	Equivalent circuit of spurline resonator	118
4.3.3	Experimental results of spurline multiresonator	121
4.4	Bistatic measurement for validation of the tag	121
4.5	Data encoding methods	123
4.5.1	Absence or presence coding technique	123
4.5.2	Experimental results of spurline multiresonator using absence or presence coding technique	127
4.5.3	Bistatic measurement results using absence or presence coding technique	128

4.5.4	Frequency shift coding technique for enhanced bit encoding capacity	128
4.5.5	Frequency shift coding applied to spurline resonator	128
4.5.6	Frequency shift coding applied to multiresonator with two spurlines	134
4.5.7	Frequency shift coding applied to multiresonator with four spurlines	139
4.5.8	Frequency shift coding applied to multiresonator with eight spurlines	144
4.6	Chapter Summary	154
4.7	Inferences	154
5	CHIPLESS RFID TAG USING E SHAPED MULTIRESONATOR	156
5.1	Introduction	156
5.2	The E shaped multiresonator	156
5.3	Evolution of E shaped multiresonator	159
5.3.1	Analysis and design of E shaped resonator	160
5.3.2	Equivalent circuit of E shaped resonator	166
5.3.3	Experimental results of E shaped multiresonator	170
5.4	Bistatic measurement for validation of the tag	171
5.5	Data encoding methods	172
5.5.1	Absence or presence coding technique	173
5.5.2	Experimental results of E shaped multiresonator using absence or presence coding technique	176
5.5.3	Bistatic measurement results using absence or presence coding technique	177
5.5.4	Frequency shift coding technique for enhanced bit encoding capacity	177
5.5.5	Frequency shift coding applied to E shaped resonator	177
5.5.6	Frequency shift coding applied to multiresonator with two E shaped resonators	183
5.5.7	Frequency shift coding applied to multiresonator with four E shaped resonators	189
5.5.8	Frequency shift coding applied to multiresonator with eight E shaped resonators	194

5.6	Chapter Summary	203
5.7	Inferences	205
6	CONCLUSION	206
6.1	Thesis highlights	206
6.2	Suggestions for future Work	208
	APPENDIX	211
A	CHIPLESS RFID TAG WITH INTEGRATED ANTENNAS	211
A.1	Introduction	211
A.2	Experimental results	212
A.3	Inference	214
B	CHIPLESS RFID TAG USING COPLANAR SPURLINE MULTIRESONATOR	215
B.1	Introduction	215
B.2	Experimental results	217
B.3	Inference	218
	REFERENCES	219
	LIST OF PAPERS BASED ON THESIS	234
	CURRICULUM VITAE	236

LIST OF FIGURES

1.1	RFID system	4
1.2	RFID tag classification	5
1.3	Passive RFID tag (Courtsey: Cisco (Cisco, May 2008))	6
1.4	Active RFID tag (Courtsey:Digikey Electronics(www.digikey.com))	6
1.5	System architecture of SAW tag. Courtesy:(Hartmann, 2002)	9
1.6	Schematic diagram of transmission delay line based ID generation circuit Courtesy:A. Chamarti (Chamarti and Varahramyan, 2006)	10
1.7	Capacitively tuned dipoles arranged as a 11-bit chipless RFID tag. (Courtesy: I. Jalaly (Jalaly and Robertson, 2005 <i>a</i>))	10
1.8	General structure and operation of spectral signature based chipless RFID tag (Courtesy: S. Preradovic(Preradovic and Karmakar, 2009))	11
1.9	Some of the multiresonators reported in the literature	12
1.10	Ultraviolet lithography process	14
1.11	Block schematic for bistatic measurement	15
1.12	Thesis outline	17
2.1	Proposed six bit U slot multiresonator	23
2.2	Simulated transmission characteristics of the six bit U slot multiresonator shown in Fig.2.1	25
2.3	Surface current distribution of individual resonators in the U slot multiresonator shown in Fig.2.1	25
2.4	U slot resonator and its simulated transmission characteristics	26
2.5	Simulated transmission characteristics by varying W_i (mm) of the U slot resonator shown in Fig.2.4(a)	28

2.6	Surface current distribution of U slot resonator shown in Fig.2.4(a) at resonant frequency of 2.87 GHz and at a non-resonant frequency of 2 GHz.	29
2.7	Equivalent circuit of the U slot resonator ($f = 2.87$ GHz) . . .	31
2.8	Frequency response of the U slot resonator equivalent circuit extracted using Agilent ADS	32
2.9	The fabricated U slot multiresonator (a) Top layer (b) Bottom layer (c) Network analyser with device under test	33
2.10	Measured transmission characteristics of the U slot multiresonator for the bit combination [111 111]	34
2.11	Block schematic for bistatic measurement using U slot multiresonator	35
2.12	(a) Disc monopole antenna [$R = 15$, $W_3 = 3$, $L_g = 0.6$, $W_{g1} = 40$ and $L_{g1} = 20$ (All dimensions in mm), $\epsilon_r = 4.3$, loss tangent = 0.02, $h = 1.6$ mm] (b) Measured reflection characteristics of disc monopole antenna	36
2.13	Measured radiation pattern of disc monopole antenna	36
2.14	Gain of the reader antenna (horn) and tag antenna (disc monopole)	37
2.15	Experimental setup for bistatic measurement of the RFID tag using U slot multiresonator	38
2.16	Measured bistatic response of the RFID tag using U slot multiresonator for the bit combination [111 111]	39
2.17	Eight bit U slot multiresonator and its simulated transmission characteristics	40
2.18	The fabricated eight bit U slot multiresonator (a) Top layer (b) Bottom layer (c) Measured transmission characteristics of eight bit U slot multiresonator	40
2.19	U slot multiresonator type 1	41
2.20	Three different types of U slot multiresonator (a) Removing the slot (b) Shorting slot at corners	41
2.21	Simulated transmission characteristics of the U slot multiresonator for different bit combinations	42
2.22	Measured transmission characteristics of U slot multiresonator for different bit combinations	43
2.23	Measured transmission characteristics of the U slot multiresonator and its post processed signal for various bit combinations	45

2.24	Measured bistatic response of the RFID tag using U slot multiresonator for different bit combinations	46
2.25	Measured bistatic response of the RFID tag using U slot multiresonator and its post processed signal for the bit combination [111 111]	46
2.26	Simulated transmission characteristics of U slot resonator shown in Fig.2.4(a) for various values of W_i (mm)	48
2.27	Measured response of the U slot resonator for two different configurations (a) Transmission characteristics of the resonator (b) Bistatic response	49
2.28	Photograph of fabricated U slot resonator	49
2.29	Layout of multiresonator with two U slots [$L = 30$ mm, $W = 27$ mm, $G = 0.9$ mm, Substrate: loss tangent = 0.0018, $\epsilon_r = 4.3$, $h = 1.6$ mm]	51
2.30	Simulated transmission characteristics of tuning the first U slot in multiresonator with two U slots shown in Fig.2.29($W_2 = 32$ mm, W_1 in mm)	52
2.31	Simulated transmission characteristics of tuning the second U slot in multiresonator with two U slots shown in Fig.2.29 ($W_1 = 47$ mm, W_2 in mm)	53
2.32	Measured response of multiresonator with two U slots for two different configurations (a) Transmission characteristics of the resonator (b) Bistatic response	54
2.33	Photograph of fabricated multiresonator with two U slots	54
2.34	Layout of multiresonator with four U slots [$L = 40$ mm, $W = 27$ mm, $G = 0.9$ mm, Substrate: loss tangent = 0.0018, $\epsilon_r = 4.3$, $h = 1.6$ mm]	55
2.35	Simulated transmission characteristics of tuning the first U slot in multiresonator with four U slots shown in Fig.2.34 ($W_2 = 40$ mm, $W_3 = 34.5$ mm, $W_4 = 28.6$ mm, W_1 in mm)	55
2.36	Simulated transmission characteristics of tuning the second U slot in multiresonator with four U slots shown in Fig.2.34 ($W_1 = 47.5$ mm, $W_3 = 34.5$ mm, $W_4 = 28.6$ mm, W_2 in mm)	56
2.37	Simulated transmission characteristics of tuning the third U slot in multiresonator with four U slots shown in Fig.2.34 ($W_1 = 47.5$ mm, $W_2 = 40$ mm, $W_4 = 28.6$ mm, W_3 in mm)	57
2.38	Simulated transmission characteristics of tuning the fourth U slot in multiresonator with four U slots shown in Fig.2.34 ($W_1 = 47.5$ mm, $W_2 = 40$ mm, $W_3 = 34.5$ mm, W_4 in mm)	58

2.39	Simulated transmission characteristics of tuning the first U slot in multiresonator with six U slots shown in Fig.2.1 ($L = 50$ mm, $W = 37$ mm, $G = 0.9$ mm, $W_2 = 41.2$ mm, $W_3 = 37.1$ mm, $W_4 = 33$ mm, $W_5 = 29.2$ mm, $W_6 = 25.8$ mm, W_1 in mm)	60
2.40	Simulated transmission characteristics of tuning the second U slot in multiresonator with six U slots shown in Fig.2.1 ($L = 50$ mm, $W = 37$ mm, $G = 0.9$ mm, $W_1 = 48.2$ mm, $W_3 = 37.1$ mm, $W_4 = 33$ mm, $W_5 = 29.2$ mm, $W_6 = 25.8$ mm, W_2 in mm) .	61
2.41	Simulated transmission characteristics of tuning the third U slot in multiresonator with six U slots shown in Fig.2.1 ($L = 50$ mm, $W = 37$ mm, $G = 0.9$ mm, $W_1 = 48.2$ mm, $W_2 = 41.2$ mm, $W_4 = 33$ mm, $W_5 = 29.2$ mm, $W_6 = 25.8$ mm, W_3 in mm) . . .	62
2.42	Simulated transmission characteristics of tuning the fourth U slot in multiresonator with six U slots shown in Fig.2.1 ($L = 50$ mm, $W = 37$ mm, $G = 0.9$ mm, $W_1 = 48.2$ mm, $W_2 = 41.2$ mm, $W_3 = 37.1$ mm, $W_5 = 29.2$ mm, $W_6 = 25.8$ mm, W_4 in mm)	63
2.43	Simulated transmission characteristics of tuning the fifth U slot in multiresonator with six U slots shown in Fig.2.1 ($L = 50$ mm, $W = 37$ mm, $G = 0.9$ mm, $W_1 = 48.2$ mm, $W_2 = 41.2$ mm, $W_3 = 37.1$ mm, $W_4 = 33$ mm, $W_6 = 25.8$ mm, W_5 in mm) . . .	64
2.44	Simulated transmission characteristics of tuning the sixth U slot in multiresonator with six U slots shown in Fig.2.1 ($L = 50$ mm, $W = 37$ mm, $G = 0.9$ mm, $W_1 = 48.2$ mm, $W_2 = 41.2$ mm, $W_3 = 37.1$ mm, $W_4 = 33$ mm, $W_5 = 29.2$ mm, W_6 in mm)	65
2.45	Measured response of the multiresonator with six U slots for two different configurations ($L = 50$ mm, $W = 37$ mm, $G = 0.9$ mm, $W_1 = 48.16$ mm, $W_2 = 43.16$ mm, $W_3 = 37.1$ mm, $W_4 = 34$ mm, $W_5 = 29$ mm) (a) Transmission characteristics of the resonator (b) Bistatic response	66
3.1	Proposed eight bit shorted stub multiresonator [$W_a = 32$, $L_a = 60$, $L_1 = 43.71$, $L_2 = 40.21$, $L_3 = 37$, $L_4 = 34.04$, $L_5 = 31.31$, $L_6 = 26.5$, $L_7 = 24.3$, $L_8 = 23.4$, $L_{txn} = 7$, $W = 1$, diameter of the via = 0.8 (All dimensions in mm) Substrate: loss tangent = 0.0018, $\epsilon_r = 4.3$, $h = 1.6$ mm]	70
3.2	Microstrip version of the shorted stub multiresonator	71
3.3	Simulated transmission characteristics of the eight bit shorted stub multiresonator shown in Fig.3.1	71
3.4	Surface current distribution of individual resonators in the shorted stub multiresonator shown in Fig.3.1	72

3.5	Shorted stub resonator and its simulated transmission characteristics [$L_a = 60$, $W_a = 15$, $L_{txn} = 7$, $L = 34.57$, $W = 1$, diameter of the via = 0.8 (All dimensions in mm), Substrate: loss tangent = 0.0018, $\epsilon_r = 4.3$, $h = 1.6$ mm]	73
3.6	Simulated transmission characteristics for various values of L (mm) of shorted stub resonator shown in Fig.3.5(a)	74
3.7	Surface current distribution of shorted stub resonator shown in Fig.3.5(a) at resonant frequency of 2.46 GHz and at a non-resonant frequency of 3 GHz.	75
3.8	Equivalent circuit of shorted stub resonator ($f = 2.46$ GHz) . .	78
3.9	Frequency response of shorted stub resonator equivalent circuit extracted using Agilent ADS	79
3.10	(a) Photograph of the fabricated shorted stub multiresonator (b) Network analyser with device under test	79
3.11	Measured transmission characteristics of the shorted stub multiresonator for the bit combination [1111 1111]	80
3.12	Block schematic for bistatic measurement using shorted stub multiresonator	80
3.13	Experimental setup for bistatic measurement of the RFID tag using shorted stub multiresonator	81
3.14	Measured bistatic response of the RFID tag using shorted stub multiresonator for the bit combination [1111 1111]	81
3.15	Shorted stub multiresonator type 1	82
3.16	Three different types of shorted stub multiresonator (a) Removing the resonator (b) Decoupling the resonator	83
3.17	Simulated transmission characteristics of the shorted stub multiresonator for different bit combinations	84
3.18	Measured transmission characteristics of the shorted stub multiresonator for different bit combinations	85
3.19	Measured transmission characteristics of the shorted stub multiresonator and its post processed signal for various bit combinations	86
3.20	Measured bistatic response of the RFID tag using shorted stub multiresonator for different bit combinations	87
3.21	Measured bistatic response of the RFID tag using shorted stub multiresonator and its post processed signal for the combination [1111 1111]	88

3.22	Simulated transmission characteristics of the shorted stub resonator shown in Fig.3.5(a) for various values of L(mm)	90
3.23	Layout of multiresonator with two shorted stubs [$L_a = 60$, $W_a = 15$, $L_{txn} = 7$, $W = 1$, diameter of the via = 0.8 (All dimensions in mm) Substrate: loss tangent = 0.0018, $\epsilon_r = 4.3$, $h = 1.6$ mm]	90
3.24	Simulated transmission characteristics of tuning the first shorted stub in multiresonator with two shorted stubs shown in Fig.3.23($L_2 = 31$ mm, L_1 in mm)	92
3.25	Simulated transmission characteristics of tuning the second shorted stub in multiresonator with two shorted stubs shown in Fig.3.23 ($L_1 = 42$ mm, L_2 in mm)	93
3.26	Measured response of the multiresonator with two shorted stubs for two different configurations (a) Transmission characteristics of the resonator (b) Bistatic response	94
3.27	Photograph of fabricated multiresonator with two shorted stubs	94
3.28	Layout of multiresonator with four shorted stubs [$L_a = 60$, $W_a = 20$, $L_{txn} = 7$, $W = 1$, diameter of the via = 0.8 (All dimensions in mm) Substrate: loss tangent = 0.0018, $\epsilon_r = 4.3$, height = 1.6 mm]	96
3.29	Simulated transmission characteristics of tuning the first shorted stub in multiresonator with four shorted stubs shown in Fig.3.28($L_2 = 30.1$ mm, $L_3 = 23.8$ mm, $L_4 = 20.2$ mm, L_1 in mm) . . .	96
3.30	Simulated transmission characteristics of tuning the second shorted stub in multiresonator with four shorted stubs shown in Fig.3.28 ($L_1 = 34.3$ mm, $L_3 = 23.8$ mm, $L_4 = 20.2$ mm, L_2 in mm) .	97
3.31	Simulated transmission characteristics of tuning the third shorted stub in multiresonator with four shorted stubs shown in Fig.3.28($L_1 = 34.3$ mm, $L_2 = 30.1$ mm, $L_4 = 20.2$ mm, L_3 in mm) . . .	98
3.32	Simulated transmission characteristics of tuning the fourth shorted stub in multiresonator with four shorted stubs shown in Fig.3.28 ($L_1 = 34.3$ mm, $L_2 = 30.1$ mm, $L_3 = 23.8$ mm, L_4 in mm) .	99
3.33	Simulated transmission characteristics of tuning the first shorted stub in multiresonator with eight shorted stubs shown in Fig.3.1 ($L_2 = 40.4$ mm, $L_3 = 37.2$ mm, $L_4 = 33.6$ mm, $L_5 = 30.5$ mm, $L_6 = 27.1$ mm, $L_7 = 25.8$ mm, $L_8 = 22.7$ mm, L_1 in mm) .	101
3.34	Simulated transmission characteristics of tuning the second shorted stub in multiresonator with eight shorted stubs shown in Fig.3.1 ($L_1 = 42.4$ mm, $L_3 = 37.2$ mm, $L_4 = 33.6$ mm, $L_5 = 30.5$ mm, $L_6 = 27.1$ mm, $L_7 = 25.8$ mm, $L_8 = 22.7$ mm, L_2 in mm) .	102

3.35	Simulated transmission characteristics of tuning the third shorted stub in multiresonator with eight shorted stubs shown in Fig.3.1 ($L_1 = 40.4$ mm, $L_2 = 42.4$ mm, $L_4 = 33.6$ mm, $L_5 = 30.5$ mm, $L_6 = 27.1$ mm, $L_7 = 25.8$ mm, $L_8 = 22.7$ mm, L_3 in mm) .	103
3.36	Simulated transmission characteristics of tuning the fourth shorted stub in multiresonator with eight shorted stubs shown in Fig.3.1 ($L_1 = 42.4$ mm, $L_2 = 40.4$ mm, $L_3 = 37.2$ mm, $L_5 = 30.5$ mm, $L_6 = 27.1$ mm, $L_7 = 25.8$ mm, $L_8 = 22.7$ mm, L_4 in mm) .	104
3.37	Simulated transmission characteristics of tuning the fifth shorted stub in multiresonator with eight shorted stubs shown in Fig.3.1 ($L_1 = 42.4$ mm, $L_2 = 40.4$ mm, $L_3 = 37.2$ mm, $L_4 = 33.6$ mm, $L_6 = 27.1$ mm, $L_7 = 25.8$ mm, $L_8 = 22.7$ mm, L_5 in mm) .	105
3.38	Simulated transmission characteristics of tuning the sixth shorted stub in multiresonator with eight shorted stubs shown in Fig.3.1 ($L_1 = 42.4$ mm, $L_2 = 40.4$ mm, $L_3 = 37.2$ mm, $L_4 = 33.6$ mm, $L_5 = 30.5$ mm, $L_7 = 25.8$ mm, $L_8 = 22.7$ mm, L_6 in mm) .	106
3.39	Simulated transmission characteristics of tuning the seventh shorted stub in multiresonator with eight shorted stubs shown in Fig.3.1 ($L_1 = 42.4$ mm, $L_2 = 40.4$ mm, $L_3 = 37.2$ mm, $L_4 = 33.6$ mm, $L_5 = 30.5$ mm, $L_6 = 27.1$ mm, $L_8 = 22.7$ mm, L_7 in mm) .	107
3.40	Simulated transmission characteristics of tuning the eighth shorted stub in multiresonator with eight shorted stubs shown in Fig.3.1 ($L_1 = 42.4$ mm, $L_2 = 40.4$ mm, $L_3 = 37.2$ mm, $L_4 = 33.6$ mm, $L_5 = 30.5$ mm, $L_6 = 27.1$ mm, $L_7 = 25.8$ mm, L_8 in mm) .	108
3.41	Measured response of the multiresonator with eight shorted stubs for two different configurations ($L_1 = 42.4$ mm, $L_2 = 40.4$ mm, $L_3 = 37.1$ mm, $L_4 = 33.0$ mm, $L_5 = 29.6$ mm, $L_6 = 27.1$ mm, $L_7 = 25.8$ mm)(a) Transmission characteristics of the resonator (b) Bistatic response	109
4.1	Proposed eight bit spurline multiresonator [$W = 0.5$, $W_1 = 10.7$, $W_t = 18$, $L_1 = 11.5$, $L_2 = 11$, $L_3 = 12.6$, $L_4 = 10.5$, $L_5 = 12.6$, $L_6 = 13$, $L_7 = 14$, $L_8 = 16$, $L_t = 45$, $T_1 = 1$, $T_2 = 2$, $T_3 = 3$, $T_4 = 5$, $T_5 = 4$, $T_6 = 3$, $T_7 = 2$, $T_8 = 1$ (All dimensions in mm), Substrate: loss tangent = 0.0018, $\epsilon_r = 4.3$, $h = 1.6$ mm] . . .	113
4.2	Microstrip version of the spurline multiresonator	113
4.3	Simulated transmission characteristics of the proposed eight bit spurline multiresonator shown in Fig.4.1	114
4.4	Surface current distribution of individual resonators in the spurline multiresonator shown in Fig.4.1	114

4.5	Single spurline resonator [$L = L_s + W_s = 17.5$, $S = 1$, $W_1 = 10.7$, $W_t = 18$, $L_t = 45$ (All dimensions in mm), Substrate: loss tangent = 0.0018, $\epsilon_r = 4.3$, $h = 1.6$ mm]	115
4.6	Simulated transmission characteristics of single spurline for different values of W_1 for $S = 1$ mm, $L = L_s + W_s = 17.5$ mm, $W_t = 18$ mm, $\epsilon_r = 4.3$, height = 1.6 mm, loss tangent 0.0018 . . .	116
4.7	Simulated transmission characteristics for various values of length 'L' (in mm) of spurline resonator shown in Fig.4.5	117
4.8	Surface current distribution of spurline resonator shown in Fig.4.5 at resonant frequency of 4.15 GHz and at a non resonant frequency of 5 GHz	118
4.9	Equivalent circuit of the spurline resonator ($f = 4.1$ GHz) . . .	120
4.10	Frequency response of the spurline resonator equivalent circuit extracted using Agilent ADS	120
4.11	(a) Photograph of the fabricated spurline multiresonator (b) Network analyser with device under test	121
4.12	Measured transmission characteristics of the spurline multiresonator for the bit combination [1111 1111]	122
4.13	Block schematic for bistatic measurement of the RFID tag using spurline multiresonator	122
4.14	Experimental setup for bistatic measurement of the RFID tag using spurline multiresonator	123
4.15	Measured bistatic response of the RFID tag using spurline multiresonator for the bit combination [1111 1111]	123
4.16	Spurline multiresonator type 1	124
4.17	Three different types of spurline multiresonator (a) Removing the resonator (b) Decoupling the resonator	125
4.18	Simulated transmission characteristics of the spurline multiresonator for different bit combinations	126
4.19	Measured transmission characteristics of the spurline multiresonator for different bit combinations	127
4.20	Measured transmission characteristics of the spurline multiresonator and its post processed signal for various bit combinations	129
4.21	Measured bistatic response of the RFID tag using spurline multiresonator for different bit combinations	130

4.22	Measured bistatic response of the RFID tag using spurline multiresonator and its post processed signal for the combination [1111 1111]	130
4.23	Simulated transmission characteristics of the spurline resonator shown in Fig.4.5 for various values of L(mm)	131
4.24	Measured response of the tag with single spurline resonator for three different configurations (a) Transmission characteristics of the resonator (b) Bistatic response	133
4.25	Photograph of fabricated spurline resonator	133
4.26	Layout of multiresonator with two spurlines [$W_1 = 10.7$, $W_t = 18$, $L_t = 45$ (All dimensions in mm), Substrate: loss tangent = 0.0018, $\epsilon_r = 4.3$, $h = 1.6$ mm]	134
4.27	Simulated transmission characteristics of tuning the first spurline in multiresonator with two spurlines shown in Fig.4.26 ($L_2 = 10$ mm, L_1 in mm)	135
4.28	Simulated transmission characteristics of tuning the second spurline in multiresonator with two spurlines shown in Fig.4.26 ($L_1 = 18.1$ mm, L_2 in mm)	136
4.29	Measured response of the multiresonator with two spurlines for two different configurations (a) Transmission characteristics of the resonator (b) Bistatic response	138
4.30	Photograph of fabricated multiresonator with two spurlines	138
4.31	Layout of multiresonator with four spurlines [$W_1 = 10.7$, $W_t = 18$, $L_t = 45$ (All dimensions in mm), Substrate: loss tangent = 0.0018, $\epsilon_r = 4.3$, $h = 1.6$ mm]	139
4.32	Simulated transmission characteristics of tuning the first spurline in multiresonator with four spurlines shown in Fig.4.31 ($L_2 = 10.8$ mm, $L_3 = 7.9$ mm, $L_4 = 5.8$ mm, L_1 in mm)	140
4.33	Simulated transmission characteristics of tuning the second spurline in multiresonator with four spurlines shown in Fig.4.31 ($L_1 = 15.1$ mm, $L_3 = 7.9$ mm, $L_4 = 5.25$ mm, L_2 in mm)	141
4.34	Simulated transmission characteristics of tuning of the third spurline in multiresonator with four spurlines shown in Fig.4.31 ($L_1 = 15.1$ mm, $L_2 = 10.8$ mm, $L_4 = 5.25$ mm, L_3 in mm)	142
4.35	Simulated transmission characteristics of tuning the fourth spurline in multiresonator with four spurlines shown in Fig.4.31 ($L_1 = 15.1$ mm, $L_2 = 10.8$ mm, $L_3 = 7.9$ mm, L_4 in mm)	143

4.36	Simulated transmission characteristics of tuning the first spurline in multiresonator with eight spurlines shown in Fig.4.1 ($L_2 = 15$ mm, $L_3 = 13.25$ mm, $L_4 = 12.4$ mm, $L_5 = 10.3$ mm, $L_6 = 8.8$ mm, $L_7 = 7.5$ mm, $L_8 = 7$ mm, L_1 in mm)	145
4.37	Simulated transmission characteristics of tuning the second spurline in multiresonator with eight spurlines shown in Fig.4.1 ($L_1 = 20$ mm, $L_3 = 13.25$ mm, $L_4 = 12.4$ mm, $L_5 = 10.3$ mm, $L_6 = 8.8$ mm, $L_7 = 7.5$ mm, $L_8 = 7$ mm, L_2 in mm)	146
4.38	Simulated transmission characteristics of tuning the third spurline in multiresonator with eight spurlines shown in Fig.4.1 ($L_1 = 20$ mm, $L_2 = 16.5$ mm, $L_4 = 12.4$ mm, $L_5 = 10.3$ mm, $L_6 = 8.8$ mm, $L_7 = 7.5$ mm, $L_8 = 7$ mm, L_3 in mm)	147
4.39	Simulated transmission characteristics of tuning the fourth spurline in multiresonator with eight spurlines shown in Fig.4.1 ($L_1 = 20$ mm, $L_2 = 16.5$ mm, $L_3 = 13.25$ mm, $L_5 = 10.3$ mm, $L_6 = 8.8$ mm, $L_7 = 7.5$ mm, $L_8 = 7$ mm, L_4 in mm)	148
4.40	Simulated transmission characteristics of tuning the fifth spurline in multiresonator with eight spurlines shown in Fig.4.1 ($L_1 = 20$ mm, $L_2 = 16.5$ mm, $L_3 = 13.25$ mm, $L_4 = 12.4$ mm, $L_6 = 8.8$ mm, $L_7 = 7.5$ mm, $L_8 = 7$ mm, L_5 in mm)	149
4.41	Simulated transmission characteristics of tuning the sixth spurline in multiresonator with eight spurlines shown in Fig.4.1 ($L_1 = 20$ mm, $L_2 = 16.5$ mm, $L_3 = 13.25$ mm, $L_4 = 12.4$ mm, $L_5 = 10.3$ mm, $L_7 = 7.5$ mm, $L_8 = 7$ mm, L_6 in mm)	150
4.42	Simulated transmission characteristics of tuning the seventh spurline in multiresonator with eight spurlines shown in Fig.4.1 ($L_1 = 20$ mm, $L_2 = 16.5$ mm, $L_3 = 13.25$ mm, $L_4 = 12.4$ mm, $L_5 = 10.3$ mm, $L_6 = 8.8$ mm, $L_8 = 7$ mm, L_7 in mm)	151
4.43	Simulated transmission characteristics of tuning the eighth spurline in multiresonator with eight spurlines shown in Fig.4.1 ($L_1 = 20$ mm, $L_2 = 16.5$ mm, $L_3 = 13.25$ mm, $L_4 = 12.4$ mm, $L_5 = 10.3$ mm, $L_6 = 8.8$ mm, $L_7 = 7.5$ mm, L_8 in mm)	152
4.44	Measured response of multiresonator with eight spurlines for two different configurations ($L_1 = 19.5$ mm, $L_2 = 15.7$ mm, $L_3 = 13$ mm, $L_4 = 12.4$ mm, $L_5 = 10.3$ mm, $L_6 = 8.8$ mm, $L_7 = 7.8$ mm) (a) Transmission characteristics of the resonator (b) Bistatic response	153

5.1	Proposed eight bit E shaped multiresonator [$W = 10, L_a = 13, L_b = 12, L_1 = 12, L_2 = 11.5, L_3 = 11, L_4 = 10.65, L_5 = 10.4, L_6 = 9.8, L_7 = 9.3, L_8 = 8.8, L_t = 59, W_t = 30, W_a = 3.5, W_b = 3, W_c = 1, G_a = 0.5, G = 1$ (All dimensions in mm), Substrate: loss tangent = 0.0018, $\epsilon_r = 4.3, h = 1.6$ mm]	157
5.2	Microstrip version of the E shaped multiresonator	157
5.3	Simulated transmission characteristics of the eight bit E shaped multiresonator shown in Fig.5.1	157
5.4	Surface current distribution of individual resonators in the E shaped multiresonator shown in Fig.5.1	158
5.5	Simulated transmission characteristics of the eight bit multiresonator in 650 MHz band. [The dimensions of the multiresonator are $L = 10, L_a = 13, L_b = 12, L_1 = 12.2, L_2 = 11.7, L_3 = 11.2, L_4 = 10.7, L_5 = 10.2, L_6 = 9.7, L_7 = 9.2, L_8 = 8.7, L_t = 59, W_t = 30, W_a = 3.5, W_b = 3, W_c = 1, G_a = 0.5, G = 1$ (All dimensions in mm) Substrate: loss tangent = 0.0018, $\epsilon_r = 4.3, h = 1.6$ mm]	159
5.6	(a) E shaped resonator [$L_j = 15, L_i = 9.54, L_k = 14, W = 10, L_l = 20, W_a = 3.5, W_c = 1, G_a = 0.5, W_b = 3$ (All dimensions in mm), Substrate: loss tangent = 0.0018, $\epsilon_r = 4.3, h = 1.6$ mm] (b) Simulated transmission characteristics of the E shaped resonator	160
5.7	(a) C shaped resonator [$L_j = 15, L_k = 14, W = 10, L_l = 20, W_a = 3.5, W_c = 1, G_a = 0.5, W_b = 3$ (All dimensions in mm), Substrate: loss tangent = 0.0018, $\epsilon_r = 4.3, h = 1.6$ mm] (b) Simulated transmission characteristics of C shaped resonator	161
5.8	Simulated transmission characteristics by varying L_i (mm) of the E shaped resonator shown in Fig.5.6(a)	161
5.9	Layout of the eight bit C shaped multiresonator	163
5.10	Simulated transmission characteristics of eight C shaped multiresonator	164
5.11	Surface current distribution of E shaped resonator at resonant frequency of 3.47 GHz and at a non-resonant frequency of 4 GHz.	165
5.12	Equivalent circuit of E shaped resonator ($f = 3.47$ GHz)	169
5.13	Frequency response of E shaped resonator extracted using Agilent ADS	169
5.14	(a) Photograph of the fabricated multiresonator (b) Network analyser with device under test	170

5.15	Measured transmission characteristics of the E shaped multiresonator for the bit combination [1111 1111]	171
5.16	Block schematic for bistatic measurement of the RFID tag using E shaped multiresonator	171
5.17	Experimental setup for bistatic measurement of the RFID tag using E shaped multiresonator	172
5.18	Measured bistatic response of the RFID tag for the bit combination [1111 1111]	172
5.19	E shaped multiresonator type 1	173
5.20	Three different types of E shaped multiresonator (a) Removing the resonator (b) Decoupling the resonator	174
5.21	Simulated transmission characteristics E shaped multiresonator for different bit combinations	175
5.22	Measured transmission characteristics of the E shaped multiresonator for different bit combinations	176
5.23	Measured transmission characteristics of the E shaped multiresonator and its post processed signal for various bit combinations	178
5.24	Measured bistatic response of the RFID tag using E shaped multiresonator for different bit combinations	179
5.25	Measured bistatic response of the the RFID tag using E shaped multiresonator and its post processed signal for the combination [1111 1111]	179
5.26	Simulated transmission characteristics of E shaped resonator shown in Fig.5.6(a) for various values of L_i (mm)	180
5.27	Measured response of the tag with single E shaped resonator for three different configurations(a) Transmission characteristics of the resonator (b) Bistatic response	182
5.28	Photograph of the fabricated E shaped resonator	182
5.29	Layout of multiresonator with two E shaped resonators $L_j = 15$, $L_k = 14$, $W = 10$, $L_l = 40$, $W_a = 3.5$, $G_a = 0.5$, $W_b = 3$ (All dimensions in mm), Substrate: loss tangent = 0.0018, $\epsilon_r = 4.3$, $h = 1.6$ mm	183
5.30	Simulated transmission characteristics of tuning the first E shaped resonator in multiresonator with two E shaped resonators shown in Fig.5.29 ($L_2 = 9$ mm, L_1 in mm)	185
5.31	Simulated transmission characteristics of tuning the second E shaped resonator in multiresonator with two E shaped resonators shown in Fig.5.29($L_1 = 12$ mm, L_2 in mm)	186

5.32	Measured response of the multiresonator with two E shaped resonators for two different configurations by varying the length of middle arm of first E (a)Transmission characteristics of the resonator (b) Bistatic response	187
5.33	Measured response of the multiresonator with two E shaped resonators for two different configurations by varying the length of middle arm of second E (a)Transmission characteristics of the resonator (b) Bistatic response	188
5.34	Photograph of fabricated multiresonator with two E shaped resonators	188
5.35	Layout of multiresonator with four E shaped resonators $L_j = 15$, $L_k = 14$, $W = 10$, $L_l = 40$, $W_a = 3.5$, $G_a = 0.5$, $W_b = 3$ (All dimensions in mm), Substrate: loss tangent = 0.0018, $\epsilon_r = 4.3$, $h = 1.6$ mm	189
5.36	Simulated transmission characteristics of tuning the first E shaped resonator in multiresonator with four E shaped resonators shown in Fig.5.35($L_2 = 8.2$ mm, $L_3 = 7.4$ mm, $L_4 = 6.5$ mm, L_1 in mm)	190
5.37	Simulated transmission characteristics of tuning the second E shaped resonator in multiresonator with four E shaped resonators shown in Fig.5.35 ($L_1 = 8.66$ mm, $L_3 = 7.4$ mm, $L_4 = 6.5$ mm, L_2 in mm)	191
5.38	Simulated transmission characteristics of tuning the third E shaped resonator in multiresonator with four E shaped resonators shown in Fig.5.35 ($L_1 = 8.66$ mm, $L_2 = 8.3$ mm, $L_4 = 5.4$ mm, L_3 in mm)	192
5.39	Simulated transmission characteristics of tuning the fourth E shaped resonator in multiresonator with four E shaped resonators shown in Fig.5.35($L_1 = 8.66$ mm, $L_2 = 8.3$ mm, $L_3 = 7.4$ mm, L_4 in mm)	193
5.40	Simulated transmission characteristics of tuning the first E shaped resonator in multiresonator with eight E shaped resonators shown in Fig.5.1 ($L_2 = 7.6$ mm, $L_3 = 6.9$ mm, $L_4 = 6.52$ mm, $L_5 = 6.1$ mm, $L_6 = 5.4$ mm, $L_7 = 5$ mm, $L_8 = 4.3$ mm, L_1 in mm)	195
5.41	Simulated transmission characteristics of tuning the second E shaped resonator in multiresonator with eight E shaped resonators shown in Fig.5.1 ($L_1 = 7.93$ mm, $L_3 = 6.9$ mm, $L_4 = 6.52$ mm, $L_5 = 6.1$ mm, $L_6 = 5.4$ mm, $L_7 = 5$ mm, $L_8 = 4.3$ mm, L_2 in mm)	196

5.42	Simulated transmission characteristics of tuning the third E shaped resonator in multiresonator with eight E shaped resonators shown in Fig.5.1 ($L_1 = 7.93$ mm, $L_2 = 7.6$ mm, $L_4 = 6.52$ mm, $L_5 = 6.1$ mm, $L_6 = 5.4$ mm, $L_7 = 5$ mm, $L_8 = 4.3$ mm, L_3 in mm)	197
5.43	Simulated transmission characteristics of tuning the fourth E shaped resonator in multiresonator with eight E shaped resonators shown in Fig.5.1 ($L_1 = 7.93$ mm, $L_2 = 7.6$ mm, $L_3 = 6.9$ mm, $L_5 = 6.1$ mm, $L_6 = 5.4$ mm, $L_7 = 5$ mm, $L_8 = 4.3$ mm, L_4 in mm)	198
5.44	Simulated transmission characteristics of tuning the fifth E shaped resonator in multiresonator with eight E shaped resonators shown in Fig.5.1 ($L_1 = 7.93$ mm, $L_2 = 7.6$ mm, $L_3 = 6.9$ mm, $L_4 = 6.52$ mm, $L_6 = 5.4$ mm, $L_7 = 5$ mm, $L_8 = 4.3$ mm, L_5 in mm)	199
5.45	Simulated transmission characteristics of tuning the sixth E shaped resonator in multiresonator with eight E shaped resonators shown in Fig.5.1 ($L_1 = 7.93$ mm, $L_2 = 7.6$ mm, $L_3 = 6.9$ mm, $L_4 = 6.52$ mm, $L_5 = 6.1$ mm, $L_7 = 5$ mm, $L_8 = 4.3$ mm, L_6 in mm)	200
5.46	Simulated transmission characteristics of tuning the seventh E shaped resonator in multiresonator with eight E shaped resonators shown in Fig.5.1 ($L_1 = 7.93$ mm, $L_2 = 7.6$ mm, $L_3 = 6.9$ mm, $L_4 = 6.52$ mm, $L_5 = 6.1$ mm, $L_6 = 5.4$ mm, $L_8 = 4.3$ mm, L_7 in mm)	201
5.47	Simulated transmission characteristics of tuning the eighth E shaped resonator in multiresonator with eight E shaped resonators shown in Fig.5.1 ($L_1 = 7.93$ mm, $L_2 = 7.6$ mm, $L_3 = 6.9$ mm, $L_4 = 6.52$ mm, $L_5 = 6.1$ mm, $L_6 = 5.4$ mm, $L_7 = 5$ mm, L_8 in mm)	202
5.48	Measured response of multiresonator with eight E shaped resonators for two different configurations ($L_1 = 7.86$ mm, $L_2 = 7.5$ mm, $L_3 = 6.8$ mm, $L_4 = 6.5$ mm, $L_5 = 6$ mm, $L_6 = 5.4$ mm, $L_7 = 5.1$ mm) (a) Transmission characteristics of the resonator (b) Bistatic response	203
A.1	Chipless RFID tag with integrated folded monopole antenna [$x_1 = 3$, $x_2 = 9.6$, $x_3 = 11$, $x_4 = 11$, $x_5 = 4$, $x_6 = 6.6$, $x_7 = 11$, $x_8 = 5$, $x_9 = 6.6$, $x_{10} = 3$, $lg_1 = 11.7$ and $Wg_1 = 23.4$ (All dimensions in mm), Substrate: loss tangent = 0.003, $\epsilon_r = 3.7$, $h = 1.6$ mm]	212

A.2	Proposed microstrip fed folded monopole reader antennas [$a_1 = 15.7$, $a_2 = 14$, $a_3 = 7$, $a_4 = 6.6$, $a_5 = 3$, $b_1 = 13.6$, $b_2 = 10$, $b_3 = 7.5$, $b_4 = 9.5$, $b_5 = 3$, $lg_1 = 10.8$, $lg_2 = 18.8$, $lg_3 = 26.8$, $lg_4 = 7$ (All dimensions in mm) Substrate: loss tangent = 0.02, $\epsilon_r = 4.3$, $h = 1.6$ mm]	212
A.3	Chipless RFID tag with integrated antennas (a)Top layer (b)Bottom layer	213
A.4	Reader antenna (a) Top layer (b) Bottom layer	213
A.5	Measurement setup	213
A.6	Measured response of the tag for different bit combinations	214
B.1	(a) Coplanar spurline resonator [$L = 12$, $W = 0.5$, $W_1 = 10.7$, $W_2 = 21.7$ (All dimensions in mm), Substrate: loss tangent = 0.0018, $\epsilon_r = 4.3$, $h = 1.6$ mm] (b) Simulated transmission characteristics of coplanar spurline resonator	216
B.2	(a) Proposed six bit coplanar multiresonator [$W=0.5$, $W_1 = 10.7$, $W_2 = 21.7$, $L_1 = 11$, $L_2 = 12$, $L_3 = 13$, $L_4 = 14$, $L_5 = 18$, $L_6 = 21$, $L_7 = 45$ (All dimensions in mm), Substrate: loss tangent = 0.0018, $\epsilon_r = 4.3$, $h = 1.6$ mm] (b) Simulated transmission characteristics of multiresonator	216
B.3	Photograph of the fabricated multiresonator	217
B.4	Measured transmission characteristics of the multiresonator for different bit combinations	217
B.5	Measured bistatic response of the tag for different bit combinations	218

LIST OF TABLES

1.1	The decades of RFID evolution (Courtsey: J.Landt (Landt, 2005))	3
2.1	Parametric study for the optimisation of slot width (G) of U slot resonator	27
2.2	Computed values of W_i for different resonant frequencies on various substrates	30
2.3	Material properties of C-MET LK-4.3 substrate	33
2.4	Proposed method of code word allocation for the U slot resonator	50
2.5	Frequency band (Δf) and resonant frequency (f) of multiresonator with two U slots (All values in GHz)	52
2.6	Frequency band (Δf) and resonant frequency (f) of multiresonator with four U slots (All values in GHz)	53
2.7	Frequency band (Δf) and resonant frequency (f) of multiresonator with six U slots (All values in GHz)	59
2.8	Performance comparison of different chipless RFID tags	68
3.1	Computed values of L for different resonant frequencies on various substrates	75
3.2	Proposed method of code word allocation for the shorted stub resonator	89
3.3	Frequency band (Δf) and resonant frequency (f) of multiresonator with two shorted stubs (All values in GHz)	91
3.4	Frequency band (Δf) and resonant frequency (f) of multiresonator with four shorted stubs (All values in GHz)	95
3.5	Frequency band (Δf) and resonant frequency (f) of multiresonator with eight shorted stubs (All values in GHz)	100
3.6	Performance comparison of different chipless RFID tag	111
4.1	Parametric study for the optimisation of slot width ‘S’ of spurline resonator	116

4.2	Computed values of L for different resonant frequencies on various substrates	119
4.3	Proposed method of code word allocation for the spurline resonator	132
4.4	Frequency band (Δf) and resonant frequency (f) of multiresonator with two spurline resonators (All values in GHz)	137
4.5	Frequency band (Δf) and resonant frequency (f) of multiresonator with four spurlines (All values in GHz)	140
4.6	Frequency band (Δf) and resonant frequency (f) of multiresonator with eight spurlines (All values in GHz)	144
4.7	Performance comparison of different chipless RFID tag	155
5.1	Variation of f , Δf , FBW for different values of length of the upper arm(L_j) of the C shaped resonator	162
5.2	Variation of f , Δf , FBW for different values of length of the middle arm(L_i) of the E shaped resonator	163
5.3	Computed values of L_i for different resonant frequencies on various substrates	166
5.4	Proposed method of code word allocation for the single resonator	181
5.5	Frequency band (Δf) and resonant frequency (f) of multiresonator with two E shaped resonators (All values in GHz) . . .	184
5.6	Frequency band (Δf) and resonant frequency (f) of multiresonator with with four E shaped resonators (All values in GHz)	190
5.7	Frequency band (Δf) and resonant frequency (f) of multiresonator with eight E shaped resonators (All values in GHz) . .	194
5.8	Performance comparison of different chipless RFID tag	205
6.1	Comparison of proposed multiresonators based on absence or presence coding technique	209
6.2	Comparison of proposed multiresonators based on frequency shift coding technique	209

ABBREVIATIONS

ADS	Advanced Design System
BAP	Battery Assisted Passive
CPW	Coplanar Waveguide
CST MWS	Computer Simulation Tool Microwave Studio
CW	Continuous Wave
FBW	Fractional Bandwidth
FSC	Frequency Shift Coding
IDT	Inter Digital Transducer
IoT	Internet of Things
PNA	Programmable Network Analyzer
RFID	Radio Frequency Identification
TDR	Time Domain Reflectometry
UWB	Ultra Wide Band

NOTATIONS

c	Velocity of light
h	Height of the dielectric substrate
Q	Quality factor
S_{21}	Transmission coefficient scattering parameter
Z_0	Characteristic impedance
α	Attenuation constant
β	Phase constant
γ	Propagation constant
ϵ_r	Relative permittivity
ϵ_{eff}	Effective permittivity
λ	Free space wavelength
λ_g	Guide wavelength
σ	Conductivity

CHAPTER 1

RFID TECHNOLOGY

1.1 Introduction

Radio frequency identification (RFID) is an electronic tagging technology which utilizes radio frequency waves to remotely detect and identify a device or an object containing an encoded tag. It serves as a radio technology to achieve internet of things (IoT) vision to create a worldwide network of smart objects (Bolic *et al.*, 2015). If all objects are equipped with radio tags, they could be identified and inventoried. To fulfil these functions, RFID tags must be data dense, inexpensive and energy efficient (Noor *et al.*, 2016). However, their widespread use is limited due to the high cost of silicon chip required. Hence, cost effective solutions are of great need. Today, RFID systems are being developed with tags that do not contain silicon chips. These tags are known as ‘chipless’ tags.

The concept of RFID was introduced during world war II. Radars used to identify the presence of an object gave no additional information about it apart from its size and location. To identify an aircraft as ‘friend or foe’ was of particular importance. A Scottish physicist named Sir Robert Alexander Watson-Watt developed a system called IFF - identification friend or foe to overcome this problem (Roberti, 2005; Bowden, 1985). A transponder that was placed on each aircraft, received signals from radar stations on the ground and broadcasted a signal back which identified the aircraft as friendly. This system formed the basis of RFID. In 1945, the first RFID tag was developed by

Leon Theremin known as ‘the Thing’, as an espionage tool for Russia, which retransmitted incident radio waves with audio information. It was embedded in a carved wooden plaque of the great seal of the United States of America (USA) and offered to the US ambassador in Moscow (Tedjini *et al.*, 2013). The gift was kept in the US embassy for many years and used by Russia for spying.

Stockman in his landmark paper on ‘communication by means of reflected power’ in 1948, demonstrated that by alternating the load of the tag antenna, it was possible to vary the amount of reflected power and therefore perform modulation (Stockman, 1948). It was termed as antenna load modulation. This new form of wireless technology was subsequently known as RFID. Further improvements were regularly introduced in RFID systems with the advancements in electronics and communication technologies like the use of transistors, integrated circuits, microprocessors and communication networks. The changes in the ways of doing business and other applications also influenced the structure and configuration of RFID systems. The evolution of RFID as explained in (Landt, 2005) is shown in Table 1.1.

RFID systems are increasingly used in many applications involving tracking and handling of assets and documents, security and access control, supply chain management etc. (Whitmore and Xui, 2015; Ramirez *et al.*, 2015; Rezaiesarlak and Manteghi, 2014; Zhu *et al.*, 2012; Chuang and Shaw, 2007; Shutzberg, 2004; Want, 2004b). In a typical RFID system having many tags and readers, it is possible to track the current location of a uniquely identifiable item by attaching an RFID tag to it. Efficient and reliable supply chain management can be implemented for business activities with the use of RFID technology. It can be used to ensure that the right goods are available in the right place without lapses or errors. As right information can be made available in real-time, administration and planning processes can be improved considerably. RFID systems

Table 1.1: The decades of RFID evolution (Courtesy: J.Landt (Landt, 2005))

Decade	Event
1940 - 1950	Functionality of radar improved for identifying aircraft as friend or foe. RFID concept introduced in 1948.
1950 - 1960	Early explorations of RFID technology, laboratory experiments.
1960 - 1970	Development of the theory of RFID. Start of applications, field trials.
1970 - 1980	Explosion of RFID development. Tests of RFID accelerate. Very early adopter implementations of RFID.
1980 - 1990	Commercial applications of RFID enter mainstream.
1990 - 2000	Emergence of standards. RFID widely deployed and becomes a part of everyday life.
2000 - 2010	Minaturisation and power saving in RFID tags. Introduction of chipless RFID tags.
2010 onwards	RFID research and development continues.

are being widely used for perfect circulation operations and asset tracking in libraries (Aruna *et al.*, 2014; Mahajan *et al.*, 2010; Butters *et al.*, 2006). Other applications include, stock management in super markets, tracking equipment, medical persons and patients in large hospitals, parking access control, luggage tracking in airlines etc (Jones *et al.*, 2015; Slack *et al.*, 2013; Mun *et al.*, 2007; Fisher and Monahan, 2008).

Various games have been developed for kids based on wearable RFID technology systems, the first being Zowie, followed by Music blocks, Ping pong plus, and Tagaboo (Elena de la, 2013; Konkel *et al.*, 2004). Another major application of RFID is tracking the movements of animals. Ensuring that the correct feed is provided to specific cattle among a herd of hundreds is difficult and time consuming. However this can be achieved automatically and cost effectively using RFID systems (Voulodimos *et al.*, 2010). RFID can also function as an

electronic key to control access to restricted areas (Want, 2004a).

1.2 RFID system

A typical RFID system is shown in Fig.1.1. The system consists of

- RFID tag
- RFID reader
- Host system

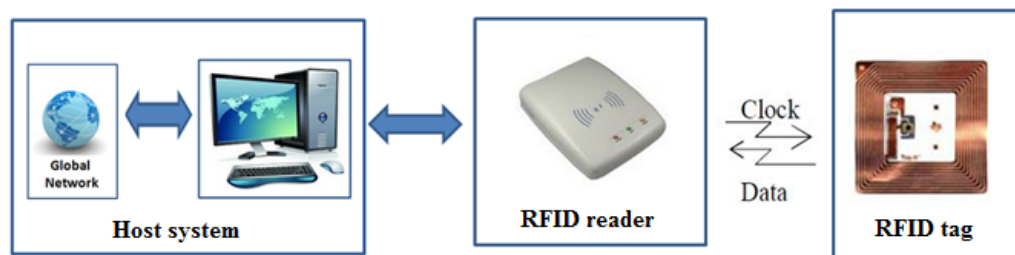


Fig. 1.1: RFID system

1.2.1 RFID tag

RFID tag is attached to an item that is to be identified or tracked. A tag is typically composed of an antenna and integrated circuitry. The identification code and sometimes additional information like specification of the item or any special care while handling is stored in the integrated circuitry. RFID tags can be classified based on different attributes like frequencies used, sources of power for operation or the presence of a silicon chip (Want, 2004b; Klaus, 2003; Finkenzeller, 2003, 1999) as illustrated in Fig.1.2.

RFID tags are available at different frequency bands like low frequency (LF), high frequency (HF), ultra high frequency (UHF) and microwave bands. LF

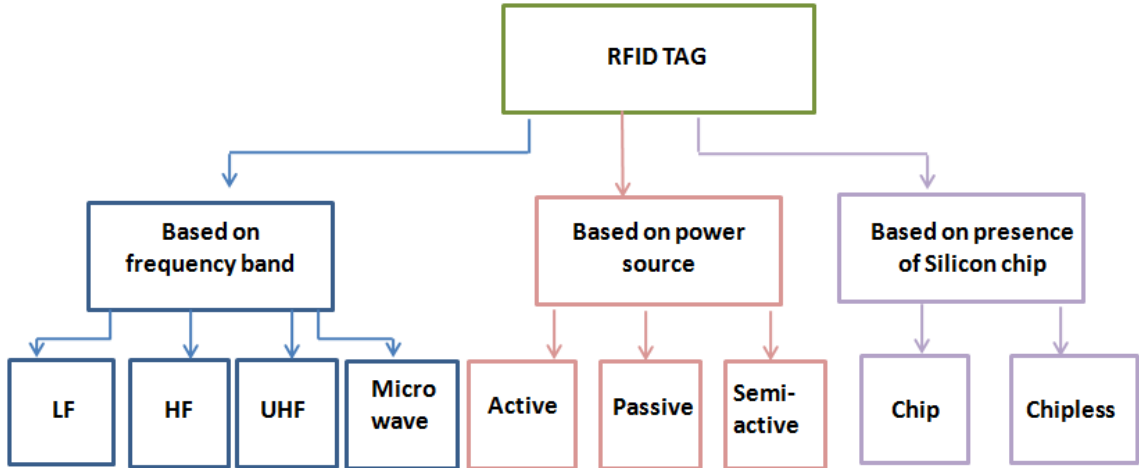


Fig. 1.2: RFID tag classification

(120 KHz - 150 KHz) and HF (13.56 MHz) RFID systems can communicate up to 1 m read range with the use of inductive coupling. UHF RFID tags, typically operating in 866 MHz - 868 MHz (European Union) and 902 MHz - 928 MHz (North American continent) have a longer read range up to 10 m or more, with a faster data rate compared to LF and HF tags. Commonly used frequencies at microwave band for RFID technologies are 2.45 GHz and 5.8 GHz having a range of 1 to 2 m.

Depending on the power source for operation, RFID tags are classified as passive tags, active tags and semiactive tags. **Passive RFID tags** consist of a silicon chip and an antenna circuit (Borriello, 2005; Lehpamer, 2012) as shown in Fig.1.3. They have neither onboard power source nor an active transmitter. The electromagnetic signal transmitted by the RFID reader inductively powers the tag, which helps it to retransmit its information. The impedance matching between the antenna and the tag circuitry determines the amount of energy that can be transferred between them. Since the tag has a limited supply of power, the amount of data transmitted is restricted. It is typically not more than the identification code. The read range of the tag mainly depends on the antenna circuit and size.

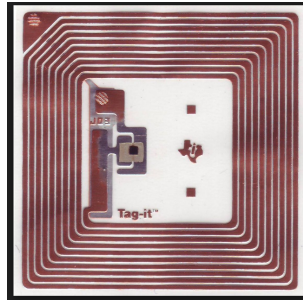


Fig. 1.3: Passive RFID tag (Courtsey: Cisco (Cisco, May 2008))

RFID tags with onboard power source and associated electronics for performing specialized tasks are called **Active RFID tags**(Cho and Baek, 2006). The active tag can be designed with a variety of specialized electronic devices, including microprocessors, different types of sensors, or I/O devices as shown in Fig.1.4. Active tags are larger in size and more expensive than passive tags, but they store more data and are commonly used for high-value asset tracking. The cost of the tag depends on the amount of memory, the battery life required, the type of sensors and the ruggedness.



Fig. 1.4: Active RFID tag (Courtsey:Digikey Electronics(www.digikey.com))

Semiactive RFID tags also have onboard battery and electronics for performing specialized tasks. The battery in this case is used only to operate the chip. Like the passive tag, the energy in the electromagnetic field wakes up the tag and transmits the encoded data to the reader. These tags are sometimes called battery assisted passive (BAP) tags.

Based on the presence or absence of silicon chip, RFID tags can be classified as tags containing silicon chip, or with out a chip termed as chipless RFID tag.

The thesis focuses on **Chipless RFID tags**, which are discussed in detail in Section 1.3.

1.2.2 RFID reader

A transceiver and antenna are usually combined to form an RFID reader. It sends the interrogation signals to an RFID tag that is being identified. The RFID reader communicates with tags that are within its interrogation zone, depending on its power output and the radio frequency used. The reader decodes the data encoded in the tag's integrated circuit and the data is passed to the host computer for processing. Readers can be placed in fixed locations in an organisation, or can be integrated to a hand held device such as a portable scanner.

1.2.3 Host system

Host system contains software components that acts as a bridge between the RFID hardware components and the host application software. It configures and manages the hardware, processes tag data, filters out duplicate tag reads and aggregates the data that is passed along to back-end applications. This can be a dedicated computer at each facility where RFID interrogators are deployed or on a networking appliance where the technology is used. The process application software can then update the data in the server through the internet.

1.3 Chipless RFID tags

Chipless RFID tags do not require any integrated circuit to store information. These are low cost tags that provide the minimal function as a read only device with a permanent unique identification number. The major challenge in designing a chipless RFID tag is data encoding and transmission. An entirely different technique compared to conventional tag is employed to encode data in spectral domain or in time domain. Each chipless RFID tag contains a planar passive circuit which reflects back a unique electromagnetic signal to the reader (Chen *et al.*, 2007; Preradovic and Karmakar, 2010), thus revealing the identity of the tag. Chipless RFID tags can be broadly classified as follows :

1. Time domain reflectometry based chipless RFID tags
2. Spectral signature based chipless RFID tags

1.3.1 Time domain reflectometry based chipless RFID tags

In time domain reflectometry (TDR) based technique, chipless tags are interrogated by sending a signal from the reader in the form of a pulse and listening to the echoes of the pulse sent by the tag. A train of pulses is thereby created, which is used for identification. The major kinds of TDR tags reported in literature include surface acoustic wave tags and delay line based tags.

Surface acoustic wave tag consisting of a piezoelectric crystal is an example of a non printable TDR based chipless RFID tag. The interrogation pulse is converted to an acoustic wave using an inter digital transducer (IDT). The wave propagates across the piezoelectric crystal and is reflected by a number of reflectors, which create a train of pulses with phase shifts as shown in Fig.1.5.

The train of pulses is converted back to an electromagnetic wave using the IDT and detected at the reader end where the tag's identity is decoded (S Harma *et al.*, 2009; Pavlina and Malocha, 2010; Han *et al.*, 2008; Liu and Yao, 2008; Harma *et al.*, 2008, 2006; Schuster *et al.*, 2005; Hartmann, 2002; Plessky *et al.*, 1995).

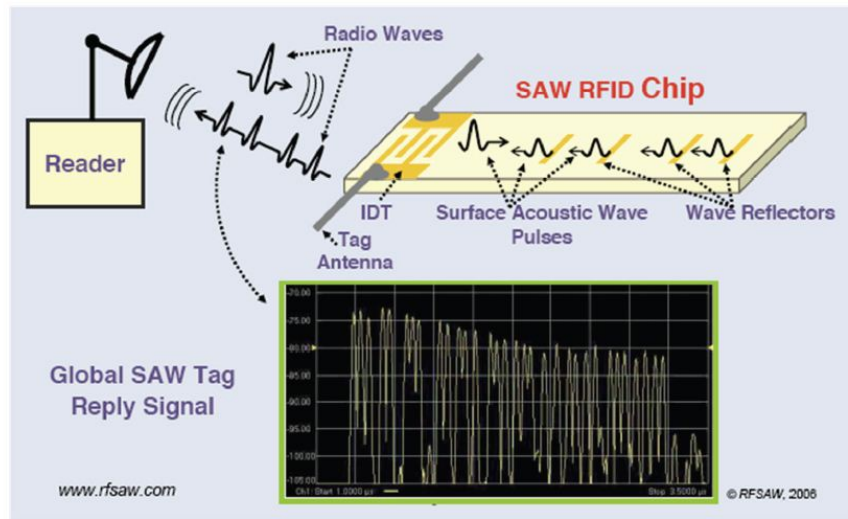


Fig. 1.5: System architecture of SAW tag. Courtesy:(Hartmann, 2002)

Delay line based chipless tags that operate using microstrip discontinuity are reported in (Vemagiri *et al.*, 2007; Shrestha *et al.*, 2007; Chamarti and Varahramyan, 2006). The tag consists of two microstrip transmission line branches - a relatively short straight branch and a longer meandered branch as shown in Fig.1.6. The ends of the microstrip branches are either terminated with a resistor equal to characteristic impedance Z_0 or with ports of similar impedance to avoid reflections. The signals in each of the branches get delayed differently. The tapped signals with different time delays are superimposed onto the straight branch to produce an output signal. Only eight bits were successfully tested with delay line method, which shows the limited potential of this technology.

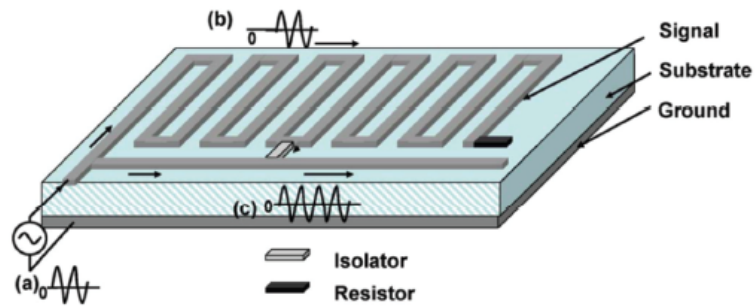


Fig. 1.6: Schematic diagram of transmission delay line based ID generation circuit
 Courtesy:A. Chamarti (Chamarti and Varahramyan, 2006)

1.3.2 Spectral signature based chipless RFID tags

Spectral signature based chipless RFID tag encodes data in the frequency spectrum with its unique spectral signature using multiresonators. Multiresonators are designed using standard planar microstrip or coplanar waveguide resonant structures. They are printed on thick, thin, and flexible laminates and polymer substrates. Capacitively tuned dipoles first reported by Jalaly (Jalaly and Robertson, 2005a) is shown in Fig.1.7.

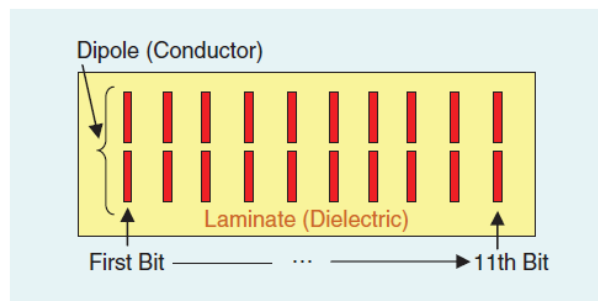


Fig. 1.7: Capacitively tuned dipoles arranged as a 11-bit chipless RFID tag. (Courtesy: I. Jalaly (Jalaly and Robertson, 2005a))

The general structure and operation of spectral signature based chipless RFID tag is shown in Fig.1.8. The tag is interrogated by the reader by sending a frequency swept continuous wave signal with constant amplitude and phase. The tag encodes its spectral signature into the interrogation signal spectrum using a multiresonating circuit usually a multiple stop band filter. The stop band resonances introduce magnitude attenuation and phase jumps to the trans-

mitted interrogation signal at their resonant frequencies which are detected as abrupt amplitude attenuations and phase jumps by the RFID reader. Fig.1.9 shows some of the multiresonators reported in the literature (Herrojo *et al.*, 2016; Casula, 2014; Bhuiyan *et al.*, 2013; Gupta and Jiang, 2013; Sarhadi *et al.*, 2013; Girbau *et al.*, 2012*b*; Chakraborty, 2011; Narkcharoen and Pranonsatit, 2011; Yang *et al.*, 2009; Balbin and Karmakar, 2009*b*; Preradovic *et al.*, 2008*a,b*; Mukherjee, 2007; Vena *et al.*, 2011*a*; Costa *et al.*, 2013; Jang *et al.*, 2010; Vena *et al.*, 2013*a*; Weng *et al.*, 2013; Balbin and Karmakar, 2009*a*).

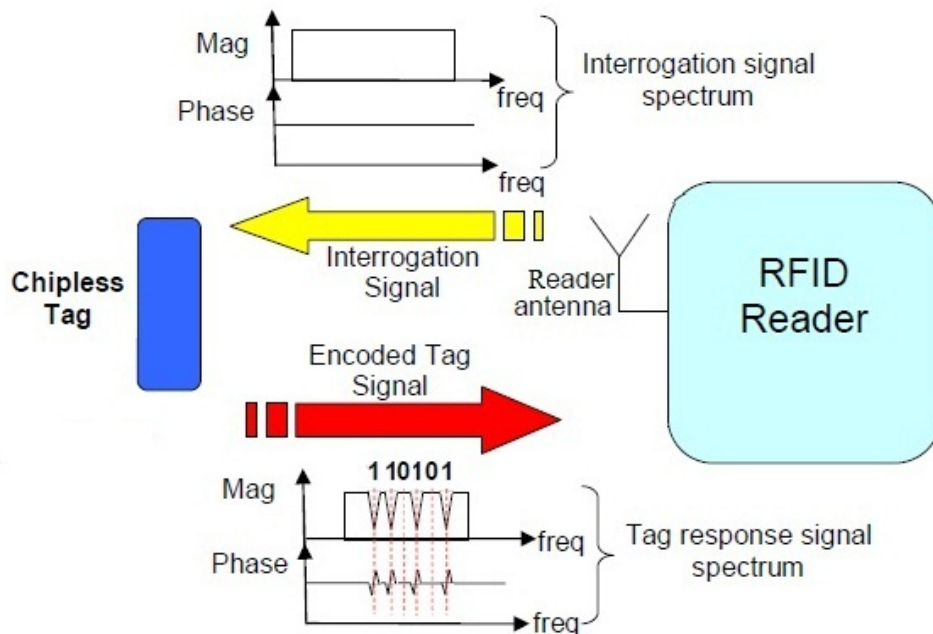


Fig. 1.8: General structure and operation of spectral signature based chipless RFID tag (Courtesy: S. Preradovic(Preradovic and Karmakar, 2009))

1.4 Motivation for the present work

Considerable research results are reported in the field of passive tags containing silicon chip. The tags so developed are employed for many commercial applications. Spectral signature based chipless RFID tag is a relatively new entry

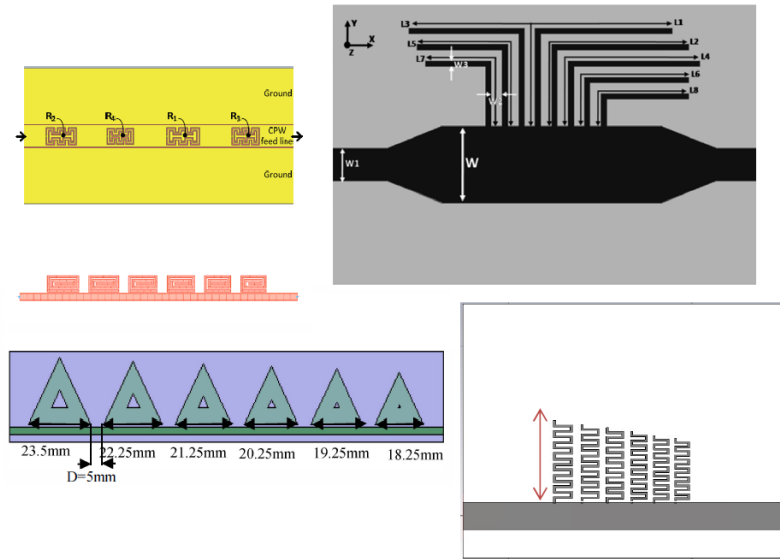


Fig. 1.9: Some of the multiresonators reported in the literature

in RFID technology (Jalaly and Robertson, 2005a). Nevertheless, there exists a research gap in the development of chipless RFID tag with enhanced bit encoding capacity. The research focuses on the development of multiresonator circuits for spectral signature based chipless RFID tag applications.

The main objectives of the work presented in the thesis are to :

- Design compact multiresonators for chipless RFID tag applications.
- Improve design flexibility by generating various bit combinations for data encoding with minimal layout changes.
- Develop methods to enhance the data encoding capacity of the tags.
- Develop simple design formula for the multiresonators.
- Design an equivalent circuit of the multiresonator for circuit analysis.

1.5 Potential applications

Chipless RFID tags based on multiresonators are proposed for applications such as barcode replacement for conveyor belt applications (Preradovic *et al.*, 2008b), tags integrated with sensor for ubiquitous environment monitoring (Preradovic and Menicanin, 2012; Vena *et al.*, 2012b; Amin and Karmakar, 2011, 2012; Amin *et al.*, 2014) wearable multiresonators to sense hand gestures (Le *et al.*, 2015), automatic reading of road signs (Reichardt *et al.*, 2010) and wireless crack sensing (Rodrigues *et al.*, 2015; Dey *et al.*, 2014; Kalansuriya *et al.*, 2012). The prototypes proposed in this work can be extended to the above mentioned applications and also in many potential applications that require features like high security and high data encoding capacity.

1.6 Methodology

This section discusses the simulation, optimization, fabrication, measurement procedures and data encoding methods for RFID tags. This methodology is followed for the development of the RFID tags discussed in Chapters 2 to 5.

1.6.1 Simulation and optimization

The simulation models of the multiresonators for the RFID tags are developed in CST microwave studio[®] (CST MWS[®]), a specialist tool for the 3D electromagnetic simulation of high frequency components, enabling fast and accurate analysis. It includes transient solver module, transmission line matrix solver, frequency domain solver module, eigenmode solver module, integral equation solver module, multilayer solver module and asymptotic solver module. CST MWS[®] is based on the description of electromagnetic problems by differential

Maxwell equations that are solved by the finite difference method (CST, 2009).

From the simulated results of the modeled multiresonator, the S parameters can be plotted as a function of frequency. The structure can then be appropriately optimized for the desired response. The surface current and field distributions can also be determined at the specified frequencies.

1.6.2 Fabrication

Prototypes of the multiresonators for this research work have been realized on the substrate CMET LK-4.3 with dielectric constant 4.3, loss tangent 0.0018 and height 1.6 mm. The structures are printed on the laminates by ultraviolet lithography. The lithography process is detailed in Fig.1.10.

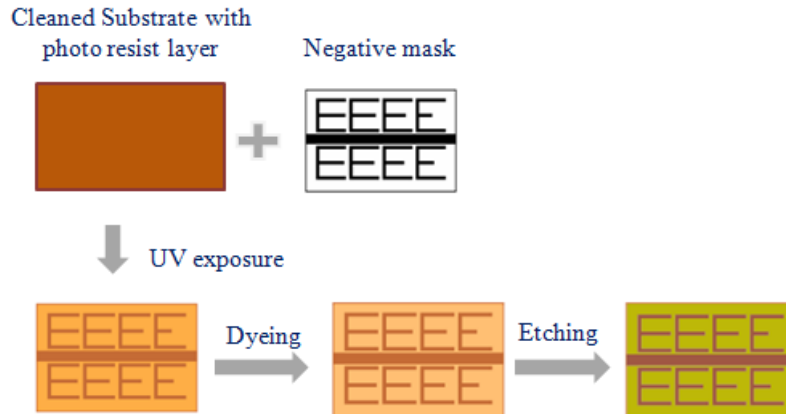


Fig. 1.10: Ultraviolet lithography process

1.6.3 Measurement

Agilent PNA E8362B network analyzer is used as test equipment for measurement of transmission characteristics of the multiresonator. The RFID tag based on multiresonator incorporates two wide band antennas, one for receiving

the interrogation signal from reader and the other for retransmitting the encoded signal from the multiresonator to the reader thereby increasing the read range. Measurement setup proposed by S. Preradovic et.al (Preradovic *et al.*, 2008*a*, 2009) is adopted for the validation of the tag. Agilent PNA E8362B network analyser with transmitted power of 0 dBm along with two cross polarized medium gain (10 dB) horn antennas form the RFID reader setup. The horn antennas are used for transmission of the continuous wave interrogation signal and reception of the retransmitted signal. The block schematic for bistatic measurement is shown in Fig.1.11.

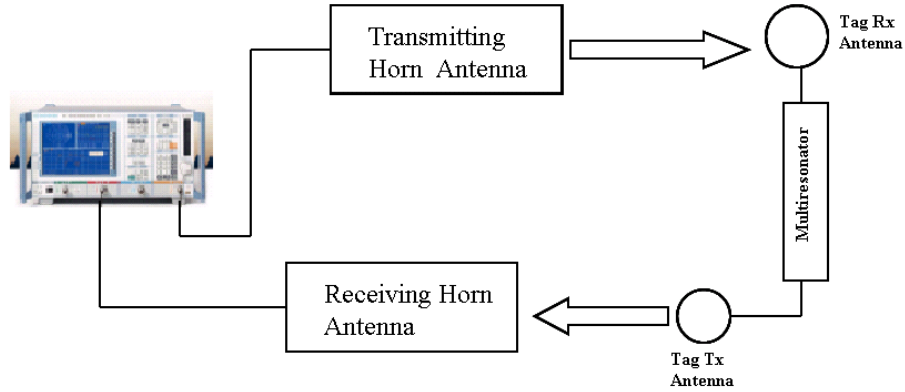


Fig. 1.11: Block schematic for bistatic measurement

1.6.4 Data encoding methods

Two different methods of encoding tag identity are used in this work

1. Absence or presence coding technique
2. Frequency shift coding technique

In **Absence or presence coding technique**, one resonator represents one bit of information. The presence of resonance at a predefined frequency is used to encode a logic 1 and the absence of resonance is used to encode a logic 0. Thus with ‘n’ resonators, only 2^n combinations are possible.

Frequency shift coding technique is applied to enhance the data encoding capacity and security of the tag. This technique allows an enhancement in coding efficiency, by encoding more than one bit per resonator. High security tags can be designed using this technique in the sense that, visually the tag seems to be similar but the identification code will be different. The coding techniques are detailed in Section 2.5.

1.7 Thesis outline

The thesis is organised as six chapters and two appendices as shown in Fig.1.12.

Chapter 1 gives an introduction to RFID systems, RFID applications and classification of RFID tags. The development of chipless RFID technology and the principle of working are explained. The chapter also explains the motivation for the present work, methodology adopted and gives a note on organisation of the thesis.

Different types of multiresonators designed for chipless RFID tag application are explained in **Chapter 2** to **Chapter 5**. **Chapter 2** deals with the use of U slot resonators as spectral signature encoding circuits. U slot resonators are etched on the ground plane of the substrate CMET/LK 4.3 with a transmission line running on the other side. Each U slot resonates at frequency corresponding to a length $\lambda_g/2$. Multiple resonance is achieved using six U slot resonators of varying dimensions. A comprehensive parametric study of single U slot resonator is performed using CST MWS[®]. Results of the analysis along with the parametric studies lead to the design equations using multivariable regression analysis. Equivalent circuit of the resonator is developed using Agilent advanced design system. Implementation of two different data encoding methods, namely absence or presence coding technique and frequency shift cod-

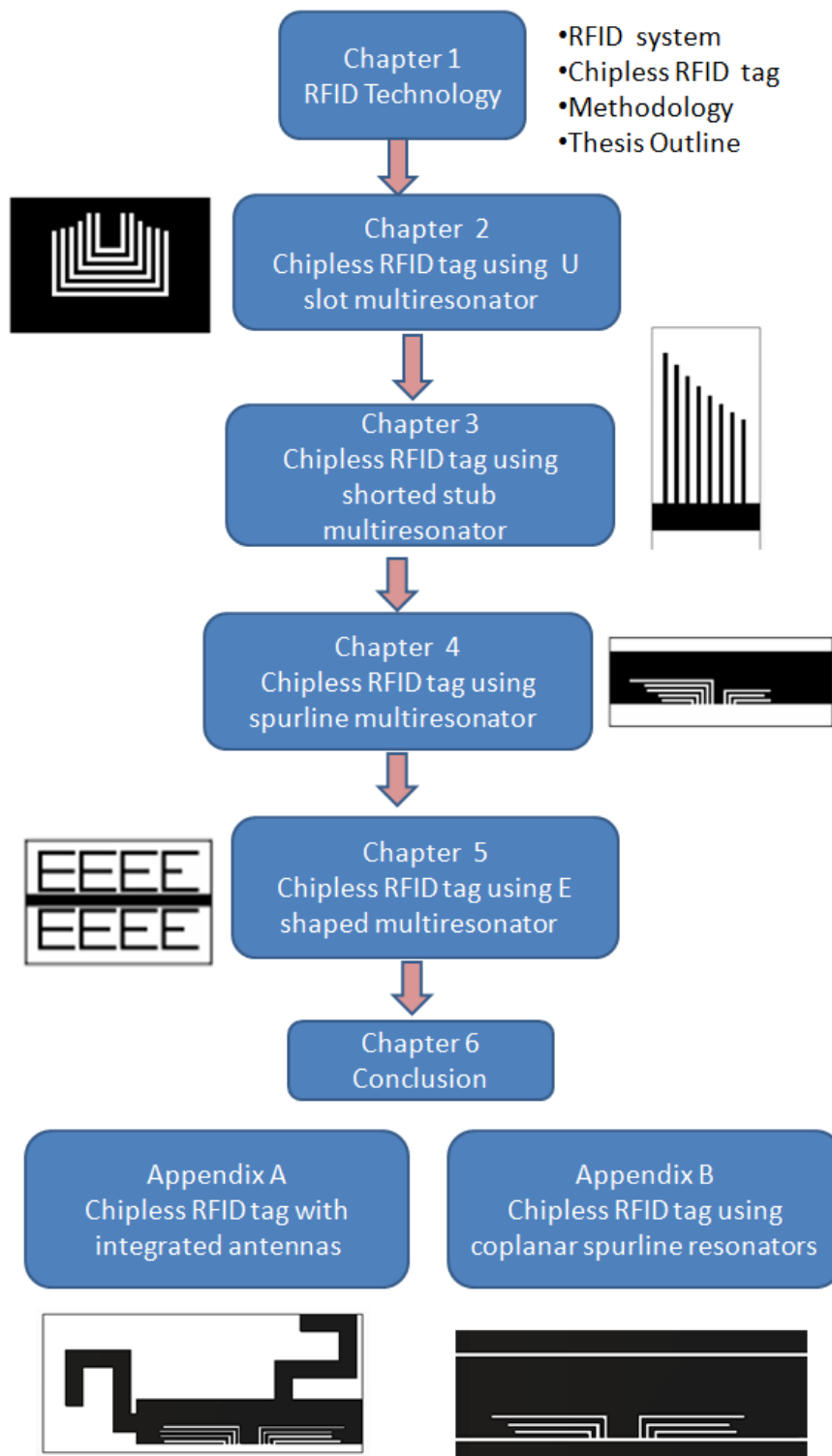


Fig. 1.12: Thesis outline

ing (FSC) technique are presented. Improved bit encoding capacity is achieved using FSC. The multiresonator can be used as an RFID tag for access control applications where the tag is in close proximity of the reader. However, for increasing the read range, two cross polarized disc monopole antennas, one for receiving the interrogation signal from reader and the other for retransmitting the encoded signal, are integrated to the multiresonator. The RFID reader setup comprises an Agilent PNA E8362B network analyser with transmitted power of 0 dBm along with two cross polarized medium gain (10 dB) horn antennas. Bistatic measurements validate the functionality of the tag. Similar procedure is followed for all resonators presented in Chapters 3 to 5.

The use of shorted stub resonators as spectral signature encoding circuits is discussed in **Chapter 3**. The resonator consists of a half wavelength long stub connected to a microstrip transmission line at one end and shorted to ground through a via at the other end. Multiple resonance is achieved by using eight shorted stub resonators of varying dimensions.

Chapter 4 discusses the use of spurline resonators as spectral signature encoding circuits. A spurline resonator is a L- shaped slot etched in a microstrip transmission line. Each resonator is excited at the resonant frequency corresponding to a length $\lambda_g/4$. Multiple resonance is achieved by engraving eight spurline resonators of varying dimensions in the transmission line.

Multiresonator based chipless RFID tag using eight E shaped resonators coupled to a microstrip transmission line is discussed in **Chapter 5**. Multiple resonances is achieved by modifying the length of middle arm of the E shaped resonators.

Chapter 6 highlights the results and important findings of this research work. A comparison of the features of the designed multiresonators based on absence or presence coding technique and frequency shift coding technique is

included. The chapter concludes with suggestions for future research.

Appendix A describes the chipless RFID tag with integrated antennas. The implementation of multiresonator using coplanar spurline resonators is discussed in **Appendix B**. The thesis includes the bibliography and a list of publications by the author in the related field.

CHAPTER 2

CHIPLESS RFID TAG USING U SLOT MULTIRESONATOR

2.1 Introduction

Multiresonator is an essential component of spectral signature based chipless RFID tag. It is a combination of multiple filtering sections which are used to encode the tag identity. The amplitude of the interrogating signal sent by the reader is modulated in the form of amplitude attenuations at the resonant frequencies of the multiresonator, thus revealing the identity of the tag.

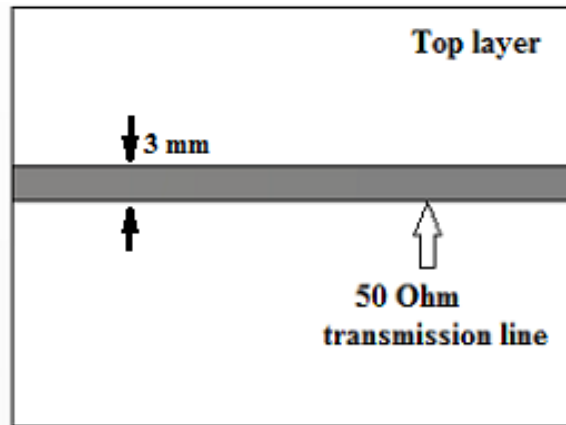
Different approaches for designing spectral signature based chipless tags are reported in (Jalaly and Robertson, 2005*b*; Tikhov and Min, 2008; McVay *et al.*, 2006; Preradovic *et al.*, 2008*a*; Preradovic and Karmakar, 2009; Preradovic *et al.*, 2008*b*; Sakouhi *et al.*, 2014; Nijas *et al.*, 2012, 2013; Narkcharoen and Pranonsatit, 2011; Kim *et al.*, 2010; Casula, 2014; Nair *et al.*, 2011; Girbau *et al.*, 2012*a*; Jalil, 2014; Nair Sreejith *et al.*, 2012). In these tags, each data bit is identified as the presence or absence of a resonance at a predetermined frequency. Majority of the tags are designed on microstrip based resonators. Capacitively tuned dipole for RFID barcode was first reported by Jalaly and Robertson (Jalaly and Robertson, 2005*b*). Here the tag consists of arrays of identical microstrip dipoles capacitively tuned to different resonant frequencies. When interrogated, the reader detects the resonant frequency of each dipole. With ‘n’ resonant dipoles, potentially 2^n items in the field can be tagged and

identified. Tag using inductance in between the dipole arms to tune the resonance is presented in (Tikhov and Min, 2008). Space-filling curves using fractal geometries such as Hilbert and Peano curves to generate the frequency signature from backscattered resonances are reported in (McVay *et al.*, 2006). To encode the data, space-filling curves need significant layout modifications while capacitively tuned dipoles have undesired mutual coupling effects between the dipole elements and large physical size.

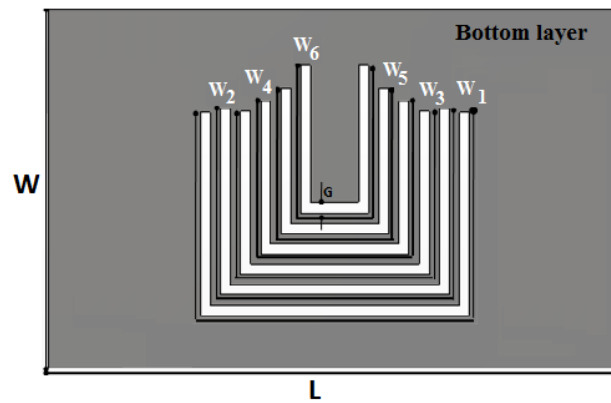
Chipless RFID tags using a set of spiral resonators for various applications are proposed by Stevan Preradovic (Preradovic and Karmakar, 2009; Preradovic *et al.*, 2008*a,b*). Multiresonance is achieved by using cascaded multiple spiral resonators placed next to a microstrip line. The power difference between reflected power levels corresponding to the presence or absence of a bit is only of the order of 1 dB. Chipless RFID tag using meander complementary split ring resonator is proposed in (Sakouhi *et al.*, 2014). The tag requires a frequency band of 4 GHz to 7GHz to encode four bits. An eight bit chipless RFID tag using quarter wave open stub resonator is reported in (Nijas *et al.*, 2012, 2013). The tag encodes eight bits in a frequency band from 2.08 GHz to 4.03 GHz. Chipless RFID multiresonator, fabricated by fill until full (FuF) technique is presented in (Narkcharoen and Pranonsatit, 2011). It reports a multiresonator which requires a frequency band of 1.94 GHz to 3.49 GHz to encode three bits. Chipless RFID tag using a bandstop resonator whose frequency can be adjusted by changing the cutting position of the resonator is discussed in (Kim *et al.*, 2010). It uses spectral signatures to encode data and has a data capacity of three bits within 2 GHz to 2.7 GHz frequency range. Since it uses a single resonator, the data capacity is limited. A two bit planar chipless RFID tag based on group delay encoding is presented in (Nair *et al.*, 2011). This tag requires very large area for encoding more number of bits. A tag using dual band resonators is proposed in (Girbau *et al.*, 2012*a*) and six bit chipless RFID

tag using straight line and meandered line open stub resonators connected to microstrip transmission line is proposed in (Jalil, 2014). The meandered line open stub resonator requires 2 GHz frequency band to encode six bits. RFID tags for secure applications are discussed in (Nair Sreejith *et al.*, 2012).

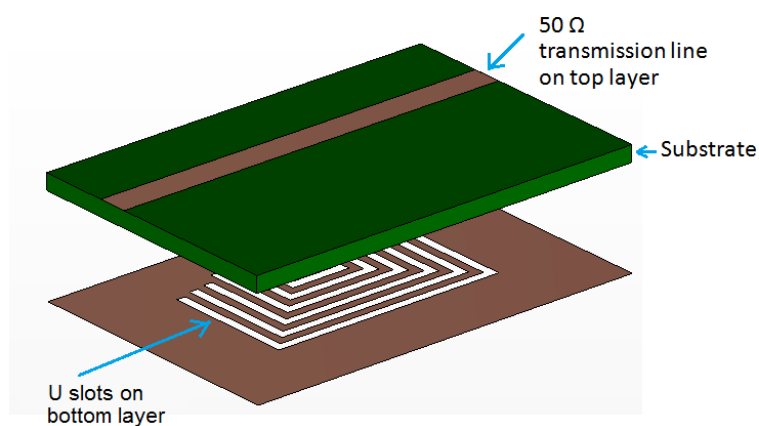
A variety of chipless RFID tags using coplanar waveguide (CPW) based multi-resonating circuits are proposed in (Weng *et al.*, 2013; Preradovic *et al.*, 2009; Ashraf *et al.*, 2015; Bhuiyan *et al.*, 2013). A spectral signature based chipless RFID tag in the ultra wide band frequency range is proposed in (Weng *et al.*, 2013). The multiresonator consists of eight coplanar waveguide resonators, representing an eight bit identification code. However the size of the multiresonator required to represent eight bits is 75 mm x 40 mm. Multiresonating circuit which comprises multiple stop band spiral resonators is proposed in (Preradovic *et al.*, 2009). Chipless RFID tag using CPW circular monopole antennas and multiresonators is reported in (Ashraf *et al.*, 2015). It reports a multiresonator which requires a frequency band of 6 GHz to 8 GHz to encode seven bits. In multiresonator circuit using modified complementary split ring resonators (Bhuiyan *et al.*, 2013) two bits are encoded by modifying (shorting or opening) the inner and outer rings of resonator. Here, the resonator is placed on the CPW feed line. Because of this arrangement, as the number of resonators increases, the amplitude distortion through the transmission line also increases. So the bit encoding capacity is limited. The present work hence focuses on tags with high data encoding capacity and design flexibility for high security applications.



(a) Top layer



(b) Bottom layer [$G = 0.9$, $W_1 = 60.82$, $W_2 = 51.96$, $W_3 = 44.64$, $W_4 = 39.12$, $W_5 = 35.8$, $W_6 = 31.5$, $W = 27$, $L = 40$ (All dimensions in mm), Substrate: loss tangent = 0.0018, $\epsilon_r = 4.3$, $h = 1.6$ mm]



(c) Microstrip version

Fig. 2.1: Proposed six bit U slot multiresonator

2.2 The U slot multiresonator

This chapter presents the design and development of spectral signature based chipless RFID tag using U slot multiresonator. The multiresonator consists of a 50Ω transmission line running on the top layer of the substrate and six U slot resonators of varying dimensions etched on the bottom layer as illustrated in Fig.2.1(a) and 2.1(b) respectively. The position of transmission line is optimised for maximum coupling to all the resonators. The prototype is simulated on substrate C-MET LK4.3 with dielectric constant 4.3, height 1.6 mm and loss tangent 0.0018 using CST MWS[®]. Microstrip version of the six bit multiresonator is shown in Fig.2.1(c). The overall dimension (L x W) is 40 mm x 27 mm. The design approach is to generate multiple resonances by optimising the overall length (W_1 - W_6) of each U slot corresponding to $\lambda_g/2$. The simulated transmission characteristics shown in Fig.2.2 illustrates the resonances at 1.99 GHz, 2.28 GHz, 2.65 GHz, 3.02 GHz, 3.3 GHz and 3.9 GHz, thus encoding six bits in a band of 1.91 GHz. The group delay gives a measure of average time delay of the input signal at each frequency indicating a measure of the dispersive nature of the device. Fig.2.3 shows surface current distribution of individual resonators at the corresponding resonant frequencies.

2.3 Evolution of U slot multiresonator

The multiresonator has evolved from a U slot resonator, on the ground plane of a 50Ω microstrip transmission line as shown in Fig.2.4(a). The transmission line is designed using standard design equations (Malherbe, 1979). Fig.2.4(b) shows the simulated transmission characteristics of the U slot resonator.

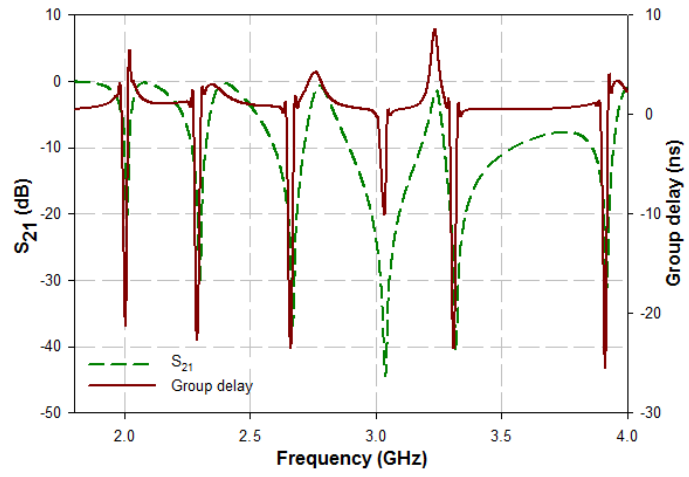


Fig. 2.2: Simulated transmission characteristics of the six bit U slot multiresonator shown in Fig.2.1

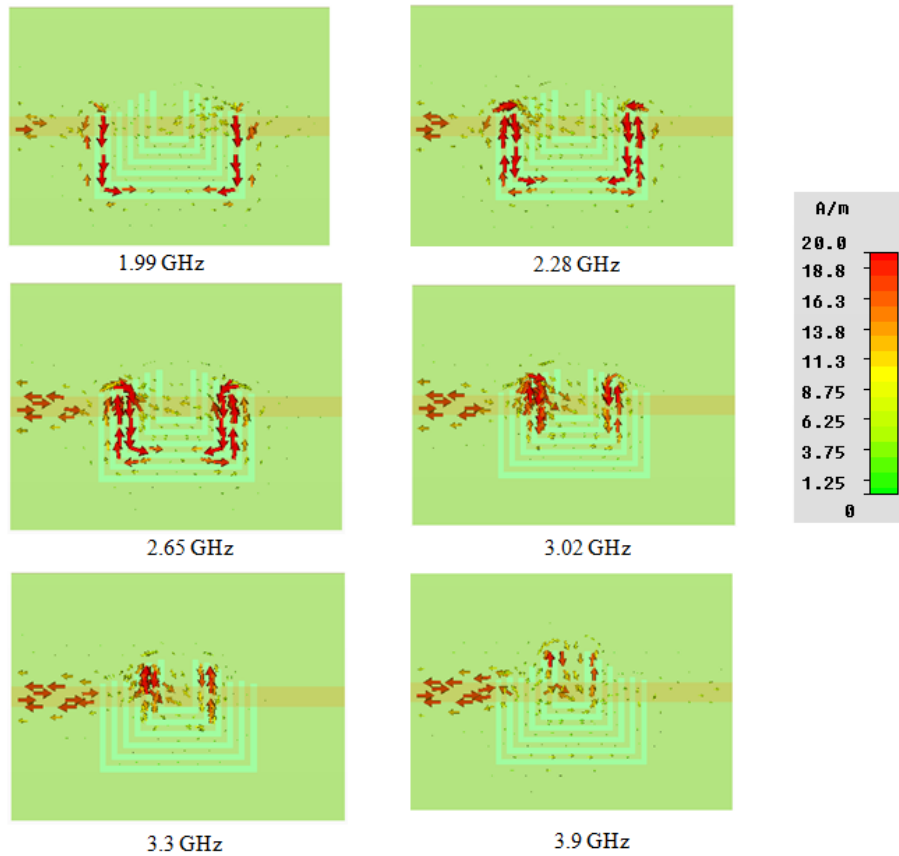
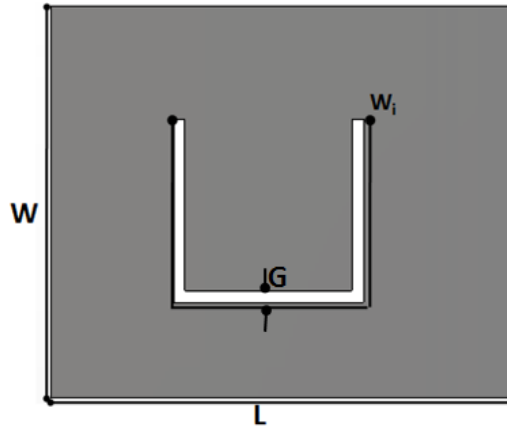
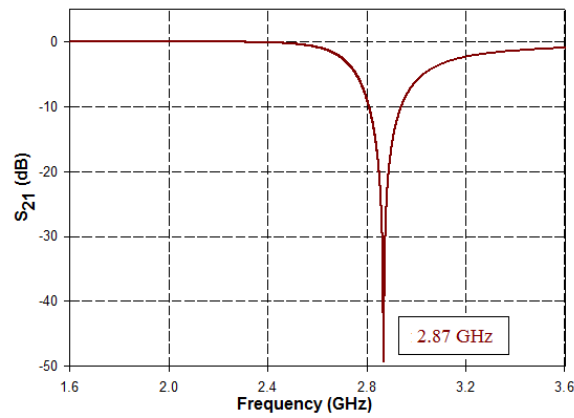


Fig. 2.3: Surface current distribution of individual resonators in the U slot multiresonator shown in Fig.2.1



(a) U slot resonator on the ground plane of a 50Ω microstrip transmission line [$L = 30$, $W = 27$, $W_i = 43.9$, $G = 0.9$, (All dimensions in mm), Substrate: loss tangent = 0.0018, $\epsilon_r = 4.3$, height = 1.6 mm]



(b) Simulated transmission characteristics of the U slot resonator

Fig. 2.4: U slot resonator and its simulated transmission characteristics

Table 2.1: Parametric study for the optimisation of slot width (G) of U slot resonator

L = 30 mm, W = 27 mm, $W_i = 41.12$ mm				
Sl.No	G (mm)	Δf (GHz)	f (GHz)	FBW(%)
1	0.9	0.317	3.06	10.3
2	1.15	0.39	3.1	12.5
3	1.4	0.482	3.19	15.1
4	1.65	0.543	3.23	16.8
5	1.9	0.57	3.25	17.5

2.3.1 Analysis and design of U slot resonator

The resonant frequency of the U slot resonator can be tuned by varying the length of the U slot (W_i). The simulated transmission characteristics shown in Fig.2.5 illustrates the shift in resonant frequency from 2.26 GHz to 3.21 GHz as W_i is varied from 53.04 mm to 39.16 mm. This property of the resonator is used for implementing multiple resonance.

Studies of a U slot resonator for different values of width (G) are carried out. Table 2.1 shows the results of the study. From Table 2.1 it is found that when the slot width increases, the fractional bandwidth ($\frac{\Delta f}{f} * 100$) of the resonator increases. The criteria required for the resonator is that it should provide a sharp resonance to accommodate maximum number of resonances in a fixed band with distinct resonant frequencies. Hence the slot width 'G' is optimised at 0.9 mm in the current study.

Considering the fringing at the slot edges, the slot resonant frequency is expressed as

$$f = \frac{c}{2 * (W_i + \Delta l) * \sqrt{\epsilon_{eff}}} \quad (2.1)$$

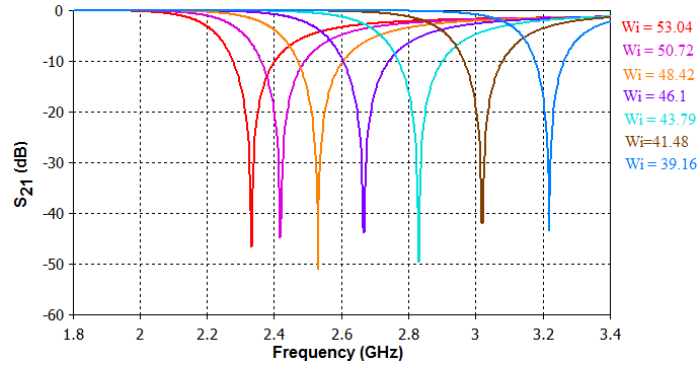


Fig. 2.5: Simulated transmission characteristics by varying W_i (mm) of the U slot resonator shown in Fig.2.4(a)

where

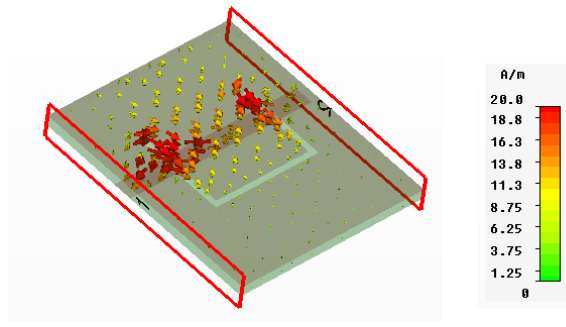
$$W_i + \Delta l = \frac{\lambda_g}{2} \quad (2.2)$$

Δl is the fringing length, $\Delta l \approx 0.04W_i$, ϵ_{eff} is the effective permittivity of the substrate and the guide wavelength(λ_g) is

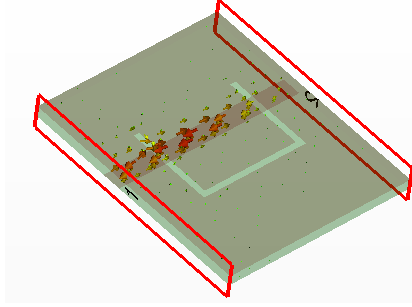
$$\lambda_g = \frac{\lambda}{\sqrt{\epsilon_{eff}}} \quad (2.3)$$

Surface current distribution of the U slot resonator at its resonant frequency (2.87 GHz) and at a non-resonant frequency (2 GHz) are depicted in Fig.2.6(a) and Fig.2.6(b) respectively. The surface current distribution is concentrated in the resonator at the resonant frequency. At its non resonant frequency, the resonator does not inhibit the surface current propagating between port 1 and port 2. From Fig.2.6(a) it is evident that there is a half wavelength variation of surface current at resonance.

Multiple regression analysis is used to develop the design equation of the resonator for a given substrate (Bindu, 2015). The equation is formulated using the regression tool in Microsoft excel (Remenyi *et al.*, 2011). It is a powerful tool for predicting the unknown value of a variable from the known values of two or more variables called the predictors. The variable whose value is to be



(a) 2.87 GHz



(b) 2 GHz

Fig. 2.6: Surface current distribution of U slot resonator shown in Fig.2.4(a) at resonant frequency of 2.87 GHz and at a non-resonant frequency of 2 GHz.

predicted is known as the dependent variable and the ones whose known values are used for prediction are known as independent variables. Here the predictors are the height of the dielectric substrate (h in mm), relative permittivity (ϵ_r) of the substrate material and resonant frequency (f in GHz). The unknown value is the length (W_i) of the U slot resonator. By conducting exhaustive simulation studies on various substrates having different values of dielectric constant and height, W_i can be expressed as in Equation 2.4. The database for the development of the design equation is created by doing parametric analysis on the overall dimension of the U slot for each substrate keeping $G = 0.9$ mm.

$$W_i = -3.61h - 16.4f - 3.07\epsilon_r + 111.12 \quad (2.4)$$

The equation is confirmed on various substrates having different values of relative permittivity and height as shown in Table 2.2. The equation is valid for

Table 2.2: Computed values of W_i for different resonant frequencies on various substrates

	ϵ_r	h(mm)	W_i (mm)	f (GHz)		%error
				Theory	CST	
1	2.25	1	55.33	2.76	2.75	0.36
2	2.4	1	54.92	2.75	2.72	1.09
3	3.27	0.8	42.27	3.41	3.39	0.58
4	4.3	1.6	43.27	2.98	2.94	1.34
5	4.8	1.6	41.4	3	2.95	1.66
6	6	1	53.99	2.14	2.1	1.86

ϵ_r and h in the range $2.25 \leq \epsilon_r \leq 6$ and $0.8 \text{ mm} \leq h \leq 1.6 \text{ mm}$ respectively.

2.3.2 Equivalent circuit of U slot resonator

Equivalent circuit is designed and simulated using Agilent advanced design system (Agilent ADS), an electronic design automation software for designing and optimizing RF and microwave circuits. Fig.2.7 shows the equivalent circuit designed with two ports connected across the 50Ω transmission line for a resonant frequency of 2.87 GHz. Fig.2.8 shows the extracted frequency response. The equivalent circuit is designed using the transformation of the maximally flat first order prototype low pass filter ($\omega_c = 1 \text{ rad/sec}$ and element value $g_1 = 2$) to a band stop filter at ω_0 (Pozar, 2009). The series element $L' = 2\text{H}$ of the low pass filter is thus transformed to a parallel LC circuit having element values given by

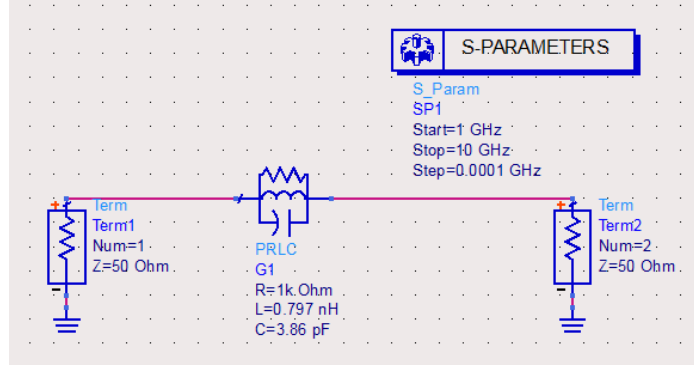


Fig. 2.7: Equivalent circuit of the U slot resonator ($f = 2.87$ GHz)

$$L = \frac{\Delta * L'}{\omega_0}$$

$$C = \frac{1}{\omega_0 * \Delta * L'}$$
(2.5)

where

$$\Delta = \frac{\omega_2 - \omega_1}{\omega_0}$$
(2.6)

ω_2 and ω_1 correspond to 3 dB cut off frequency and ω_0 corresponds to resonant frequency.

Impedance scaling of the filter results in

$$L = \frac{\Delta * L' * Z_0}{\omega_0}$$

$$C = \frac{1}{\omega_0 * \Delta * L' * Z_0}$$
(2.7)

The resistance R accounting for the losses can be found as follows:

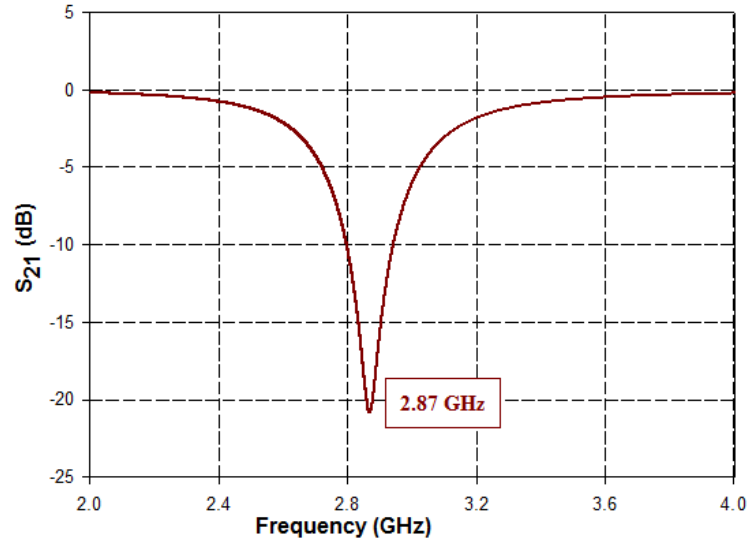


Fig. 2.8: Frequency response of the U slot resonator equivalent circuit extracted using Agilent ADS

$$\begin{aligned}
 Q &= \frac{R}{\omega_0 * L} \\
 Q &= \frac{1}{\Delta}
 \end{aligned}
 \tag{2.8}$$

The values of L, C and R computed using Equations 2.7 and 2.8 for a resonant frequency of 2.87 GHz are 0.797 nH, 3.86 pF and 1 K Ω respectively.

2.3.3 Experimental results of U slot multiresonator

The multiresonator is designed on substrate C-MET LK4.3. The material properties specified by the manufacturer are given in Table 2.3. Fig.2.9(a) and Fig.2.9(b) show the photograph of the top layer and bottom layer respectively of the fabricated U slot multiresonator. Measurements are conducted using the PNA E8362B vector network analyser. The device under test (multiresonator) is connected between the two ports of the vector network analyser as shown in Fig.2.9(c).

Table 2.3: Material properties of C-MET LK-4.3 substrate

C-MET LK-4.3	Value
Dielectric constant	4.3 ± 0.03
Loss tangent	0.0018
Temperature coefficient of dielectric constant	$-27 \text{ ppm}/^\circ\text{C}$
Linear coefficient of thermal expansion	$19 \text{ ppm}/^\circ\text{C}$
Copper peel strength	1.2 N/mm
Water absorption	0.05%
Thermal conductivity	$> 1 \text{ W/mK}$

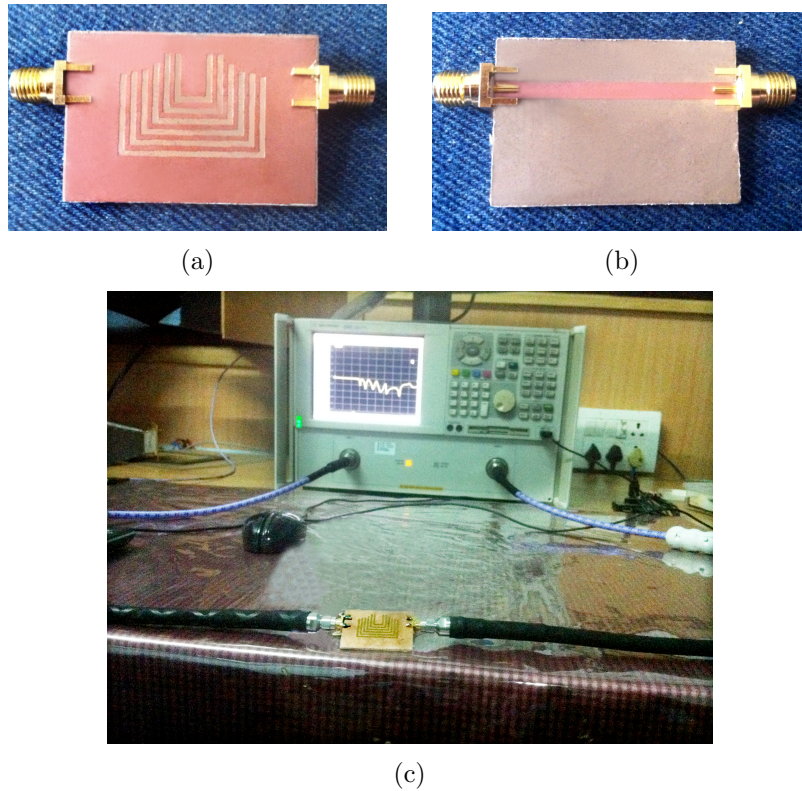


Fig. 2.9: The fabricated U slot multiresonator (a) Top layer (b) Bottom layer (c) Network analyser with device under test

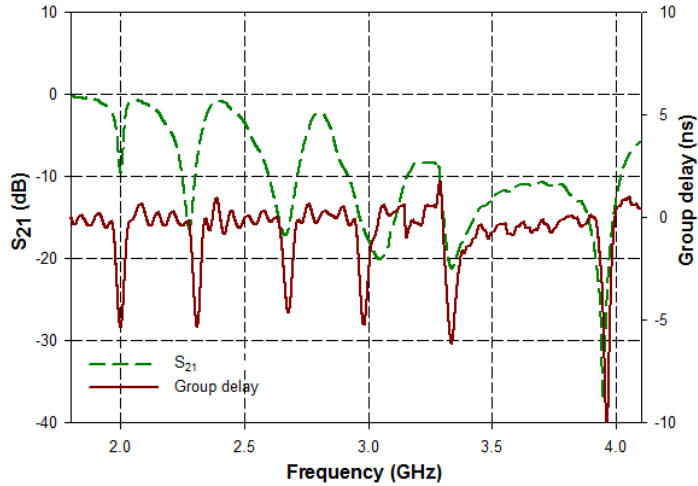


Fig. 2.10: Measured transmission characteristics of the U slot multiresonator for the bit combination [111 111]

Fig.2.10 shows the measured transmission characteristics of the U slot multiresonator for the bit combination [111 111]. Each bit individually represents the resonance of a U slot. The presence of resonance is used to encode a logic 1 and the absence of resonance is used to encode a logic 0. Data encoding techniques to generate various other bit combinations are discussed in Section 2.5.

The proposed U slot multiresonator can be used as an RFID tag for access control applications where the tag is in close proximity of the reader. However the tag needs modification in its design for range enhancement. This is discussed in Section 2.4.

2.4 Bistatic measurement for validation of the tag

The block schematic of bistatic measurement is shown in Fig.2.11. The set up proposed by S. Preradovic et.al (Preradovic *et al.*, 2009; Preradovic and Karmakar, 2009; Preradovic *et al.*, 2008a) is used. The tag is fully passive and

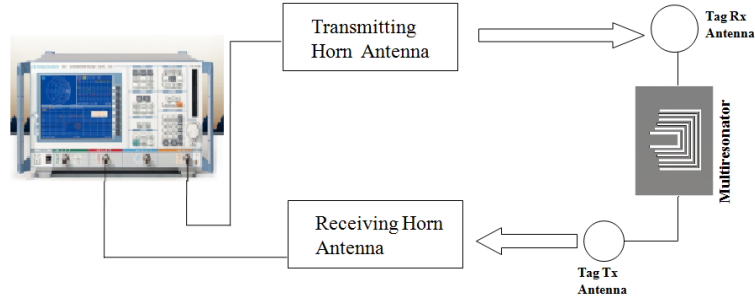


Fig. 2.11: Block schematic for bistatic measurement using U slot multiresonator

hence requires an external source of electromagnetic signal for identification. Two cross polarized medium gain (10 dB) horn antennas are used at the reader for transmission of the continuous wave (CW) interrogation signal and reception of the retransmitted signal. Two wide band antennas, one for receiving the interrogation signal from reader and the other for retransmitting the encoded signal from the multiresonator to the reader, are also incorporated to increase the read range. Various types of antennas for chipless RFID tag applications are reported in literature (Ashraf *et al.*, 2015; Perret *et al.*, 2014; Moscato *et al.*, 2014; Casula, 2014; Weng *et al.*, 2013; Girbau *et al.*, 2012a; Amin *et al.*, 2012; Preradovic and Karmakar, 2011; Kim *et al.*, 2010; Preradovic *et al.*, 2009, 2008a).

The tag can be designed to operate in various frequency bands. To cater to the different frequency band requirements, the microstrip disc monopole antenna is opted due to its simple structure and wide band operation. Fig.2.12 shows the geometry and measured reflection characteristics of the disc monopole antenna. The operating band is from 1.9 GHz to 12 GHz. The measured radiation patterns of the antenna, both in H plane and E plane at different frequencies in the operating band are shown in Fig.2.13. Fig.2.14 shows the gain of the reader antenna (horn) and tag antenna (disc monopole). In the required frequency band, the reader horn antenna and tag antenna exhibit an average gain of 10.78 dB and 1.9 dB respectively.

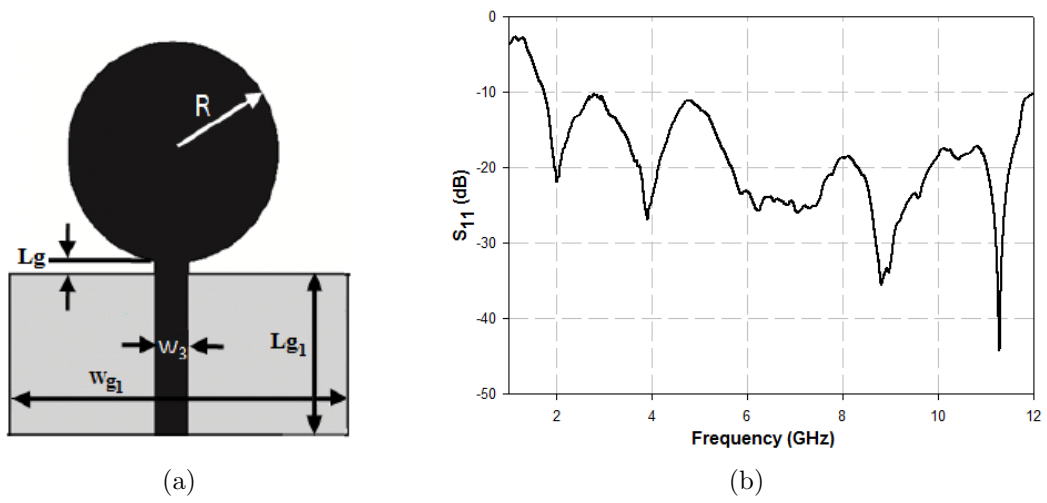


Fig. 2.12: (a) Disc monopole antenna [$R = 15$, $W_3 = 3$, $L_g = 0.6$, $W_{g1} = 40$ and $L_{g1} = 20$ (All dimensions in mm), $\epsilon_r = 4.3$, loss tangent = 0.02, $h = 1.6$ mm] (b) Measured reflection characteristics of disc monopole antenna

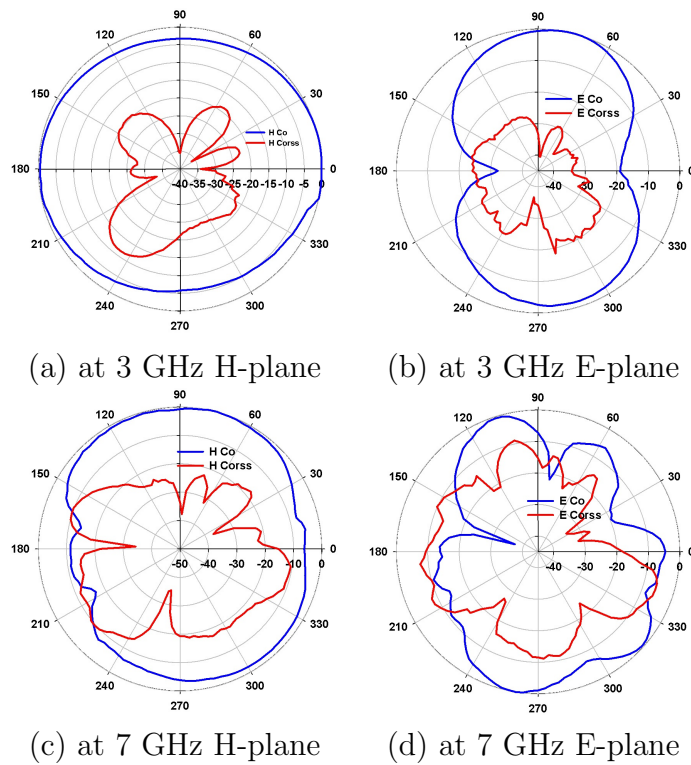


Fig. 2.13: Measured radiation pattern of disc monopole antenna

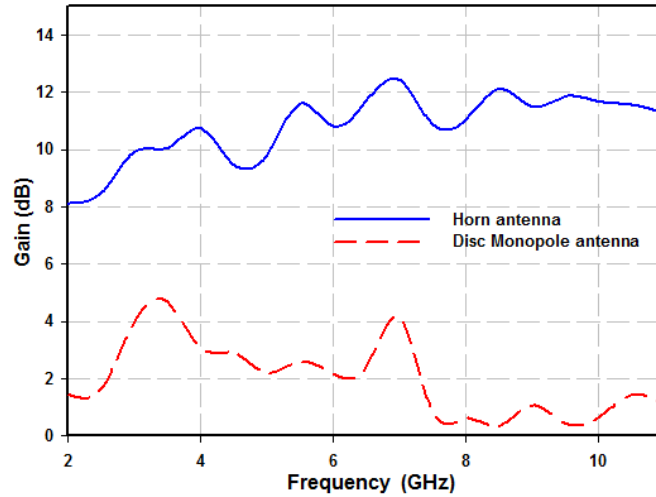


Fig. 2.14: Gain of the reader antenna (horn) and tag antenna (disc monopole)

The tag receives the interrogation signal through the receiving monopole antenna and encodes its spectral signature using the multiresonator. The encoded signal is then sent back to the reader by the transmitting monopole antenna. To provide isolation between the transmitting and receiving signals, the transmitting and receiving antennas are cross polarized.

Fig.2.15 shows the experimental setup for bistatic measurement of the RFID tag using U slot multiresonator. Agilent PNA E8362B vector network analyser with transmitted power of 0 dBm is used. The tag is placed 15 cm away from the reader. Fig.2.16 shows the measured bistatic response for bit combination [111 111]. The bistatic response clearly indicates the abrupt variations at resonance, as in the case of multiresonator [Fig.2.10].

The encoding capacity of the U slot multiresonator discussed above can be further increased by incorporating more U slots. Fig.2.17(a) shows the layout of a eight bit U slot multiresonator. The simulated transmission characteristics shown in Fig.2.17(b) illustrates the resonances at 1.47 GHz, 1.74 GHz, 1.97 GHz, 2.27 GHz, 2.62 GHz, 2.90 GHz, 3.21 GHz and 3.46 GHz. Fig.2.18(a) and Fig.2.18(b) show the photograph of the top layer and bottom layer respectively

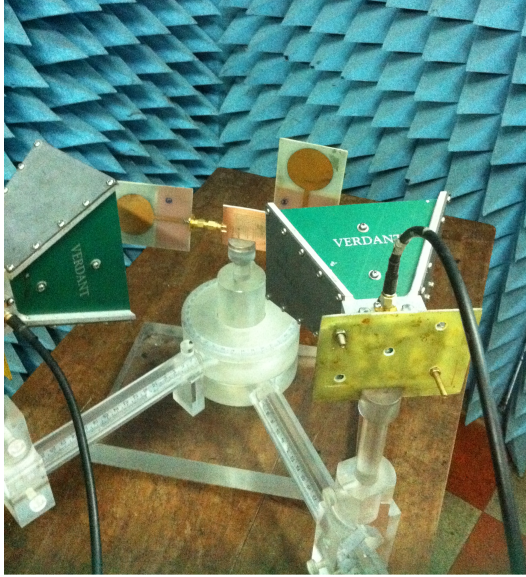


Fig. 2.15: Experimental setup for bistatic measurement of the RFID tag using U slot multiresonator

of the fabricated eight bit U slot multiresonator. Fig.2.18(c) shows the measured transmission characteristics of the eight bit U slot multiresonator. It is observed that the first two resonances fall below the operating band of the disc monopole antenna used for range enhancement. Since the same antenna is used for all multiresonator prototypes presented in the thesis, this chapter focuses on six bit U slot multiresonator.

2.5 Data encoding methods

The previous sections were concerned with the multiresonator. Further, the identity of the tag needs to be encoded into the multiresonator. Two different methods of data encoding are used in this work.

1. Absence or presence coding technique
2. Frequency shift coding technique

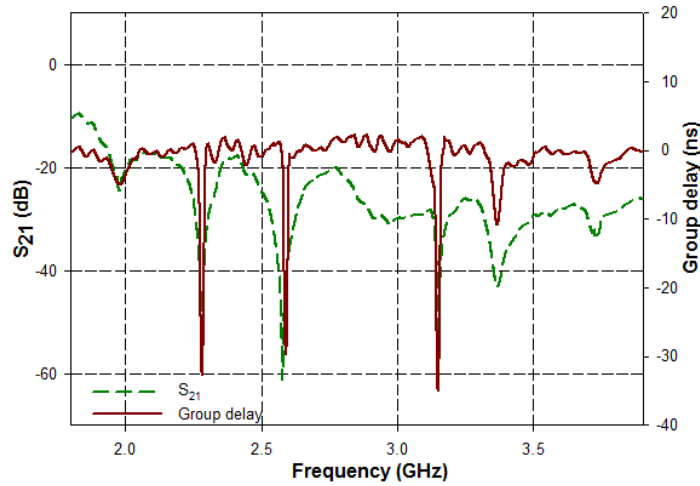
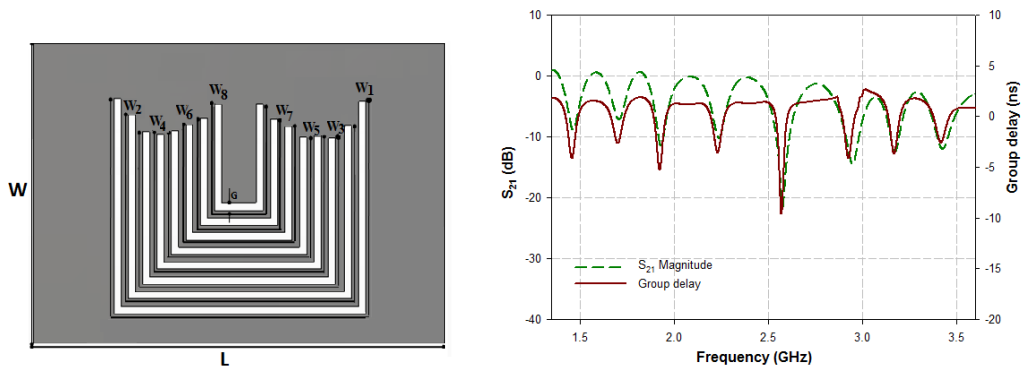


Fig. 2.16: Measured bistatic response of the RFID tag using U slot multiresonator for the bit combination [111 111]

2.5.1 Absence or presence coding technique

In absence or presence coding technique, one resonator represents one bit of information. The presence of resonance at a particular frequency is used to encode logic 1 and the absence of resonance is used to encode logic 0. So with ‘n’ resonators 2^n combinations are possible. In U slot multiresonator type 1 [Fig.2.19] all the six slots are present, resulting in a bit combination [111 111]. Slot 1 corresponds to the most significant bit and slot 6 corresponds to the least significant bit.

The absence of a specific resonance can be achieved by either removing the corresponding slot [Fig.2.20(a)] or isolating the slot by shorting the slot at corners [Fig.2.20(b)]. It is to be noted that 2^6 different combinations are possible with 6 resonators. Several such combinations have been validated experimentally and through simulation. Three different types of such resonators are shown in Fig.2.20.



(a) [$G = 0.9$, $W_1 = 78.76$, $W_2 = 67.67$, $W_3 = 58.36$, $W_4 = 51.96$, $W_5 = 43.53$, $W_6 = 39.12$, $W_7 = 34.42$, $W_8 = 31.33$, $W = 37$, $L = 50$ (All dimensions in mm), Substrate: loss tangent = 0.0018, $\epsilon_r = 4.3$, $h = 1.6$ mm]

(b) Simulated transmission characteristics of eight bit U slot multiresonator

Fig. 2.17: Eight bit U slot multiresonator and its simulated transmission characteristics

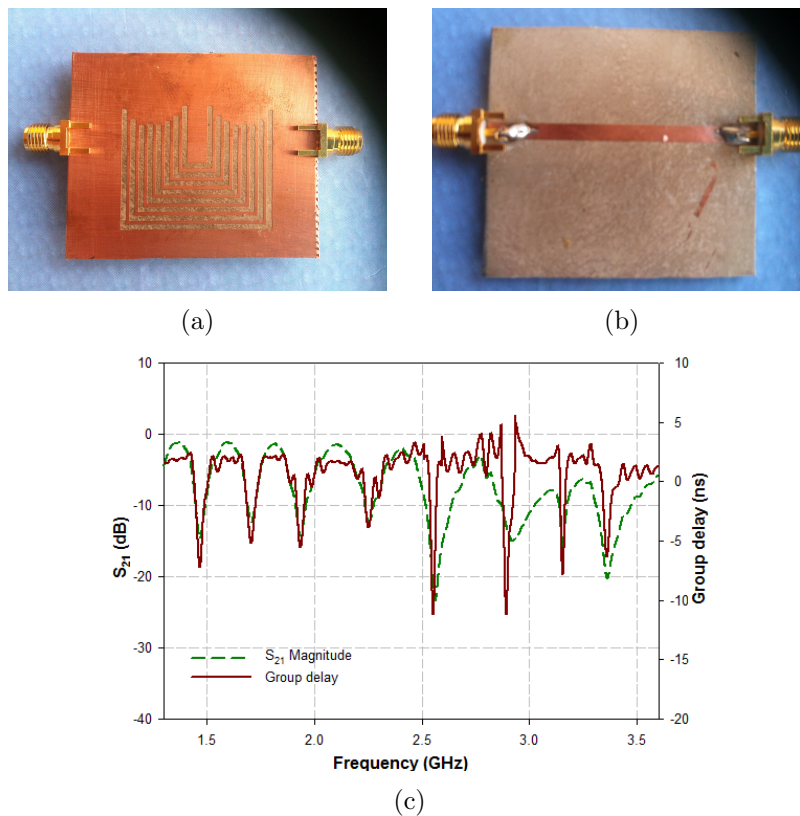


Fig. 2.18: The fabricated eight bit U slot multiresonator (a) Top layer (b) Bottom layer (c) Measured transmission characteristics of eight bit U slot multiresonator

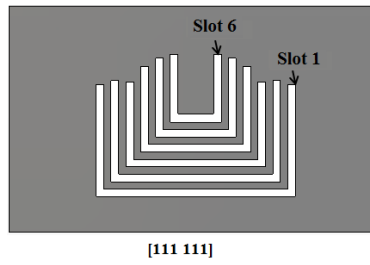
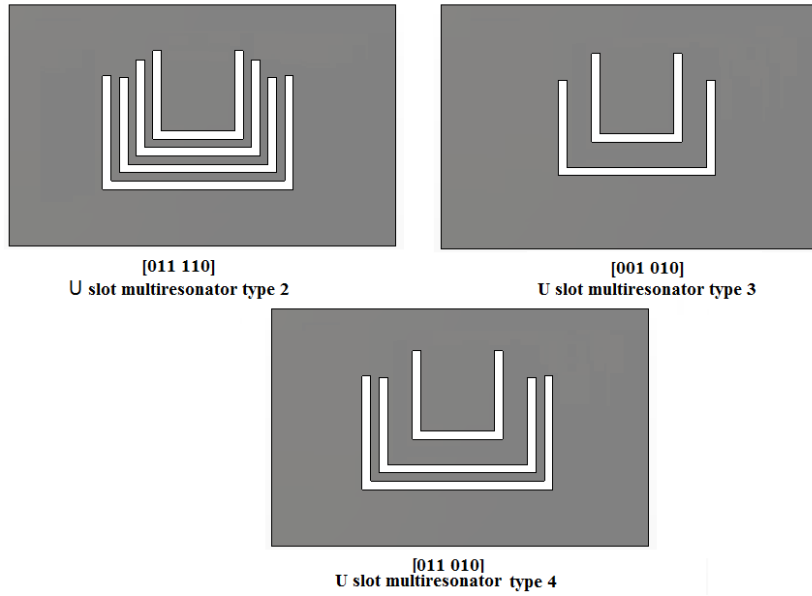
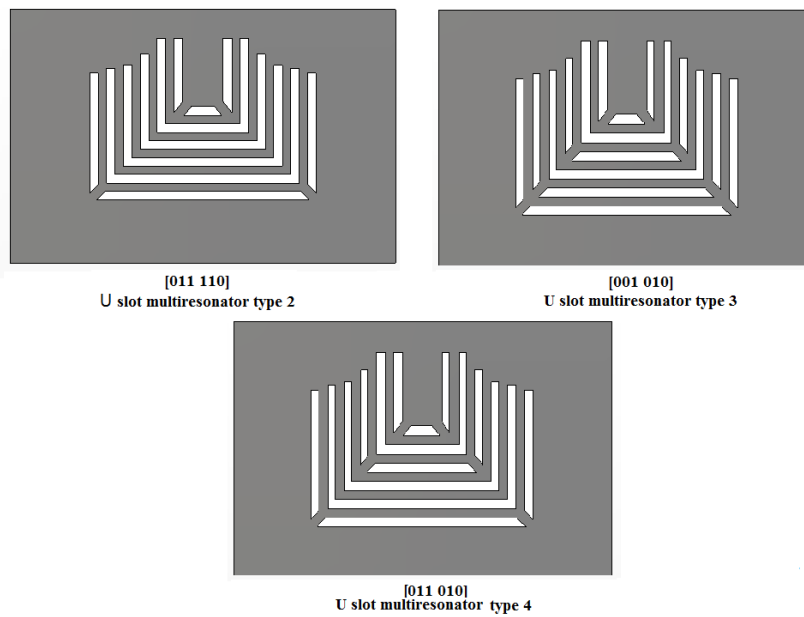


Fig. 2.19: U slot multiresonator type 1



(a) Removing the slot



(b) Shorting slot at corners

Fig. 2.20: Three different types of U slot multiresonator (a) Removing the slot (b) Shorting slot at corners

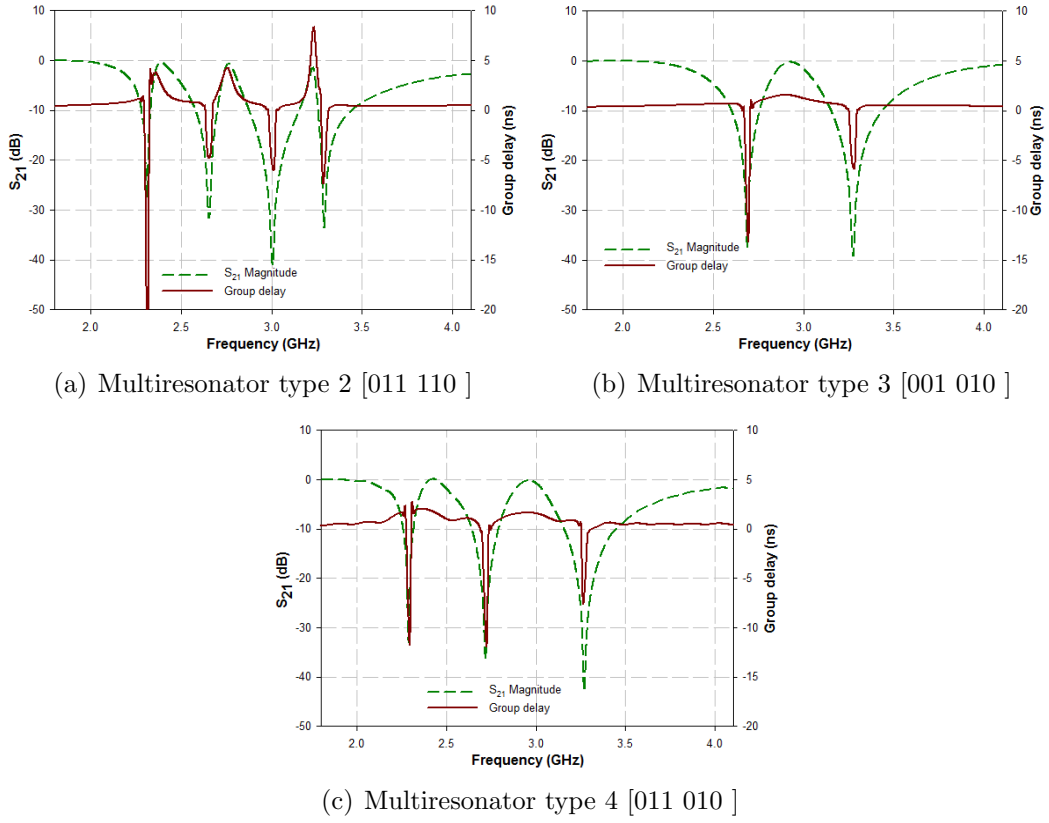


Fig. 2.21: Simulated transmission characteristics of the U slot multiresonator for different bit combinations

In U slot multiresonator type 2 resonances due to slot 1 and slot 6 are absent, leading to [011 110]. In U slot multiresonator type 3 resonances due to slot 1, slot 2, slot 4 and slot 6 are absent, resulting in [001 010]. In U slot multiresonator type 4 resonances due to slot 1, slot 4 and slot 6 are absent, resulting in [011 010]. Fig.2.21 shows the simulated transmission characteristics of the three types of multiresonators. The small shift in resonant frequency may be due to the mutual coupling between the resonators. The simulated transmission characteristics of [111 111] was shown in Fig.2.2.

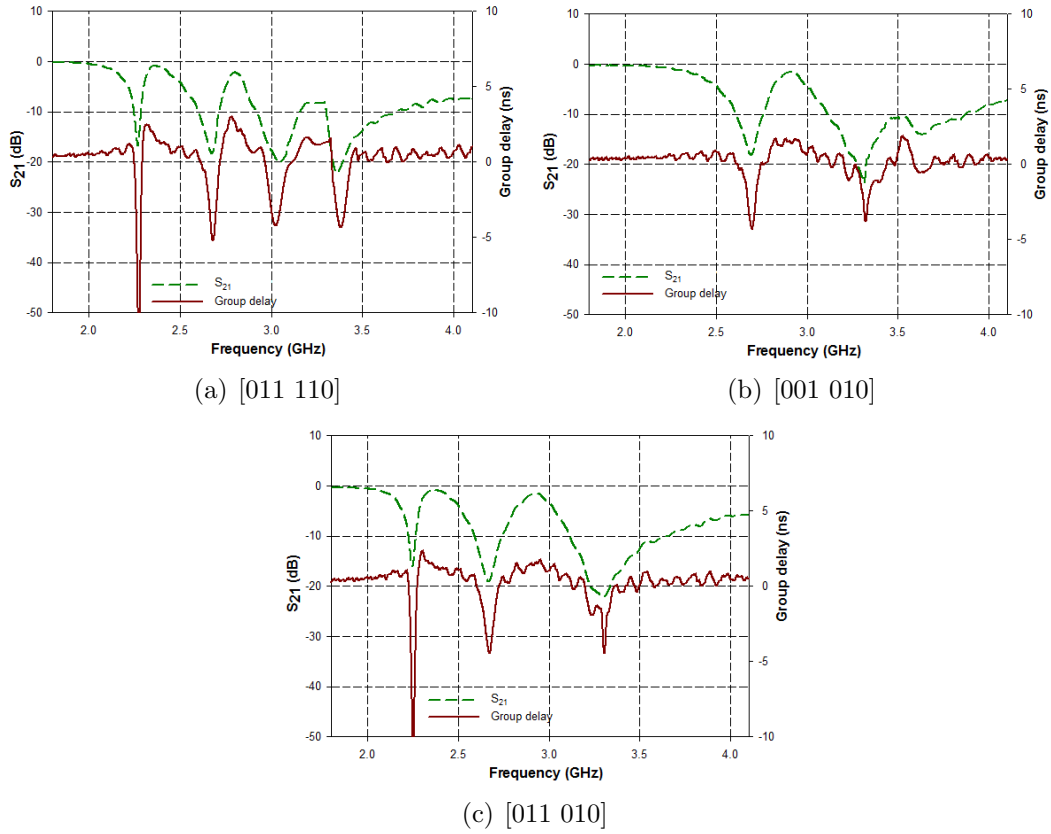


Fig. 2.22: Measured transmission characteristics of U slot multiresonator for different bit combinations

2.5.2 Experimental results of U slot multiresonator using absence or presence coding technique

Using the technique mentioned in Section 2.5.1 different types of multiresonators are fabricated. The transmission characteristics is measured using Agilent PNA E8362B vector network analyzer by connecting the multiresonator between the two ports. Measured transmission characteristics of the multiresonator for the bit combinations [011 110], [001 010] and [011 010] are shown in Fig.2.22. The measured result of [111 111] was shown in Fig.2.10.

The tag identity can be confirmed from the absolute value of S_{21} or group delay. Since absolute value is different for different resonant frequencies, exact resonant frequency can be identified by a simple post processing method (Nijas

et al., 2014) using a difference operation technique (Equation 2.9).

$$y'(i) = y(i) - y(i + 1) \quad (2.9)$$

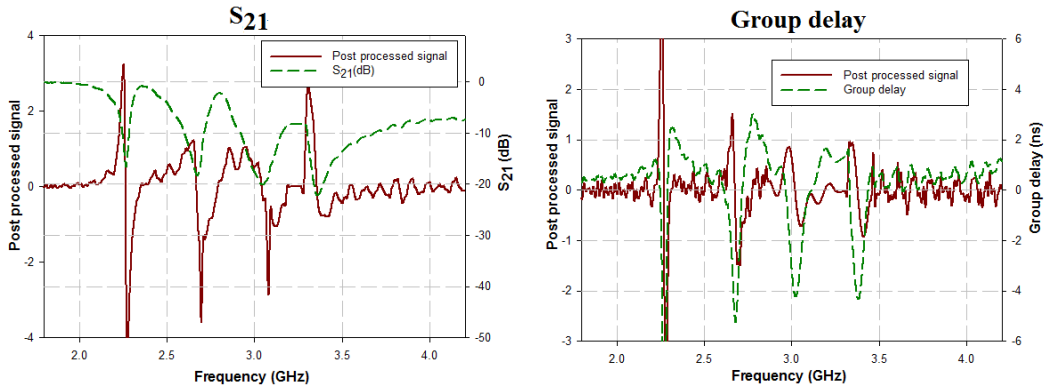
where $y(i)$ is the S_{21} or group delay of the signal at i^{th} frequency point. Employing this method the tag detection becomes virtually independent of absolute value of S_{21} or group delay. This detection method is carried out and validated for various bit combinations. A peak variation at resonance is visible from the post processed signal for the bit combinations [011 110], [001 010] and [011 010] as shown in Fig.2.23.

2.5.3 Bistatic measurement results using absence or presence coding technique

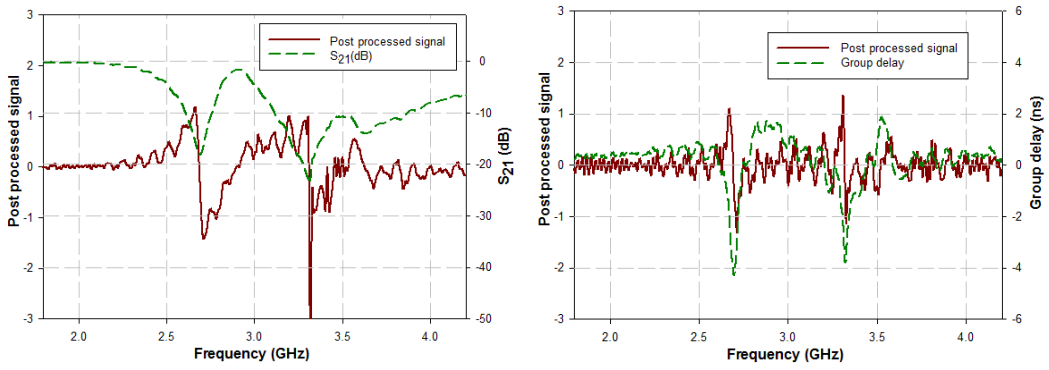
Bistatic measurement is done to validate the tag for various bit combinations. Fig.2.24 shows the measured bistatic response for bit combinations [011 110], [001 010] and [011 010]. The measured result of [111 111] was shown in Fig.2.16. As explained in Section 2.5.2, post processing method is applied to the bistatic measured results. Fig.2.25 shows the post processed signal for the bit combination [111 111].

2.5.4 Frequency shift coding technique for enhanced bit encoding capacity

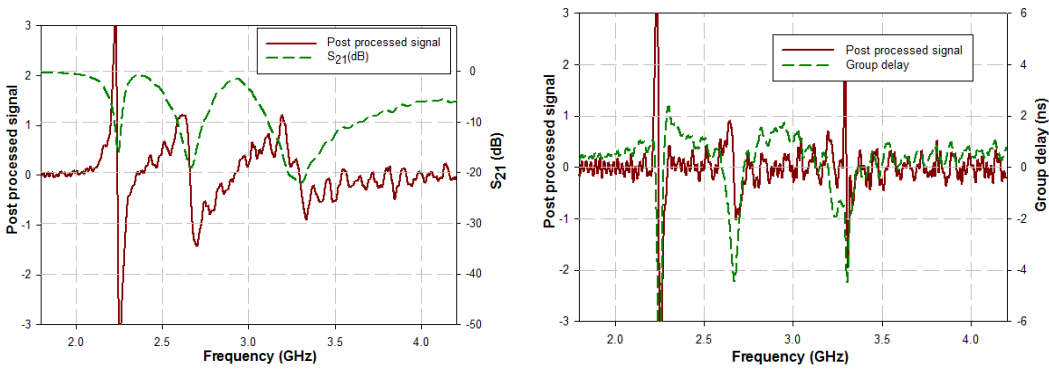
In absence or presence coding method, maximum bits that can be represented by an RFID tag is limited by the number of resonators. The bit encoding capacity of the tag can be enhanced using frequency shift coding (FSC) technique, by encoding more than one bit per resonator (Vena *et al.*, 2013b, 2012a,



(a) [011 110]



(b) [001 010]



(c) [011 010]

Fig. 2.23: Measured transmission characteristics of the U slot multiresonator and its post processed signal for various bit combinations

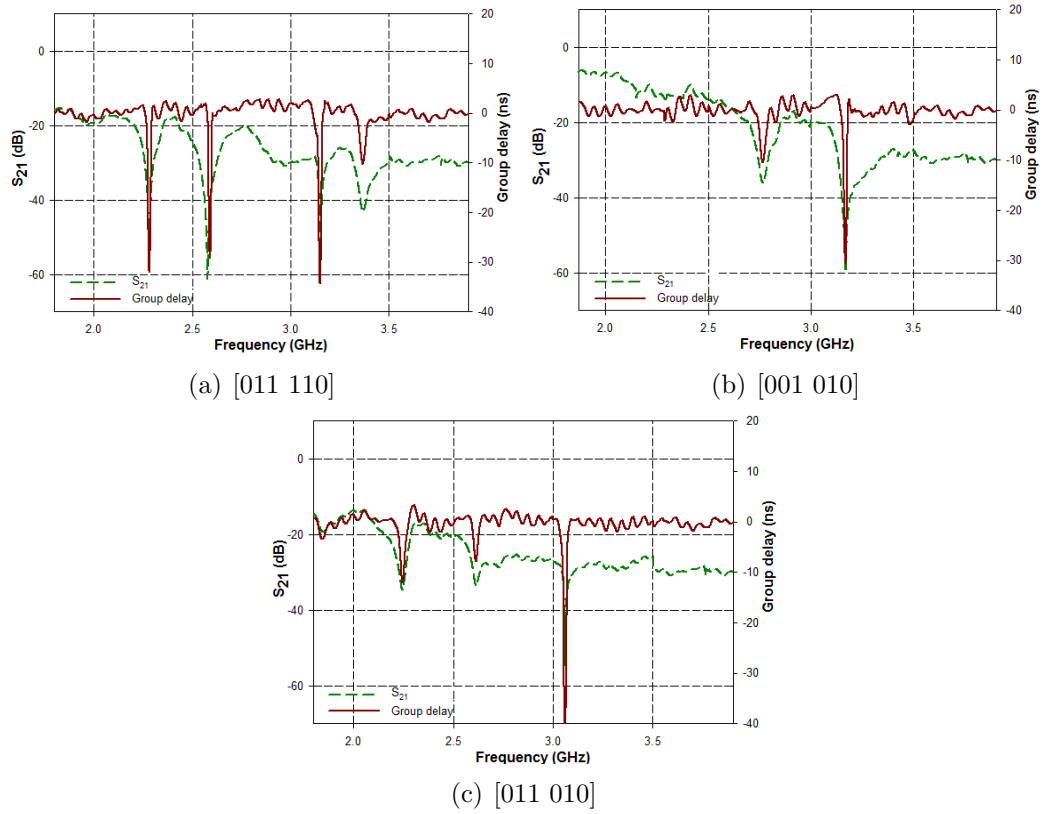


Fig. 2.24: Measured bistatic response of the RFID tag using U slot multiresonator for different bit combinations

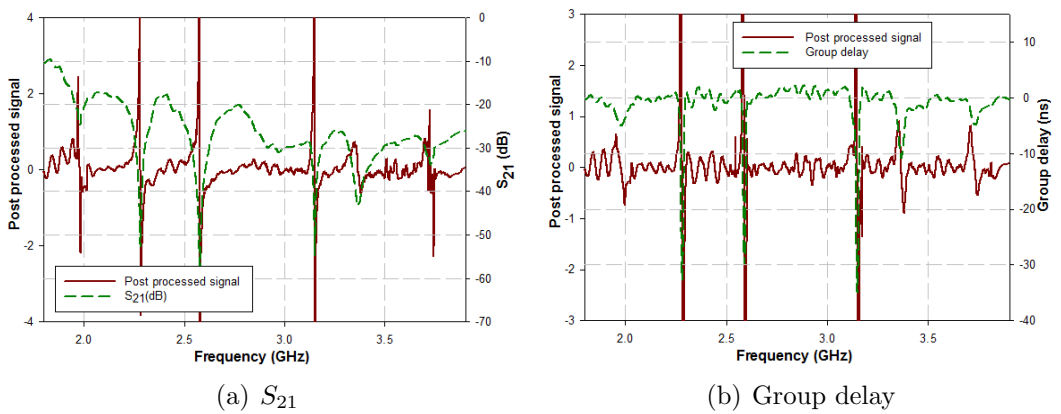
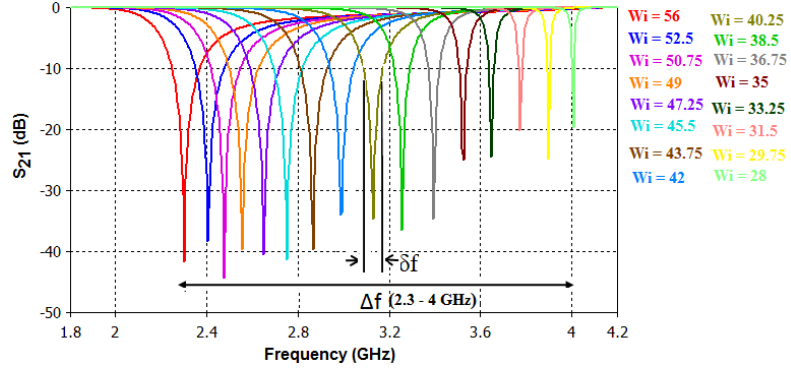


Fig. 2.25: Measured bistatic response of the RFID tag using U slot multiresonator and its post processed signal for the bit combination [111 111]

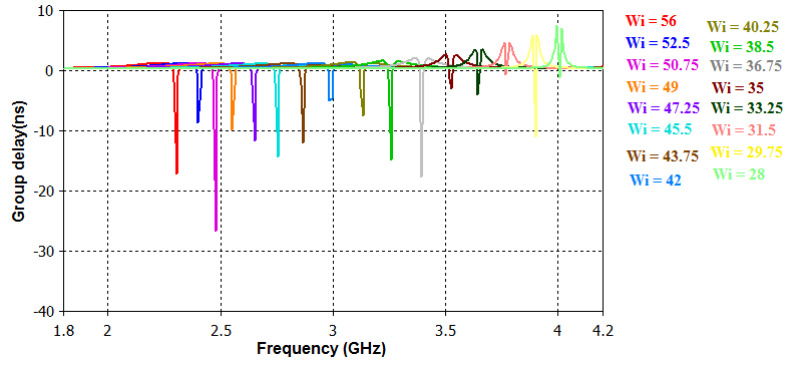
2011*b,a*). This method is more appropriate in the case where large data encoding is required with less number of resonators. Another advantage is the design of high security tags, ie; the tags appear to be similar, but the identification code will be different. The subsequent sections explain the method by which FSC is applied to various U slot resonator configurations.

2.5.5 Frequency shift coding applied to U slot resonator

The simulated transmission characteristics for various values of W_i of U slot resonator [Fig.2.4(a)] are shown in Fig.2.26. In a frequency band (Δf) from 2.3 GHz to 4 GHz, 16 frequency bands are possible. δf is the frequency band for each resonator required to faithfully represent its resonant frequency, thus determining the frequency resolution. Table 2.4 shows a proposed method of code word allocation for the U slot resonator. The variation in slot dimension (W_i) is restricted due to the presence of higher harmonics. While absence or presence coding of a resonator can encode only two code words (0/1) using a single U resonator, use of FSC allows an improvement to 16 code words. The enhanced bit capacity of FSC in comparison with absence or presence coding is evident from the above result. Two resonators with $W_i = 57$ mm and $W_i = 53$ mm corresponding to code words [0000] and [0001] respectively are fabricated to validate the simulation results. The measured resonator response and the bistatic response are shown in Fig.2.27. Fig.2.28 shows the photograph of the fabricated U slot resonator.



(a) S_{21}



(b) Group delay

Fig. 2.26: Simulated transmission characteristics of U slot resonator shown in Fig.2.4(a) for various values of W_i (mm)

2.5.6 Frequency shift coding applied to multiresonator with two U slots

Fig.2.29 shows the layout of multiresonator with two U slots whose slot dimension (W_i) is individually varied for FSC. The frequency band (Δf) and resonant frequency (f) of each resonator are listed in Table 2.5.

In FSC, the frequency band (Δf) can be selected depending on the available frequency spectrum and the number of resonators. Variation of the slot dimensions of the first resonator, keeping the dimensions of the second resonator constant, results in ten different resonant frequencies as shown in Fig.2.30. Similarly, variation of the slot dimension of the second resonator, keeping the dimensions of the first resonator constant, results in ten different resonant fre-

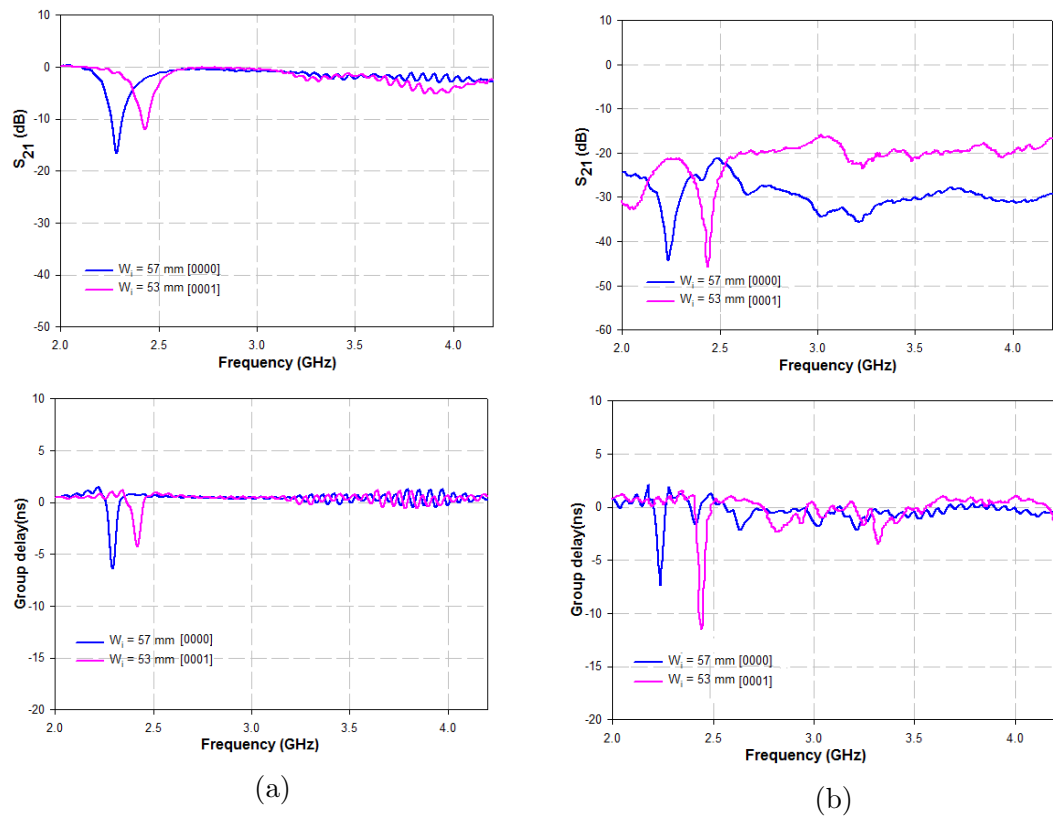


Fig. 2.27: Measured response of the U slot resonator for two different configurations
 (a) Transmission characteristics of the resonator (b) Bistatic response

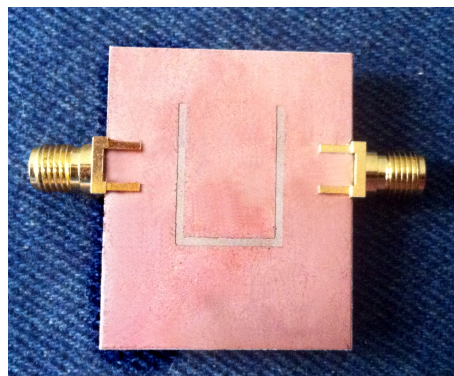


Fig. 2.28: Photograph of fabricated U slot resonator

Table 2.4: Proposed method of code word allocation for the U slot resonator

Sl.no	W_i (mm)	f (GHz)	Code word
1	57	2.3	0000
2	53	2.40	0001
3	50.75	2.47	0010
4	49	2.55	0011
5	47.25	2.64	0100
6	45.5	2.75	0101
7	43.75	2.86	0110
8	42	2.98	0111
9	40.25	3.12	1000
10	38.5	3.25	1001
11	36.75	3.32	1010
12	35	3.52	1011
13	33.25	3.64	1100
14	31.5	3.77	1101
15	29.75	3.89	1110
16	28	4.0	1111

quencies as shown in Fig.2.31. Further increase in the number of resonant frequencies is limited by the presence of higher harmonics. Unique identification code can be assigned to each combination of resonant frequencies. Since ten different resonant frequencies are possible for each resonator, combining the two, 100 different codes ranging from [000 0000] to [110 0011] are possible with two resonators. The measured resonator response and the bistatic response of the multiresonator with two U slot for two different configurations are shown in Fig.2.32. Fig.2.33 shows photograph of the fabricated multiresonator with two U slots.

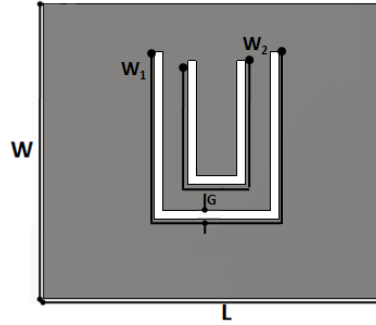


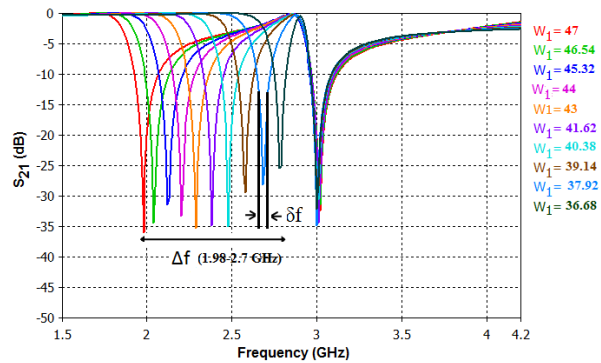
Fig. 2.29: Layout of multiresonator with two U slots [$L = 30$ mm, $W = 27$ mm, $G = 0.9$ mm, Substrate: loss tangent = 0.0018, $\epsilon_r = 4.3$, $h = 1.6$ mm]

2.5.7 Frequency shift coding applied to multiresonator with four U slots

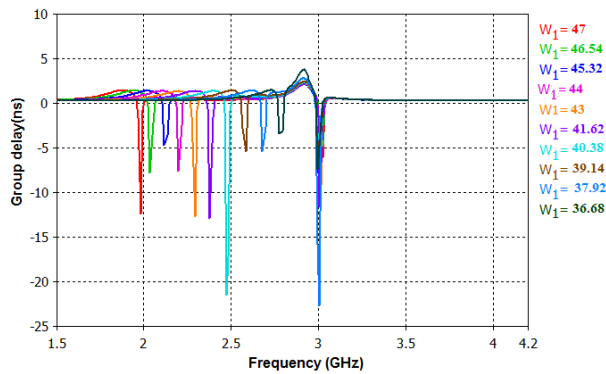
Fig.2.34 shows the layout of multiresonator with four U slots whose slot dimension (W_i) is individually varied for FSC. The frequency band (Δf) and resonant frequency (f) of each resonator are listed in Table 2.6. Variation of the slot dimension of the first resonator, keeping the dimensions of other resonators constant, results in five different resonant frequencies. Fig.2.35 to Fig.2.38 show the results obtained by individually varying the slot dimension of each resonator. While varying the dimension of each resonator, care must be taken that the resonance due to other resonators remain unaffected. In FSC for bit encoding, precautions must also be taken so that merging of resonant bands (Δf) does not occur and harmonics of the lower frequency resonators do not interfere with the resonance of higher frequency resonators. Unique identification code can be assigned to each combination of resonant frequencies. Since five different resonant frequencies are exhibited by each resonator, combining the four, 625 (5^4) different codes are possible.

Table 2.5: Frequency band (Δf) and resonant frequency (f) of multiresonator with two U slots (All values in GHz)

	Δf_1 (1.98-2.7)	Δf_2 (2.9 - 3.8)
f_1	1.98	2.9
f_2	2.03	2.98
f_3	2.11	3.07
f_4	2.19	3.18
f_5	2.28	3.27
f_6	2.37	3.37
f_7	2.47	3.49
f_8	2.57	3.62
f_9	2.67	3.75
f_{10}	2.7	3.8

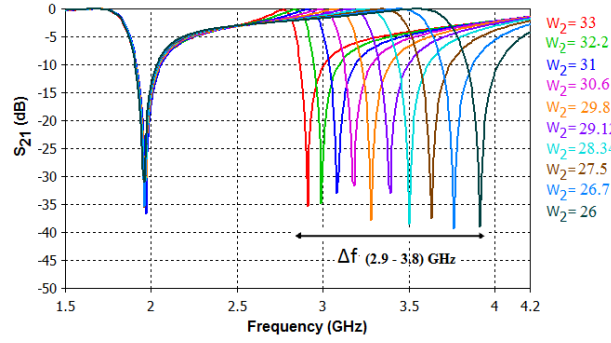


(a) S_{21}

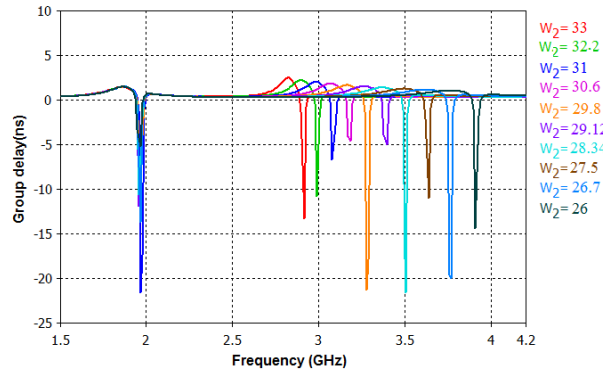


(b) Group delay

Fig. 2.30: Simulated transmission characteristics of tuning the first U slot in multiresonator with two U slots shown in Fig.2.29 ($W_2 = 32$ mm, W_1 in mm)



(a) S_{21}



(b) Group delay

Fig. 2.31: Simulated transmission characteristics of tuning the second U slot in multiresonator with two U slots shown in Fig.2.29 ($W_1 = 47$ mm, W_2 in mm)

Table 2.6: Frequency band (Δf) and resonant frequency (f) of multiresonator with four U slots (All values in GHz)

Resonator	Δf	f_1	f_2	f_3	f_4	f_5
1	1.86 - 2.12	1.86	1.92	1.98	2.05	2.12
2	2.21 - 2.45	2.21	2.26	2.32	2.37	2.45
3	2.67 - 3.07	2.67	2.75	2.84	2.94	3.07
4	3.13 - 3.5	3.13	3.22	3.32	3.44	3.5

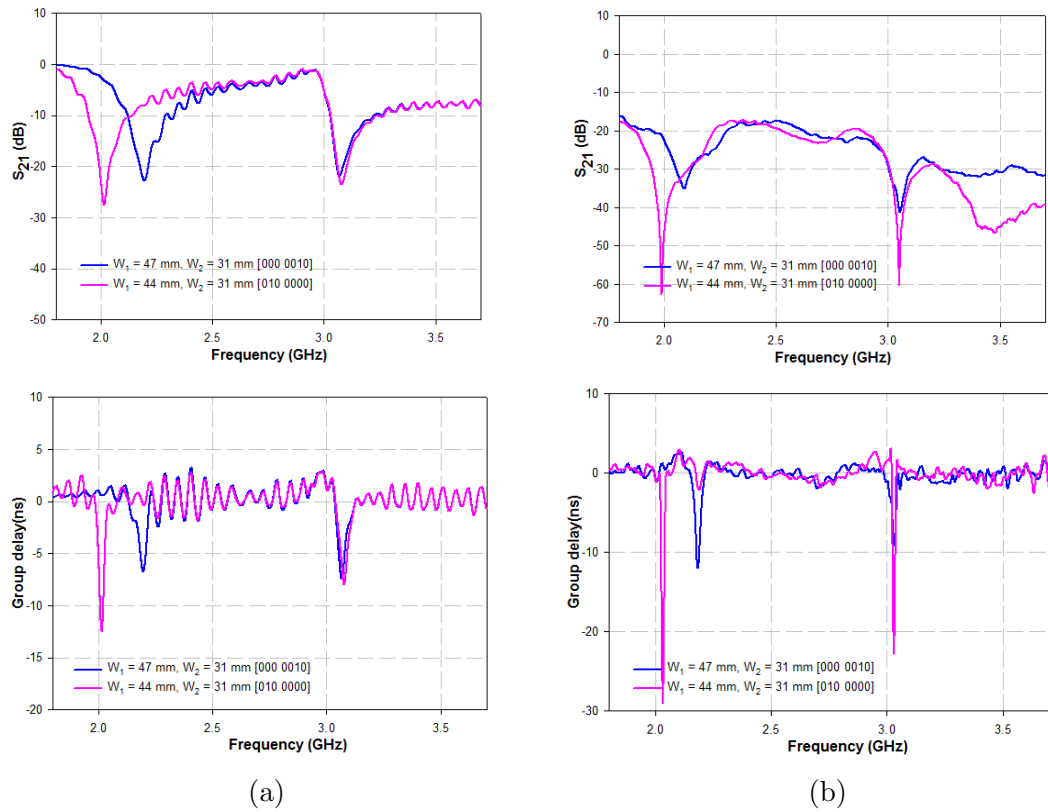


Fig. 2.32: Measured response of multiresonator with two U slots for two different configurations (a) Transmission characteristics of the resonator (b) Bistatic response

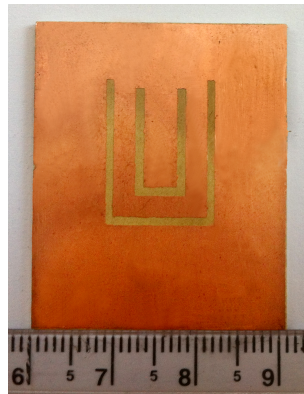


Fig. 2.33: Photograph of fabricated multiresonator with two U slots

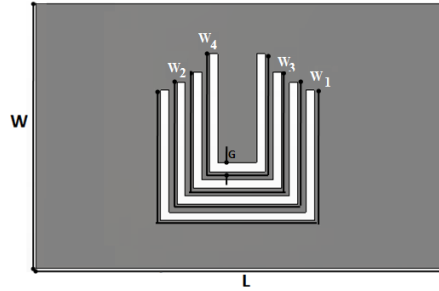
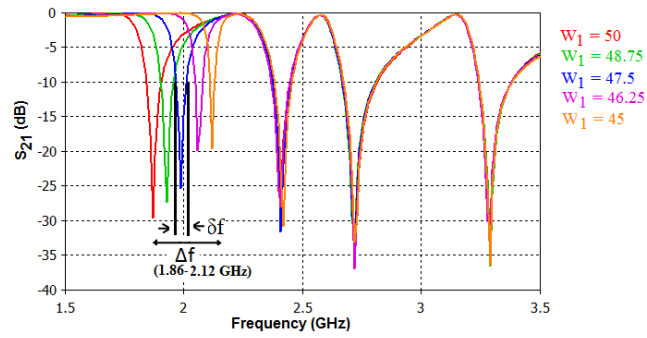
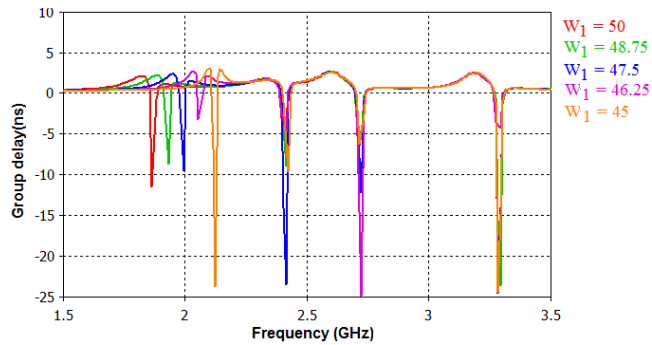


Fig. 2.34: Layout of multiresonator with four U slots [$L = 40$ mm, $W = 27$ mm, $G = 0.9$ mm, Substrate: loss tangent = 0.0018, $\epsilon_r = 4.3$, $h = 1.6$ mm]

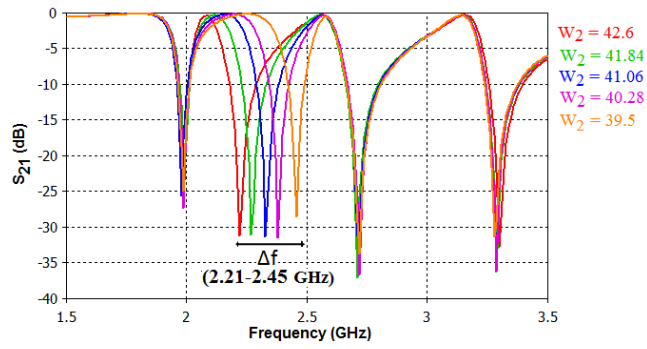


(a) S_{21}

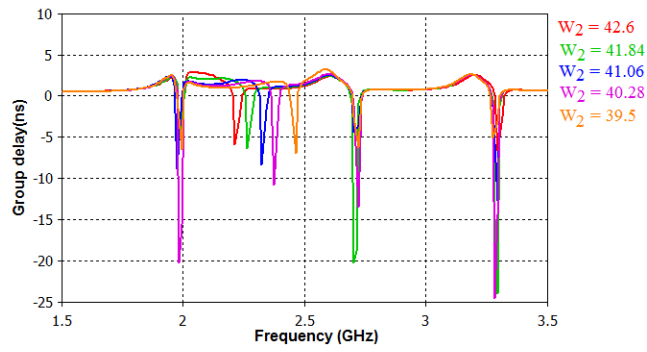


(b) Group delay

Fig. 2.35: Simulated transmission characteristics of tuning the first U slot in multiresonator with four U slots shown in Fig.2.34 ($W_2 = 40$ mm, $W_3 = 34.5$ mm, $W_4 = 28.6$ mm, W_1 in mm)

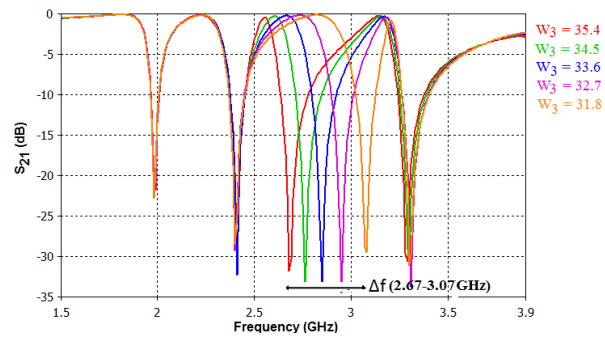


(a) S_{21}

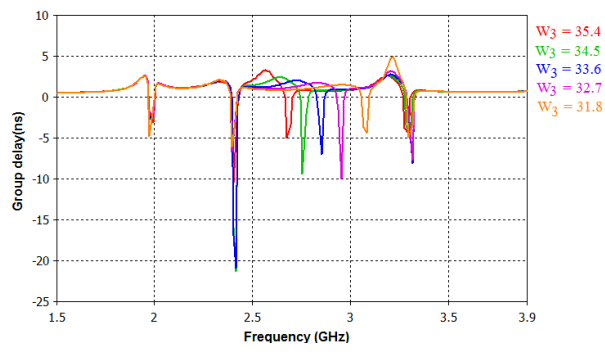


(b) Group delay

Fig. 2.36: Simulated transmission characteristics of tuning the second U slot in multiresonator with four U slots shown in Fig.2.34 ($W_1 = 47.5$ mm, $W_3 = 34.5$ mm, $W_4 = 28.6$ mm, W_2 in mm)

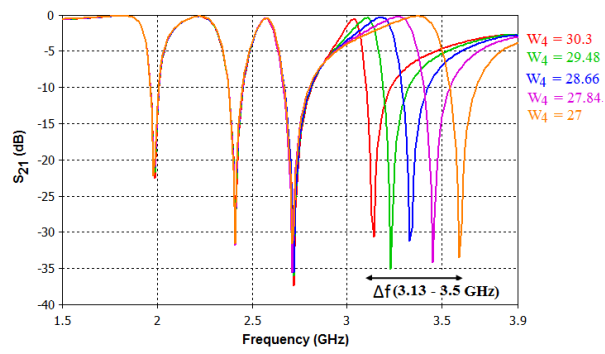


(a) S_{21}

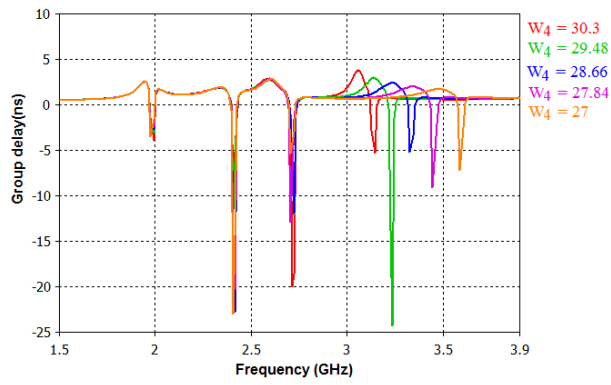


(b) Group delay

Fig. 2.37: Simulated transmission characteristics of tuning the third U slot in multiresonator with four U slots shown in Fig.2.34 ($W_1 = 47.5$ mm, $W_2 = 40$ mm, $W_4 = 28.6$ mm, W_3 in mm)



(a) S_{21}



(b) Group delay

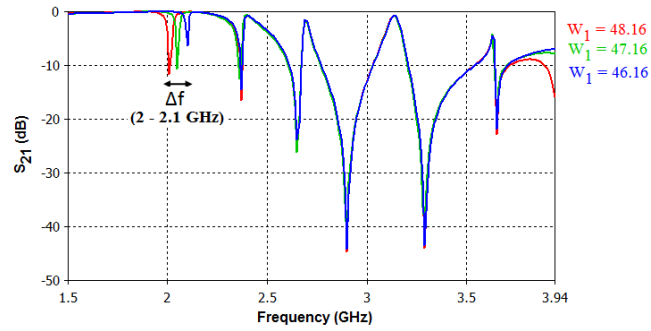
Fig. 2.38: Simulated transmission characteristics of tuning the fourth U slot in multiresonator with four U slots shown in Fig.2.34 ($W_1 = 47.5$ mm, $W_2 = 40$ mm, $W_3 = 34.5$ mm, W_4 in mm)

Table 2.7: Frequency band (Δf) and resonant frequency (f) of multiresonator with six U slots (All values in GHz)

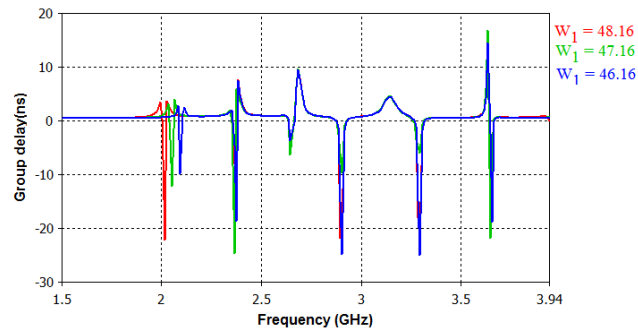
Resonator	Δf	f_1	f_2	f_3
1	2 - 2.1	2.0	2.04	2.1
2	2.25 - 2.37	2.25	2.30	2.37
3	2.46 - 2.57	2.46	2.52	2.57
4	2.87 - 3.07	2.87	2.97	3.07
5	3.11 - 3.32	3.11	3.19	3.32
6	3.65 - 3.88	3.65	3.71	3.88

2.5.8 Frequency shift coding applied to multiresonator with six U slots

When the concept of FSC is applied to a multiresonator with six resonators [Fig.2.1], six different frequency bands (Δf) occur as detailed in Table 2.7. Variation of the slot dimension of one resonator, keeping the dimensions of the other resonators constant, results in three different resonant frequencies. Fig.2.39 to Fig.2.44 show the results obtained by individually varying the slot dimension of each resonator. Since three different resonant frequencies are exhibited by each resonator, combining the six resonators, 729 (3^6) different codes are possible. On the other hand, using absence or presence coding only 64 (2^6) different codes are possible with six resonators. Fig.2.45 shows measured resonator response and bistatic response for varying dimensions of the sixth resonator (W_6).

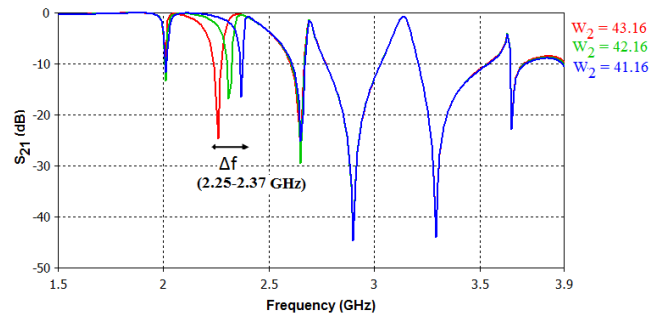


(a) S_{21}

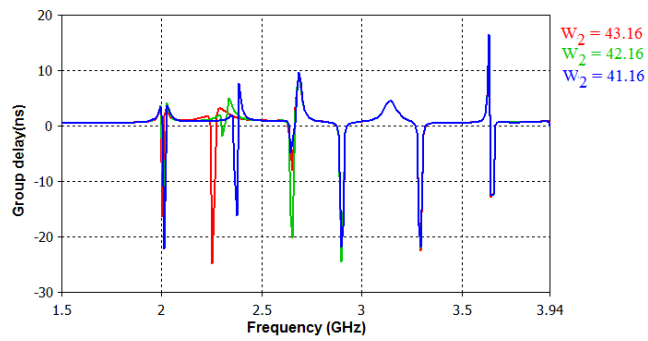


(b) Group delay

Fig. 2.39: Simulated transmission characteristics of tuning the first U slot in multiresonator with six U slots shown in Fig.2.1 ($L = 50$ mm, $W = 37$ mm, $G = 0.9$ mm, $W_2 = 41.2$ mm, $W_3 = 37.1$ mm, $W_4 = 33$ mm, $W_5 = 29.2$ mm, $W_6 = 25.8$ mm, W_1 in mm)

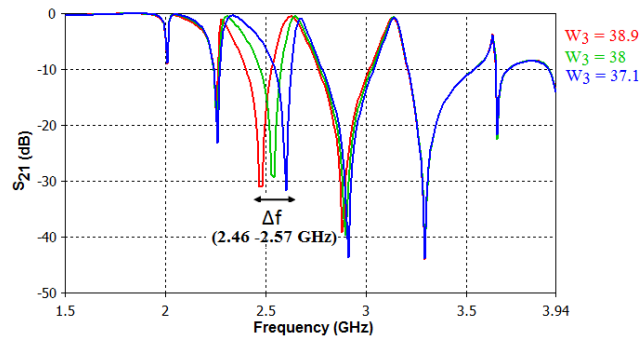


(a) S_{21}

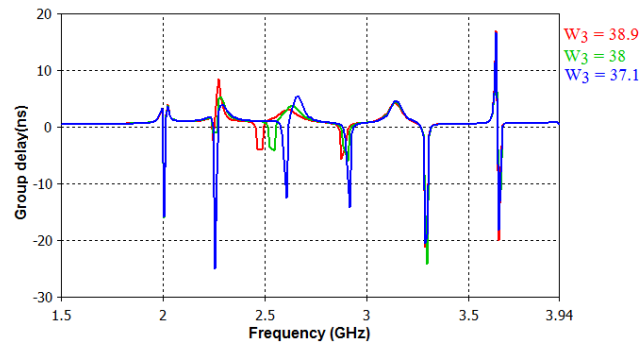


(b) Group delay

Fig. 2.40: Simulated transmission characteristics of tuning the second U slot in multiresonator with six U slots shown in Fig.2.1 ($L = 50$ mm, $W = 37$ mm, $G = 0.9$ mm, $W_1 = 48.2$ mm, $W_3 = 37.1$ mm, $W_4 = 33$ mm, $W_5 = 29.2$ mm, $W_6 = 25.8$ mm, W_2 in mm)

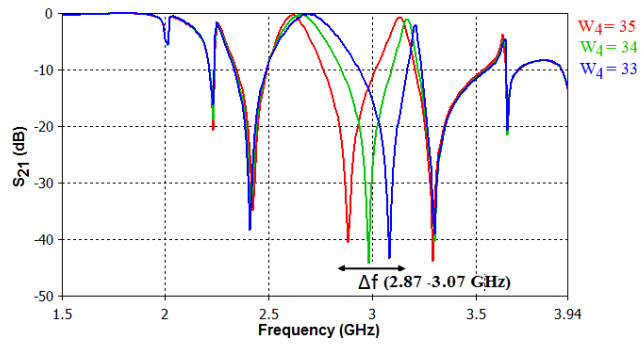


(a) S_{21}

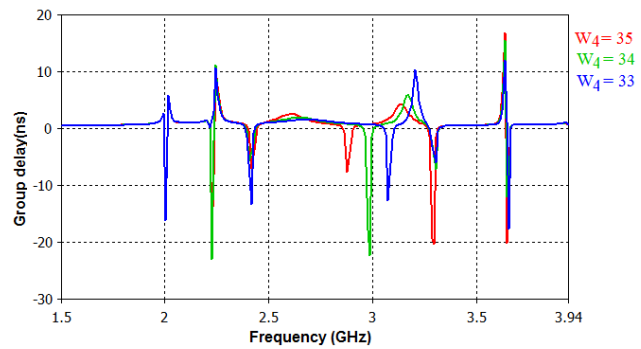


(b) Group delay

Fig. 2.41: Simulated transmission characteristics of tuning the third U slot in multiresonator with six U slots shown in Fig.2.1 ($L = 50$ mm, $W = 37$ mm, $G = 0.9$ mm, $W_1 = 48.2$ mm, $W_2 = 41.2$ mm, $W_4 = 33$ mm, $W_5 = 29.2$ mm, $W_6 = 25.8$ mm, W_3 in mm)

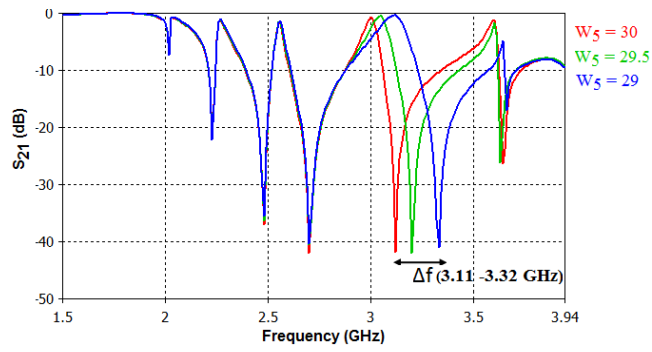


(a) S_{21}

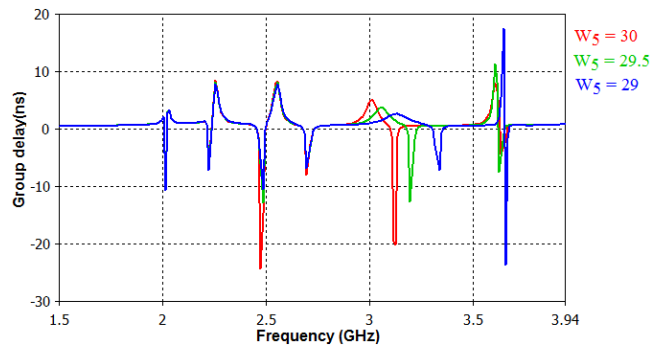


(b) Group delay

Fig. 2.42: Simulated transmission characteristics of tuning the fourth U slot in multiresonator with six U slots shown in Fig.2.1 ($L = 50$ mm, $W = 37$ mm, $G = 0.9$ mm, $W_1 = 48.2$ mm, $W_2 = 41.2$ mm, $W_3 = 37.1$ mm, $W_5 = 29.2$ mm, $W_6 = 25.8$ mm, W_4 in mm)

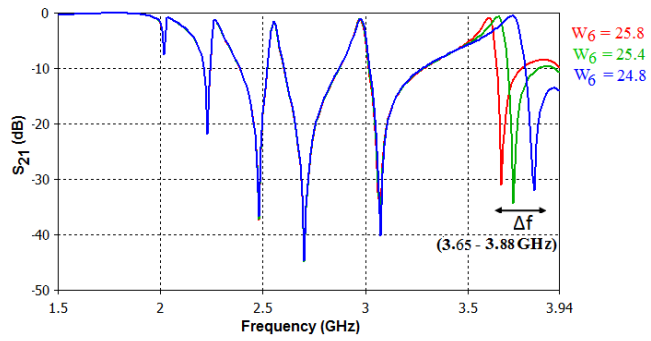


(a) S_{21}

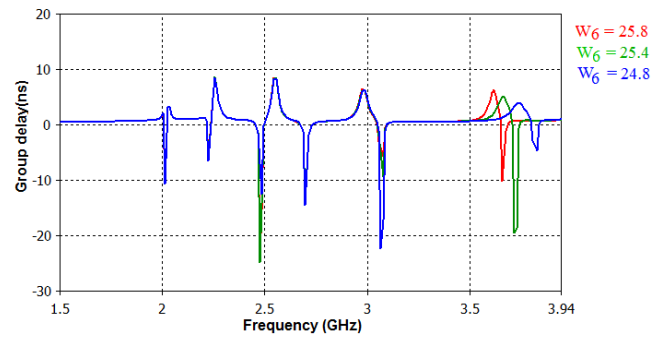


(b) Group delay

Fig. 2.43: Simulated transmission characteristics of tuning the fifth U slot in multiresonator with six U slots shown in Fig.2.1 ($L = 50$ mm, $W = 37$ mm, $G = 0.9$ mm, $W_1 = 48.2$ mm, $W_2 = 41.2$ mm, $W_3 = 37.1$ mm, $W_4 = 33$ mm, $W_6 = 25.8$ mm, W_5 in mm)



(a) S_{21}



(b) Group delay

Fig. 2.44: Simulated transmission characteristics of tuning the sixth U slot in multiresonator with six U slots shown in Fig.2.1 ($L = 50$ mm, $W = 37$ mm, $G = 0.9$ mm, $W_1 = 48.2$ mm, $W_2 = 41.2$ mm, $W_3 = 37.1$ mm, $W_4 = 33$ mm, $W_5 = 29.2$ mm, W_6 in mm)

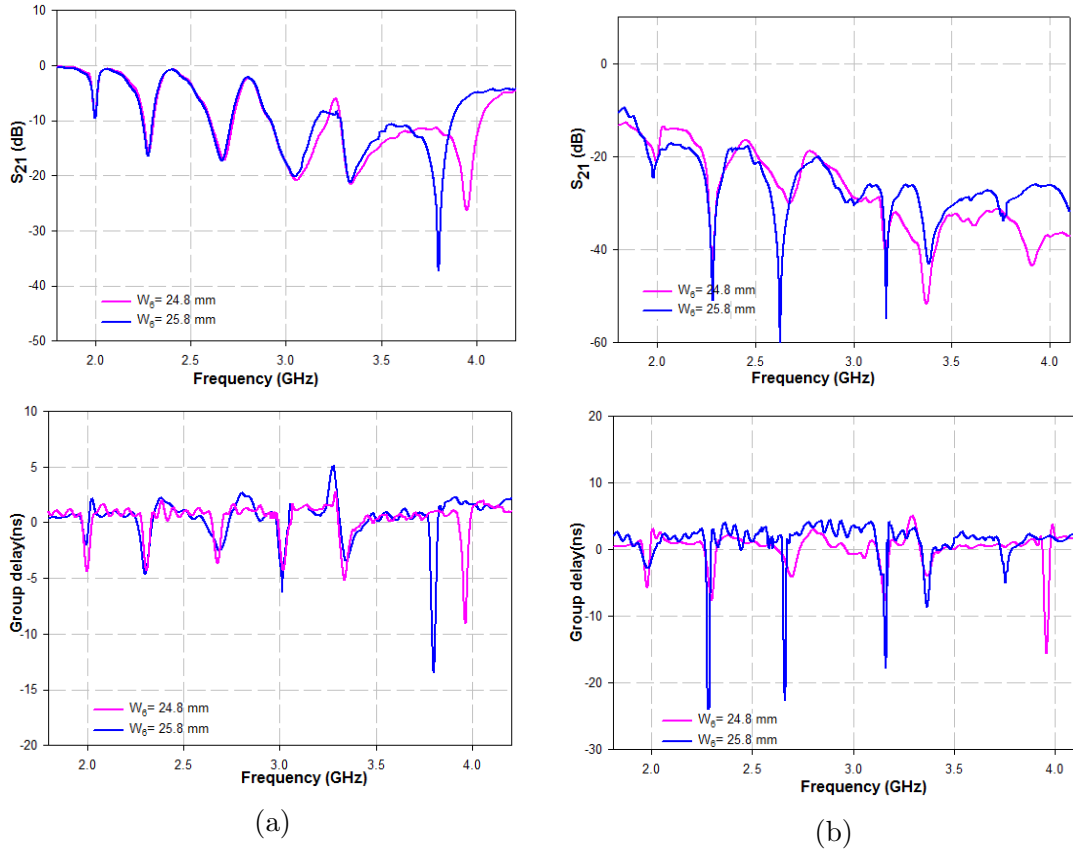


Fig. 2.45: Measured response of the multiresonator with six U slots for two different configurations ($L = 50$ mm, $W = 37$ mm, $G = 0.9$ mm, $W_1 = 48.16$ mm, $W_2 = 43.16$ mm, $W_3 = 37.1$ mm, $W_4 = 34$ mm, $W_5 = 29$ mm) (a) Transmission characteristics of the resonator (b) Bistatic response

All the above results reveal the design flexibility and high data encoding capacity of the proposed U slot multiresonator for chipless RFID applications.

2.6 Chapter summary

This chapter explains the implementation of chipless RFID tag using U slot multiresonator. The multiresonator consisting of six U slot resonators is developed by varying the slot dimension. Equivalent circuit model of the resonator is developed using Agilent ADS. Design equation of the resonator is developed using multiple regression analysis. Orthogonally polarized circular monopole antennas are integrated to the multiresonator for range enhancement. The concept is validated using bistatic measurement for a six bit prototype. The tag can encode data in magnitude and group delay. Two different methods of data encoding namely absence or presence coding technique and FSC technique are discussed. In absence or presence coding technique, maximum bits that can be represented by an RFID tag is equal to the number of resonators. The bit coding capacity of the tag can be enhanced using FSC technique. This is validated for various tag configurations. It is found that using six resonators, the number of code words in FSC increases to 729 (3^6) compared to 64 (2^6) in the case of absence or presence coding method. Table 2.8 gives a comparison of the proposed chipless RFID tags with other reported tag designs. The comparison is done based on absence or presence coding technique. The proposed tag requires less bandwidth to encode 2^6 code words compared to other designs.

2.7 Inferences

1. It is inferred that sharper resonance of the individual resonators can lead to increased bit capacity. The tags presented in the subsequent chapters exhibit higher bit capacity.
2. The data capacity of the proposed U slot RFID tag is limited due to the lower frequency limit imposed by the operating band of the monopole

Table 2.8: Performance comparison of different chipless RFID tags

Parameters	(Kim <i>et al.</i> , 2010)	(Jalil, 2014)	(Lee <i>et al.</i> , 2013)	Proposed tag
RFID operating band (GHz)	2-2.7	3-5	3 - 6.2	1.99 - 3.9
Bandwidth required	700 MHz	2 GHz	3.2	1.91 GHz
Bit states per resonator	3	2	2	2
Number of resonators	1	6	5	6
Number of code words	3	2^6	2^5	2^6
Bandwidth requirement for each bit (MHz)	> 100	< 100	> 100	< 100
Surface coding density (bits/cm ²)	0.59	0.57	Not specified	0.55

antenna as well as the higher frequency limit imposed by the harmonics of the slot resonant frequencies.

3. Nevertheless, higher data capacity is possible with the existing configuration, if two more U resonators are added without affecting the other resonances. However this demands tag and reader antennas with wider operating range.

CHAPTER 3

CHIPLESS RFID TAG USING SHORTED STUB MULTIRESONATOR

3.1 Introduction

The need for multiresonator in the design of chipless RFID tags has been already discussed in detail in Chapter 2. Multiresonator circuit is a series of narrow band rejection filters consisting of different resonators. It will alter the amplitude of the interrogating signal. This chapter presents the design and development of spectral signature based chipless RFID tag using multiple shorted stub resonators. Each resonator independently resonates at its half wave length frequency.

3.2 The shorted stub multiresonator

The multiresonator consists of eight half wavelength long stubs, connected to a transmission line at one end and shorted to ground through via at the other end as illustrated in Fig.3.1. The prototype is simulated on substrate C-MET/LK4.3 with dielectric constant 4.3, height 1.6 mm and loss tangent 0.0018 using CST MWS[®]. Fig.3.2 shows the microstrip version of the multiresonator. The overall dimension ($W_a \times L_a$) is 32 mm x 60 mm. The bottom plane acts as ground. The design approach is to generate multiple resonances by optimising the length of each shorted stub ($L_1 - L_8$) in the multiresonator. Each shorted

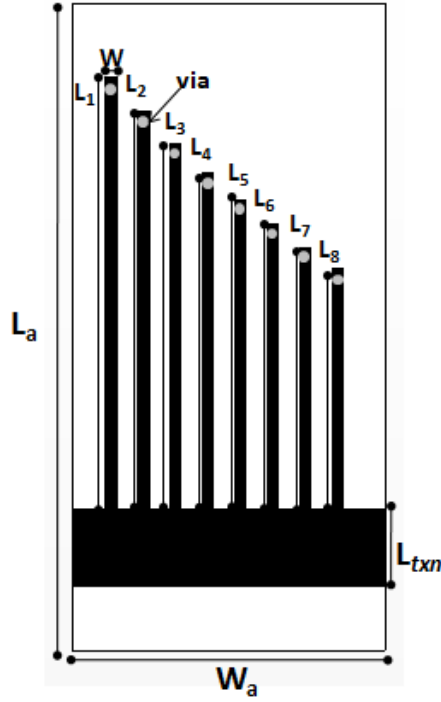


Fig. 3.1: Proposed eight bit shorted stub multiresonator [$W_a = 32$, $L_a = 60$, $L_1 = 43.71$, $L_2 = 40.21$, $L_3 = 37$, $L_4 = 34.04$, $L_5 = 31.31$, $L_6 = 26.5$, $L_7 = 24.3$, $L_8 = 23.4$, $L_{txn} = 7$, $W = 1$, diameter of the via = 0.8 (All dimensions in mm) Substrate: loss tangent = 0.0018, $\epsilon_r = 4.3$, $h = 1.6$ mm]

stub of different length introduces different stop band resonance, which can be identified from the transmission characteristics as shown in Fig.3.3. Individual resonators operate at frequencies 1.93 GHz, 2.17 GHz, 2.35 GHz, 2.53 GHz, 2.76 GHz, 3.21 GHz, 3.42 GHz and 3.74 GHz, thus encoding eight bits in a band of 1.81 GHz. Fig.3.4 shows surface current distribution of individual resonators at the corresponding resonant frequencies. The evolution of the shorted stub multiresonator is discussed in the following section.

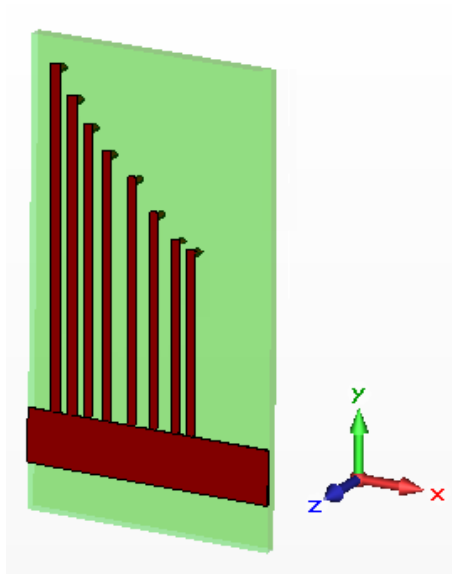


Fig. 3.2: Microstrip version of the shorted stub multiresonator

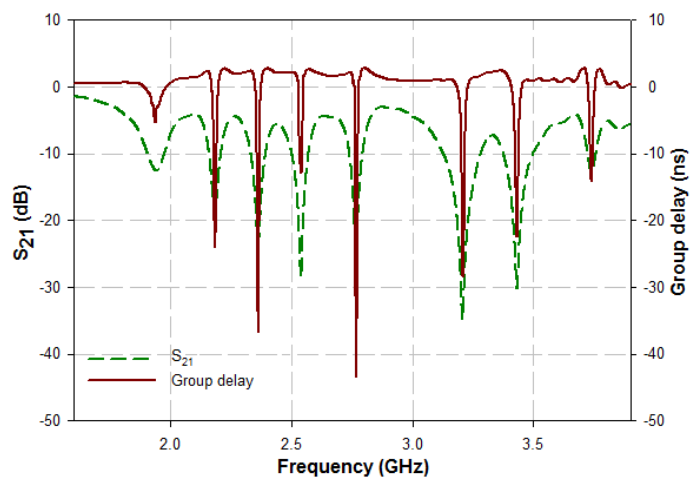


Fig. 3.3: Simulated transmission characteristics of the eight bit shorted stub multiresonator shown in Fig.3.1

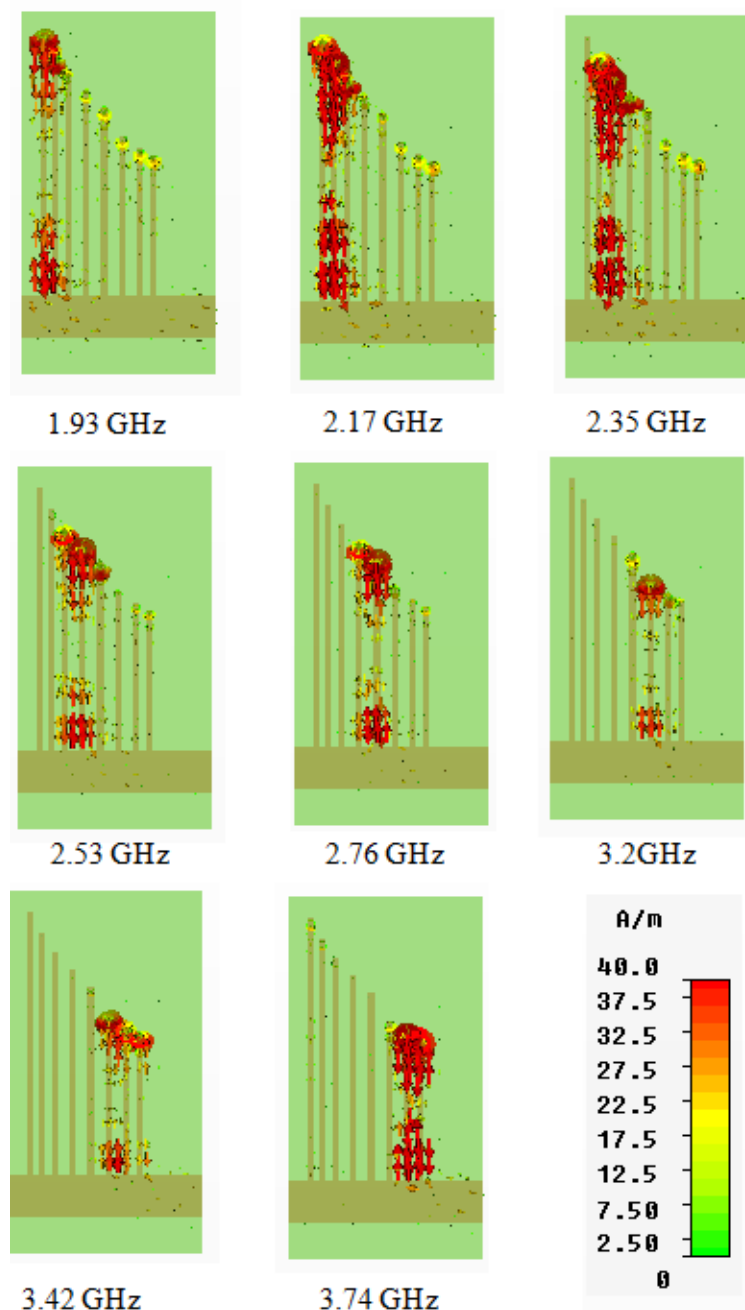


Fig. 3.4: Surface current distribution of individual resonators in the shorted stub multiresonator shown in Fig.3.1

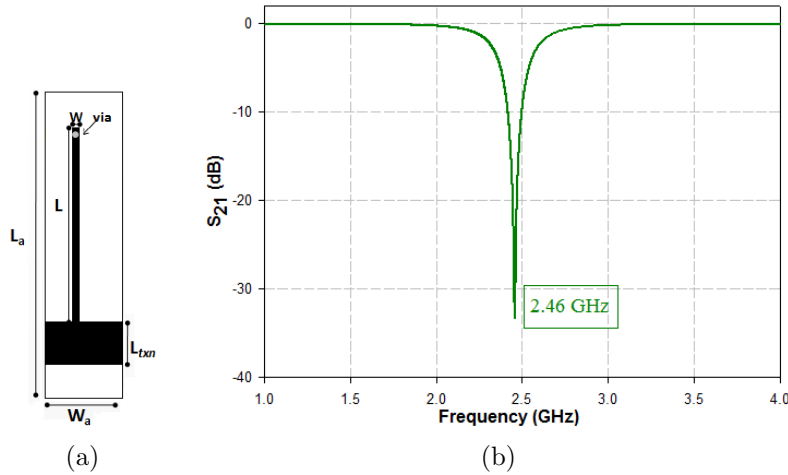


Fig. 3.5: Shorted stub resonator and its simulated transmission characteristics [$L_a = 60$, $W_a = 15$, $L_{txn} = 7$, $L = 34.57$, $W = 1$, diameter of the via = 0.8 (All dimensions in mm), Substrate: loss tangent = 0.0018, $\epsilon_r = 4.3$, $h = 1.6$ mm]

3.3 Evolution of shorted stub multiresonator

The multiresonator has evolved from a shorted stub resonator. A half wavelength long stub ($\lambda_g/2$) connected to microstrip transmission line at one end and shorted to ground at the other end through a via of diameter 0.8 mm is shown in Fig.3.5(a). The bottom plane acts as ground. Fig.3.5(b) shows the simulated transmission characteristics of the shorted stub resonator.

3.3.1 Analysis and design of shorted stub resonator

The resonant frequency can be tuned by varying the length (L) of the stub. The simulated transmission characteristics shown in Fig.3.6 illustrate the shift in resonant frequency from 2.56 GHz to 4.48 GHz as length is varied from 32.84 mm to 17.97 mm. This property of achieving multiple resonances by varying the length of the stub is used for designing the multiresonator.

Surface current distribution of the shorted stub resonator at its resonant frequency (2.46 GHz) and at a non-resonant frequency (3 GHz) are depicted in

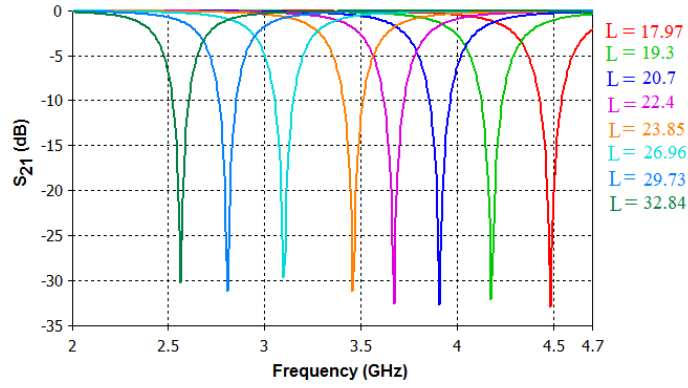


Fig. 3.6: Simulated transmission characteristics for various values of L (mm) of shorted stub resonator shown in Fig.3.5(a)

Fig.3.7(a) and Fig.3.7(b) respectively. The surface current distribution is concentrated in the resonator at the resonant frequency. It is clear that there is no transmission from port 1 to port 2 at the resonant frequency and transmission occurs at non-resonant frequency. From Fig.3.7(a) it is evident that there is half wavelength variation of surface current at resonance.

Multiple regression analysis is used to develop a generalised design equation of the resonator for a chosen substrate of relative permittivity (ϵ_r) and height (h in mm). The length of the shorted stub ' L ' (in mm), computed for a resonant frequency (f in GHz) can be expressed as in Equation 3.1. The database for the development of the design equation is created by doing parametric analysis by varying the length of the stub for each substrate keeping $W = 1$ mm.

$$L = -2.07h - 8.36f - 3.18\epsilon_r + 70.83 \quad (3.1)$$

The equation is valid for ϵ_r and h in the range $2.25 \leq \epsilon_r \leq 5.4$ and $0.7 \text{ mm} \leq h \leq 1.6 \text{ mm}$ respectively. The equation is confirmed on various substrates having different values of relative permittivity and height as shown in Table 3.1.

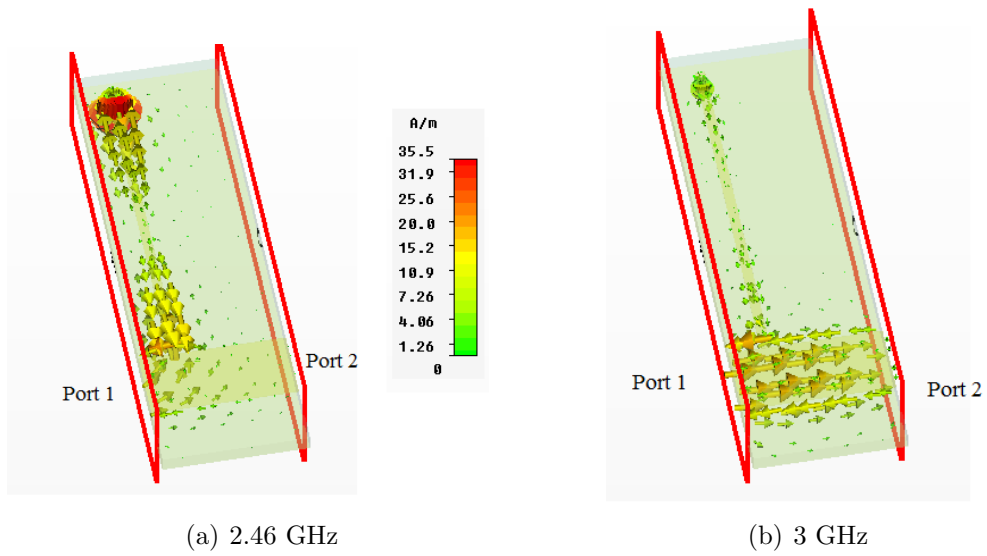


Fig. 3.7: Surface current distribution of shorted stub resonator shown in Fig.3.5(a) at resonant frequency of 2.46 GHz and at a non-resonant frequency of 3 GHz.

Table 3.1: Computed values of L for different resonant frequencies on various substrates

	ϵ_r	h (mm)	L(mm)	f (GHz)		%error
				Theory	CST	
1	4.3	1.6	24.582	3.5	3.4	2.85
2	2.4	1	27.7	4	3.9	2.5
3	5.4	1.25	22.641	3.4	3.3	2.94
4	4.8	1.6	24.662	3.3	3.4	3.03
5	2.25	1	23.995	4.5	4.53	0.66

3.3.2 Equivalent circuit of shorted stub resonator

The shorted stub resonator can be modeled as short circuited transmission line of length $\lambda_g/2$. The input impedance of a transmission line of length 'l' is given by (Pozar, 2009; Malherbe, 1979)

$$Z_{in} = Z_0 \frac{Z_L + Z_0 \tanh \gamma l}{Z_0 + Z_L \tanh \gamma l} \quad (3.2)$$

$\gamma = \alpha + j\beta$, α is the attenuation constant, β is the phase constant, Z_0 is the characteristic impedance and Z_L is the load impedance. For a short circuited transmission line of length $\lambda/2$, Equation 3.2 can be written as

$$\begin{aligned} Z_{in} &= Z_0 \tanh(\alpha + j\beta)l \\ Z_{in} &= Z_0 \frac{\tanh \alpha l + j \tan \beta l}{1 + j \tan \beta l \tanh \alpha l} \end{aligned} \quad (3.3)$$

Since the resonator is designed with a low loss material ($\alpha l \ll 1$)

$$\tanh \alpha l \approx \alpha l \quad (3.4)$$

$$\alpha = \alpha_c + \alpha_d \quad (3.5)$$

α_c is the attenuation due to conductor loss and α_d is the dielectric loss.

$$\alpha_c = \frac{R_s}{Z_0 W} \quad (3.6)$$

R_s is the surface resistivity of the conductor and W is the width of the shorted stub resonator

$$R_s = \sqrt{\frac{\omega \mu_0}{2\sigma}} \quad (3.7)$$

μ_0 is the permeability of free space and σ is the conductivity of copper.

$$\begin{aligned}\alpha_d &= \frac{K_0 \epsilon_r (\epsilon_e - 1) \tan \delta}{2\sqrt{\epsilon_e} (\epsilon_r - 1)} \\ K_0 &= \frac{2\pi f}{c}\end{aligned}\tag{3.8}$$

At a frequency (ω) near resonance (ω_0), $\omega = \omega_0 + \Delta\omega$,

$$\beta l = \frac{\omega l}{v_p} = \frac{\omega_0 l}{v_p} + \frac{\Delta\omega l}{v_p}$$

v_p is the phase velocity of the transmission line. Since $l = \lambda/2$ at $\omega = \omega_0$

$$\begin{aligned}\beta l &= \pi + \frac{\Delta\omega\pi}{\omega_0} \\ \tan \beta l &= \tan\left(\pi + \frac{\Delta\omega\pi}{\omega_0}\right) = \tan\left(\frac{\Delta\omega\pi}{\omega_0}\right) \approx \frac{\Delta\omega\pi}{\omega_0}\end{aligned}\tag{3.9}$$

These results when substituted in Equation 3.3 gives

$$Z_{in} \approx Z_0 \frac{\alpha l + j \frac{(\Delta\omega\pi)}{\omega_0}}{1 + j \frac{(\Delta\omega\alpha l\pi)}{\omega_0}} \approx Z_0 \left(\alpha l + j \frac{\Delta\omega\pi}{\omega_0} \right)\tag{3.10}$$

since $\frac{\Delta\omega\alpha l}{\omega_0} \ll 1$ Equation 3.10 resembles the input impedance of a series RLC resonant circuit,

$$Z_{in} = R + 2jL\Delta\omega\tag{3.11}$$

where resistance of the equivalent circuit is

$$R = Z_0 \alpha l\tag{3.12}$$

and inductance of the equivalent circuit is

$$L = \frac{\pi Z_0}{2\omega_0}\tag{3.13}$$

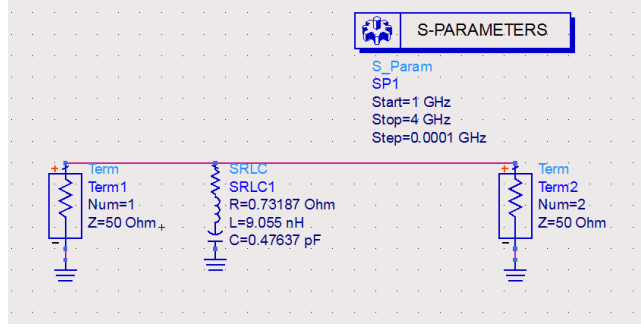


Fig. 3.8: Equivalent circuit of shorted stub resonator ($f = 2.46$ GHz)

where $\omega_0 = \frac{2\pi c}{\lambda_g \sqrt{\epsilon_{eff}}}$, $\lambda_g = 2l$, l is the length of the shorted stub resonator and c is the velocity of light. Substituting for ω_0 in Equation 3.13

$$L = \frac{lZ_0\sqrt{\epsilon_{eff}}}{2c} \quad (3.14)$$

the capacitance of the equivalent circuit is

$$C = \frac{1}{\omega^2 L} \quad (3.15)$$

The shorted stub resonator is therefore modeled as a series RLC resonant circuit, where R , L and C are determined from the stub parameters (l , W , ϵ_{eff}) using Equations 3.12, 3.14 and 3.15. Fig.3.8 shows the equivalent circuit designed in Agilent ADS software with two ports connected across the 50Ω transmission line for a resonant frequency of 2.46 GHz. Fig.3.9 shows the frequency response extracted using Agilent ADS. The frequency response extracted from equivalent circuit matches with the result obtained using CST MWS[®] as shown in Fig.3.5(b).

3.3.3 Experimental results of shorted stub multiresonator

Fig.3.10(a) shows the photograph of the fabricated shorted stub multiresonator. Measurements are conducted using the PNA E8362B vector network analyser. The device under test (multiresonator) is connected between the two ports

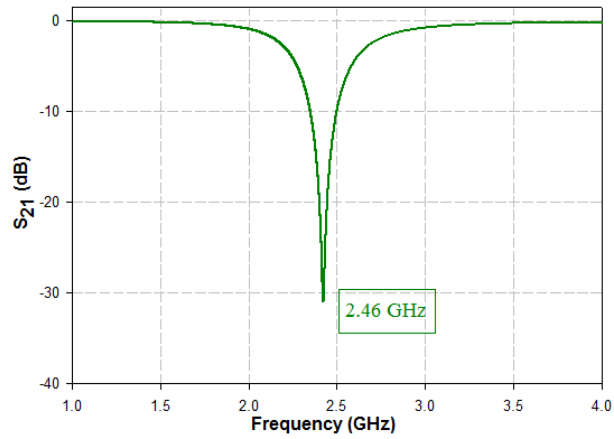


Fig. 3.9: Frequency response of shorted stub resonator equivalent circuit extracted using Agilent ADS

of the vector network analyser as shown in Fig.3.10(b). Fig.3.11 shows the measured transmission characteristics of the shorted stub multiresonator for bit combination [1111 1111]. Data encoding techniques discussed in Section 3.5.1 are used to generate various bit combinations. The proposed shorted stub can be used as an RFID tag for access control applications where the tag is in close proximity of the reader. However the tag needs modification in its design for range enhancement. This is discussed in Section 3.4.

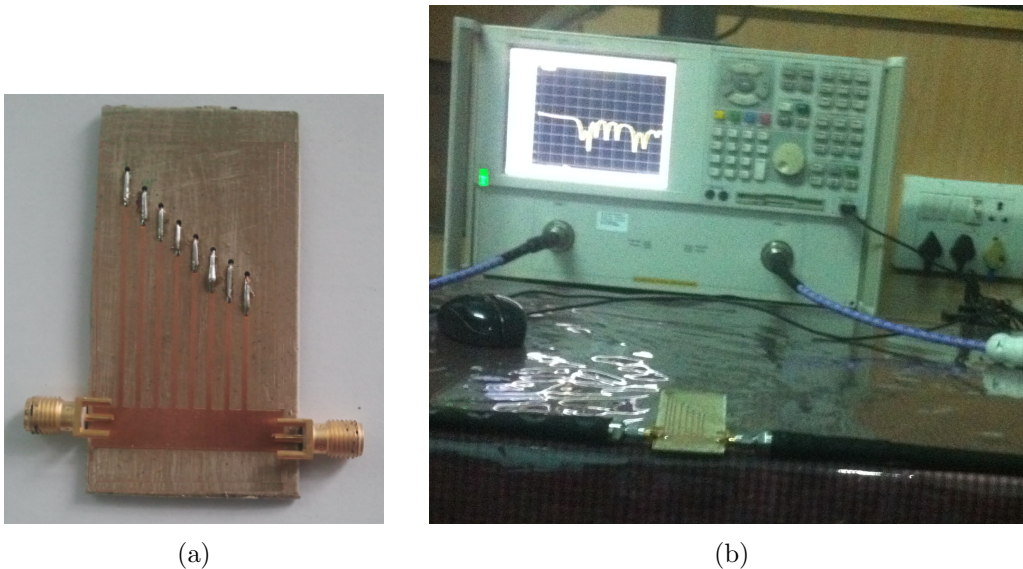


Fig. 3.10: (a) Photograph of the fabricated shorted stub multiresonator (b) Network analyser with device under test

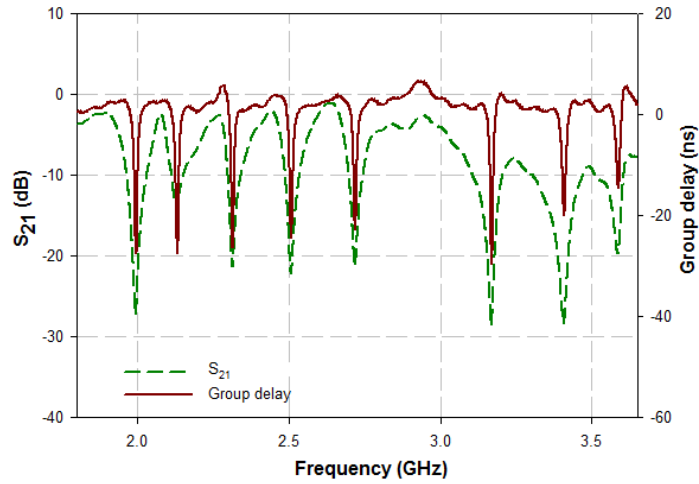


Fig. 3.11: Measured transmission characteristics of the shorted stub multiresonator for the bit combination [1111 1111]

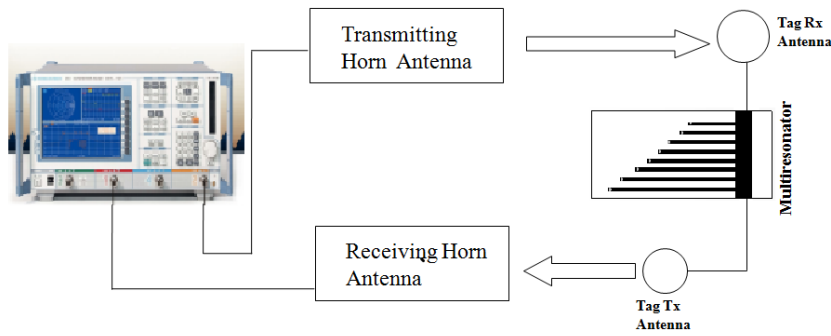


Fig. 3.12: Block schematic for bistatic measurement using shorted stub multiresonator

3.4 Bistatic measurement for validation of the tag

The block schematic of bistatic measurement of the RFID tag using shorted stub multiresonator is shown in Fig.3.12. Two wide band antennas are incorporated to increase the range of multiresonator as explained in Section 2.4. Two cross polarized medium gain (10 dB) horn antennas are used for transmission and reception of the signal at the reader (Preradovic and Karmakar, 2009; Preradovic *et al.*, 2009, 2008a).

Fig.3.13 shows the experimental setup for bistatic measurement of the RFID



Fig. 3.13: Experimental setup for bistatic measurement of the RFID tag using shorted stub multiresonator

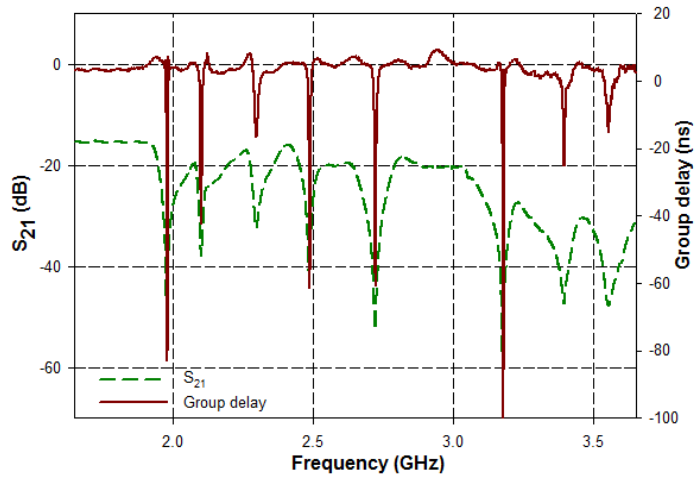


Fig. 3.14: Measured bistatic response of the RFID tag using shorted stub multiresonator for the bit combination [1111 1111]

tag using shorted stub multiresonator. The tag is placed 15 cm away from horn antennas. Fig.3.14 shows the measured bistatic response for bit combination [1111 1111] when all the eight shorted stub resonators are connected to the transmission line. The bistatic response clearly indicates the abrupt variations at resonance, as in the case of multiresonator [Fig.3.11].

3.5 Data encoding methods

Absence or presence coding technique and frequency shift coding technique, as discussed in Section. 2.5, are employed for data encoding.

3.5.1 Absence or presence coding technique

The presence of resonance is used to encode a logic 1 and the absence of resonance is used to encode a logic 0. In shorted stub multiresonator type 1 [Fig.3.15] all the eight stubs are connected to transmission line and ground through via resulting in a bit combination [1111 1111], stub 1 corresponds to the most significant bit and stub 8 corresponds to the least significant bit.

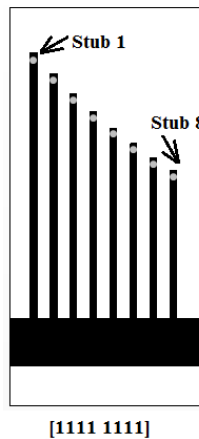
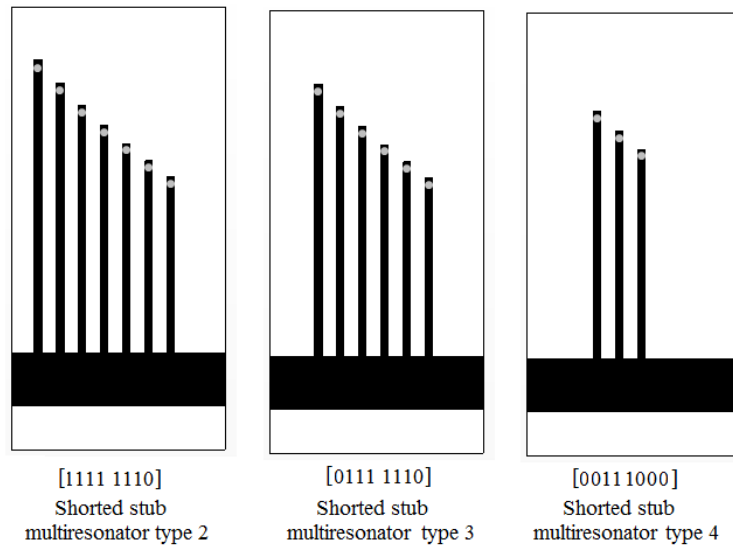
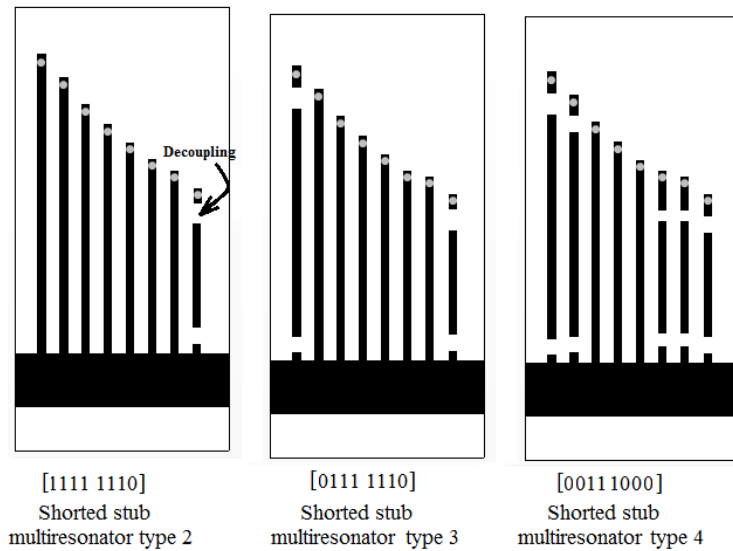


Fig. 3.15: Shorted stub multiresonator type 1

The absence of a specific resonance can be achieved either by removing the corresponding resonator [Fig.3.16(a)] or decoupling the stub from the transmission line and from the ground plane [Fig.3.16(b)]. Three different types of such resonators are shown in Fig.3.16.



(a) Removing the resonator



(b) Decoupling the resonator

Fig. 3.16: Three different types of shorted stub multiresonator (a) Removing the resonator (b) Decoupling the resonator

In shorted stub multiresonator type 2 resonance due to stub 8 is absent leading to a bit combination [1111 1110]. In shorted stub multiresonator type 3 resonances due to stub 1 and stub 8 are absent resulting in [0111 1110]. In shorted stub multiresonator type 4 resonances due to stub 1, stub 2, stub 6, stub 7 and stub 8 are absent resulting in [0011 1000]. Fig.3.17 shows the simulated

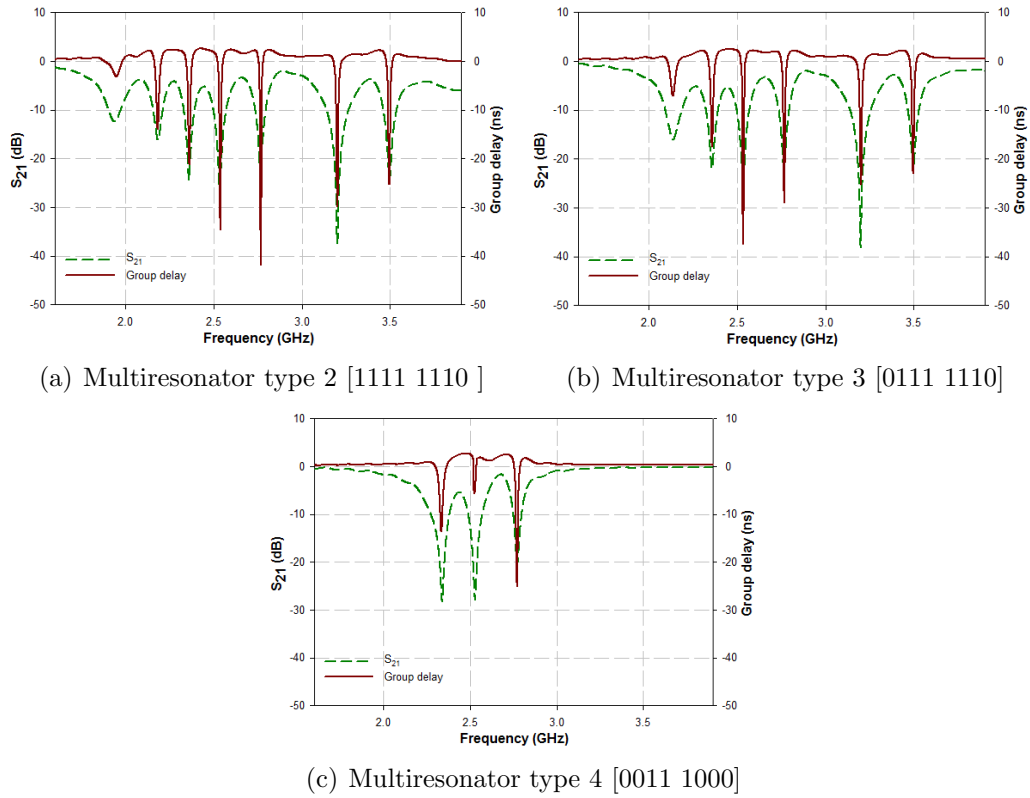


Fig. 3.17: Simulated transmission characteristics of the shorted stub multiresonator for different bit combinations

transmission characteristics of the three types of resonators. The small shift in resonant frequency may be due to the mutual coupling between the resonators. The simulated transmission characteristics of [1111 1111] was shown in Fig.3.3.

3.5.2 Experimental results of shorted stub multiresonator using absence or presence coding technique

Using the technique mentioned in Section 3.5.1 different types of multiresonators are fabricated. The transmission characteristics is measured using Agilent PNA E8362B vector network analyzer by connecting the multiresonator between the ports of analyzer. Measured transmission characteristics of the shorted stub multiresonator for the bit combinations [1111 1110], [0111 1110] and [0011 1000] are shown in Fig.3.18. The measured result of [1111 1111] was

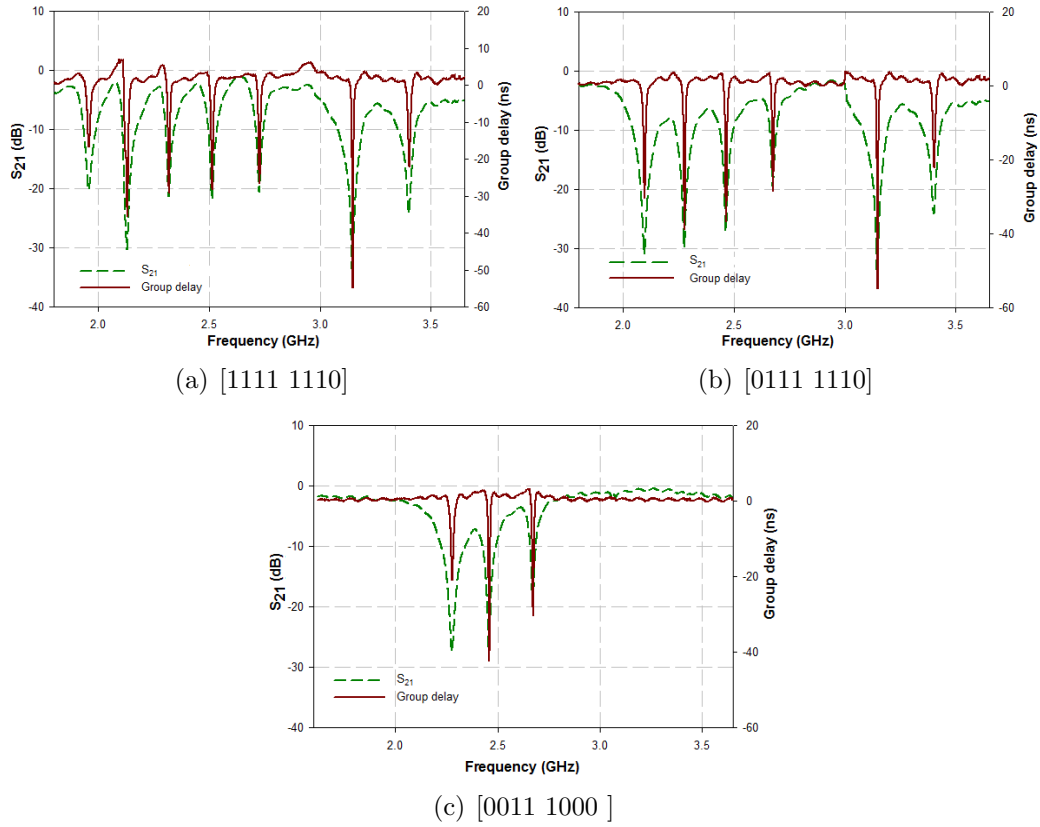
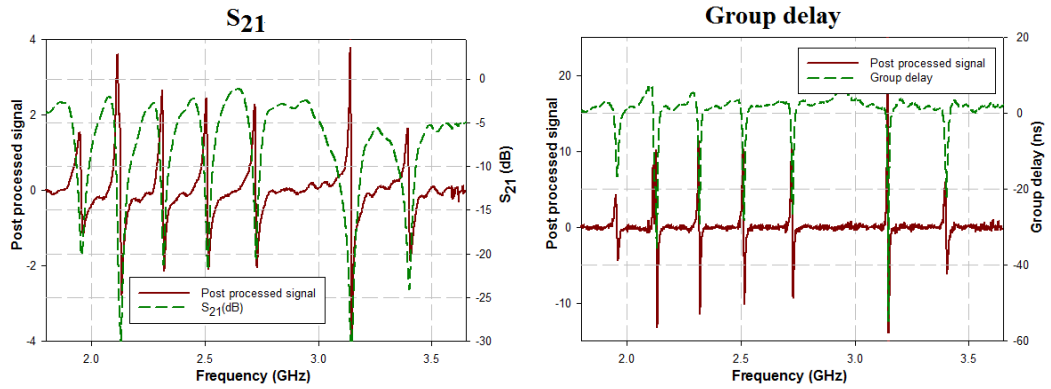


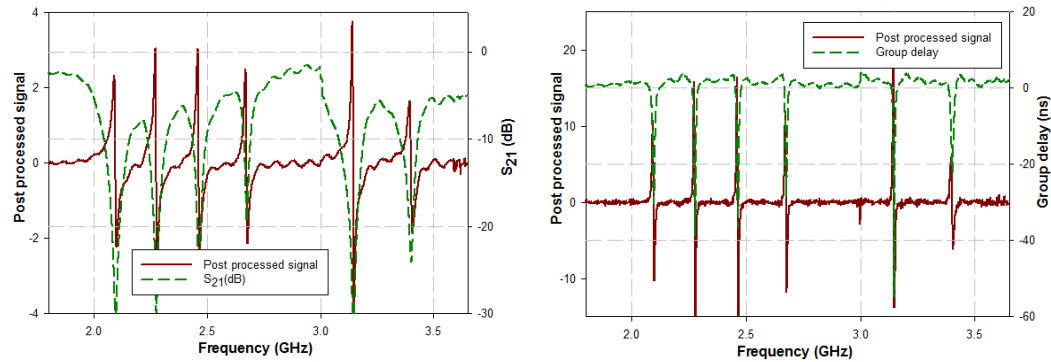
Fig. 3.18: Measured transmission characteristics of the shorted stub multiresonator for different bit combinations

shown in Fig.3.11.

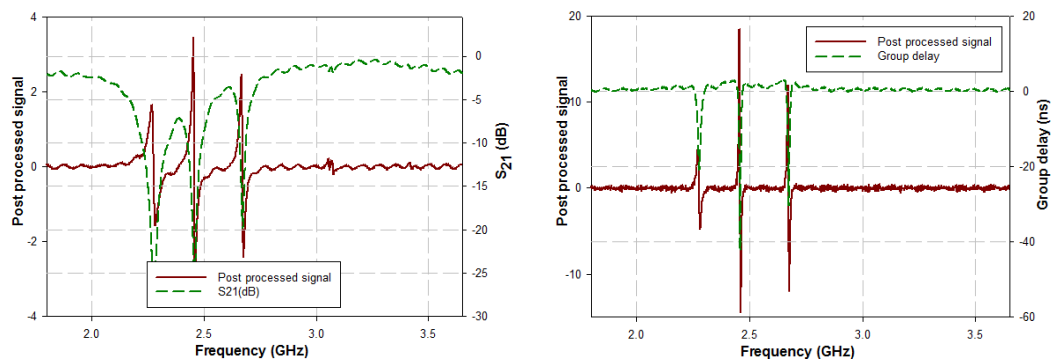
The tag identity can be confirmed from the absolute value of S_{21} or group delay. The tag detection can be made virtually independent of absolute value of S_{21} or group delay by a post processing method using a difference operation technique as detailed in Section 2.5.2. A peak variation at resonance is clearly visible from the post processed signal for the bit combination [1111 1110], [0111 1110] and [0011 1000] as shown in Fig.3.19.



(a) [1111 1110]



(b) [0111 1110]



(c) [0011 1000]

Fig. 3.19: Measured transmission characteristics of the shorted stub multiresonator and its post processed signal for various bit combinations

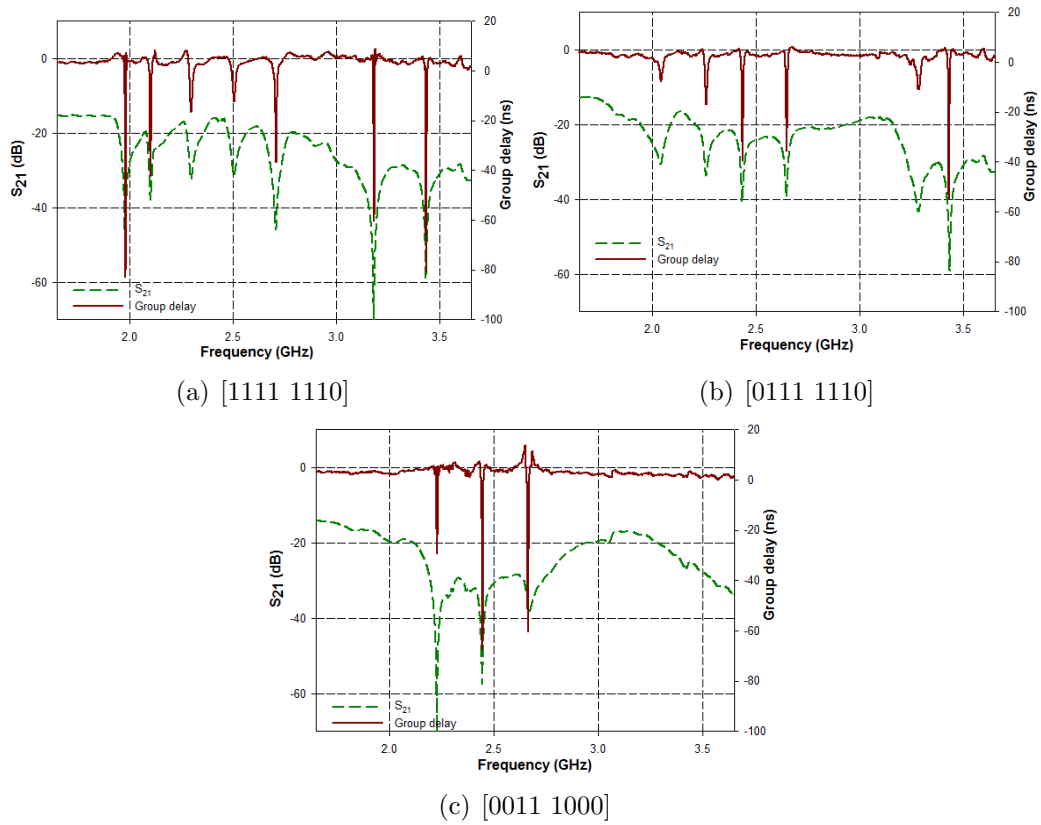


Fig. 3.20: Measured bistatic response of the RFID tag using shorted stub multiresonator for different bit combinations

3.5.3 Bistatic measurement results using absence or presence coding technique

Bistatic measurement is done to validate the tag for various bit combinations. Fig.3.20 shows the measured bistatic response for bit combinations [1111 1110], [0111 1110] and [0011 1000]. The measured result of [1111 1111] was shown in Fig.3.14. Fig.3.21 shows the post processed signal for the bit combination [1111 1111].

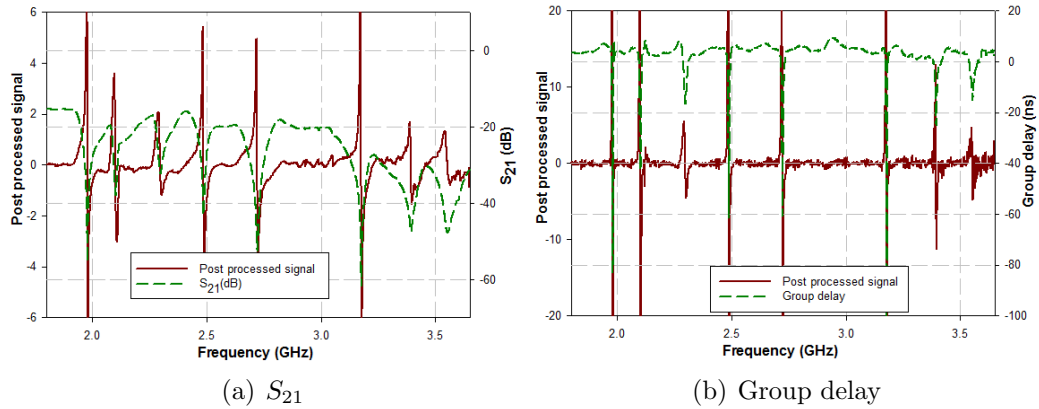


Fig. 3.21: Measured bistatic response of the RFID tag using shorted stub multiresonator and its post processed signal for the combination [1111 1111]

3.5.4 Frequency shift coding technique for enhanced bit encoding capacity

The bit encoding capacity of the tag can be enhanced using frequency shift coding (FSC) technique, by encoding more than one bit per resonator as explained in Section 2.5.4. This section explains the method by which FSC is applied to various shorted stub resonator configurations.

3.5.5 Frequency shift coding applied to shorted stub resonator

The simulated transmission characteristics for various values of length (L) of shorted stub resonator [Fig.3.5(a)] are shown in Fig.3.22. In a frequency band (Δf) from 2.45 GHz to 4.48 GHz, 12 frequency bands are possible. δf is the frequency band for each resonator required to faithfully represent its resonant frequency, thus determining the frequency resolution. Table 3.2 shows a proposed method of code word allocation for the shorted stub resonator. The code words are allotted for each frequency, corresponding to each value of length. The variation in length is restricted due to the presence of higher harmonics.

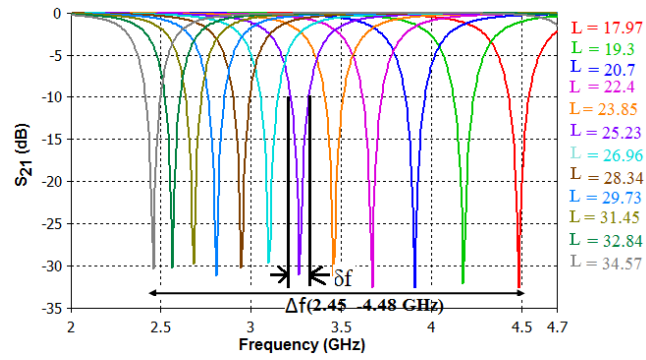
Table 3.2: Proposed method of code word allocation for the shorted stub resonator

Sl.no	L (mm)	f (GHz)	Code word
1	34.5	2.45	0000
2	32.8	2.56	0001
3	31.5	2.68	0010
4	29.7	2.80	0011
5	28.3	2.94	0100
6	26.9	3.09	0101
7	25.2	3.26	0110
8	23.8	3.45	0111
9	22.4	3.67	1000
10	20.7	3.90	1001
11	19.3	4.17	1010
12	17.9	4.48	1011

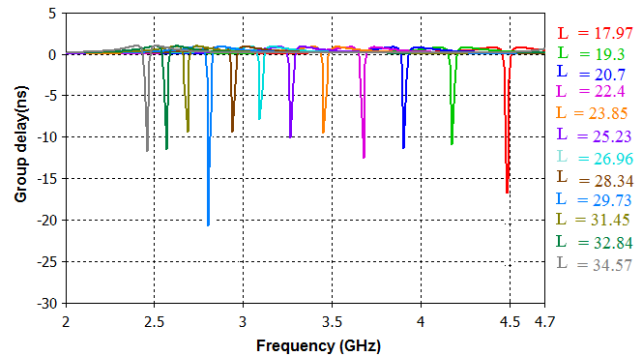
While absence or presence coding of a resonator can encode only two code words (0/1) using a single shorted stub resonator, use of FSC allows an improvement to 12 code words.

3.5.6 Frequency shift coding applied to multiresonator with two shorted stubs

Fig.3.23 shows the layout of multiresonator with two shorted stubs whose length (L_i) is individually varied for FSC. The frequency band (Δf) and resonant frequency(f) of each resonator are listed in Table.3.3. Variation of the length of the first stub, keeping the length of the second stub constant, results in ten different resonant frequencies as shown in Fig.3.24. Similarly, variation of length of the second stub, keeping the length of the first stub constant, results in ten



(a) S_{21}



(b) Group delay

Fig. 3.22: Simulated transmission characteristics of the shorted stub resonator shown in Fig.3.5(a) for various values of L (mm)

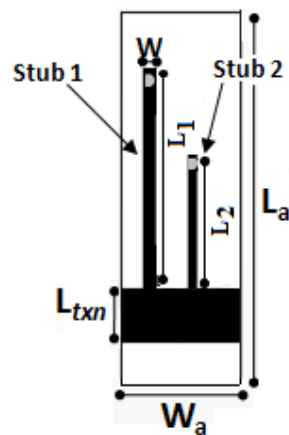
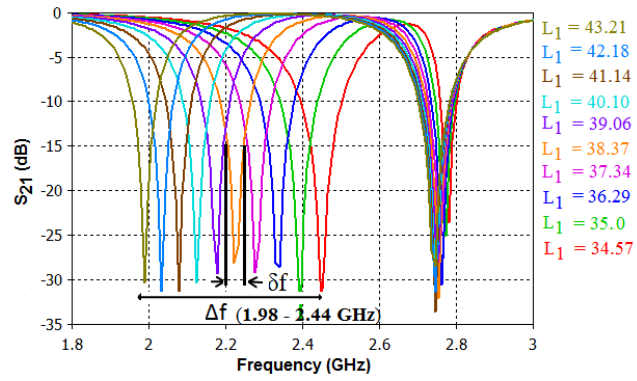


Fig. 3.23: Layout of multiresonator with two shorted stubs [$L_a = 60$, $W_a = 15$, $L_{txn} = 7$, $W = 1$, diameter of the via = 0.8 (All dimensions in mm) Substrate: loss tangent = 0.0018, $\epsilon_r = 4.3$, $h = 1.6$ mm]

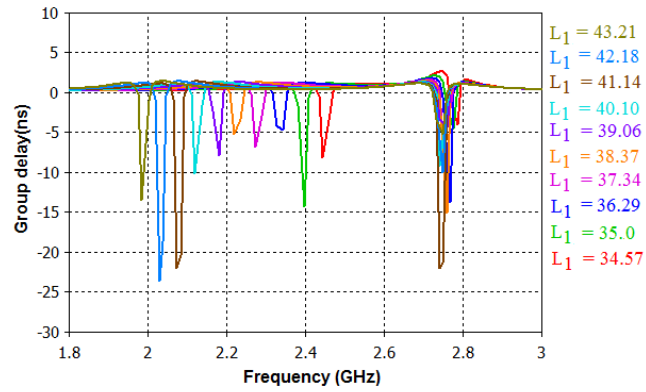
Table 3.3: Frequency band (Δf) and resonant frequency (f) of multiresonator with two shorted stubs (All values in GHz)

	Δf_1 (1.98- 2.44)	Δf_2 (2.65 - 3.67)
f_1	1.98	2.65
f_2	2.03	2.72
f_3	2.07	2.82
f_4	2.12	2.92
f_5	2.17	3.02
f_6	2.22	3.14
f_7	2.27	3.25
f_8	2.33	3.39
f_9	2.39	3.52
f_{10}	2.44	3.67

different resonant frequencies as shown in Fig.3.25. Further increase in the number of resonant frequencies is limited by the presence of higher harmonics. Unique identification code can be assigned to each combination of resonant frequencies. Since ten different resonant frequencies are exhibited by each resonator, combining the two, 100 different codes ranging from [000 0000] to [110 0011] are possible with two resonators. The measured resonator response and the bistatic response of the multiresonator with two shorted stubs for two different configurations are shown in Fig.3.26. Fig.3.27 shows the photograph of fabricated multiresonator with two shorted stubs.

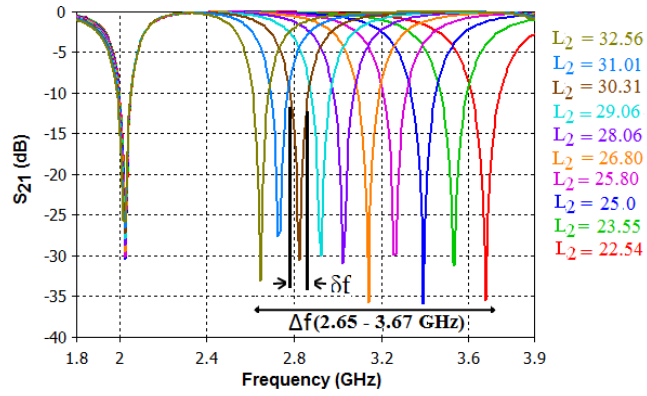


(a) S_{21}

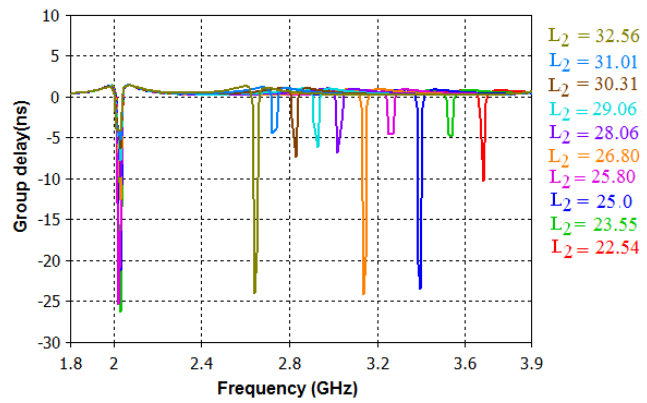


(b) Group delay

Fig. 3.24: Simulated transmission characteristics of tuning the first shorted stub in multiresonator with two shorted stubs shown in Fig.3.23 ($L_2 = 31$ mm, L_1 in mm)



(a) S_{21}



(b) Group delay

Fig. 3.25: Simulated transmission characteristics of tuning the second shorted stub in multiresonator with two shorted stubs shown in Fig.3.23 ($L_1 = 42$ mm, L_2 in mm)

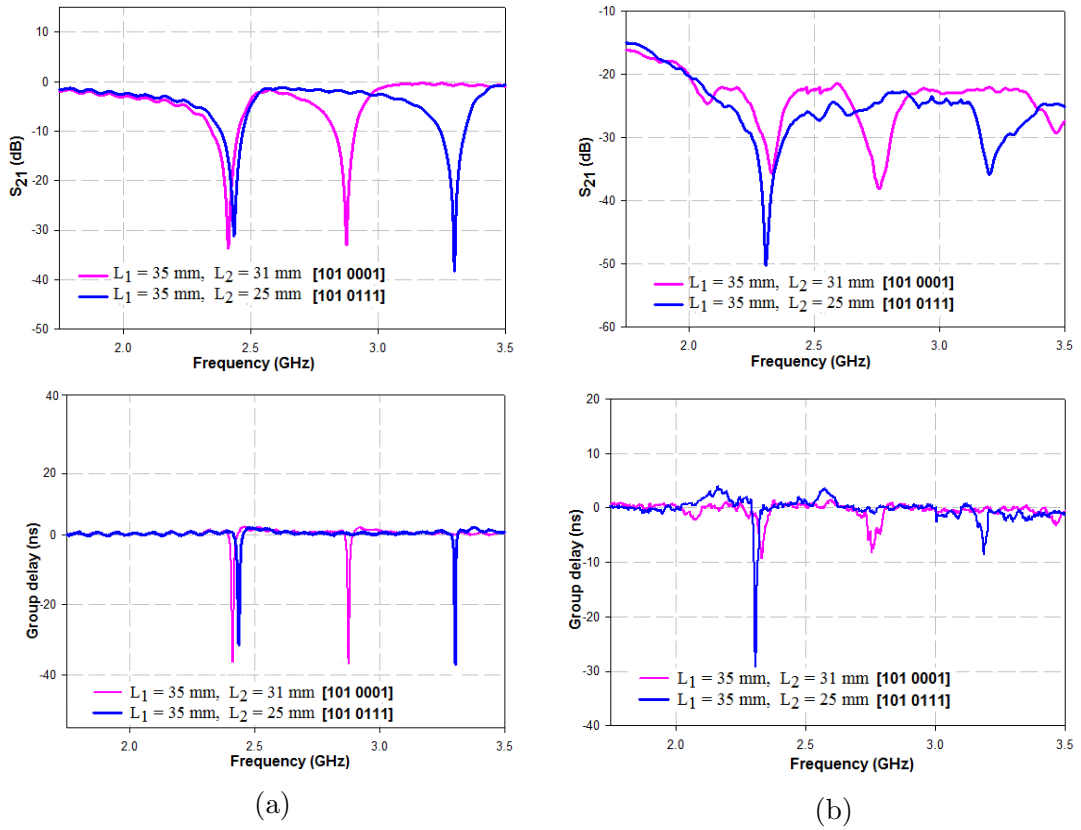


Fig. 3.26: Measured response of the multiresonator with two shorted stubs for two different configurations (a) Transmission characteristics of the resonator (b) Bistatic response



Fig. 3.27: Photograph of fabricated multiresonator with two shorted stubs

Table 3.4: Frequency band (Δf) and resonant frequency (f) of multiresonator with four shorted stubs (All values in GHz)

Resonator	Δf	f_1	f_2	f_3	f_4	f_5
1	2.28 - 2.52	2.28	2.33	2.4	2.46	2.52
2	2.68 - 3.08	2.68	2.77	2.86	2.96	3.08
3	3.30 - 3.66	3.30	3.38	3.47	3.56	3.66
4	3.86 - 4.26	3.86	3.95	4.07	4.14	4.26

3.5.7 Frequency shift coding applied to multiresonator with four shorted stubs

Fig.3.28 shows the layout of multiresonator with four shorted stub resonators whose length (L_i) is individually varied for FSC. The frequency band (Δf) and resonant frequency (f) of each resonator is listed in Table 3.4. Variation of the length of one resonator, keeping the dimensions of other resonators constant, results in five different resonant frequencies. Fig.3.29 to Fig.3.32 show the results obtained by individually varying the length of each resonator. While varying the length of each resonator care must be taken that the resonance due to other resonators should remain unaffected. In FSC for bit encoding, precautions must also be taken so that merging of resonant bands (Δf) does not occur and harmonics of the lower frequency resonators do not interfere with the resonance of higher frequency resonators. Unique identification code can be assigned to each combination of resonant frequencies. Since five different resonant frequencies are exhibited by each resonator, combining the four, 625 (5^4) different codes are possible with four resonators.

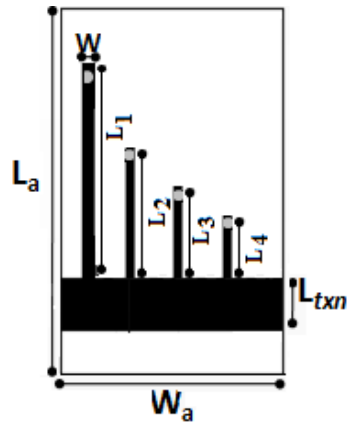
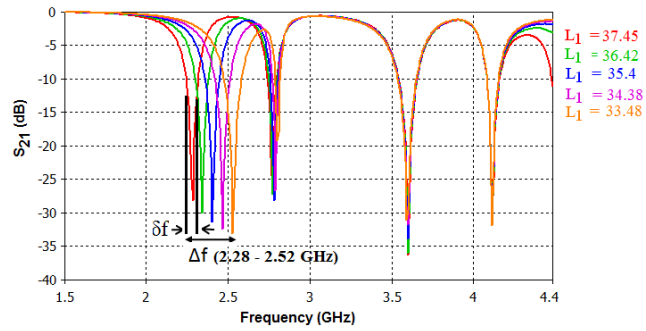
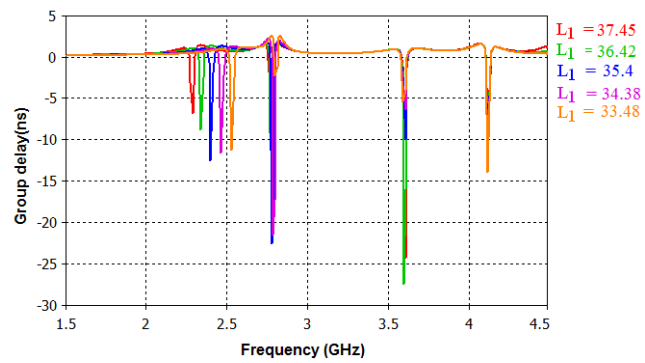


Fig. 3.28: Layout of multiresonator with four shorted stubs [$L_a = 60$, $W_a = 20$, $L_{txn} = 7$, $W = 1$, diameter of the via = 0.8 (All dimensions in mm) Substrate: loss tangent = 0.0018, $\epsilon_r = 4.3$, height = 1.6 mm]

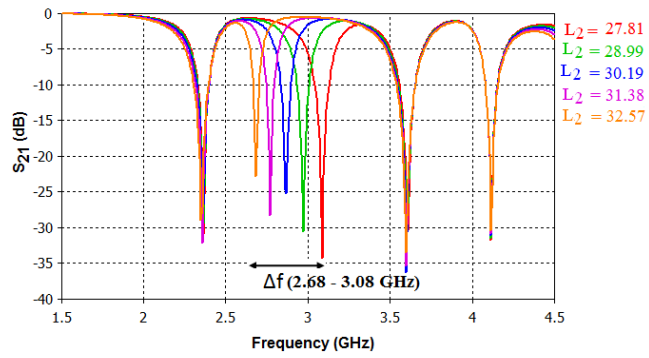


(a) S_{21}

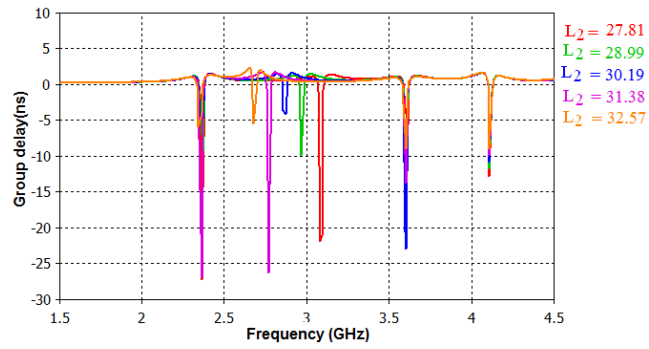


(b) Group delay

Fig. 3.29: Simulated transmission characteristics of tuning the first shorted stub in multiresonator with four shorted stubs shown in Fig.3.28 ($L_2 = 30.1$ mm, $L_3 = 23.8$ mm, $L_4 = 20.2$ mm, L_1 in mm)

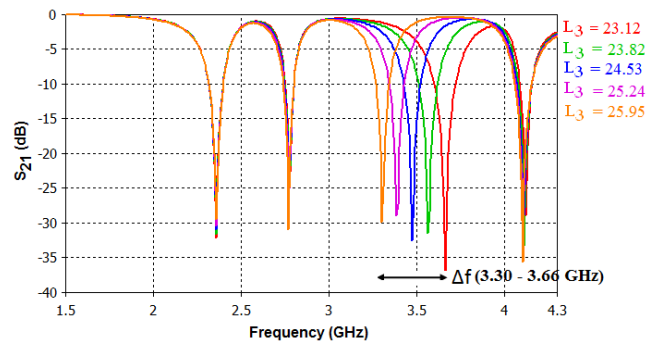


(a) S_{21} magnitude

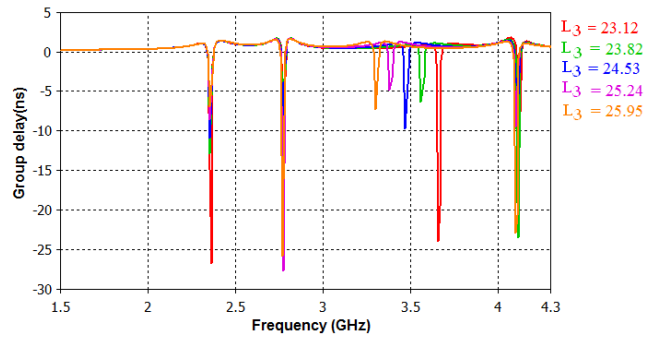


(b) Group delay

Fig. 3.30: Simulated transmission characteristics of tuning the second shorted stub in multiresonator with four shorted stubs shown in Fig.3.28 ($L_1 = 34.3$ mm, $L_3 = 23.8$ mm, $L_4 = 20.2$ mm, L_2 in mm)

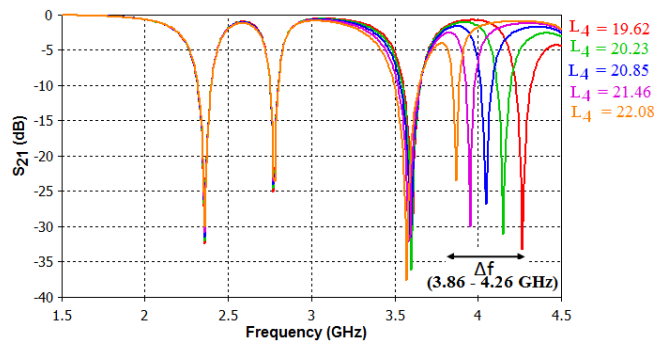


(a) S_{21}

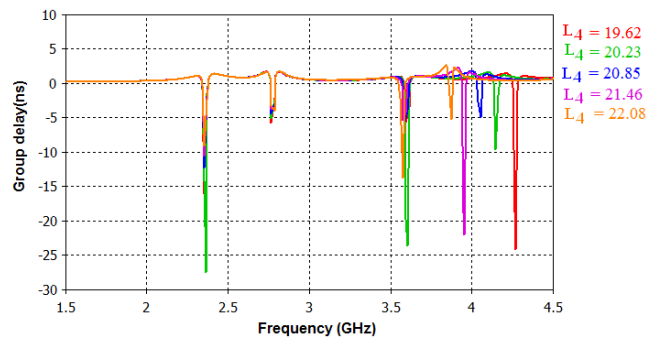


(b) Group delay

Fig. 3.31: Simulated transmission characteristics of tuning the third shorted stub in multiresonator with four shorted stubs shown in Fig.3.28 ($L_1 = 34.3$ mm, $L_2 = 30.1$ mm, $L_4 = 20.2$ mm, L_3 in mm)



(a) S_{21}



(b) Group delay

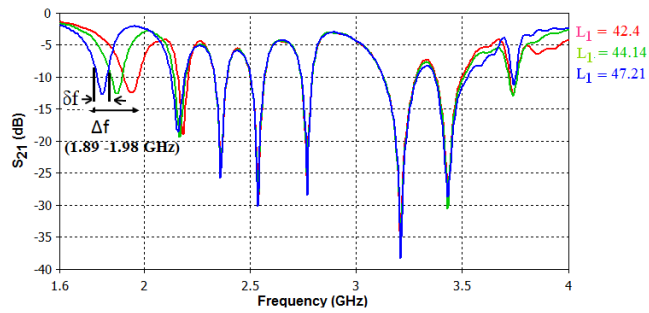
Fig. 3.32: Simulated transmission characteristics of tuning the fourth shorted stub in multiresonator with four shorted stubs shown in Fig.3.28 ($L_1 = 34.3$ mm, $L_2 = 30.1$ mm, $L_3 = 23.8$ mm, L_4 in mm)

Table 3.5: Frequency band (Δf) and resonant frequency (f) of multiresonator with eight shorted stubs (All values in GHz)

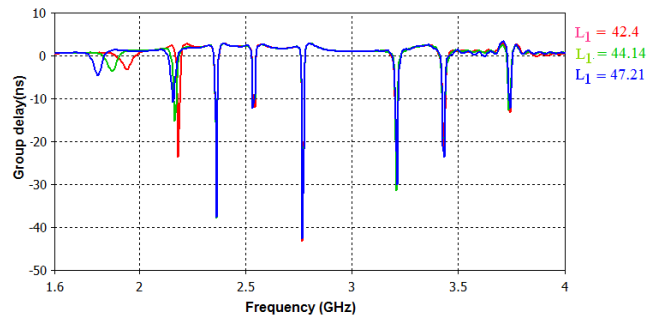
Resonator	Δf	f_1	f_2	f_3
1	1.89 - 1.98	1.89	1.92	1.98
2	2.14 - 2.20	2.14	2.17	2.20
3	2.31 - 2.38	2.31	2.35	2.38
4	2.51 - 2.58	2.51	2.55	2.58
5	2.82 - 2.97	2.82	2.89	2.97
6	3.04 - 3.14	3.04	3.09	3.14
7	3.22 - 3.30	3.22	3.26	3.30
8	3.6 - 3.72	3.6	3.66	3.72

3.5.8 Frequency shift coding applied to multiresonator with eight shorted stubs

When the concept of FSC is applied to a multiresonator with eight shorted stubs [Fig.3.1], eight different frequency bands (Δf) occur as detailed in Table 3.5. Variation of the length of one resonator, keeping the dimensions of other resonators constant, results in three different resonant frequencies. Fig.3.33 to Fig.3.40 show the results obtained by individually varying the length of each resonator. Since three different resonant frequencies are exhibited by each resonator, combining the eight, 6561 (3^8) different codes are possible with eight resonators. Fig.3.41 shows the measured resonator response and bistatic response for varying dimensions of the eighth resonator (L_8).

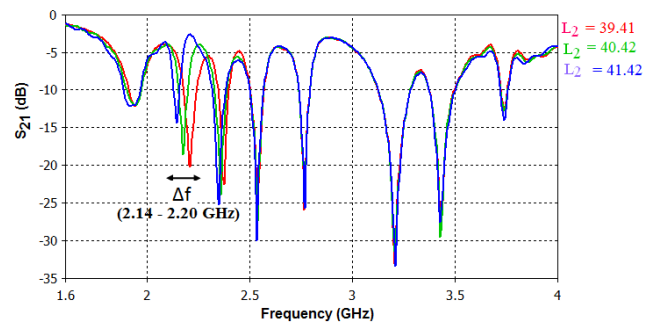


(a) S_{21}

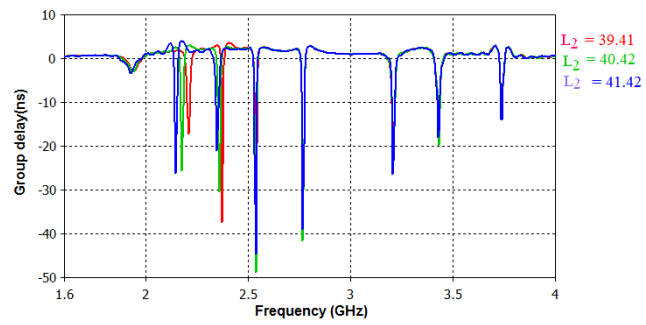


(b) Group delay

Fig. 3.33: Simulated transmission characteristics of tuning the first shorted stub in multiresonator with eight shorted stubs shown in Fig.3.1 ($L_2 = 40.4$ mm, $L_3 = 37.2$ mm, $L_4 = 33.6$ mm, $L_5 = 30.5$ mm, $L_6 = 27.1$ mm, $L_7 = 25.8$ mm, $L_8 = 22.7$ mm, L_1 in mm)

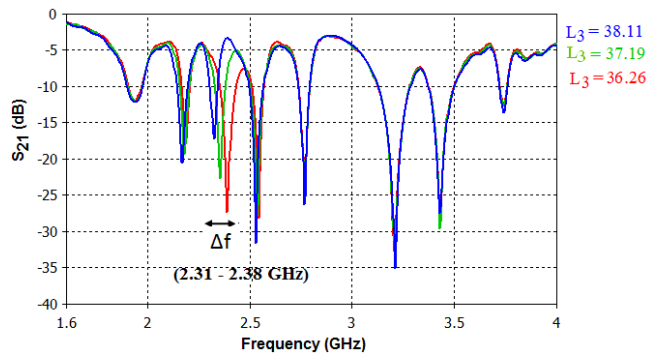


(a) S_{21}

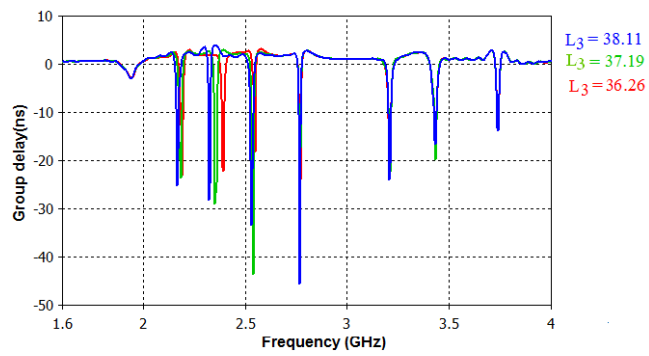


(b) Group delay

Fig. 3.34: Simulated transmission characteristics of tuning the second shorted stub in multiresonator with eight shorted stubs shown in Fig.3.1 ($L_1 = 42.4$ mm, $L_3 = 37.2$ mm, $L_4 = 33.6$ mm, $L_5 = 30.5$ mm, $L_6 = 27.1$ mm, $L_7 = 25.8$ mm, $L_8 = 22.7$ mm, L_2 in mm)

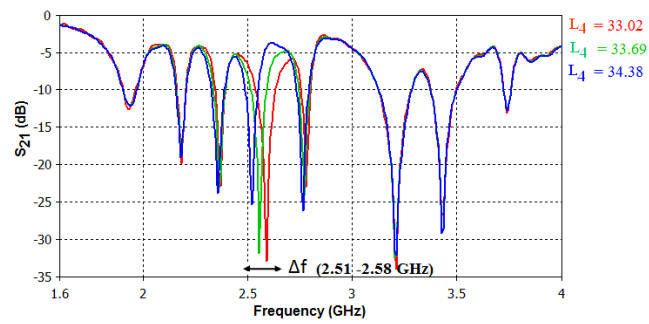


(a) S_{21}

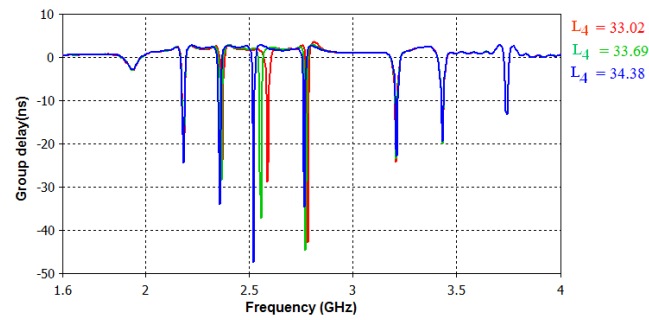


(b) Group delay

Fig. 3.35: Simulated transmission characteristics of tuning the third shorted stub in multiresonator with eight shorted stubs shown in Fig.3.1 ($L_1 = 40.4$ mm, $L_2 = 42.4$ mm, $L_4 = 33.6$ mm, $L_5 = 30.5$ mm, $L_6 = 27.1$ mm, $L_7 = 25.8$ mm, $L_8 = 22.7$ mm, L_3 in mm)

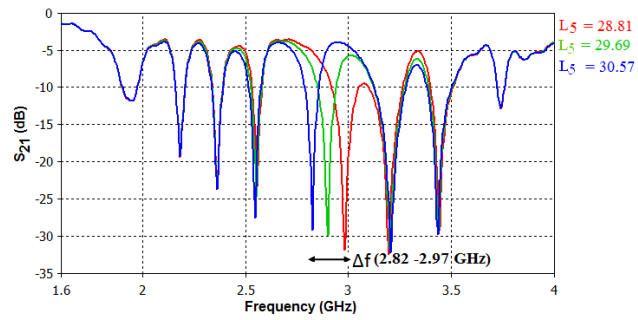


(a) S_{21}

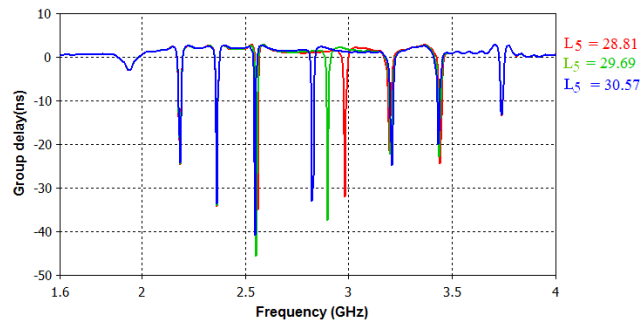


(b) Group delay

Fig. 3.36: Simulated transmission characteristics of tuning the fourth shorted stub in multiresonator with eight shorted stubs shown in Fig.3.1 ($L_1 = 42.4$ mm, $L_2 = 40.4$ mm, $L_3 = 37.2$ mm, $L_5 = 30.5$ mm, $L_6 = 27.1$ mm, $L_7 = 25.8$ mm, $L_8 = 22.7$ mm, L_4 in mm)

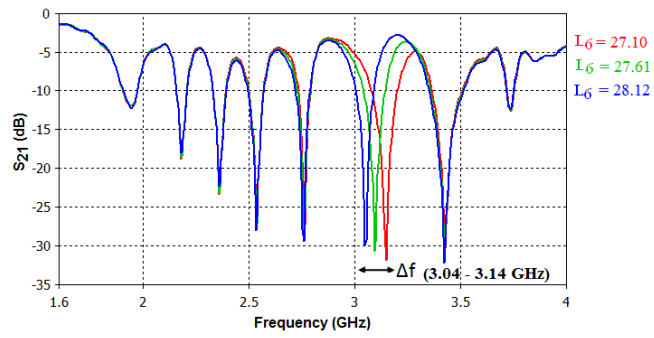


(a) S_{21}

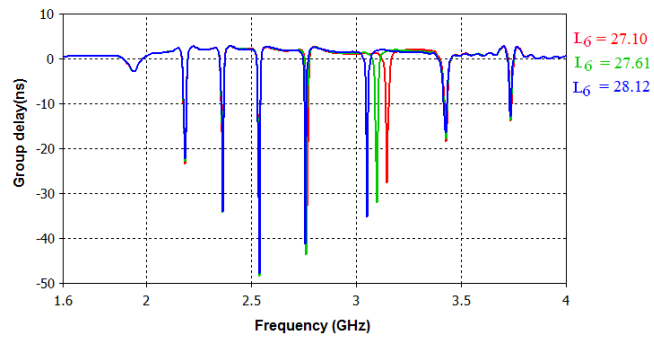


(b) Group delay

Fig. 3.37: Simulated transmission characteristics of tuning the fifth shorted stub in multiresonator with eight shorted stubs shown in Fig.3.1 ($L_1 = 42.4$ mm, $L_2 = 40.4$ mm, $L_3 = 37.2$ mm, $L_4 = 33.6$ mm, $L_6 = 27.1$ mm, $L_7 = 25.8$ mm, $L_8 = 22.7$ mm, L_5 in mm)

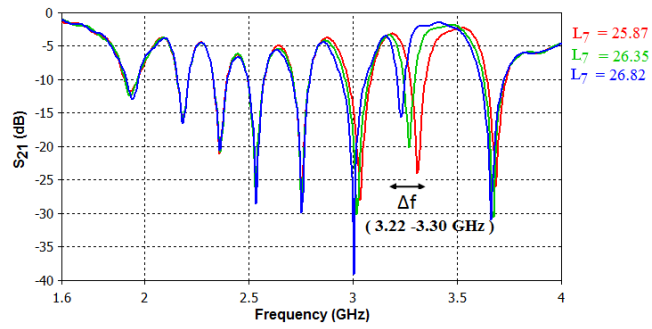


(a) S_{21}

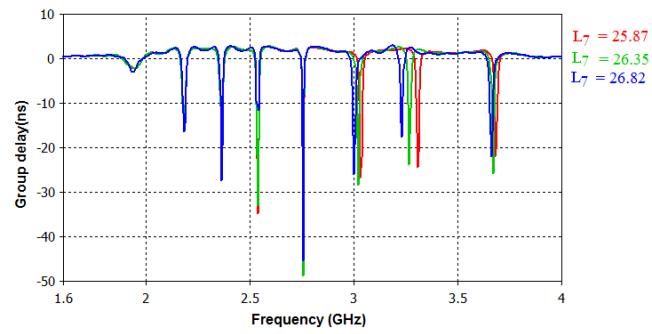


(b) Group delay

Fig. 3.38: Simulated transmission characteristics of tuning the sixth shorted stub in multiresonator with eight shorted stubs shown in Fig.3.1 ($L_1 = 42.4$ mm, $L_2 = 40.4$ mm, $L_3 = 37.2$ mm, $L_4 = 33.6$ mm, $L_5 = 30.5$ mm, $L_7 = 25.8$ mm, $L_8 = 22.7$ mm, L_6 in mm)

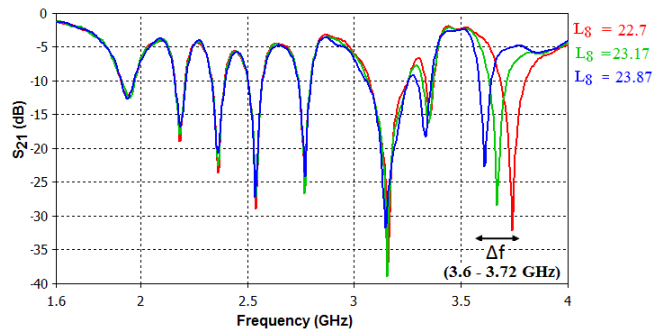


(a) S_{21}

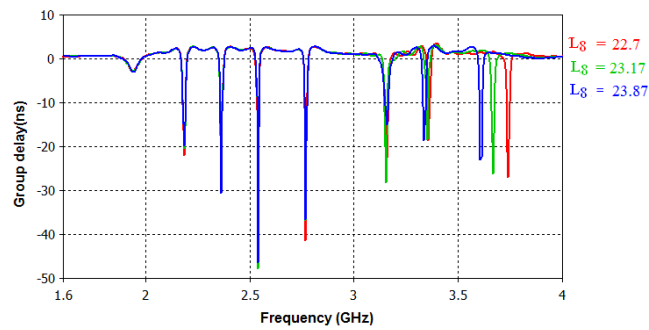


(b) Group delay

Fig. 3.39: Simulated transmission characteristics of tuning the seventh shorted stub in multiresonator with eight shorted stubs shown in Fig.3.1 ($L_1 = 42.4$ mm, $L_2 = 40.4$ mm, $L_3 = 37.2$ mm, $L_4 = 33.6$ mm, $L_5 = 30.5$ mm, $L_6 = 27.1$ mm, $L_8 = 22.7$ mm, L_7 in mm)



(a) S_{21}



(b) Group delay

Fig. 3.40: Simulated transmission characteristics of tuning the eighth shorted stub in multiresonator with eight shorted stubs shown in Fig.3.1 ($L_1 = 42.4$ mm, $L_2 = 40.4$ mm, $L_3 = 37.2$ mm, $L_4 = 33.6$ mm, $L_5 = 30.5$ mm, $L_6 = 27.1$ mm, $L_7 = 25.8$ mm, L_8 in mm)

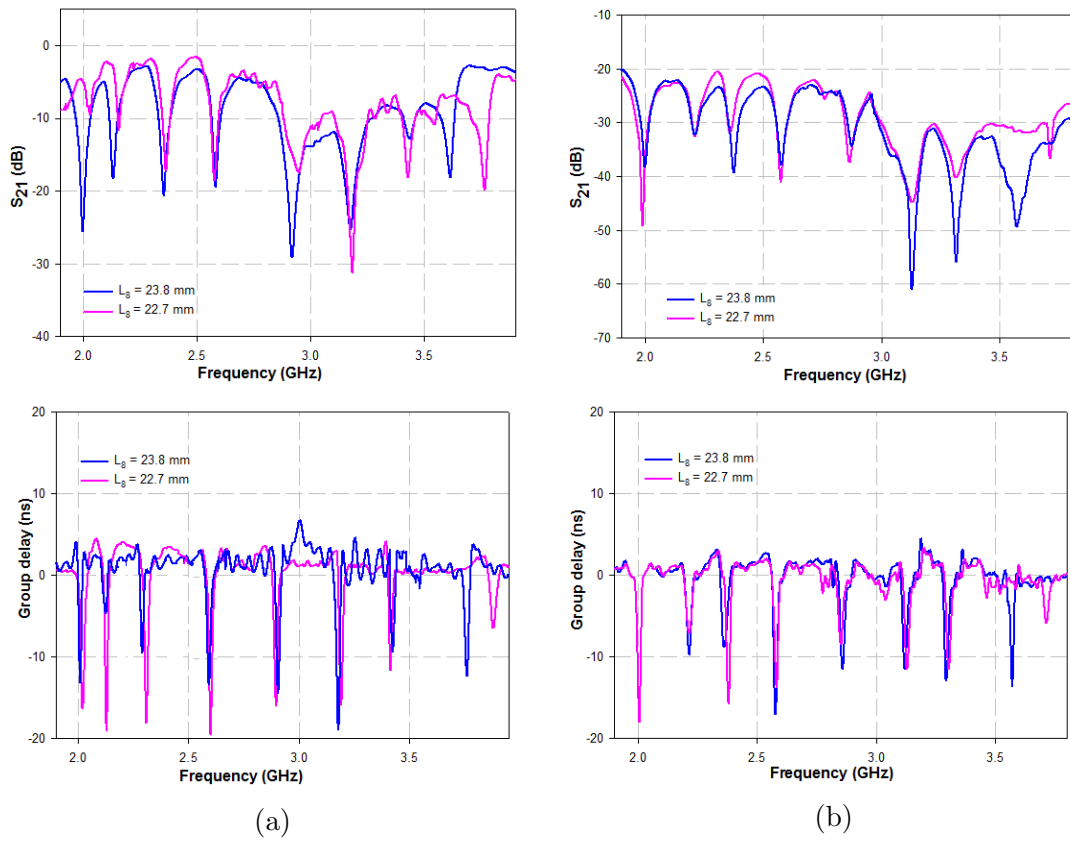


Fig. 3.41: Measured response of the multiresonator with eight shorted stubs for two different configurations ($L_1 = 42.4$ mm, $L_2 = 40.4$ mm, $L_3 = 37.1$ mm, $L_4 = 33.0$ mm, $L_5 = 29.6$ mm, $L_6 = 27.1$ mm, $L_7 = 25.8$ mm)(a) Transmission characteristics of the resonator (b) Bistatic response

All the above results reveal the design flexibility and high data encoding capacity of the proposed shorted stub multiresonator for chipless RFID applications.

3.6 Chapter summary

This chapter explains the implementation of chipless RFID tag using shorted stub multiresonator. The multiresonator consisting of eight shorted stub resonators is developed by varying the length of the stub. The resonator is a short-circuited half wavelength line which can be modeled as a series RLC circuit. Equivalent circuit model is validated using Agilent ADS. Design equation of the resonator is developed using multiple regression analysis. Orthogonally polarized circular monopole antennas are integrated to the multiresonator for range enhancement. The concept is validated using bistatic measurement for an eight bit prototype. The tag can encode data in magnitude and group delay. Various bit combinations for the absence or presence method of encoding the tag identity is generated, either by removing or decoupling the corresponding shorted stub resonator. In this method, maximum bits that can be represented by an RFID tag is equal to the number of resonators. The bit coding capacity of the tag can be enhanced using FSC technique. It is found that using eight resonators, the number of code words in FSC increases to 6561 (3^8) compared to 256 (2^8) in the case of absence or presence method. Table. 3.6 gives a comparison of the proposed chipless RFID tags with other reported tag designs. The comparison is done based on absence or presence coding technique. The proposed tag requires less bandwidth to encode 2^8 code word compared to other designs.

Table 3.6: Performance comparison of different chipless RFID tag

Parameters	(Jalil <i>et al.</i> , 2015)	(Zainud D <i>et al.</i> , 2012)	(Girbau <i>et al.</i> , 2012 <i>a</i>)	(Kim <i>et al.</i> , 2010)	Proposed tag
RFID operating band (GHz)	2.5 - 6.5	4-7	UWB	2-2.7	1.93 - 3.74
Bandwidth required	4 GHz	3 GHz	UWB	700 MHz	1.81 GHz
Bit states per resonator	4	2	3	3	2
Number of resonators	4	6	4	1	8
Number of code words	4 ⁴	2 ⁶	3 ⁴	3	2 ⁸
Bandwidth requirement for each bit (MHz)	> 100	< 100	< 100	> 100	< 100
Surface coding density (bits/cm ²)	1.6	0.13	Not specified	0.59	0.416

3.7 Inferences

1. The multiresonator requires eight vias to short the individual stubs to the ground, which makes the structure complex. But compared to the multiresonator discussed in Chapter 2, the bit encoding capacity of the tag increases from 729 to 6561 using FSC.
2. To generate various bit combinations for absence or presence coding technique, the stub has to be decoupled from the transmission line and also from the ground plane. This makes the layout changes for different bit combinations difficult. The tags presented in the subsequent chapters need only minimal layout modifications for generation of bit combinations.

CHAPTER 4

CHIPLESS RFID TAG USING SPURLINE MULTIRESONATOR

4.1 Introduction

Multiresonator based chipless RFID tag implemented using spurline resonators is discussed in this chapter. The spurline resonator, a term coined by Schiffman (Schiffman and Matthaei, 1964), is a L-shaped slot etched in a microstrip transmission line. The slot is quarter wavelength long at the resonant frequency. The harmonics of the spurline repeat only at odd multiples of the resonant frequency (Bates, 1977). Spurline resonators are usually used in the design and construction of transmission line band stop filters.

4.2 The spurline multiresonator

The multiresonator consists of eight spurline resonators in the microstrip line as illustrated in Fig.4.1. Each resonator is excited at the resonant frequency corresponding to a slot length of $\lambda_g/4$. The prototype is simulated on substrate C-MET/LK4.3 with dielectric constant 4.3, height 1.6 mm and loss tangent 0.0018 using CST MWS[®]. Fig.4.2 shows the microstrip version of the multiresonator. The overall dimension ($L_t \times W_t$) is 45 mm x 18 mm. The bottom plane acts as ground. The design approach is to generate multiple resonances by modifying the length of the spurline. Each spurline introduces a different stop

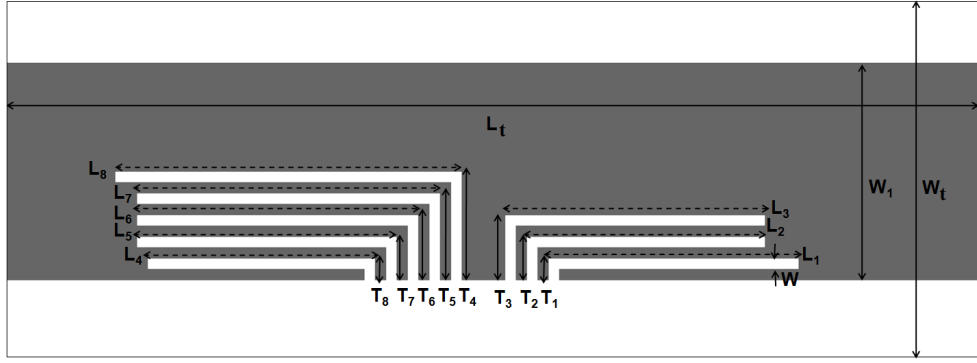


Fig. 4.1: Proposed eight bit spurline multiresonator [$W = 0.5$, $W_1 = 10.7$, $W_t = 18$, $L_1 = 11.5$, $L_2 = 11$, $L_3 = 12.6$, $L_4 = 10.5$, $L_5 = 12.6$, $L_6 = 13$, $L_7 = 14$, $L_8 = 16$, $L_t = 45$, $T_1 = 1$, $T_2 = 2$, $T_3 = 3$, $T_4 = 5$, $T_5 = 4$, $T_6 = 3$, $T_7 = 2$, $T_8 = 1$ (All dimensions in mm), Substrate: loss tangent = 0.0018, $\epsilon_r = 4.3$, $h = 1.6$ mm]

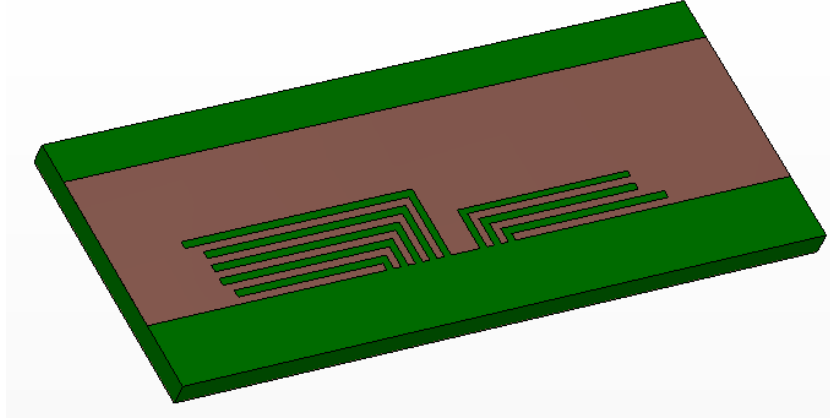


Fig. 4.2: Microstrip version of the spurline multiresonator

band resonance, which can be identified from the transmission characteristics as shown in Fig.4.3. Individual resonators operate at frequencies 2.39 GHz, 2.75 GHz, 3.09 GHz, 3.20 GHz, 3.40 GHz, 3.75 GHz, 3.97 GHz and 4.19 GHz, thus encoding eight bits in a band of 1.8 GHz. Fig.4.4 shows surface current distribution of individual resonators at the corresponding resonant frequencies. The evolution of the spurline multiresonator is discussed in the following section.

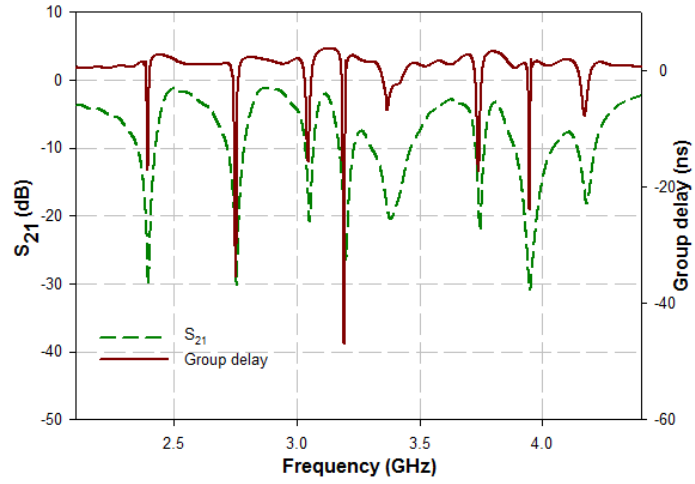


Fig. 4.3: Simulated transmission characteristics of the proposed eight bit spurline multiresonator shown in Fig.4.1

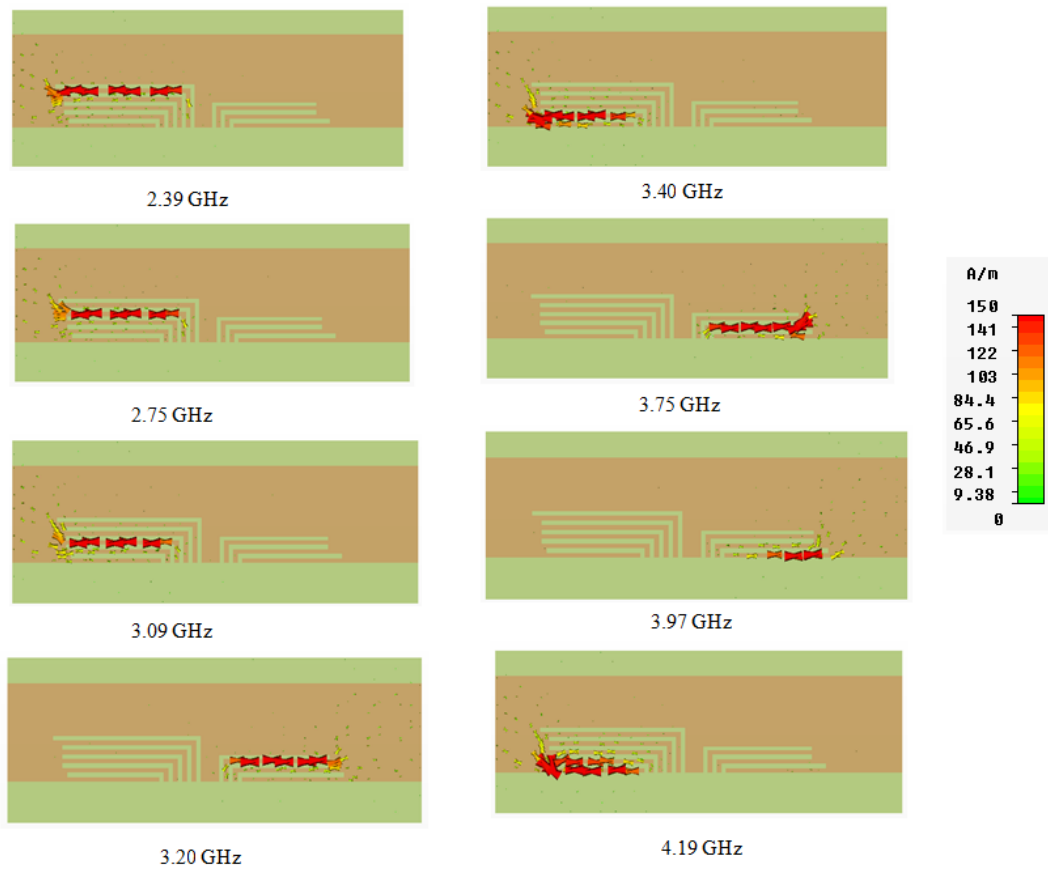


Fig. 4.4: Surface current distribution of individual resonators in the spurline multiresonator shown in Fig.4.1

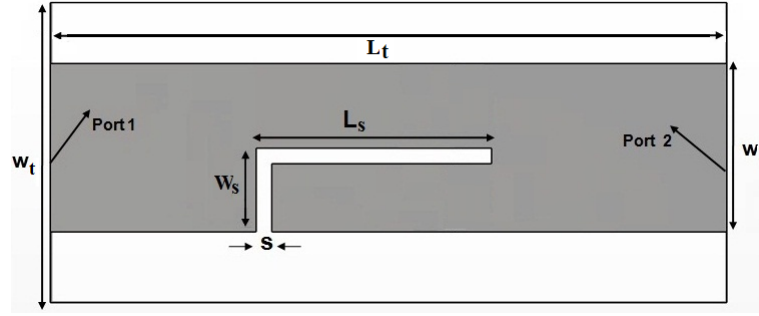


Fig. 4.5: Single spurline resonator [$L = L_s + W_s = 17.5$, $S = 1$, $W_1 = 10.7$, $W_t = 18$, $L_t = 45$ (All dimensions in mm), Substrate: loss tangent = 0.0018, $\epsilon_r = 4.3$, $h = 1.6$ mm]

4.3 Evolution of spurline multiresonator

The multiresonator has evolved from a spurline resonator. A spurline resonator is a L-shaped slot etched in a microstrip transmission line as shown in Fig.4.5 (Liu *et al.*, 2012; Wang *et al.*, 2012; Kumar and Verma, 2011; Cho and Kim, 2011; Liu *et al.*, 2010, 2008, 2007; Nguyen, 1983; Bates, 1977). The bottom plane acts as ground. The slot length is quarter wavelength ($\lambda_g/4$) long at the resonant frequency. The structure can be viewed as a coupled pair of microstrip lines with open circuit at one end and short circuit at the other end (Chongcheawchamnan, 2011; Liu *et al.*, 2008).

4.3.1 Analysis and design of spurline resonator

The dimensions of the spurline need to be optimised to get high Q at the notch frequency. Study of transmission characteristics of a single spurline is done for different values of W_1 . From the simulated transmission characteristics shown in Fig.4.6, it is observed that the Q of the system increases as W_1 increases. This high Q characteristics of the spurline is employed for the efficient coding of the chipless RFID tag. W_1 is optimised at 10.7 mm.

Studies of a spurline resonator for different values of slot width ‘S’ is done

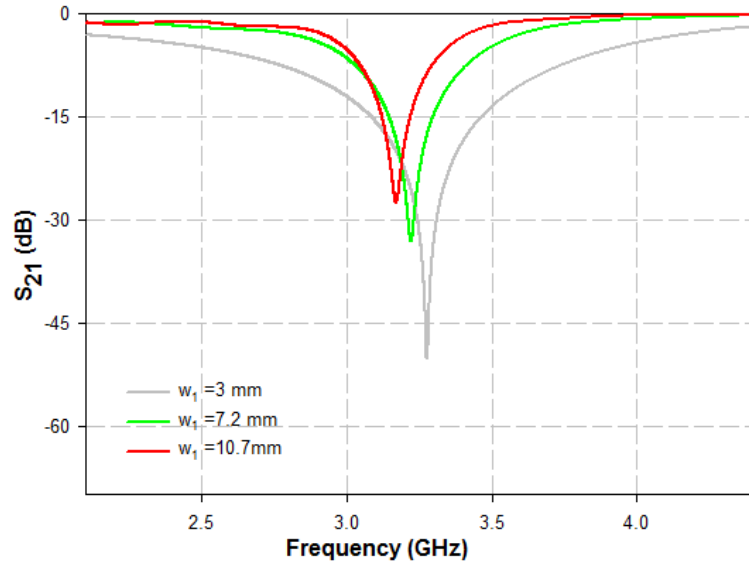


Fig. 4.6: Simulated transmission characteristics of single spurline for different values of W_1 for $S = 1$ mm, $L = L_s + W_s = 17.5$ mm, $W_t = 18$ mm, $\epsilon_r = 4.3$, height = 1.6 mm, loss tangent 0.0018

and the results are tabulated in Table 4.1. From Table 4.1, it is found that when the width of the spurline ‘S’ decreases, the fractional band width ($\frac{\Delta f}{f} * 100$) decreases. A sharp resonance is possible only if the resonator has a low value of fractional band width(FBW). The width ‘S’ is optimised at 0.5 mm in the current study.

Various spurlines have to be engraved in the transmission line to implement

Table 4.1: Parametric study for the optimisation of slot width ‘S’ of spurline resonator

L = 12 mm, $W_1 = 10.7$ mm, $W_2 = 18$ mm.				
Sl.No	S (mm)	Δf (GHz)	f (GHz)	FBW(%)
1	0.5	0.18	4.11	4.47
2	0.6	0.20	4.13	4.89
3	0.8	0.25	4.21	5.93
4	1	0.28	4.25	6.57

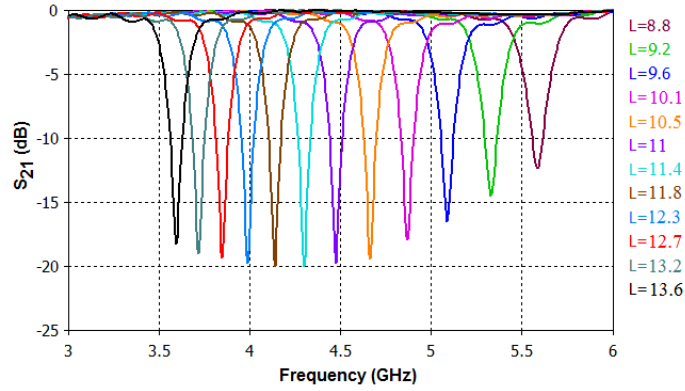


Fig. 4.7: Simulated transmission characteristics for various values of length ‘L’ (in mm) of spurline resonator shown in Fig.4.5

the multiresonating structure. The resonant frequency can be tuned by varying the length ($L = L_s + W_s$) of the spurline. The simulated transmission characteristics, shown in Fig.4.7 illustrate the shift in resonant frequency from 3.6 GHz to 5.6 GHz as length is varied from 13.6 mm to 8.8 mm. This property of achieving multiple resonances by varying the length of the spurline is used for designing the multiresonator.

Surface current distribution of the spurline resonator at its resonant frequency (4.15 GHz) and at a non-resonant frequency (5 GHz) are depicted in Fig.4.8(a) and Fig.4.8(b) respectively. The surface current distribution is concentrated in the resonator at the resonant frequency. It is clear that there is no transmission from port 1 to port 2 at the resonant frequency and transmission occurs at non-resonant frequency.

Multiple regression analysis is used to develop a generalised design equation of the spurline resonator for a chosen substrate of relative permittivity(ϵ_r) and height(h in mm). The length ‘L’ (in mm) computed for a resonant frequency(f in GHz) can be expressed as in Equation 4.1. The database for the development of the design equation is created by doing parametric analysis by varying the length of the spurline for each substrate keeping $S = 0.5$ mm, $W_1 = 10.7$ mm

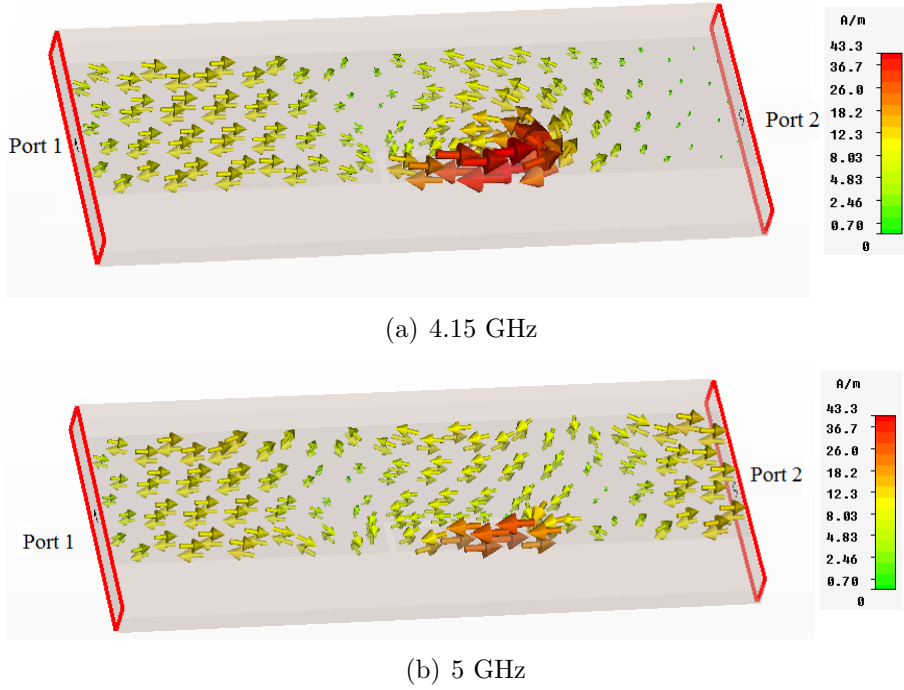


Fig. 4.8: Surface current distribution of spurline resonator shown in Fig.4.5 at resonant frequency of 4.15 GHz and at a non resonant frequency of 5 GHz

and $W_t = 18$ mm.

$$L = 1.34h - 2.5f - 1.27\epsilon_r + 25.85 \quad (4.1)$$

The equation is valid for ϵ_r and h in the range $2.25 \leq \epsilon_r \leq 5.4$ and $1 \text{ mm} \leq h \leq 1.6 \text{ mm}$ respectively. The equation is confirmed on various substrates having different values of relative permittivity and height as shown in Table 4.2.

4.3.2 Equivalent circuit of spurline resonator

Equivalent circuit is designed and simulated using Agilent ADS. Fig.4.9 shows the equivalent circuit and Fig.4.10 shows extracted frequency response. The equivalent circuit is designed using the transformation of the maximally flat first order prototype low pass filter ($\omega_c = 1$ rad/sec and element value $g_1 = 2$) to a band stop filter at ω_0 (Pozar, 2009). The series element $L' = 2$ H of the low pass filter is thus transformed to a parallel LC circuit having element

Table 4.2: Computed values of L for different resonant frequencies on various substrates

	ϵ_r	h (mm)	L (mm)	f (GHz)		%error
				Theory	CST	
1	4.4	1.6	13.79	3.5	3.44	1.71
2	2.4	1	14.14	4	3.97	0.75
3	5.4	1.25	12.17	3.4	3.36	1.17
4	3.27	0.8	14.27	3.4	3.33	2.05
5	4.8	1.6	13.66	3.3	3.24	1.81
6	2.25	1	13.1	4.5	4.42	1.77

values given by

$$\begin{aligned}
 L &= \frac{\Delta * L'}{\omega_0} \\
 C &= \frac{1}{\omega_0 * \Delta * L'}
 \end{aligned}
 \tag{4.2}$$

where

$$\Delta = \frac{\omega_2 - \omega_1}{\omega_0}
 \tag{4.3}$$

ω_2 and ω_1 correspond to 3 dB cut off frequency and ω_0 corresponds to resonant frequency. Impedance scaling of the filter results in

$$\begin{aligned}
 L &= \frac{\Delta * L' * Z_0}{\omega_0} \\
 C &= \frac{1}{\omega_0 * \Delta * L' * Z_0}
 \end{aligned}
 \tag{4.4}$$

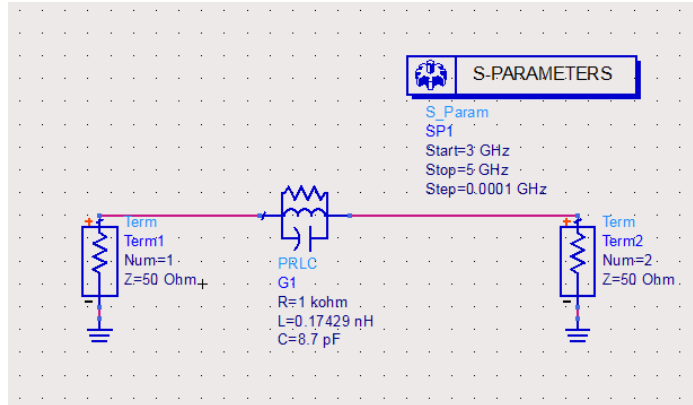


Fig. 4.9: Equivalent circuit of the spurline resonator ($f = 4.1$ GHz)

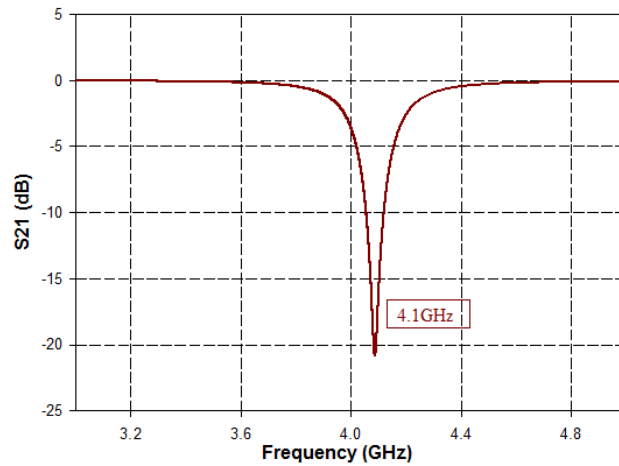
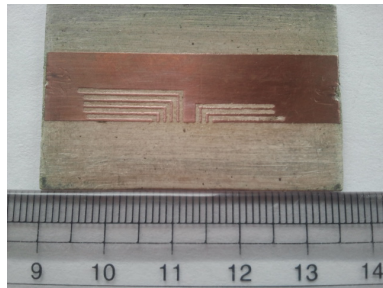


Fig. 4.10: Frequency response of the spurline resonator equivalent circuit extracted using Agilent ADS

The resistance R accounting for the losses can be found from

$$\begin{aligned}
 Q &= \frac{R}{\omega_0 * L} \\
 Q &= \frac{1}{\Delta}
 \end{aligned}
 \tag{4.5}$$

The values of L , C and R computed using Equations 4.4 and 4.5 for a resonant frequency of 4.1 GHz are 0.17429 nH, 8.7 pF and 1 K Ω respectively.



(a)



(b)

Fig. 4.11: (a) Photograph of the fabricated spurline multiresonator (b) Network analyser with device under test

4.3.3 Experimental results of spurline multiresonator

Fig.4.11(a) shows the photograph of the fabricated spurline multiresonator. Measurements are conducted using the PNA E8362B vector network analyser. The device under test (multiresonator) is connected between the two ports of the vector network analyser as shown in Fig.4.11(b). Fig.4.12 shows the measured transmission characteristics for the bit combination [1111 1111]. Data encoding techniques discussed in Section 4.5.1 are used to generate various bit combinations. The proposed spurline multiresonator can be used as an RFID tag for access control applications where the tag is in close proximity of the reader. However the tag needs modification in its design for range enhancement. This is discussed in Section 4.4.

4.4 Bistatic measurement for validation of the tag

The block schematic of the bistatic measurement of the RFID tag using spurline multiresonator is shown in Fig.4.13. Two wide band antennas are incorporated

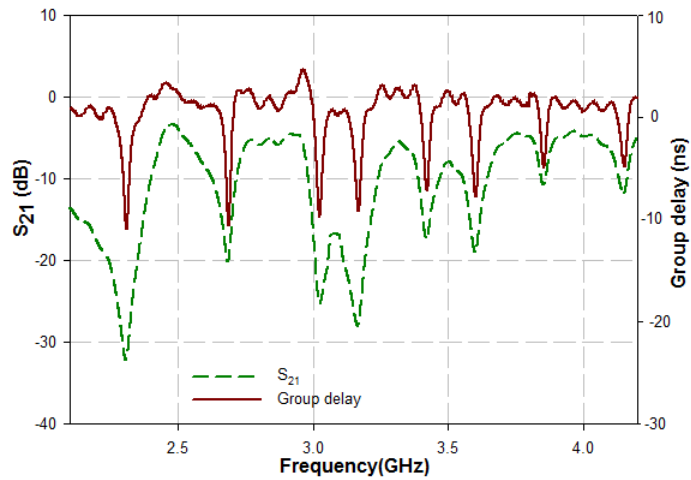


Fig. 4.12: Measured transmission characteristics of the spurline multiresonator for the bit combination [1111 1111]

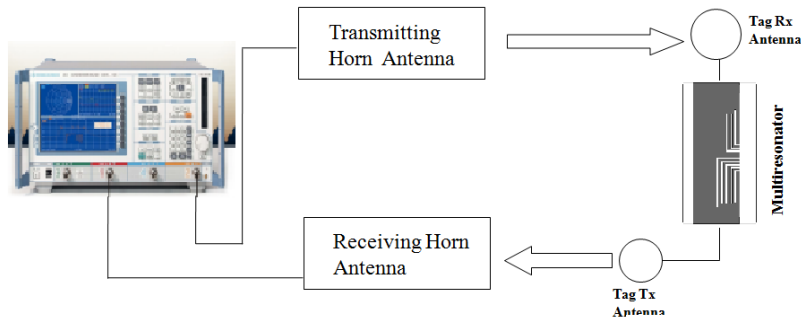


Fig. 4.13: Block schematic for bistatic measurement of the RFID tag using spurline multiresonator

to increase the range of multiresonator as explained in Section 2.4. Two cross polarized medium gain (10 dB) horn antennas are used for transmission and reception of the signal at the reader (Preradovic and Karmakar, 2009; Preradovic *et al.*, 2009, 2008a).

Fig.4.14 shows the experimental setup for bistatic measurement of the RFID tag using spurline multiresonator. The tag is placed 15 cm away from horn antennas. Fig.4.15 shows the measured bistatic response for bit combination [1111 1111] when all the eight spurline resonators are present in the transmission line. The bistatic response clearly indicates the abrupt variations at resonance, as in the case of multiresonator [Fig.4.12].

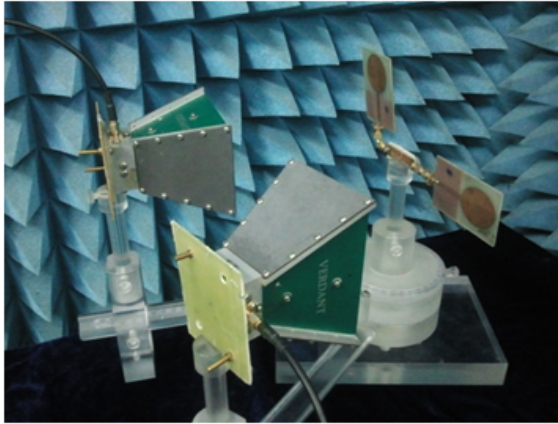


Fig. 4.14: Experimental setup for bistatic measurement of the RFID tag using spurline multiresonator

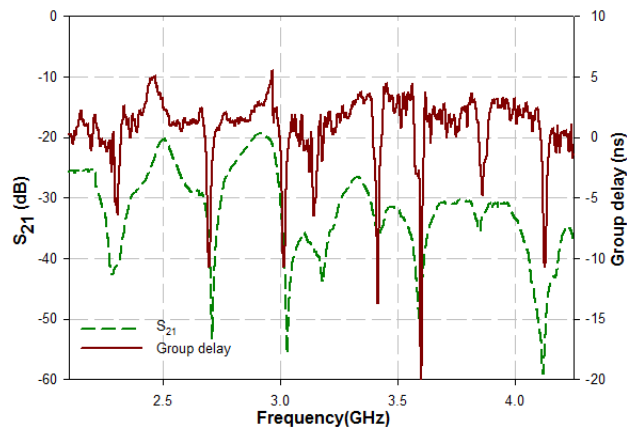


Fig. 4.15: Measured bistatic response of the RFID tag using spurline multiresonator for the bit combination [1111 1111]

4.5 Data encoding methods

Absence or presence coding technique and frequency shift coding technique, as discussed in Section. 2.5, are employed for data encoding.

4.5.1 Absence or presence coding technique

The presence of resonance is used to encode a logic 1 and the absence of resonance is used to encode a logic 0. In spurline multiresonator type 1 [Fig.4.16],

all the eight spurlines are present resulting in a bit combination [1111 1111], spurline 1 corresponds to the most significant bit and spurline 8 corresponds to the least significant bit.

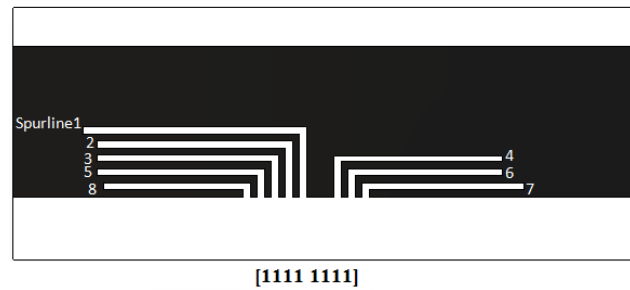
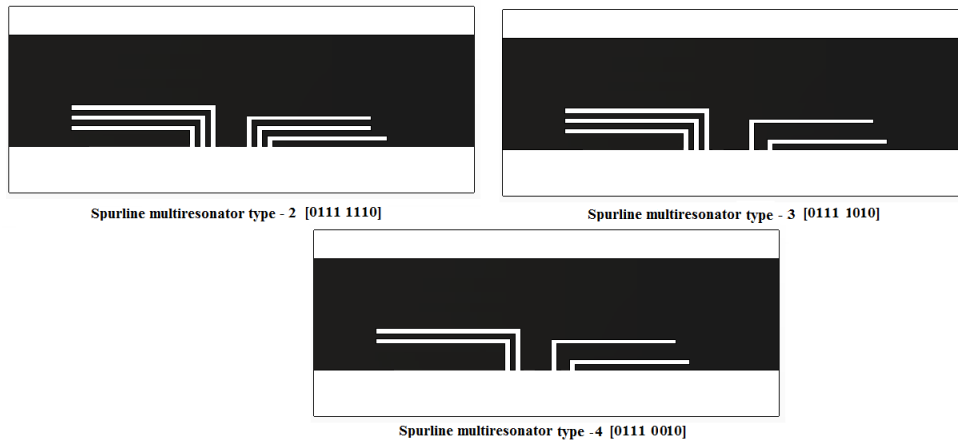
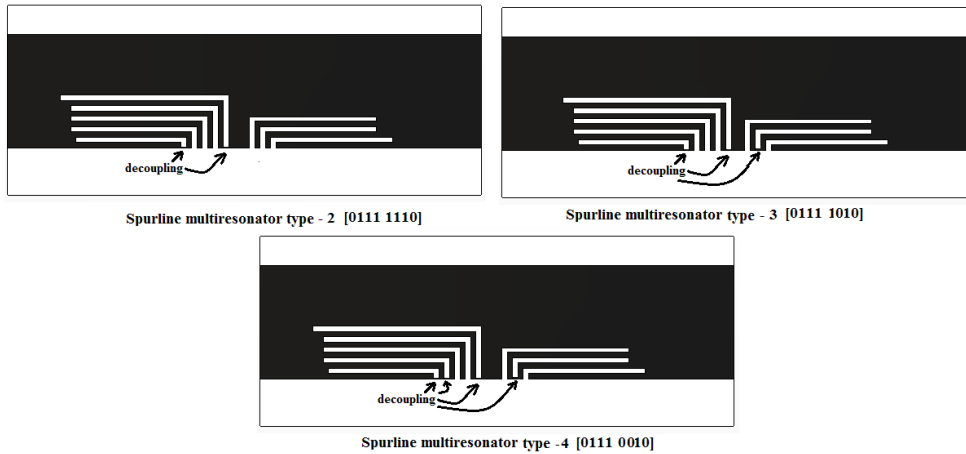


Fig. 4.16: Spurline multiresonator type 1

The absence of a specific resonance can be achieved either by removing the corresponding spurline [Fig.4.17(a)] or by decoupling (shorting) the spurline [Fig.4.17(b)]. Three different types of such resonators are shown in Fig.4.17.



(a) Removing the resonator



(b) Decoupling the resonator

Fig. 4.17: Three different types of spurline multiresonator (a) Removing the resonator
(b) Decoupling the resonator

In spurline multiresonator type 2 resonances due to spurlines 1 and 8 are absent leading to a bit combination [0111 1110]. In spurline multiresonator type 3 resonances due to spurlines 1,6 and 8 are absent resulting in [0111 1010]. In spurline multiresonator type 4 resonances due to spurlines 1,5,6 and 8 are absent resulting in [0111 0010]. Fig.4.18 shows the simulated transmission characteristics of the three types of resonators. The small shift in resonant frequency may be due to the mutual coupling between the resonators. The simulated transmission characteristics of [1111 1111] was shown in Fig.4.3.

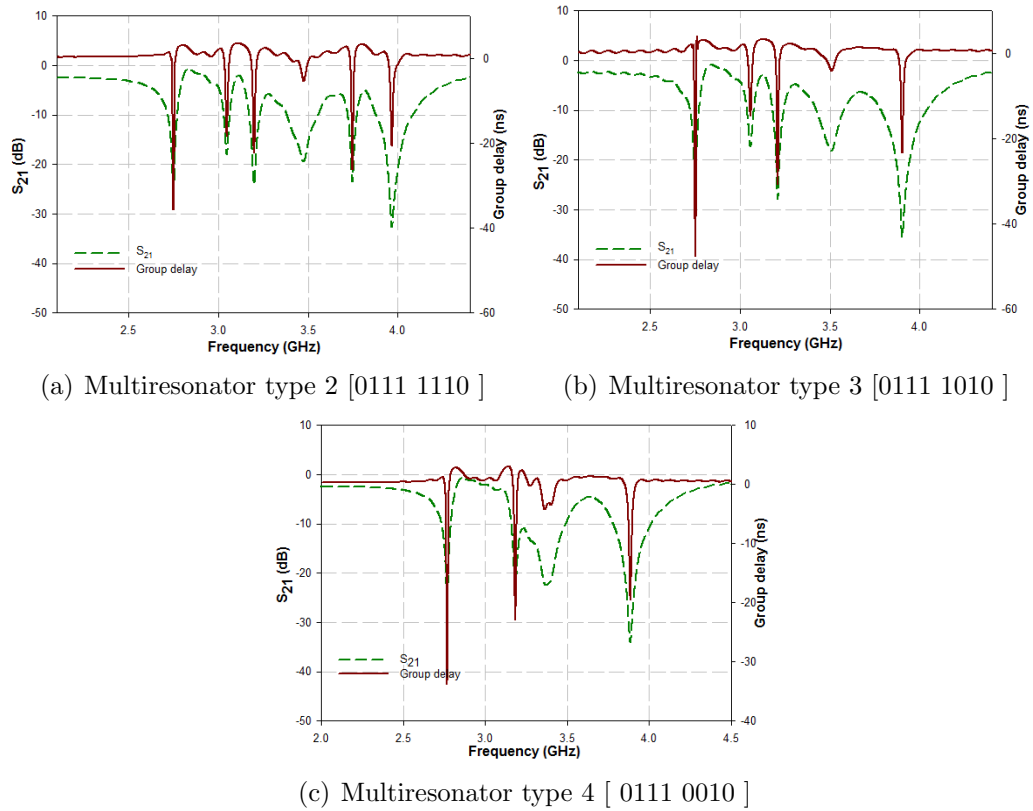


Fig. 4.18: Simulated transmission characteristics of the spurline multiresonator for different bit combinations

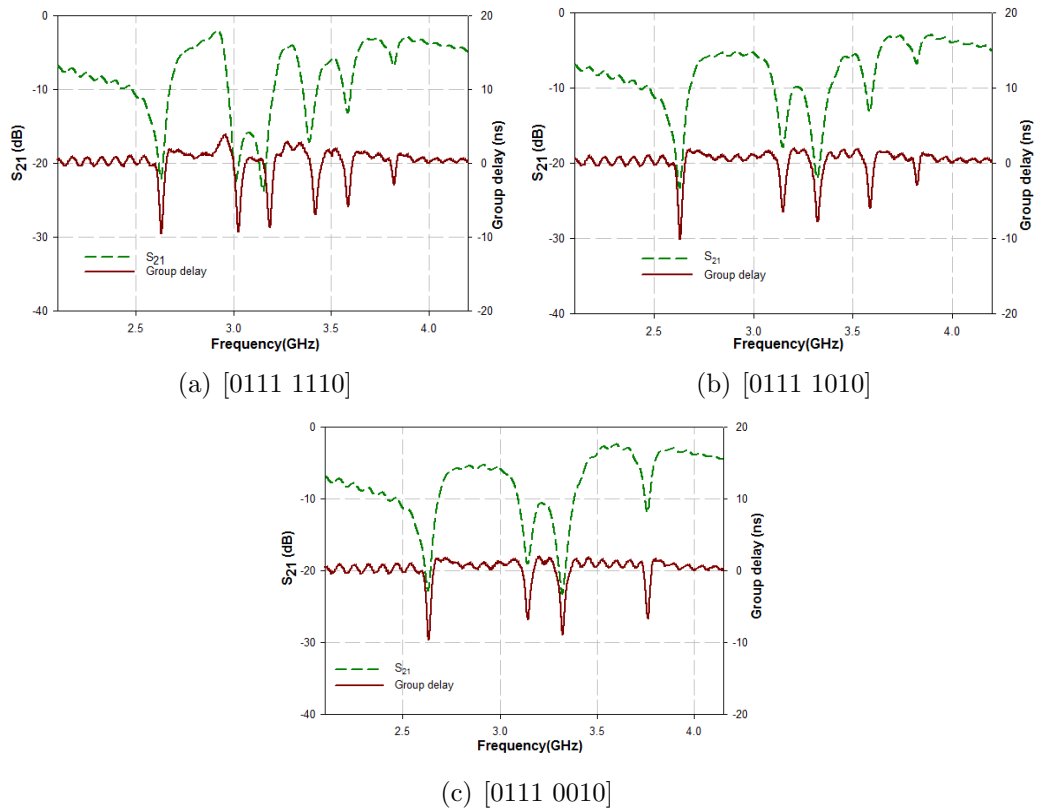


Fig. 4.19: Measured transmission characteristics of the spurline multiresonator for different bit combinations

4.5.2 Experimental results of spurline multiresonator using absence or presence coding technique

Using the technique mentioned in Section 4.5.1, different types of multiresonators are fabricated. The transmission characteristics is measured using Agilent PNA E8362B vector network analyzer by connecting the multiresonator between the ports of analyzer. Measured transmission characteristics of the multiresonator for the bit combination [0111 1110], [0111 1010] and [0111 0010] are shown in Fig.4.19. The measured result of [1111 1111] was shown in Fig.4.12.

The tag identity can be confirmed from the absolute value of S_{21} or group delay. The tag detection can be made virtually independent of absolute value of S_{21} or group delay by a post processing method using a difference operation

technique as detailed in Section 2.5.2. A peak variation at resonance is clearly visible from the post processed signal for the bit combination [0111 1110], [0111 1010] and [0111 0010] as shown in Fig.4.20.

4.5.3 Bistatic measurement results using absence or presence coding technique

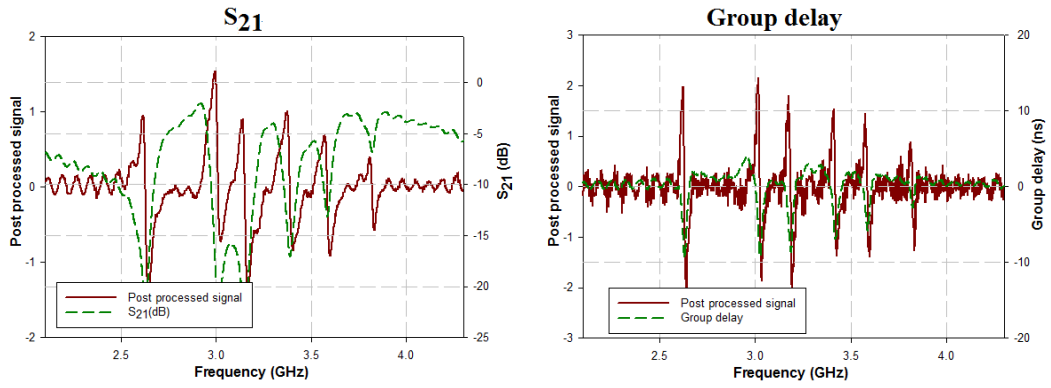
Bistatic measurement is done to validate the tag for various bit combinations. Fig.4.21 shows the measured bistatic response for bit combinations [0111 1110], [0111 1010] and [0111 0010]. The measured result of [1111 1111] was shown in Fig.4.15. As explained in Section 2.5.2, post processing method is applied to the measured bistatic results. Fig.4.22 shows the post processed signal for the bit combination [1111 1111].

4.5.4 Frequency shift coding technique for enhanced bit encoding capacity

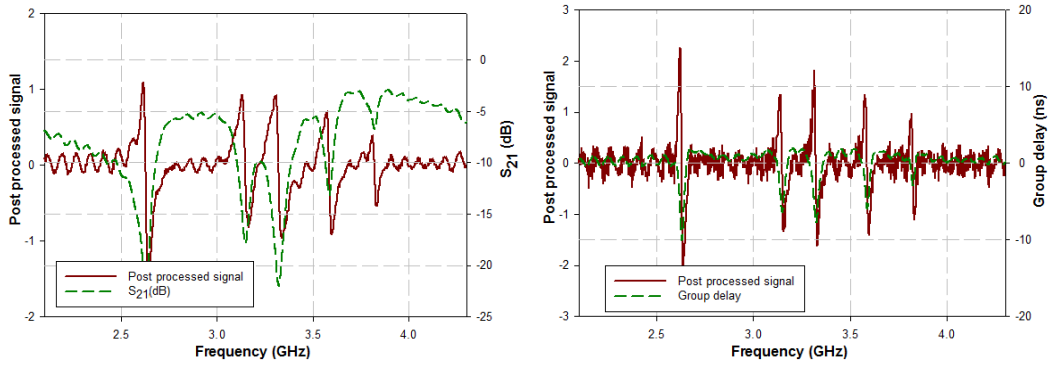
The bit encoding capacity of the tag can be enhanced using frequency shift coding (FSC) technique, by encoding more than one bit per resonator as explained in Section 2.5.4. This section explains the method by which FSC is applied to various spurline resonator configurations.

4.5.5 Frequency shift coding applied to spurline resonator

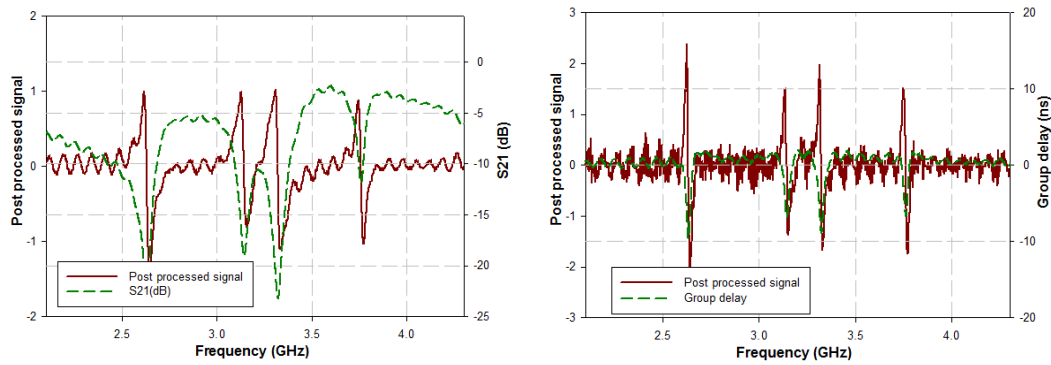
The simulated transmission characteristics for various values of length (L) of spurline resonator [Fig.4.5] are shown in Fig.4.23. In a frequency band (Δf) from 2.7 GHz to 7 GHz, 16 frequency bands are possible. δf is the frequency band for each resonator required to faithfully represent its resonant frequency,



(a) [0111 1110]



(b) [0111 1010]



(c) [0111 0010]

Fig. 4.20: Measured transmission characteristics of the spurline multiresonator and its post processed signal for various bit combinations

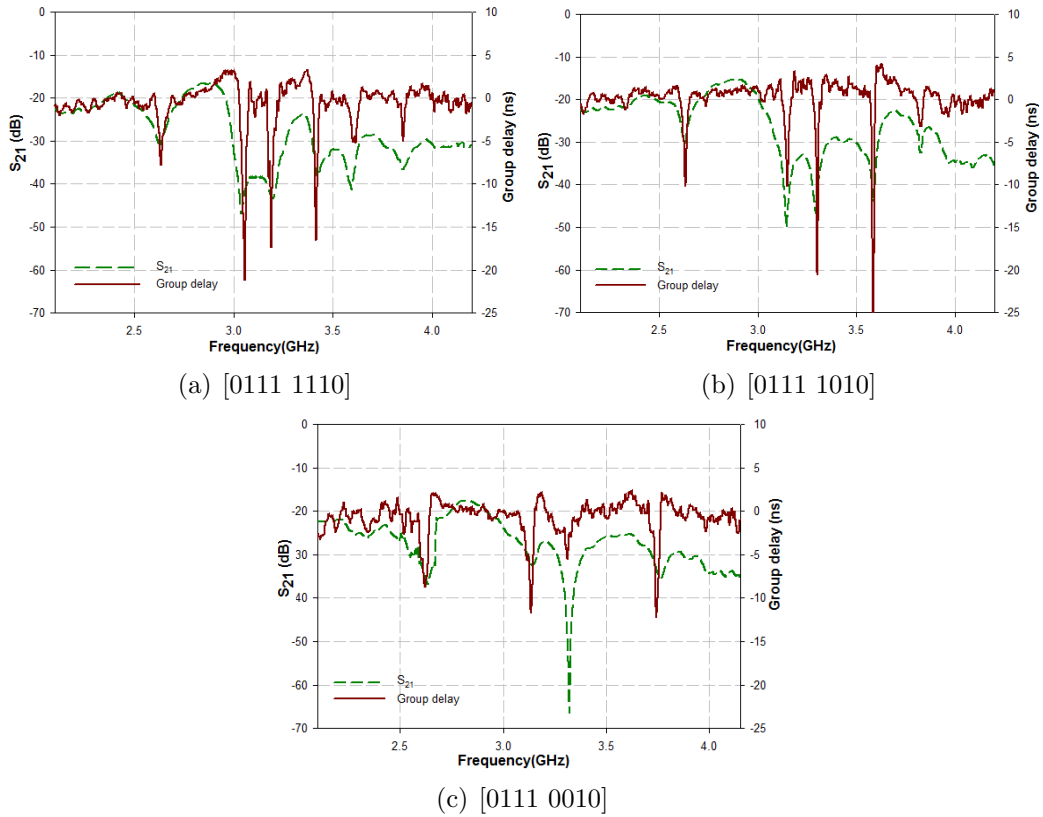


Fig. 4.21: Measured bistatic response of the RFID tag using spurline multiresonator for different bit combinations

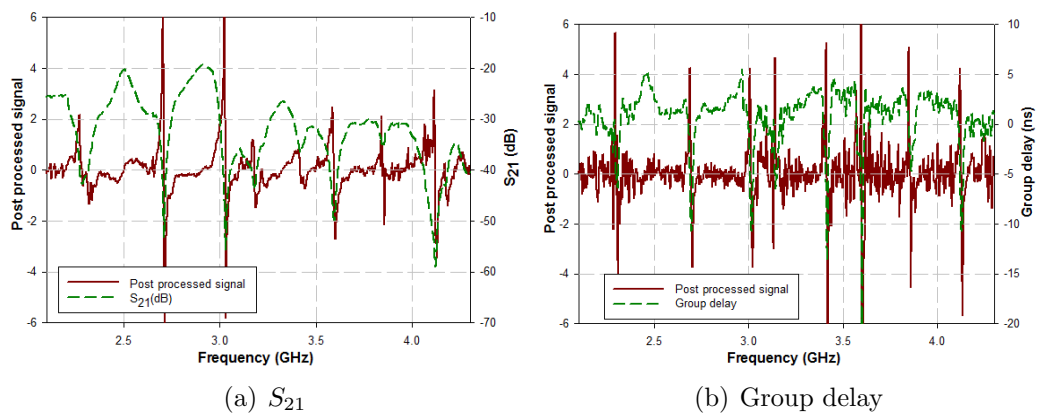
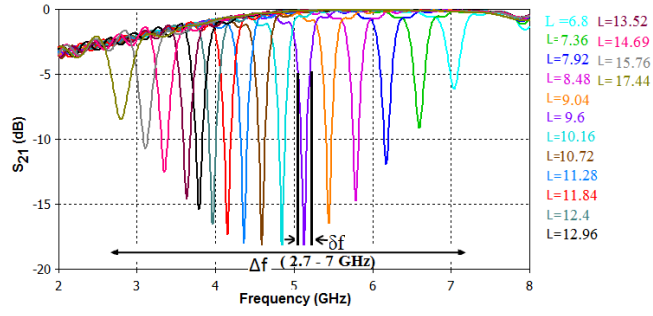
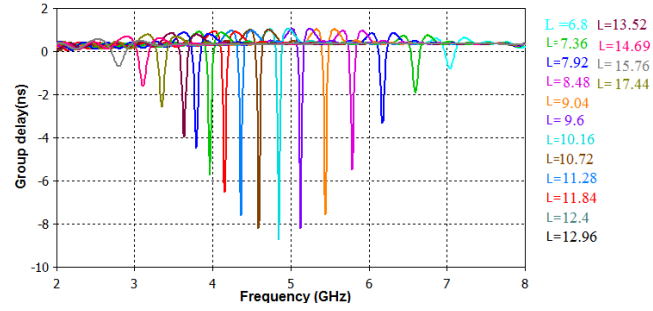


Fig. 4.22: Measured bistatic response of the RFID tag using spurline multiresonator and its post processed signal for the combination [1111 1111]



(a) S_{21}



(b) Group delay

Fig. 4.23: Simulated transmission characteristics of the spurline resonator shown in Fig.4.5 for various values of L (mm)

thus determining the frequency resolution. Table 4.3 shows a proposed method of code word allocation for the spurline resonator. The code words are allotted for each frequency, corresponding to each value of length. The variation in length is restricted due to the presence of higher harmonics, which repeats at odd multiples of the resonant frequency. While absence or presence coding of a resonator can encode only two code words (0/1) using a single spurline resonator, use of FSC allows an improvement to 16 code words. Three resonators with $L = 14.69$ mm, $L = 13.52$ mm and $L = 12.96$ mm corresponding to code words [0010], [0011] and [0100] respectively are fabricated to validate the simulation results. The measured resonator response and the bistatic response are shown in Fig.4.24. Fig.4.25 shows the photograph of the fabricated spurline resonator.

Table 4.3: Proposed method of code word allocation for the spurline resonator

Sl.no	L (mm)	f (GHz)	Code word
1	17.44	2.7	0000
2	15.76	3.1	0001
3	14.69	3.3	0010
4	13.52	3.5	0011
5	12.96	3.7	0100
6	12.2	3.9	0101
7	11.84	4.2	0110
8	11.28	4.4	0111
9	10.72	4.6	1000
10	10.16	4.8	1001
11	9.6	5.1	1010
12	9.04	5.4	1011
13	8.48	5.7	1100
14	7.92	6.1	1101
15	7.36	6.5	1110
16	6.8	7	1111

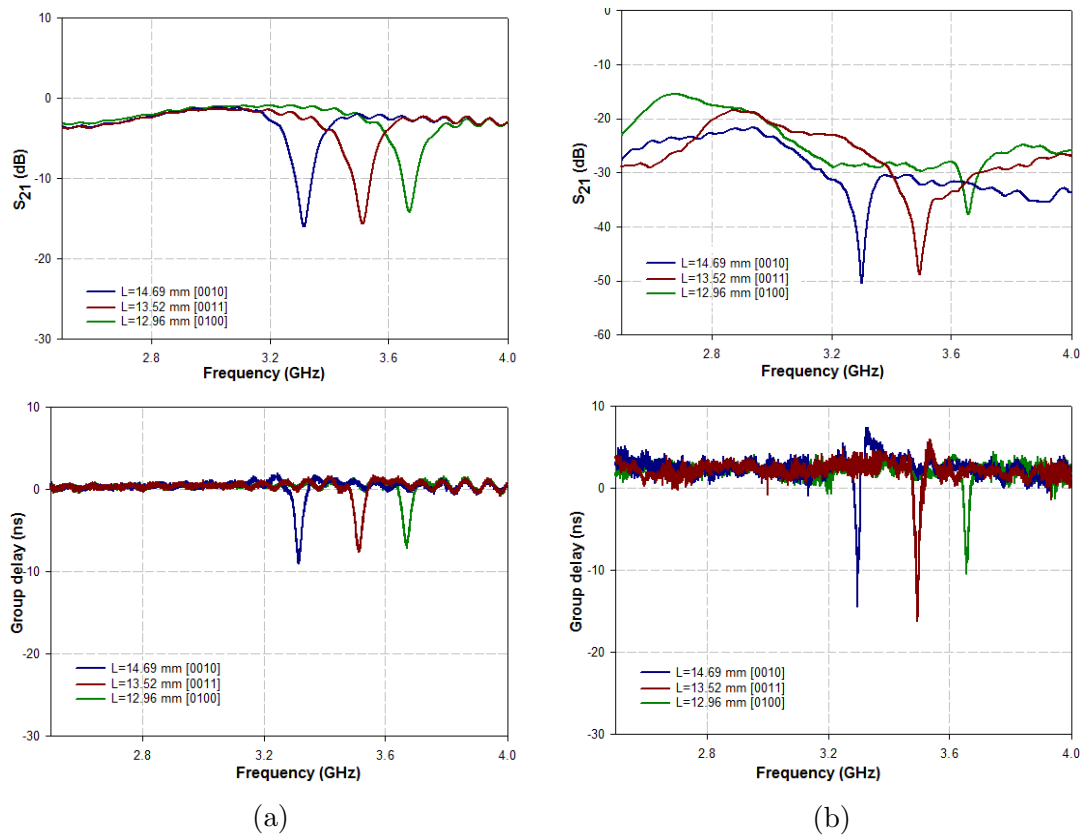


Fig. 4.24: Measured response of the tag with single spurline resonator for three different configurations (a) Transmission characteristics of the resonator (b) Bistatic response



Fig. 4.25: Photograph of fabricated spurline resonator

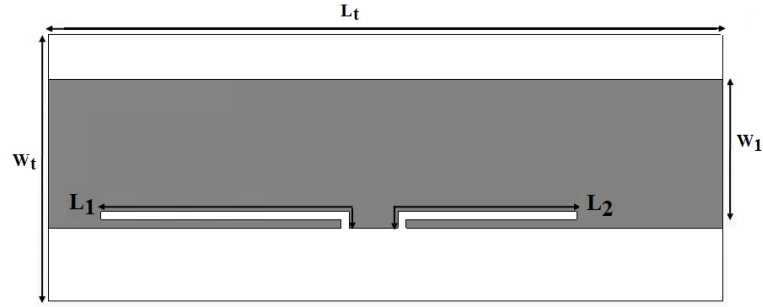
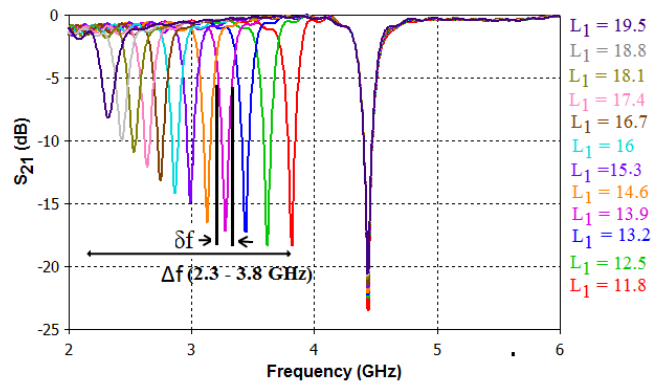


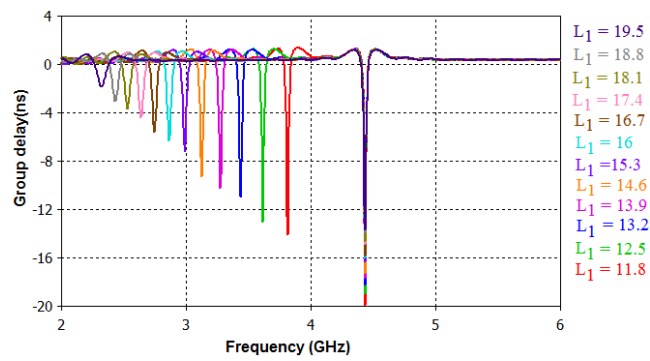
Fig. 4.26: Layout of multiresonator with two spurlines [$W_1 = 10.7$, $W_t = 18$, $L_t = 45$ (All dimensions in mm), Substrate: loss tangent = 0.0018, $\epsilon_r = 4.3$, $h = 1.6$ mm]

4.5.6 Frequency shift coding applied to multiresonator with two spurlines

Fig.4.26 shows the layout of multiresonator with two spurlines whose length (L) is individually varied for FSC. The frequency band (Δf) and resonant frequency (f) of each resonator are listed in Table 4.4. Variation of the length of the first spurline, keeping the dimensions of the second spurline constant, results in twelve different resonant frequencies as shown in Fig.4.27. Similarly, variation of length of the second spurline, keeping the dimensions of the first spurline constant, results in twelve different resonant frequencies as shown in Fig.4.28. Unique identification code can be assigned to each combination of resonant frequency. Since twelve different resonant frequencies are exhibited by each resonator, combining the two, 144 different codes ranging from [0000 0000] to [1000 1111] are possible with two resonators. The measured resonator response and the bistatic response of the multiresonator with two spurlines for two different configurations are shown in Fig.4.29. Fig.4.30 shows the photograph of fabricated multiresonator with two spurlines.

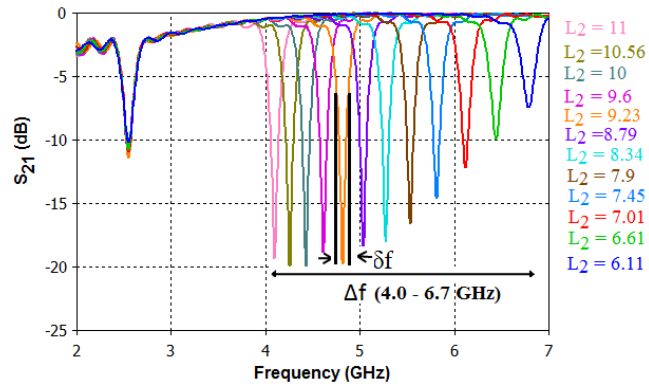


(a) S_{21}

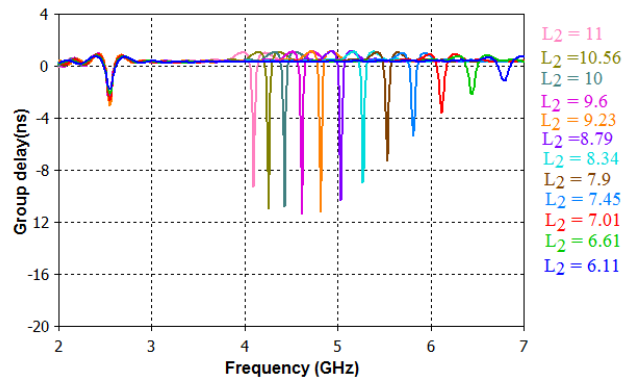


(b) Group delay

Fig. 4.27: Simulated transmission characteristics of tuning the first spurline in multiresonator with two spurlines shown in Fig.4.26 ($L_2 = 10$ mm, L_1 in mm)



(a) S_{21}



(b) Group delay

Fig. 4.28: Simulated transmission characteristics of tuning the second spurline in multiresonator with two spurlines shown in Fig.4.26 ($L_1 = 18.1$ mm, L_2 in mm)

Table 4.4: Frequency band (Δf) and resonant frequency (f) of multiresonator with two spurline resonators (All values in GHz)

	Δf_1 (2.3 - 3.8)	Δf_2 (4.0 - 6.7)
f_1	2.3	4.0
f_2	2.42	4.25
f_3	2.52	4.42
f_4	2.63	4.61
f_5	2.74	4.81
f_6	2.86	5.03
f_7	2.98	5.26
f_8	3.12	5.52
f_9	3.27	5.80
f_{10}	3.43	6.11
f_{11}	3.61	6.43
f_{12}	3.8	6.7

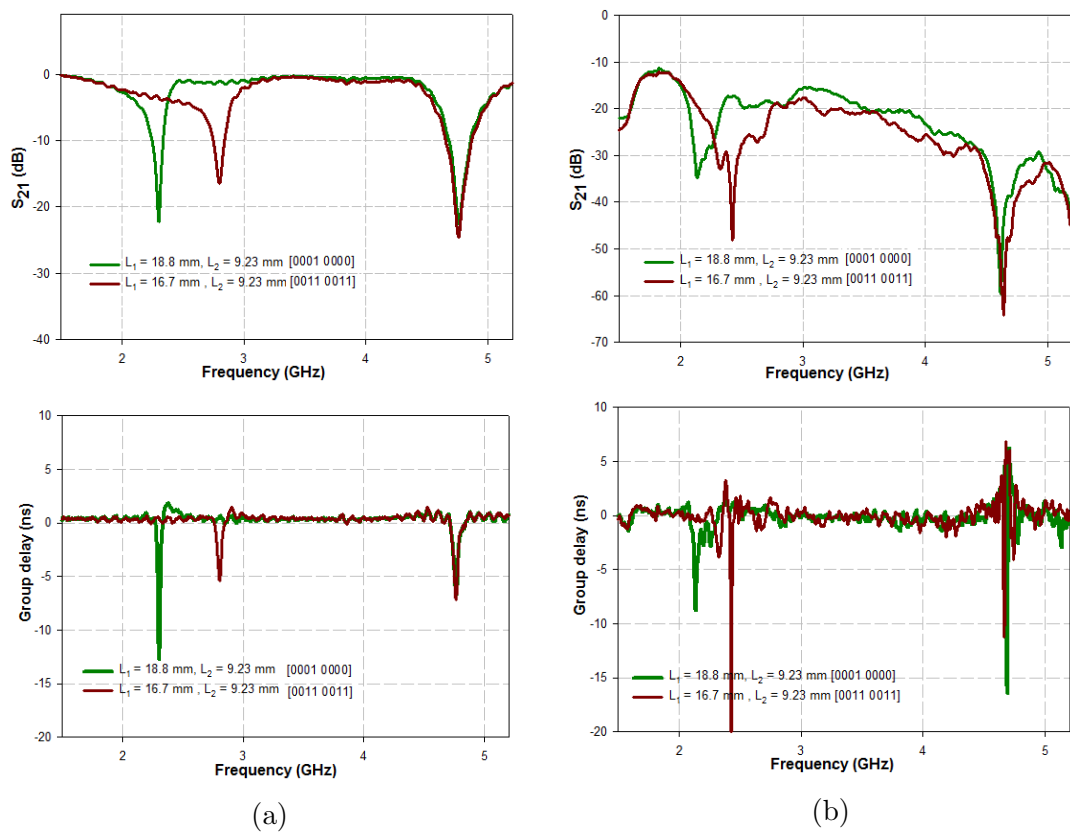


Fig. 4.29: Measured response of the multiresonator with two spurlines for two different configurations (a) Transmission characteristics of the resonator (b) Bistatic response



Fig. 4.30: Photograph of fabricated multiresonator with two spurlines

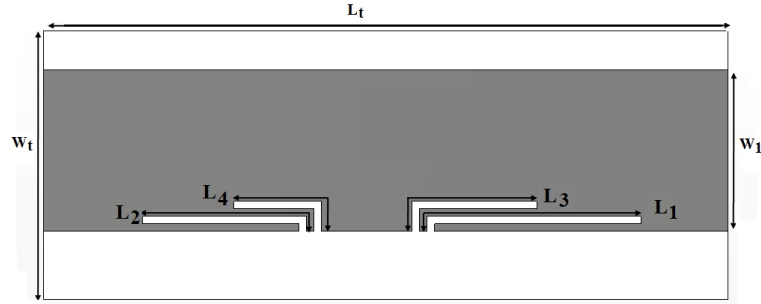


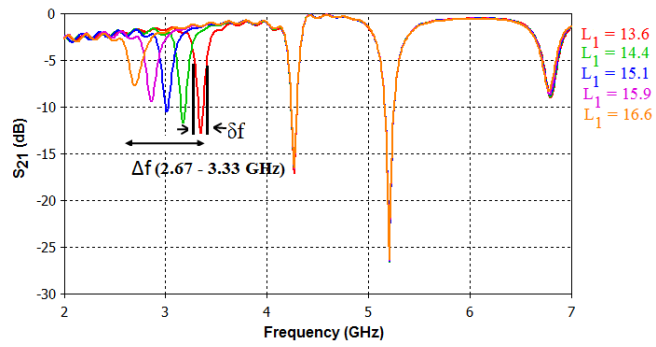
Fig. 4.31: Layout of multiresonator with four spurlines [$W_1 = 10.7$, $W_t = 18$, $L_t = 45$ (All dimensions in mm), Substrate: loss tangent = 0.0018, $\epsilon_r = 4.3$, $h = 1.6$ mm]

4.5.7 Frequency shift coding applied to multiresonator with four spurlines

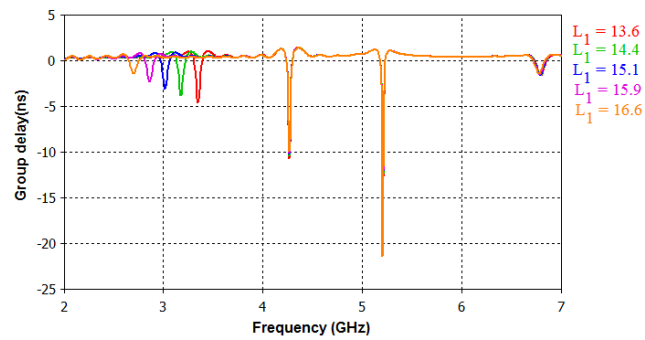
Fig.4.31 shows the layout of multiresonator with four spurline resonators whose length (L) is individually varied for FSC. The frequency band (Δf) and resonant frequency (f) of each resonator is listed in Table 4.5. Variation of the length of one resonator, keeping the dimensions of other resonators constant, results in five different resonant frequencies. Fig.4.32 to Fig.4.35 show the results obtained by individually varying the length of each resonator. While varying the length of each resonator care must be taken that the resonance due to other resonators should remain unaffected. In FSC for bit encoding, precautions must also be taken so that merging of resonant bands (Δf) does not occur and harmonics of the lower frequency resonators do not interfere with the resonance of higher frequency resonators. Unique identification code can be assigned to each combination of resonant frequencies. Since five different resonant frequencies are exhibited by each resonator, combining the four, 625 (5^4) different codes are possible with four resonators.

Table 4.5: Frequency band (Δf) and resonant frequency (f) of multiresonator with four spurlines (All values in GHz)

Resonator	Δf	f_1	f_2	f_3	f_4	f_5
1	2.67 - 3.33	2.67	2.84	3	3.16	3.33
2	3.76 - 4.26	3.76	3.87	3.99	4.12	4.26
3	5.06 - 5.67	5.06	5.20	5.35	5.51	5.67
4	6.22 - 7.03	6.22	6.41	6.6	6.81	7.03

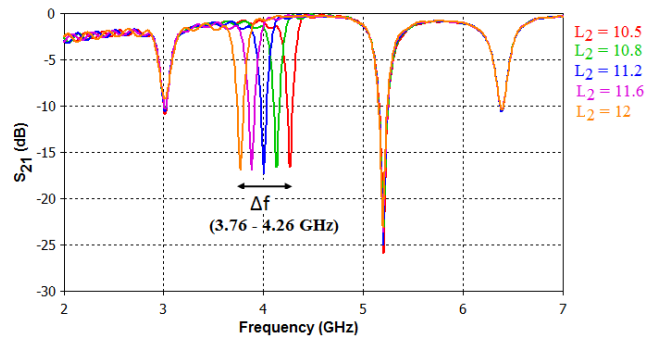


(a) S_{21}

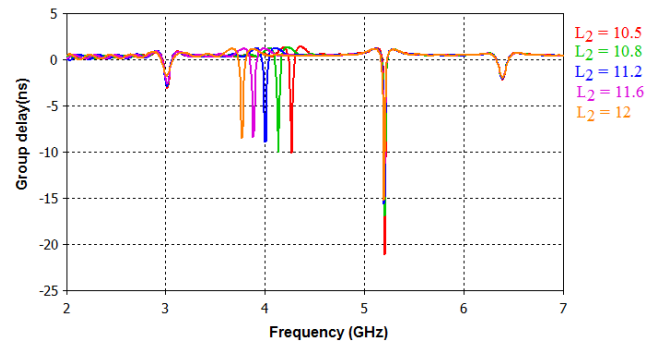


(b) Group delay

Fig. 4.32: Simulated transmission characteristics of tuning the first spurline in multiresonator with four spurlines shown in Fig.4.31 ($L_2 = 10.8$ mm, $L_3 = 7.9$ mm, $L_4 = 5.8$ mm, L_1 in mm)

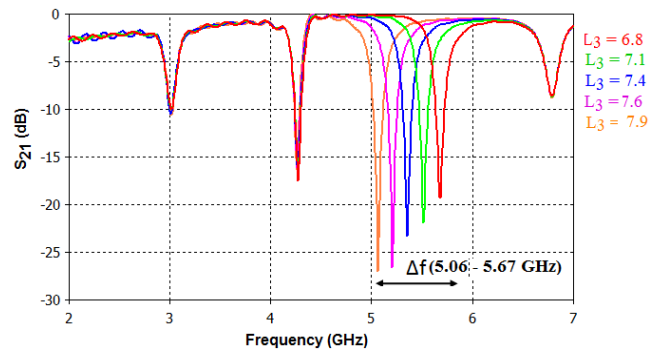


(a) S_{21}

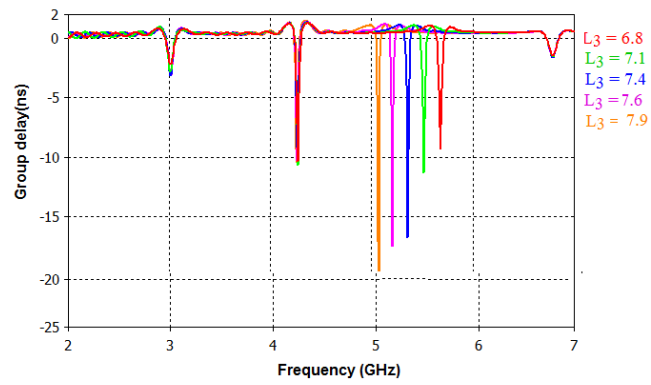


(b) Group delay

Fig. 4.33: Simulated transmission characteristics of tuning the second spurline in multiresonator with four spurlines shown in Fig.4.31 ($L_1 = 15.1$ mm, $L_3 = 7.9$ mm, $L_4 = 5.25$ mm, L_2 in mm)

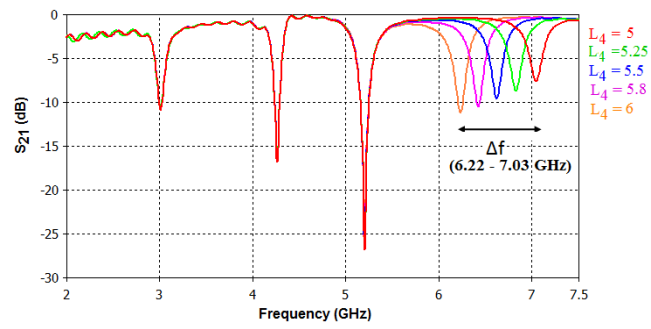


(a) S_{21}

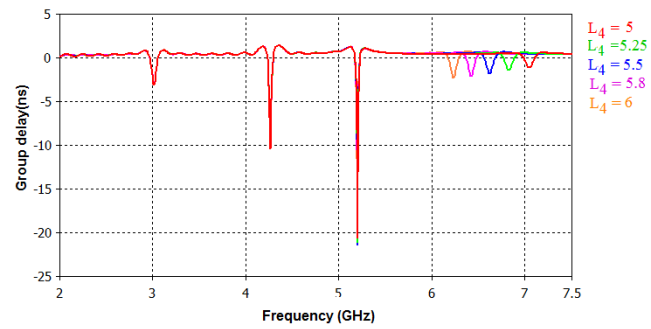


(b) Group delay

Fig. 4.34: Simulated transmission characteristics of tuning of the third spurline in multiresonator with four spurlines shown in Fig.4.31 ($L_1 = 15.1$ mm, $L_2 = 10.8$ mm, $L_4 = 5.25$ mm, L_3 in mm)



(a) S_{21}



(b) Group delay

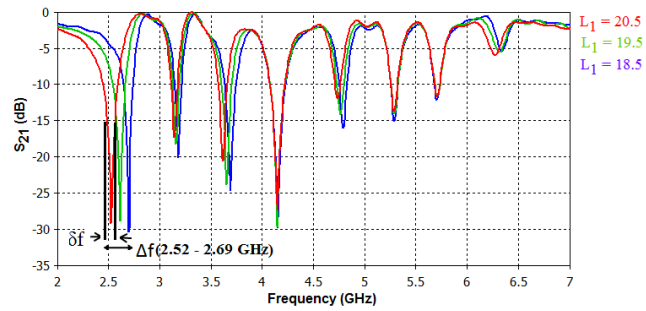
Fig. 4.35: Simulated transmission characteristics of tuning the fourth spurline in multiresonator with four spurlines shown in Fig.4.31 ($L_1 = 15.1$ mm, $L_2 = 10.8$ mm, $L_3 = 7.9$ mm, L_4 in mm)

Table 4.6: Frequency band (Δf) and resonant frequency (f) of multiresonator with eight spurlines (All values in GHz)

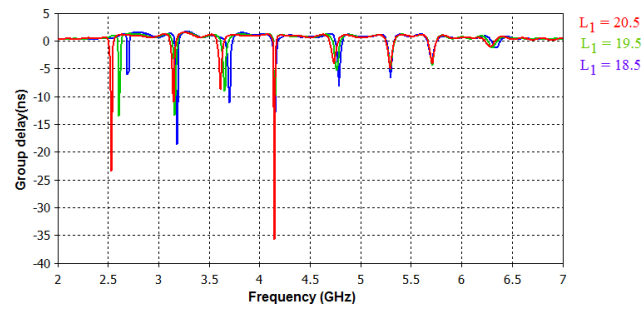
Resonator	Δf	f_1	f_2	f_3
1	2.52 - 2.69	2.52	2.61	2.69
2	2.9 - 3.1	2.9	2.99	3.1
3	3.42 - 3.71	3.42	3.56	3.71
4	4.0 - 4.29	4.0	4.14	4.29
5	4.5 - 4.8	4.5	4.6	4.8
6	4.94 - 5.25	4.94	5	5.25
7	5.38 - 5.68	5.38	5.53	5.68
8	5.87 - 6.4	5.87	6.2	6.4

4.5.8 Frequency shift coding applied to multiresonator with eight spurlines

When the concept of FSC is applied to a multiresonator with eight spurlines [Fig.4.1], eight different frequency bands (Δf) occur as detailed in Table 4.6. Variation of the length of one resonator, keeping the dimensions of other resonators constant, results in three different resonant frequencies. Fig.4.36 to Fig.4.43 show the results obtained by individually varying the length of each resonator. Since three different resonant frequencies are exhibited by each resonator, combining the eight, 6561 (3^8) different codes are possible with eight resonators. Fig.4.44 shows the measured resonator response and bistatic response for varying dimensions of the eighth resonator (L_8).

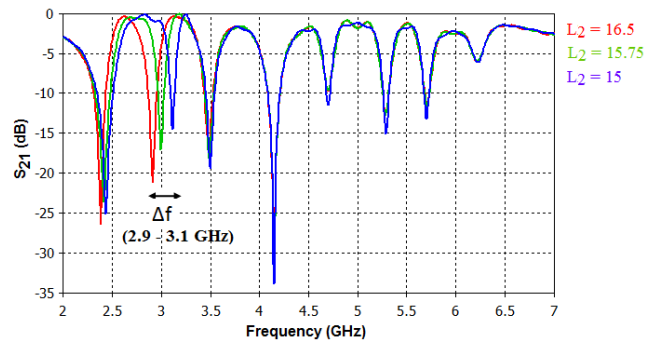


(a) S_{21}

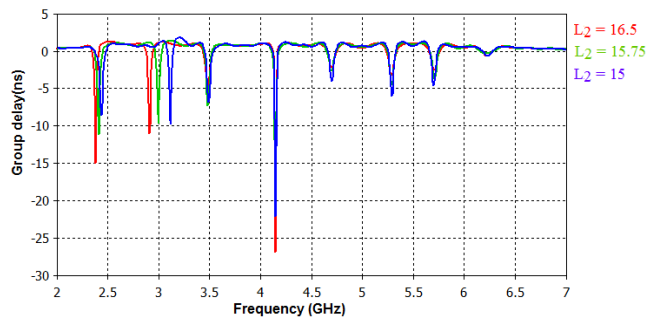


(b) Group delay

Fig. 4.36: Simulated transmission characteristics of tuning the first spurline in multiresonator with eight spurlines shown in Fig.4.1 ($L_2 = 15$ mm, $L_3 = 13.25$ mm, $L_4 = 12.4$ mm, $L_5 = 10.3$ mm, $L_6 = 8.8$ mm, $L_7 = 7.5$ mm, $L_8 = 7$ mm, L_1 in mm)

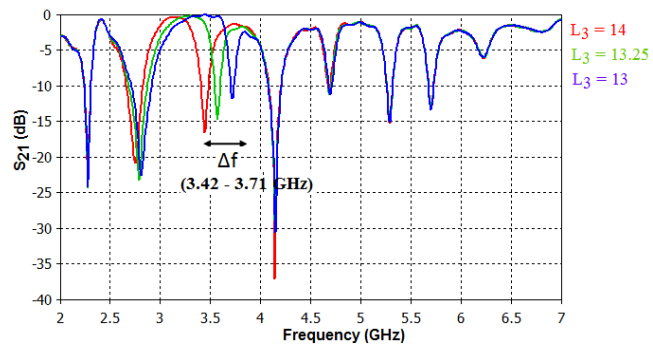


(a) S_{21}

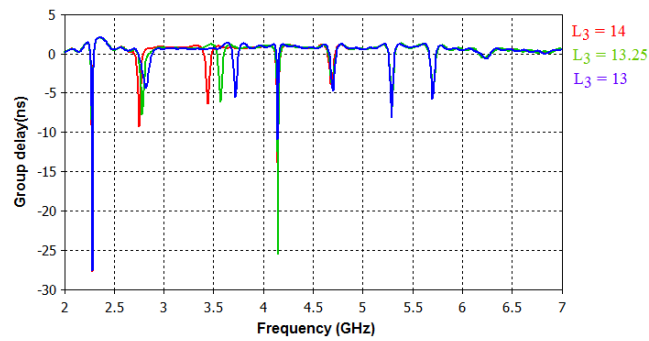


(b) Group delay

Fig. 4.37: Simulated transmission characteristics of tuning the second spurline in multiresonator with eight spurlines shown in Fig.4.1 ($L_1 = 20$ mm, $L_3 = 13.25$ mm, $L_4 = 12.4$ mm, $L_5 = 10.3$ mm, $L_6 = 8.8$ mm, $L_7 = 7.5$ mm, $L_8 = 7$ mm, L_2 in mm)

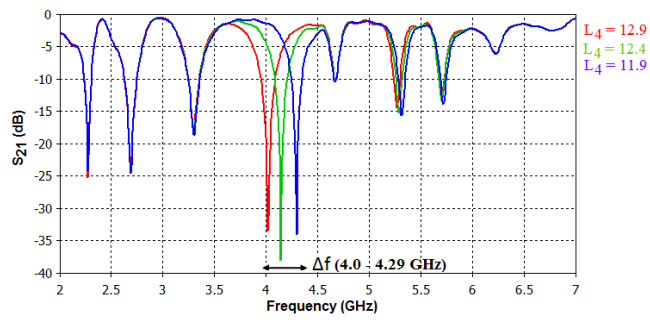


(a) S_{21}

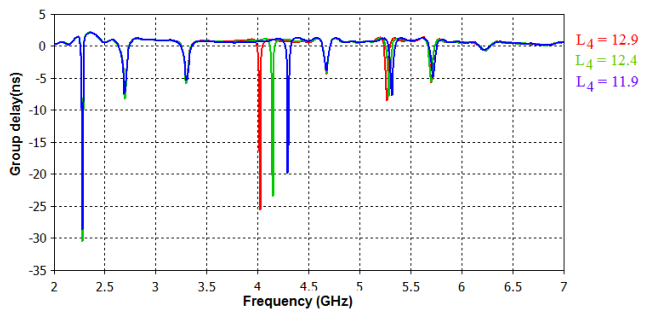


(b) Group delay

Fig. 4.38: Simulated transmission characteristics of tuning the third spurline in multiresonator with eight spurlines shown in Fig.4.1 ($L_1 = 20$ mm, $L_2 = 16.5$ mm, $L_4 = 12.4$ mm, $L_5 = 10.3$ mm, $L_6 = 8.8$ mm, $L_7 = 7.5$ mm, $L_8 = 7$ mm, L_3 in mm)

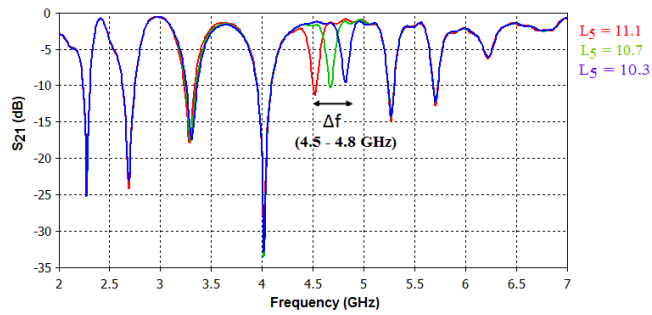


(a) S_{21}

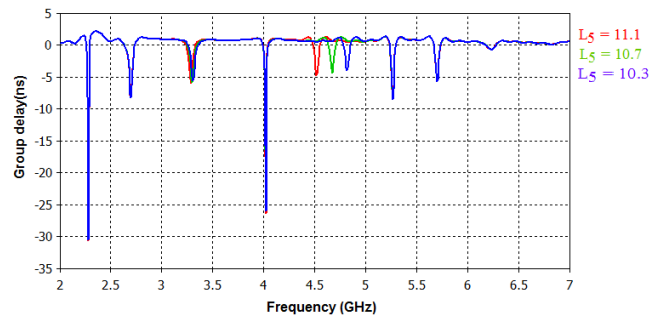


(b) Group delay

Fig. 4.39: Simulated transmission characteristics of tuning the fourth spurline in multiresonator with eight spurlines shown in Fig.4.1 ($L_1 = 20$ mm, $L_2 = 16.5$ mm, $L_3 = 13.25$ mm, $L_5 = 10.3$ mm, $L_6 = 8.8$ mm, $L_7 = 7.5$ mm, $L_8 = 7$ mm, L_4 in mm)

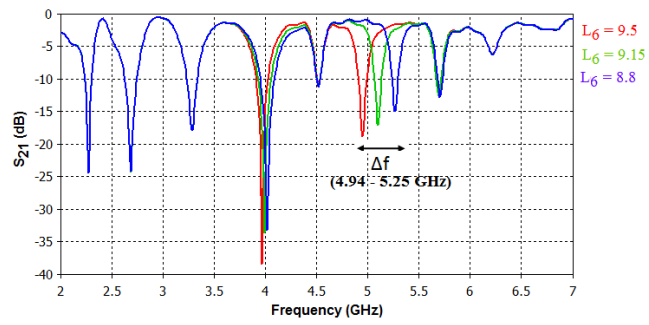


(a) S_{21}

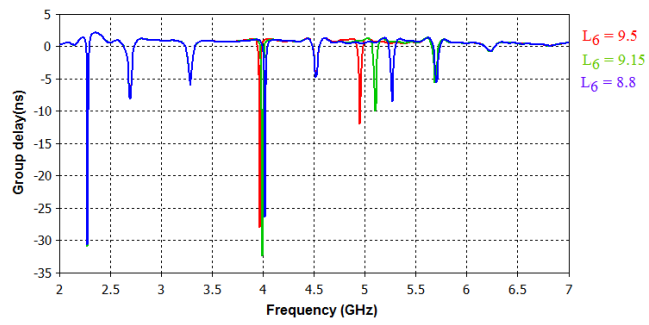


(b) Group delay

Fig. 4.40: Simulated transmission characteristics of tuning the fifth spurline in multiresonator with eight spurlines shown in Fig.4.1 ($L_1 = 20$ mm, $L_2 = 16.5$ mm, $L_3 = 13.25$ mm, $L_4 = 12.4$ mm, $L_6 = 8.8$ mm, $L_7 = 7.5$ mm, $L_8 = 7$ mm, L_5 in mm)

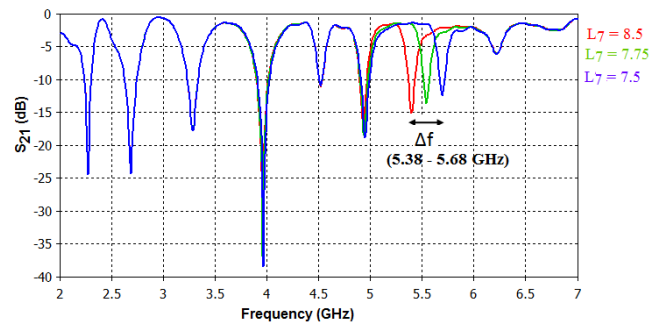


(a) S_{21}

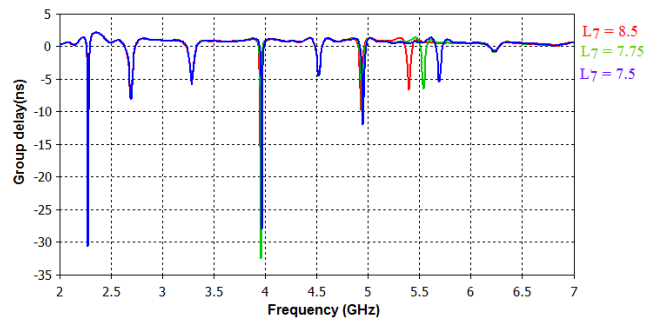


(b) Group delay

Fig. 4.41: Simulated transmission characteristics of tuning the sixth spurline in multiresonator with eight spurlines shown in Fig.4.1 ($L_1 = 20$ mm, $L_2 = 16.5$ mm, $L_3 = 13.25$ mm, $L_4 = 12.4$ mm, $L_5 = 10.3$ mm, $L_7 = 7.5$ mm, $L_8 = 7$ mm, L_6 in mm)

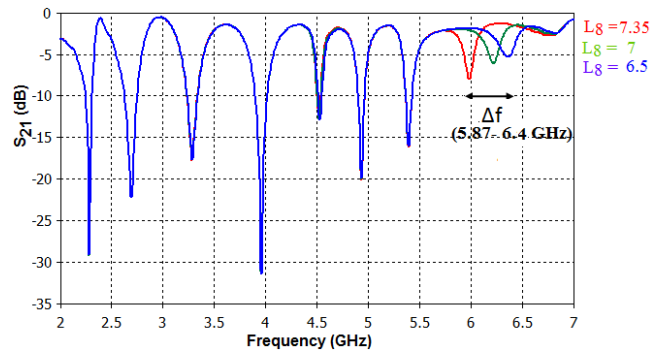


(a) S_{21}

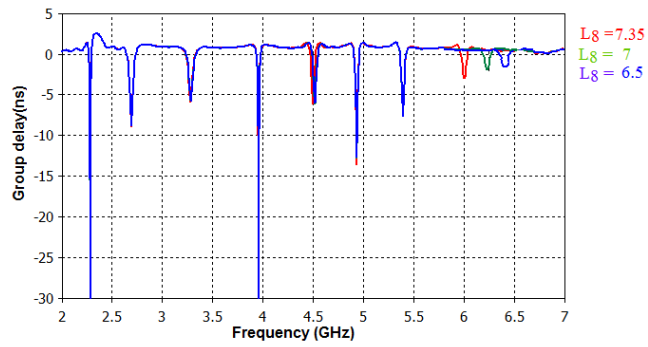


(b) Group delay

Fig. 4.42: Simulated transmission characteristics of tuning the seventh spurline in multiresonator with eight spurlines shown in Fig.4.1 ($L_1 = 20$ mm, $L_2 = 16.5$ mm, $L_3 = 13.25$ mm, $L_4 = 12.4$ mm, $L_5 = 10.3$ mm, $L_6 = 8.8$ mm, $L_8 = 7$ mm, L_7 in mm)



(a) S_{21}



(b) Group delay

Fig. 4.43: Simulated transmission characteristics of tuning the eighth spurline in multi-resonator with eight spurlines shown in Fig.4.1 ($L_1 = 20$ mm, $L_2 = 16.5$ mm, $L_3 = 13.25$ mm, $L_4 = 12.4$ mm, $L_5 = 10.3$ mm, $L_6 = 8.8$ mm, $L_7 = 7.5$ mm, L_8 in mm)

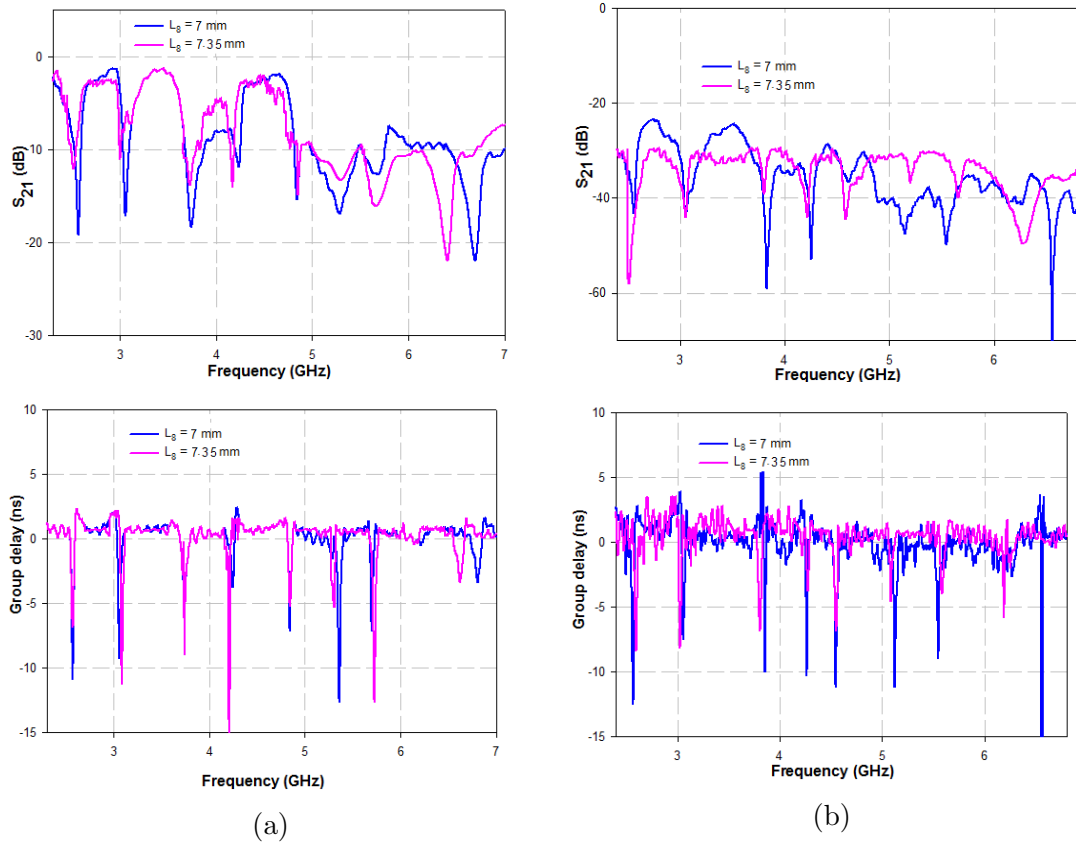


Fig. 4.44: Measured response of multiresonator with eight spurlines for two different configurations ($L_1 = 19.5$ mm, $L_2 = 15.7$ mm, $L_3 = 13$ mm, $L_4 = 12.4$ mm, $L_5 = 10.3$ mm, $L_6 = 8.8$ mm, $L_7 = 7.8$ mm) (a) Transmission characteristics of the resonator (b) Bistatic response

All the above results reveal the design flexibility and high data encoding capacity of the proposed spurline multiresonator for chipless RFID applications.

4.6 Chapter Summary

This chapter explains the implementation of chipless RFID tag using spurline multiresonator. The multiresonator consisting of eight spurline resonators is developed by varying the length of the spurline. The quarter wavelength long resonator can be modeled as a parallel RLC circuit at the resonant frequency. Equivalent circuit model is validated using Agilent ADS. Design equation of the resonator is developed using multiple regression analysis. Orthogonally polarized circular monopole antennas are connected to the multiresonator for range enhancement. The concept is validated using bistatic measurement for an eight bit prototype. The tag can encode data in magnitude and group delay. Various bit combinations for the absence or presence method of encoding the tag identity is generated, either by removing or decoupling the corresponding spurline resonator. In this method, maximum bits that can be represented by an RFID tag is equal to the number of resonators. The bit coding capacity of the tag can be enhanced using FSC technique. It is found that using eight resonators, the number of code words in FSC increases to 6561 (3^8) compared to 256 (2^8) in the case of absence or presence method. Table 4.7 gives a comparison of the proposed chipless RFID tags with other reported tag designs. The comparison is done based on absence or presence coding technique. The proposed tag requires less bandwidth to encode 2^8 code words compared to other designs.

4.7 Inferences

1. The proposed multiresonator represents 256 bit combinations within 1.8 GHz using absence or presence coding technique. However, a sharper resonance of the individual resonators can achieve the same bit capacity within a narrower band.

Table 4.7: Performance comparison of different chipless RFID tag

Parameters	(Bhuiyan <i>et al.</i> , 2013)	(Lee <i>et al.</i> , 2013)	(Zainud D <i>et al.</i> , 2012)	(Nijas <i>et al.</i> , 2012)	Proposed tag
RFID operating band (GHz)	7.5 - 11	3 - 6.2	4-7	2.08 - 4.03	2.39 - 4.19
Bandwidth required (GHz)	3.5	3.2	3	1.95	1.8
Bit states per resonator	4	2	2	2	2
Number of resonators	4	5	6	8	8
Number of code words	4^4	2^5	2^6	2^8	2^8
Bandwidth requirement for each bit (MHz)	> 100	> 100	< 100	< 100	< 100
Surface coding density (bits/cm ²)	0.769	Not specified	0.133	0.533	0.987

2. FSC technique results in 6561 bit combinations within 4.08 GHz. The increased bit encoding capacity of FSC technique can also be fully exploited with a sharper resonance of the individual resonators.
3. The tags presented in next chapter addresses these issues, resulting in efficient utilization of bandwidth.

CHAPTER 5

CHIPLESS RFID TAG USING E SHAPED MULTIRESONATOR

5.1 Introduction

Multiresonator based chipless RFID tag using E shaped resonators coupled to a microstrip transmission line is proposed in this chapter. The configuration of the resonator resembles the letter ‘E’ and hence the term.

5.2 The E shaped multiresonator

The multiresonator consists of eight E shaped resonators excited by a 50Ω microstrip transmission line as shown in Fig.5.1. The prototype is simulated on the substrate C-MET/LK4.3 with dielectric constant 4.3, height 1.6 mm and loss tangent 0.0018 using CST MWS[®]. Fig.5.2 shows the microstrip version of the multiresonator. The overall dimension ($L_t \times W_t$) is 59 mm x 30 mm. The bottom plane acts as ground. The design approach is to generate multiple resonances by modifying the middle arm of each E shaped resonator ($R_1 - R_8$). The simulated transmission characteristics of the multiresonator shown in Fig.5.3 illustrate resonance at 3.15 GHz, 3.24 GHz, 3.30 GHz, 3.37 GHz, 3.45 GHz, 3.55 GHz, 3.65 GHz and 3.77 GHz, thus encoding eight bits in a band of 620 MHz. Fig.5.4 shows surface current distribution of individual resonators at the corresponding resonant frequencies. Each resonator is excited when the length ($L_i + W_a + L_k$) is approximately equal to $\lambda_g/2$ [Fig.5.6(a)].

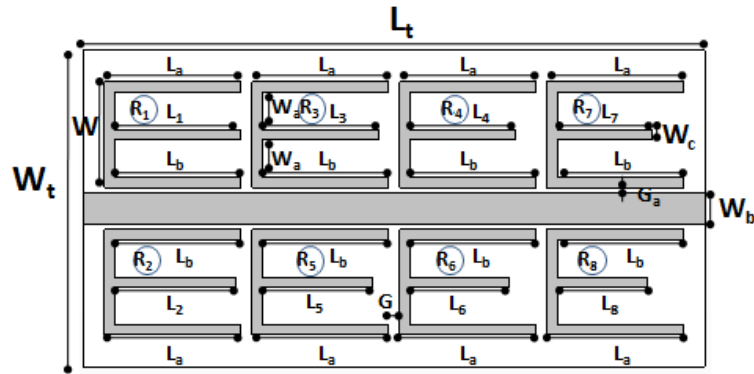


Fig. 5.1: Proposed eight bit E shaped multiresonator [$W = 10$, $L_a = 13$, $L_b = 12$, $L_1 = 12$, $L_2 = 11.5$, $L_3 = 11$, $L_4 = 10.65$, $L_5 = 10.4$, $L_6 = 9.8$, $L_7 = 9.3$, $L_8 = 8.8$, $L_t = 59$, $W_t = 30$, $W_a = 3.5$, $W_b = 3$, $W_c = 1$, $G_a = 0.5$, $G = 1$ (All dimensions in mm), Substrate: loss tangent = 0.0018, $\epsilon_r = 4.3$, $h = 1.6$ mm]

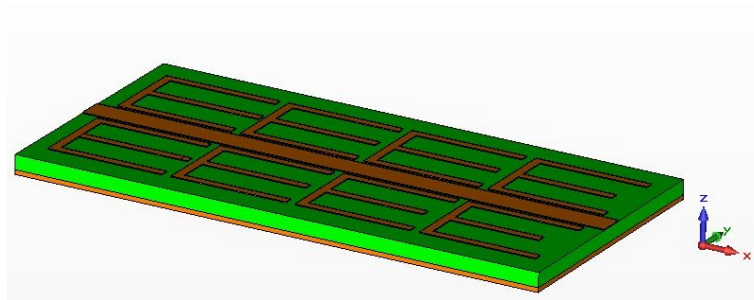


Fig. 5.2: Microstrip version of the E shaped multiresonator

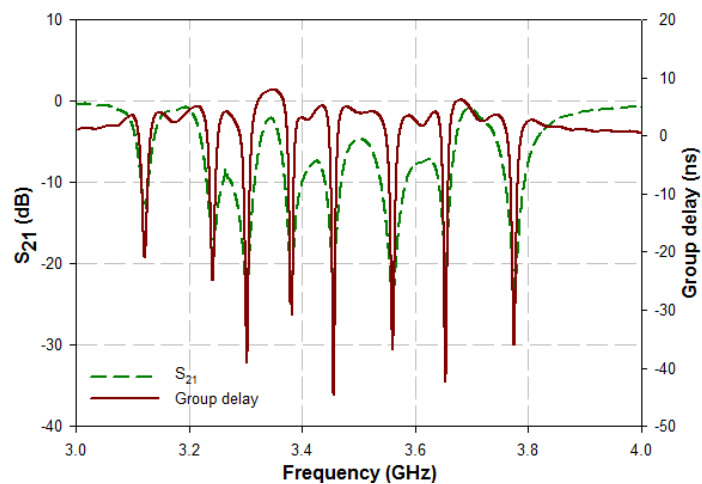


Fig. 5.3: Simulated transmission characteristics of the eight bit E shaped multiresonator shown in Fig.5.1

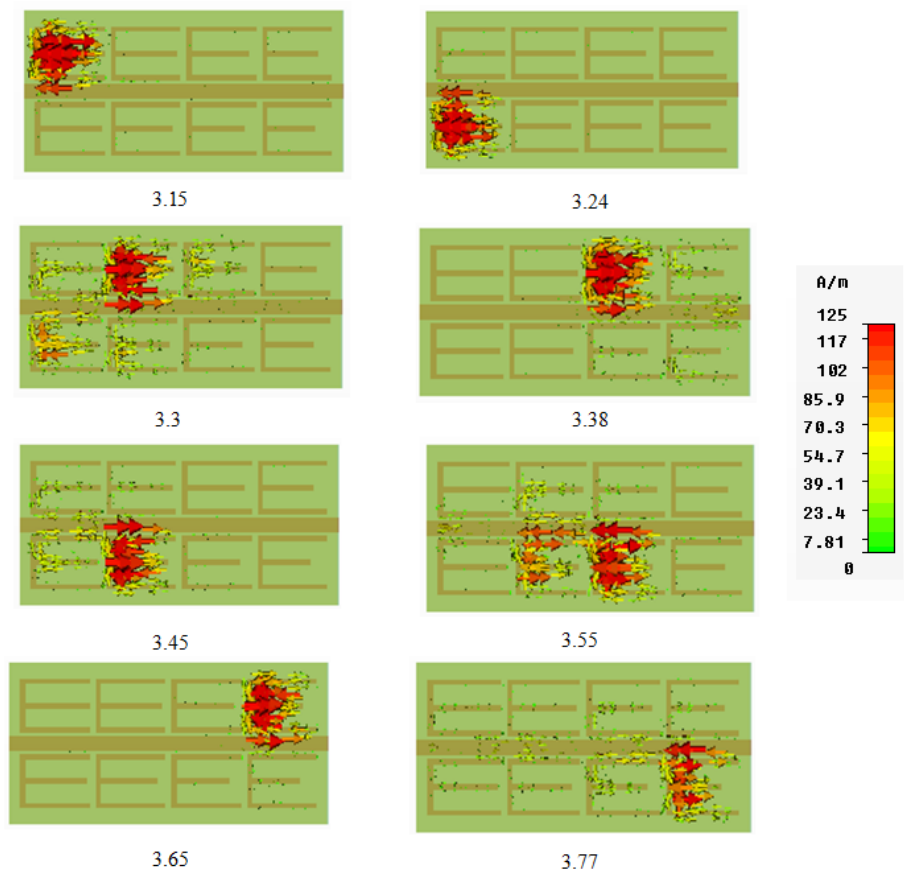


Fig. 5.4: Surface current distribution of individual resonators in the E shaped multiresonator shown in Fig.5.1

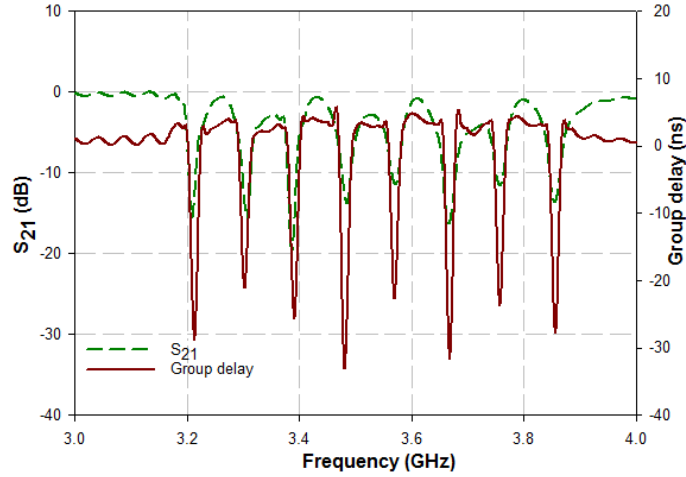


Fig. 5.5: Simulated transmission characteristics of the eight bit multiresonator in 650 MHz band. [The dimensions of the multiresonator are $L = 10$, $L_a = 13$, $L_b = 12$, $L_1 = 12.2$, $L_2 = 11.7$, $L_3 = 11.2$, $L_4 = 10.7$, $L_5 = 10.2$, $L_6 = 9.7$, $L_7 = 9.2$, $L_8 = 8.7$, $L_t = 59$, $W_t = 30$, $W_a = 3.5$, $W_b = 3$, $W_c = 1$, $G_a = 0.5$, $G = 1$ (All dimensions in mm) Substrate: loss tangent = 0.0018, $\epsilon_r = 4.3$, $h = 1.6$ mm]

Different sets of resonant frequencies in 650 MHz band can be derived by choosing a different set of values for middle arm L_i ($i=1$ to 8), with all other parameters remaining the same as in Fig.5.1. The individual resonators operate at frequencies 3.21 GHz, 3.28 GHz, 3.39 GHz, 3.48 GHz, 3.57 GHz, 3.67 GHz, 3.74 GHz and 3.86 GHz as illustrated in Fig.5.5. This feature provides the designer a greater advantage of designing variety of RFID tags with minimal layout modifications. The evolution of the E shaped multiresonator is discussed in the following section.

5.3 Evolution of E shaped multiresonator

The multiresonator has evolved from a resonator with E shaped structure. The performance of E shaped resonator is evaluated in the following section to justify its candidature for RFID applications.

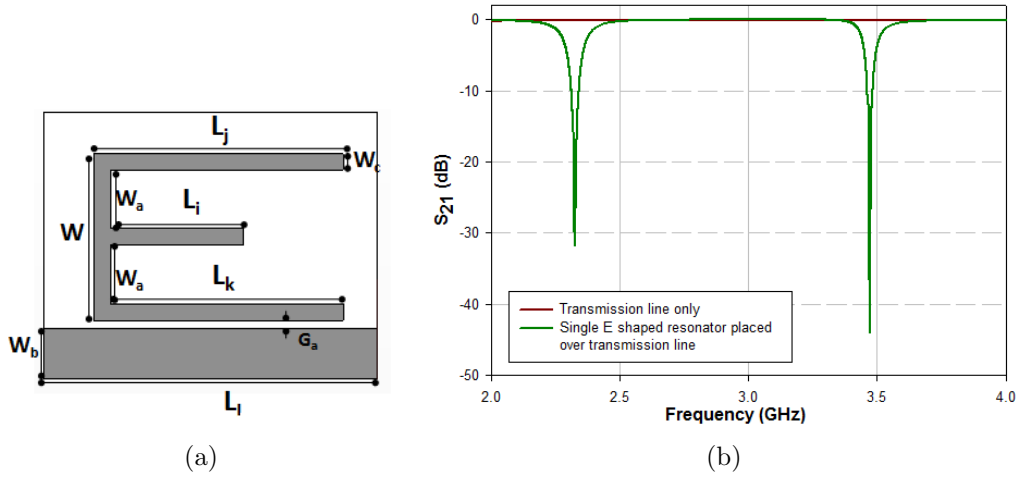


Fig. 5.6: (a) E shaped resonator [$L_j = 15$, $L_i = 9.54$, $L_k = 14$, $W = 10$, $L_l = 20$, $W_a = 3.5$, $W_c = 1$, $G_a = 0.5$, $W_b = 3$ (All dimensions in mm), Substrate: loss tangent = 0.0018, $\epsilon_r = 4.3$, $h = 1.6$ mm] (b) Simulated transmission characteristics of the E shaped resonator

5.3.1 Analysis and design of E shaped resonator

A single E shaped resonator excited by a microstrip transmission line is illustrated in Fig.5.6(a). Fig.5.6(b) shows the simulated transmission characteristics of a transmission line alone and that of a single E shaped resonator coupled to the transmission line. The structure exhibits two resonant frequencies at 2.32 GHz and 3.47 GHz. The resonance at lower frequency is due to the C shaped resonator shown in Fig.5.7(a), obtained by removing the middle arm of the E shaped resonator.

Fig.5.7(b) shows the simulated transmission characteristics of a C shaped resonator coupled to transmission line. It is evident from Fig.5.7(b) that the lower frequency is still present at 2.32 GHz, whereas the upper resonance has been eliminated. A detailed simulation study is conducted by varying the length of the middle arm of the E shaped resonator from 6.5 mm to 12.5 mm and the simulated transmission characteristics is shown in Fig.5.8. It is clear from Fig.5.8 that the lower resonance remains constant at 2.32 GHz whereas the higher resonance shifts from 3.89 GHz to 3.09 GHz when the length of the

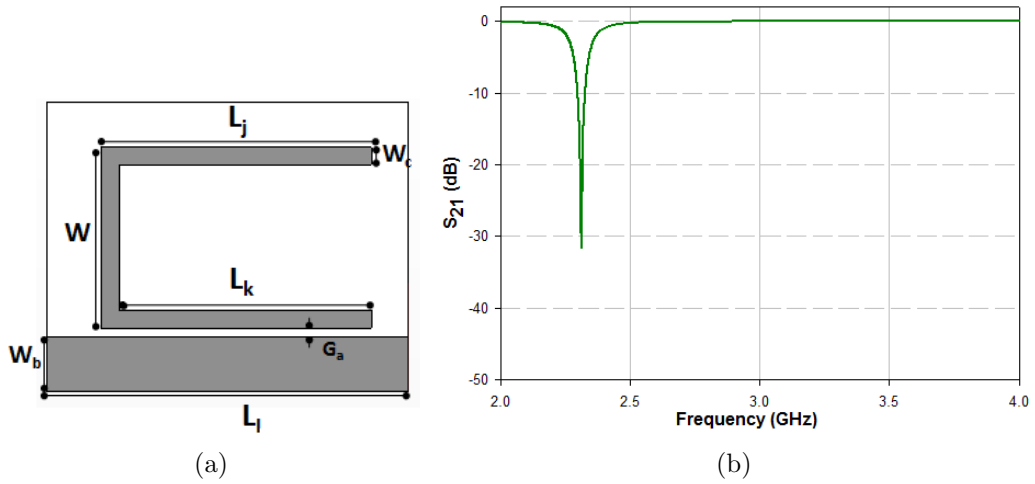


Fig. 5.7: (a) C shaped resonator [$L_j = 15$, $L_k = 14$, $W = 10$, $L_l = 20$, $W_a = 3.5$, $W_c = 1$, $G_a = 0.5$, $W_b = 3$ (All dimensions in mm), Substrate: loss tangent = 0.0018, $\epsilon_r = 4.3$, $h = 1.6$ mm] (b) Simulated transmission characteristics of C shaped resonator

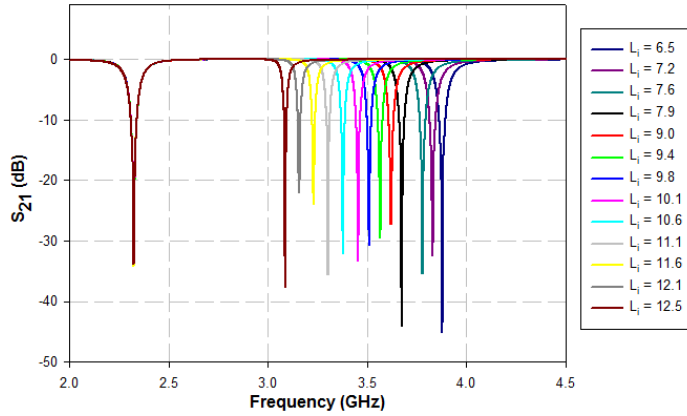


Fig. 5.8: Simulated transmission characteristics by varying L_i (mm) of the E shaped resonator shown in Fig.5.6(a)

middle arm varies from 6.5 mm to 12.5 mm. This feature is used for designing the multiresonator.

A sharp resonance is essential for chipless RFID applications since it exhibits narrow band width, which helps to accommodate large number of bits in particular frequency range with distinct resonant frequencies. The E geometry is preferred over C geometry, by virtue of the narrow FBW ($\frac{\Delta f}{f} * 100$) exhibited by its resonance. This fact is ascertained by the following study. Varying the length of the upper arm(L_j) of the C shaped resonator and the middle arm(L_i)

Table 5.1: Variation of f , Δf , FBW for different values of length of the upper arm(L_j) of the C shaped resonator

$L_k = 14$ mm, $L_l = 20$ mm				
$W = 10$ mm, $W_a = 3.5$ mm, $W_b = 3$ mm, $W_c = 1$ mm				
	L_j (mm)	f (GHz)	Δf (MHz)	FBW(%)
1	1	3.57	191	5.351
2	2	3.43	187	5.452
3	3	3.3	182	5.516
4	4	3.	163	5.126
5	5	3.07	153	4.984
6	6	2.97	140	4.714
7	7	2.87	145	5.053
8	8	2.78	123	4.425
9	9	2.69	119	4.424
10	10	2.6	100	3.847
11	12	2.45	106	4.327
12	13	2.38	95	3.992

of the E shaped resonator result in variation of FBW as illustrated in Table 5.1 and Table 5.2 respectively.

It is clear that an E shaped resonator exhibits lower FBW compared to C shaped resonator. To further validate the choice of E over C, a detailed study is done to encode eight bits. An eight bit C shaped multiresonator is formed by varying the length of the upper arm of each C shaped resonator as shown in Fig.5.9. The simulated transmission characteristics is shown in Fig.5.10. The C shaped multiresonator requires a bandwidth of 1.38 GHz in frequency range from 2.34 GHz to 3.72 GHz to encode eight bits whereas E shaped multiresonator requires only a bandwidth of 620 MHz in frequency range from 3.15 GHz to 3.77 GHz.

Table 5.2: Variation of f , Δf , FBW for different values of length of the middle arm(L_i) of the E shaped resonator

$L_k = 14 \text{ mm}, L_l = 20 \text{ mm}, L_j = 15 \text{ mm}$ $W = 10 \text{ mm}, W_a = 3.5 \text{ mm}, W_b = 3 \text{ mm}, W_c = 1 \text{ mm}$				
	$L_i(\text{mm})$	$f(\text{GHz})$	$\Delta f(\text{MHz})$	FBW(%)
1	7.9	3.77	92	2.45
2	8.3	3.72	81	2.18
3	8.7	3.67	77	2.1
4	9	3.62	70	1.94
5	9.4	3.57	66	1.85
6	9.7	3.51	62	1.77
7	10	3.46	52	1.51
8	11	3.3	48	1.46
9	12	3.16	44	1.4
10	13	3.01	34	1.13
11	14	2.89	31	1.08
12	15.6	2.72	23	0.85

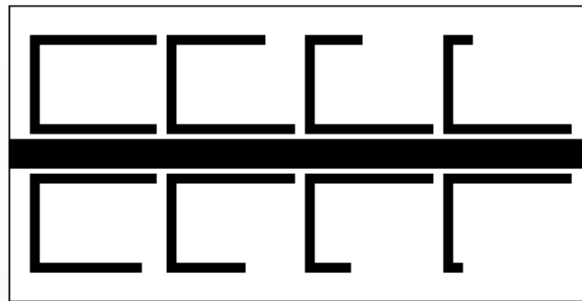


Fig. 5.9: Layout of the eight bit C shaped multiresonator

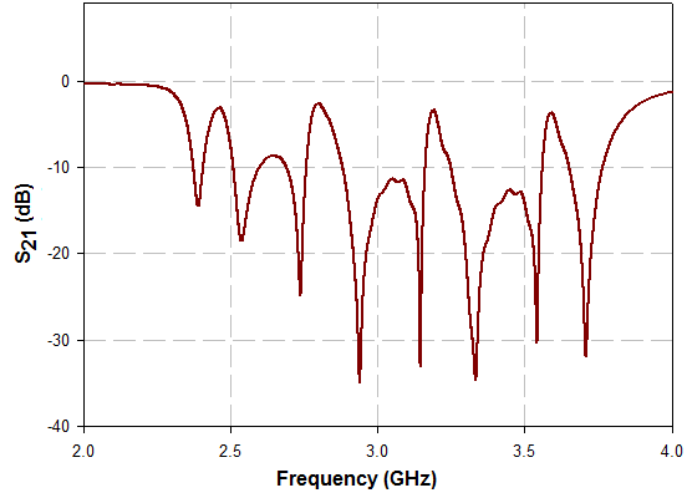


Fig. 5.10: Simulated transmission characteristics of eight C shaped multi-resonator

The resonant frequency of the E shaped resonator can be found by the relation

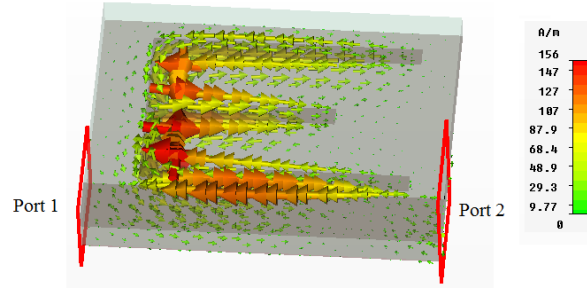
$$f = \frac{c}{2 * (L_i + W_a + L_k + \Delta L) \sqrt{\epsilon_{eff}}} \quad (5.1)$$

where ΔL is the fringing length, ϵ_{eff} is the effective permittivity of the substrate and λ_g is the guide wavelength evaluated at the resonant frequency.

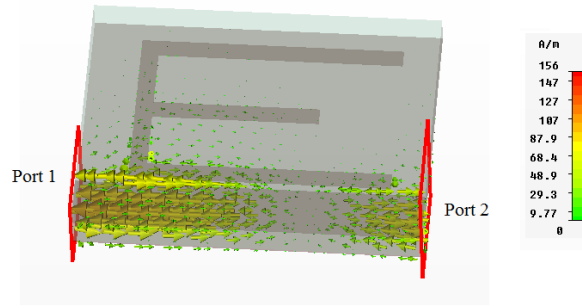
$$\lambda_g = \frac{\lambda}{\sqrt{\epsilon_{eff}}} \quad (5.2)$$

Surface current distribution of E shaped resonator at its resonant frequency (3.47 GHz) and at a non-resonant frequency (4 GHz) are depicted in Fig.5.11 . The surface current distribution is concentrated in the resonator at the resonant frequency. It is clear that there is no transmission from port 1 to port 2 at the resonant frequency and transmission occurs at non-resonant frequency.

Multiple regression analysis is used to develop the design equation of the E shaped resonator for a chosen substrate of relative permittivity(ϵ_r) and height(h in mm). The length L_i (in mm) computed for a resonant frequency(f in GHz)



(a) 3.47 GHz



(b) 4 GHz

Fig. 5.11: Surface current distribution of E shaped resonator at resonant frequency of 3.47 GHz and at a non-resonant frequency of 4 GHz.

can be expressed as in Equation 5.3. The database for the development of the design equation is created by doing parametric analysis on the middle arm of the E shaped resonator for each substrate keeping $W_a = 3.5$ mm, $L_k = 14$ mm, $W_c = 1$ mm, $W = 10$ mm and $G_a = 0.5$ mm.

$$L_i = 2.062h - 6.259f - 3.048\epsilon_r + 41.41 \quad (5.3)$$

The equation is valid for ϵ_r and h in the range $2.25 \leq \epsilon_r \leq 5.4$ and 0.8 mm $\leq h \leq 1.6$ mm respectively. The equation is confirmed on various substrates having different values of relative permittivity and height as shown in Table 5.3.

Table 5.3: Computed values of L_i for different resonant frequencies on various substrates

	ϵ_r	h (mm)	L_i (mm)	$f(GHz)$		%error
				Theory	CST	
1	2.25	1	8.4	4.5	4.6	2.2
2	2.4	1	11.1	4	3.98	0.5
3	3.27	0.8	6.8	4.2	4.19	0.23
4	4.4	1.6	9.3	3.5	3.57	0.57
5	4.8	1.6	9.4	3.3	3.35	1.5
6	5.4	1.25	6.2	3.4	3.48	2.3

5.3.2 Equivalent circuit of E shaped resonator

The resonator can be modeled as an open circuited transmission line of length $\lambda_g/2$. The input impedance for length 'l' is given by (Pozar, 2009).

$$Z_{in} = Z_0 \frac{Z_L + Z_0 \tanh \gamma l}{Z_0 + Z_L \tanh \gamma l} \quad (5.4)$$

$\gamma = \alpha + j\beta$, α is the attenuation constant, β is the phase constant, Z_0 is the characteristic impedance and Z_L is the load impedance. For an open circuited transmission line of length $\lambda_g/2$, Equation. 5.4 can be written as

$$\begin{aligned} Z_{in} &= Z_0 \coth(\alpha + j\beta)l \\ Z_{in} &= Z_0 \frac{1 + j \tan \beta l \tanh \alpha l}{\tanh \alpha l + j \tan \beta l} \end{aligned} \quad (5.5)$$

Since the resonator is designed with a low loss material ($\alpha l \ll 1$)

$$\tanh \alpha l \approx \alpha l$$

$$\alpha = \alpha_c + \alpha_d \quad (5.6)$$

α_c is the attenuation due to conductor loss and α_d is the dielectric loss.

$$\alpha_c = \frac{R_s}{Z_0 W_c} \quad (5.7)$$

R_s is the surface resistivity of the conductor and W_c is the width of the arm of the E shaped resonator.

$$R_s = \sqrt{\frac{\omega \mu_0}{2\sigma}} \quad (5.8)$$

where μ_0 is the permeability of free space and σ is the conductivity of copper.

$$\begin{aligned} \alpha_d &= \frac{K_0 \epsilon_r (\epsilon_e - 1) \tan \delta}{2\sqrt{\epsilon_e} (\epsilon_r - 1)} \\ K_0 &= \frac{2\pi f}{c} \end{aligned} \quad (5.9)$$

At a frequency(ω) near resonance (ω_0), let $\omega = \omega_0 + \Delta\omega$,

$$\beta l = \frac{\omega l}{v_p} = \frac{\omega_0 l}{v_p} + \frac{\Delta\omega l}{v_p}$$

where v_p = is the phase velocity of the transmission line. Since $l = \frac{\lambda}{2} = \frac{\pi v_p}{\omega_0}$ for $\omega = \omega_0$

$$\begin{aligned} \beta l &= \pi + \frac{\Delta\omega \pi}{\omega_0} \\ \tan \beta l &= \tan\left(\pi + \frac{\Delta\omega \pi}{\omega_0}\right) = \tan\left(\frac{\Delta\omega \pi}{\omega_0}\right) \approx \frac{\Delta\omega \pi}{\omega_0} \end{aligned} \quad (5.10)$$

These results when substituted in 5.5 gives

$$Z_{in} \approx Z_0 \frac{1 + j \frac{(\Delta\omega \pi)}{\omega_0} \alpha l}{\alpha l + j \frac{(\Delta\omega \pi)}{\omega_0}} \approx \frac{Z_0}{(\alpha l + j \frac{\Delta\omega \pi}{\omega_0})} \quad (5.11)$$

since $\frac{\Delta\omega \alpha l}{\omega_0} \ll 1$

Equation 5.11 resembles the input impedance of a parallel RLC resonant circuit,

$$Z_{in} = \frac{R}{1 + 2jRC\Delta\omega} \quad (5.12)$$

where resistance of the equivalent RLC circuit is

$$R = \frac{Z_0}{\alpha l} \quad (5.13)$$

and capacitance of the equivalent circuit is

$$C = \frac{\pi}{2\omega_0 Z_0} \quad (5.14)$$

where $\omega_0 = \frac{2\pi c}{\lambda_g \sqrt{\epsilon_{eff}}}$, $\lambda_g = 2l$, l is the length of the resonator in mm and c is the velocity of light. Substituting,

$$C = \frac{2l\sqrt{\epsilon_{eff}}}{4cZ_0} \quad (5.15)$$

For the E resonator, the length ' l ' is given by $l = L_i + W_a + L_k$

the inductance of the equivalent circuit is

$$L = \frac{1}{\omega^2 C} \quad (5.16)$$

The E resonator is therefore modeled as a parallel RLC resonant circuit. The value of R, L and C are determined using Equations 5.13, 5.16 and 5.15 respectively. Fig.5.12 shows the equivalent circuit designed in Agilent ADS software with two ports connected across the 50Ω transmission line for a resonant frequency of 3.47 GHz. Fig.5.13 shows the frequency response extracted using Agilent ADS.

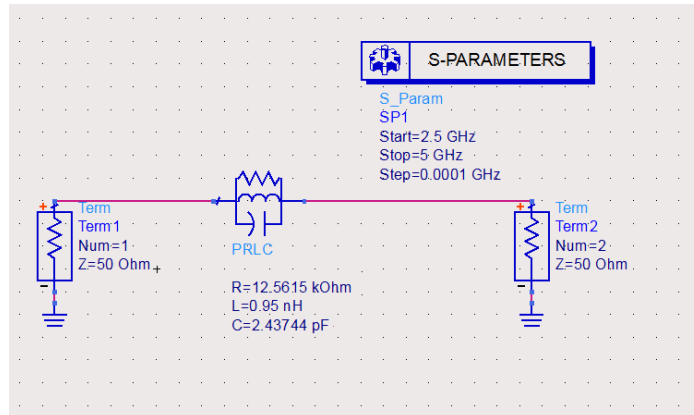


Fig. 5.12: Equivalent circuit of E shaped resonator ($f = 3.47$ GHz)

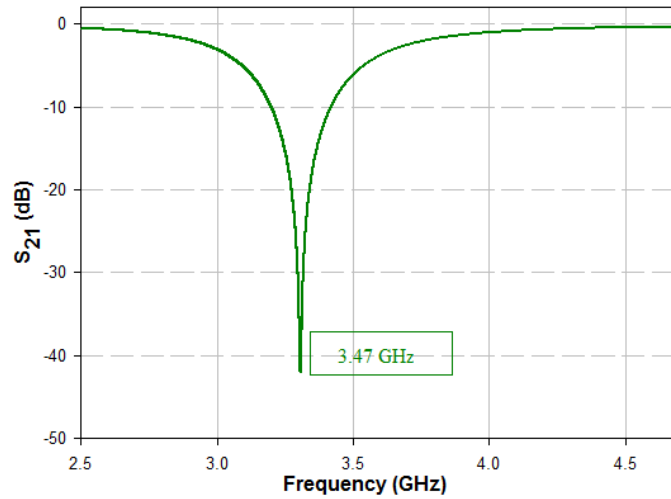
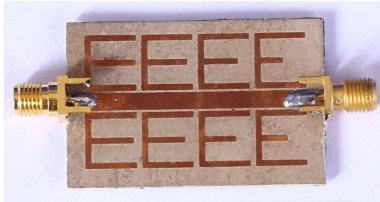


Fig. 5.13: Frequency response of E shaped resonator extracted using Agilent ADS



(a)



(b)

Fig. 5.14: (a) Photograph of the fabricated multiresonator (b) Network analyser with device under test

5.3.3 Experimental results of E shaped multiresonator

Fig.5.14(a) shows the photograph of the fabricated multiresonator. Measurements are conducted using the PNA E8362B network analyser. The device under test (multiresonator) is connected between the two ports of the vector network analyser as shown in Fig.5.14(b). Fig.5.15 shows the measured transmission characteristics of the E shaped multiresonator for bit combination [1111 1111]. The design parameters of the high frequency resolution multiresonator have been chosen in order to obtain a frequency bandwidth as narrow as possible, so as to encode eight bits in a frequency band of 620 MHz. The eight bits are represented by eight resonant nulls between 3.15 GHz and 3.77 GHz. Data encoding techniques discussed in Section 2.5 are used to generate various bit combinations.

The proposed E shaped multiresonator can be used as an RFID tag for access control applications where the tag is in close proximity of the reader. However, the tag needs modification in its design for range enhancement. This is discussed in Section 5.4.

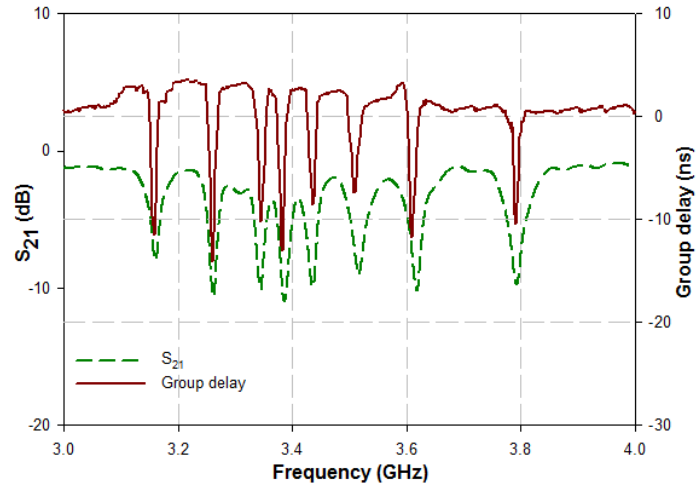


Fig. 5.15: Measured transmission characteristics of the E shaped multiresonator for the bit combination [1111 1111]

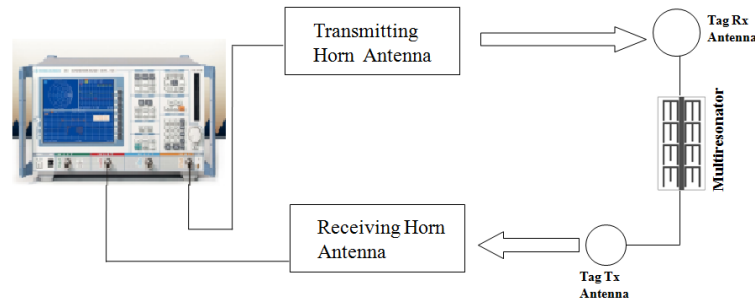


Fig. 5.16: Block schematic for bistatic measurement of the RFID tag using E shaped multiresonator

5.4 Bistatic measurement for validation of the tag

The block schematic of the bistatic measurement of the RFID tag using E shaped multiresonator is shown in Fig.5.16. Two wide band antennas are incorporated to increase the range of multiresonator as explained in Section 2.4. Two cross polarized medium gain(10 dB) horn antennas are used for transmission and reception of the signal at the reader (Preradovic and Karmakar, 2009; Preradovic *et al.*, 2009, 2008a).

Fig.5.17 shows the experimental set up for bistatic measurement of the RFID tag using E shaped multiresonator. The tag is placed 20 cm away from horn

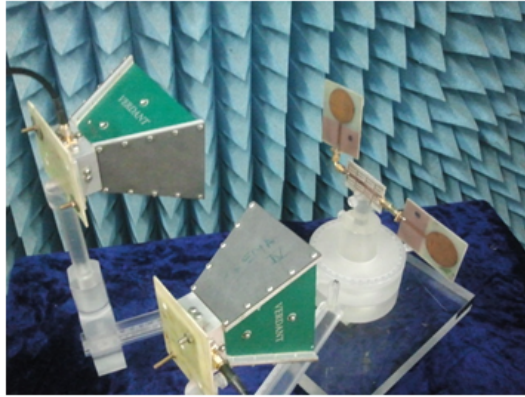


Fig. 5.17: Experimental setup for bistatic measurement of the RFID tag using E shaped multiresonator

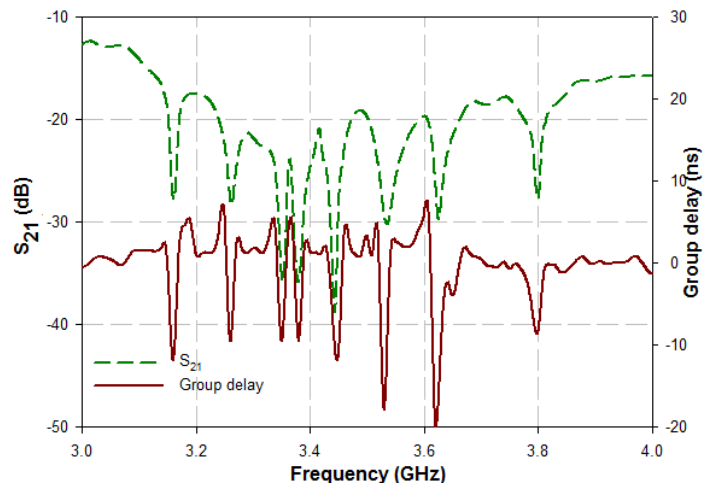


Fig. 5.18: Measured bistatic response of the RFID tag for the bit combination [1111 1111]

antennas. Fig.5.18 shows the measured bistatic response for bit combination [1111 1111] when all the eight E shaped resonators are coupled to the transmission line. The bistatic response clearly indicates the abrupt variations at resonance, as in the case of multiresonator[Fig.5.15].

5.5 Data encoding methods

Absence or presence coding technique and frequency shift coding technique, as discussed in Section. 2.5, are employed for data encoding.

5.5.1 Absence or presence coding technique

The presence of resonance is used to encode a logic 1 and the absence of resonance is used to encode a logic 0. In E shaped multiresonator type 1 [Fig.5.19] all the eight E shaped resonators are present resulting in bit combination [1111 1111], R_1 corresponds to the most significant bit and R_8 corresponds to the least significant bit.

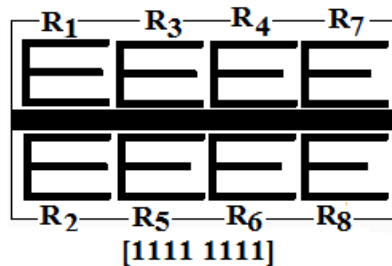
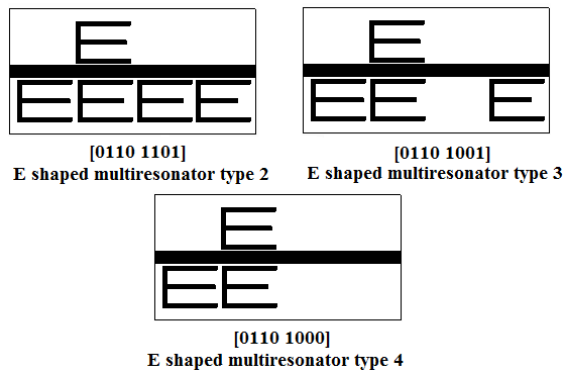


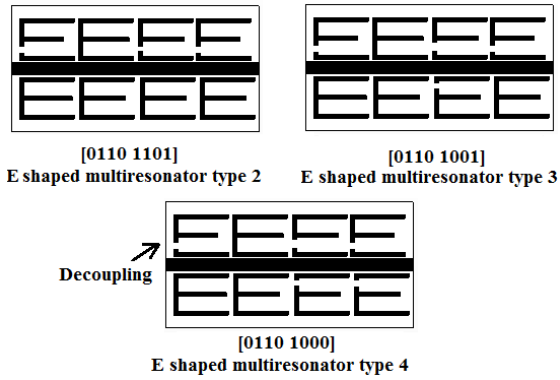
Fig. 5.19: E shaped multiresonator type 1

The absence of a specific resonance can be achieved either by removing the corresponding resonator Fig.5.20(a) or decoupling the corresponding E resonator Fig.5.20(b). Three different types of such resonators are shown in Fig.5.20.

In E shaped multiresonator type 2 resonances due to R_1 , R_4 and R_7 , are absent leading to a bit combination [0110 1101]. In E shaped multiresonator type 3 resonances due to R_1 , R_4 , R_6 and R_7 are absent resulting in [0110 1001]. In E shaped multiresonator type 4 resonances due to R_1 , R_4 , R_6 , R_7 and R_8 are absent resulting in [0110 1000]. Fig.5.21 shows the simulated transmission characteristics of the three types of resonators. The small shift in resonant frequency may be due to the mutual coupling between the resonators. The simulated transmission characteristics of [1111 1111] was shown in Fig.5.3.

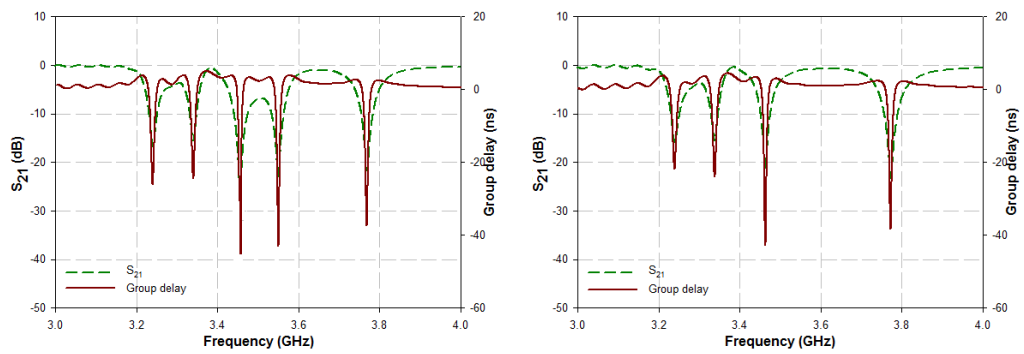


(a) Removing the resonator



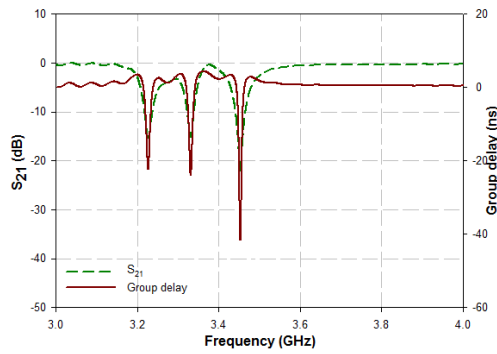
(b) Decoupling the resonator

Fig. 5.20: Three different types of E shaped multiresonator (a) Removing the resonator (b) Decoupling the resonator



(a) Multiresonator type 2 [0110 1101]

(b) Multiresonator type 3 [0110 1001]



(c) Multiresonator type 4 [0110 1000]

Fig. 5.21: Simulated transmission characteristics E shaped multiresonator for different bit combinations

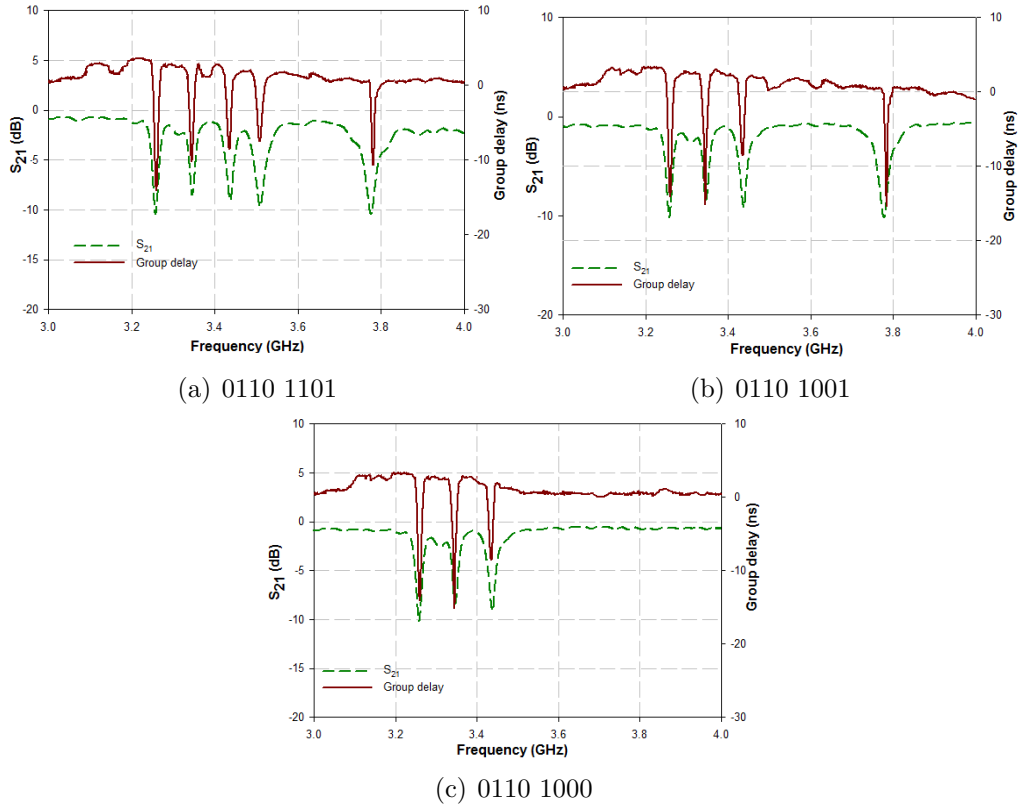


Fig. 5.22: Measured transmission characteristics of the E shaped multiresonator for different bit combinations

5.5.2 Experimental results of E shaped multiresonator using absence or presence coding technique

Using the technique mentioned in Section 5.5.1 different types of multiresonators are fabricated. The transmission characteristics is measured using Agilent PNA E8362B network analyzer by connecting the multiresonator between the ports of analyzer after doing calibration. Measured transmission characteristics of the multiresonator for the bit combination [0110 1101], [0110 1001], [0110 1000] are shown in Fig.5.22.

The tag identity can be confirmed from the absolute value of S_{21} or group delay. The tag detection can be made virtually independent of absolute value of S_{21} or group delay by a post processing method using a difference operation

technique as detailed in Section 2.5.2. A peak variation at resonance is clearly visible from the post processed signal for the bit combination [0110 1101], [0110 1001] and [0110 1000] as shown in Fig.5.23.

5.5.3 Bistatic measurement results using absence or presence coding technique

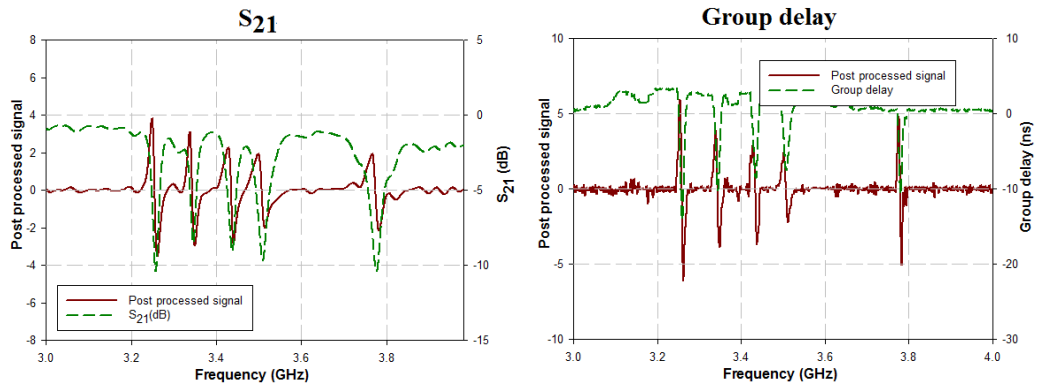
Bistatic measurement is done to validate the tag for various bit combinations. Fig.5.24 shows the measured bistatic response for bit combinations [0110 1101], [0110 1001] and [0110 1000]. The measured result of [1111 1111] was shown in Fig.5.18. As explained in Section 2.5.2, post processing method is applied to the measured bistatic results. Fig.5.25 shows the post processed signal for the bit combination [1111 1111].

5.5.4 Frequency shift coding technique for enhanced bit encoding capacity

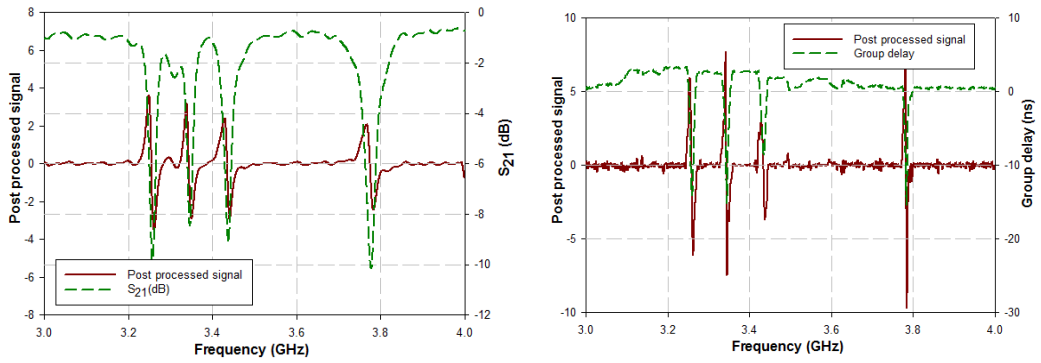
The bit encoding capacity of the tag can be enhanced using frequency shift coding (FSC) technique, by encoding more than one bit per resonator as explained in Section 2.5.4. This section explains the method by which FSC is applied to various E shaped resonator configurations.

5.5.5 Frequency shift coding applied to E shaped resonator

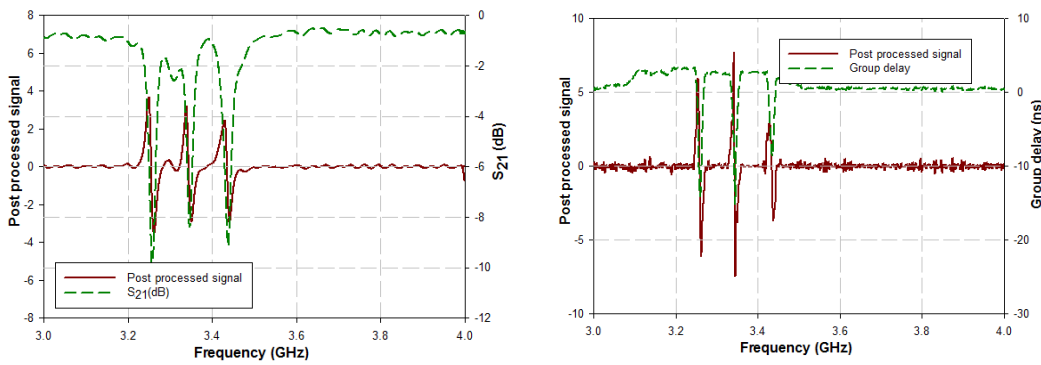
The simulated transmission characteristics for length (L_i) of E shaped resonator [Fig.5.6(a)] varying from 4.4 mm to 13.3 mm are shown in Fig.5.26. In a fre-



(a) [0110 1101]



(b) [0110 1001]



(c) [0110 1000]

Fig. 5.23: Measured transmission characteristics of the E shaped multiresonator and its post processed signal for various bit combinations

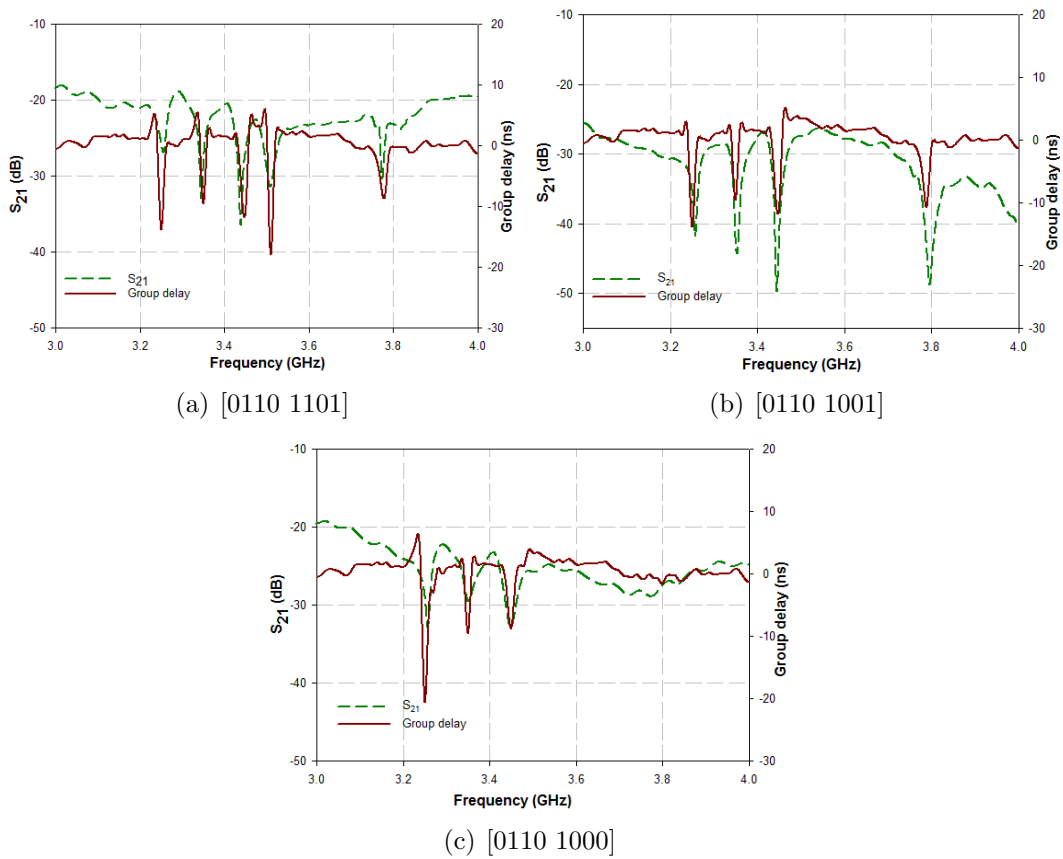


Fig. 5.24: Measured bistatic response of the RFID tag using E shaped multiresonator for different bit combinations

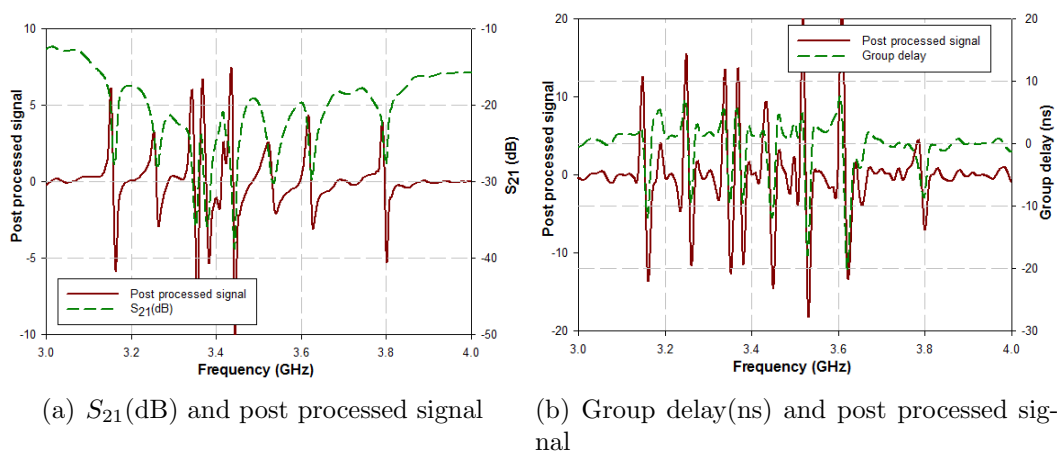
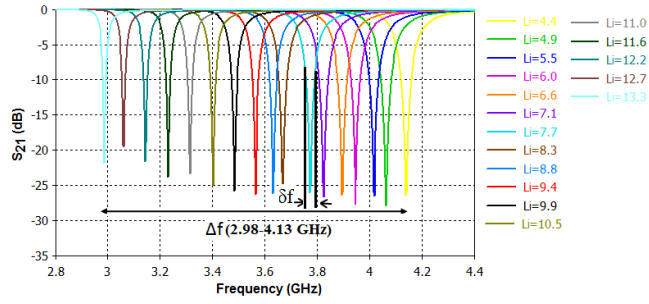
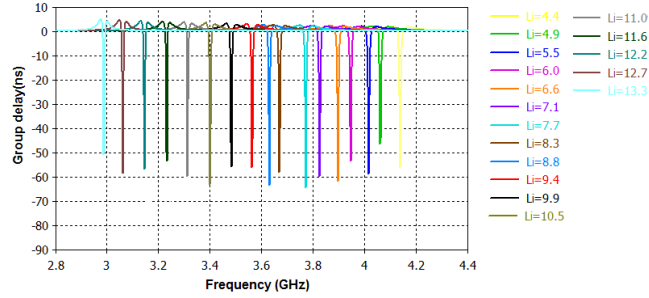


Fig. 5.25: Measured bistatic response of the the RFID tag using E shaped multiresonator and its post processed signal for the combination [1111 1111]



(a) S_{21}



(b) Group delay

Fig. 5.26: Simulated transmission characteristics of E shaped resonator shown in Fig.5.6(a) for various values of L_i (mm)

quency band (Δf) from 2.98 GHz to 4.13 GHz, 17 frequency bands are possible. δf is the frequency band for each resonator required to faithfully represent its resonant frequency, thus determining the frequency resolution. Table 5.4 shows a proposed method of code word allocation for the E shaped resonator. The code words are allotted for each frequency, corresponding to each length. The middle arm length (L_i) is limited to 13.3 mm to retain the E geometry. While absence or presence coding of a resonator can encode only two code words (0/1) using a single E shaped resonator, use of FSC allows an improvement to 17 code words. Three resonators with $L_i = 11$ mm, $L_i = 10.7$ mm and $L_i = 9.9$ mm corresponding to code words [01100], [01011] and [01001] respectively are fabricated to validate the simulation results. The measured resonator response and the bistatic response are shown in Fig.5.27. Fig.5.28 shows the photograph of the fabricated E shaped resonator.

Table 5.4: Proposed method of code word allocation for the single resonator

Sl.no	L_i (mm)	f (GHz)	Code word
1	4.4	4.13	00000
2	4.9	4.106	00001
3	5.5	4.01	00010
4	6.0	3.94	00011
5	6.6	3.89	00100
6	7.1	3.82	00101
7	7.7	3.76	00110
8	8.3	3.66	00111
9	8.8	3.62	01000
10	9.9	3.49	01001
11	10	3.42	01010
12	10.7	3.40	01011
13	11	3.31	01100
14	11.6	3.22	01101
15	12.2	3.14	01110
16	12.7	3.05	01111
17	13.3	2.98	10000

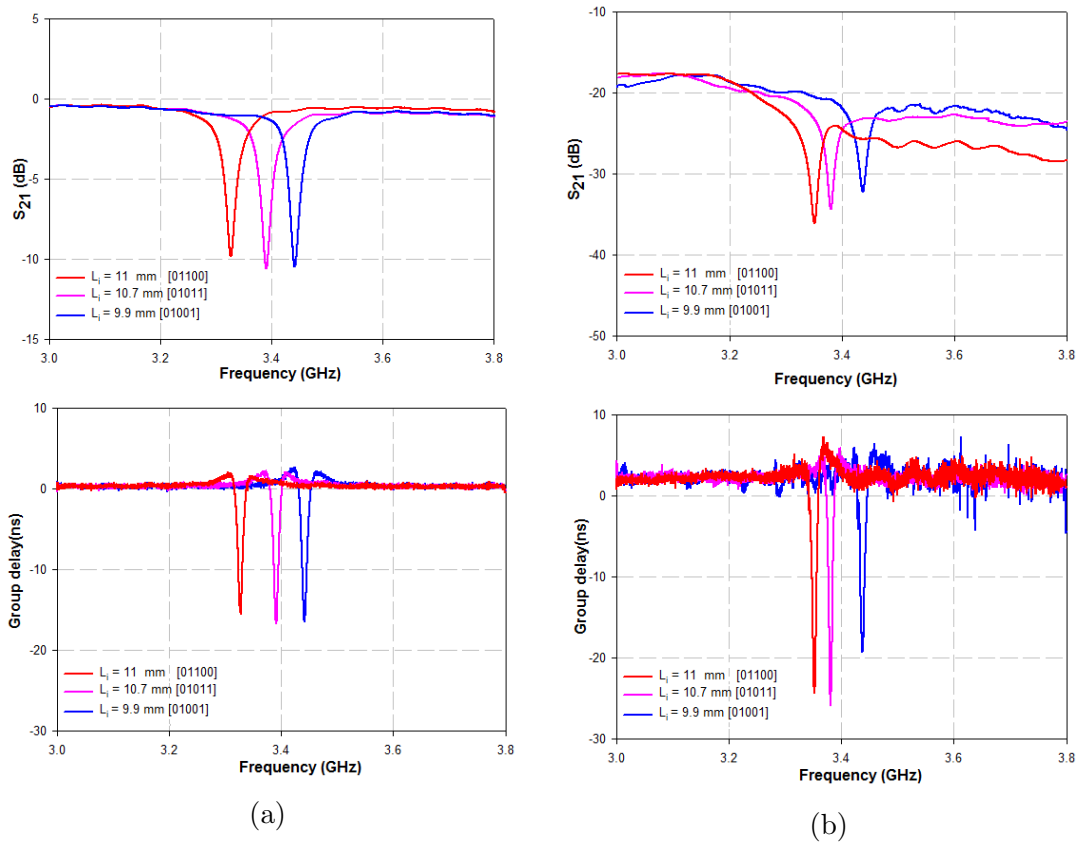


Fig. 5.27: Measured response of the tag with single E shaped resonator for three different configurations (a) Transmission characteristics of the resonator (b) Bistatic response

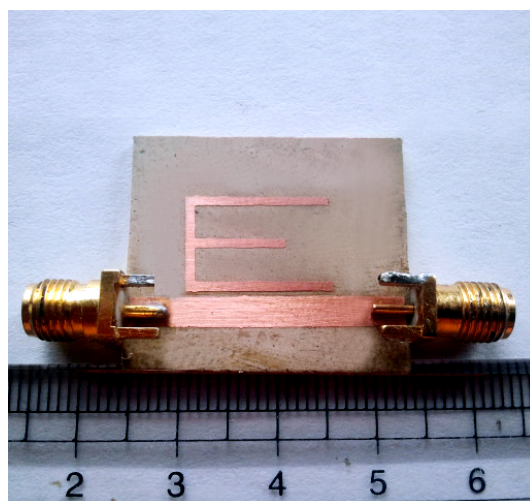


Fig. 5.28: Photograph of the fabricated E shaped resonator

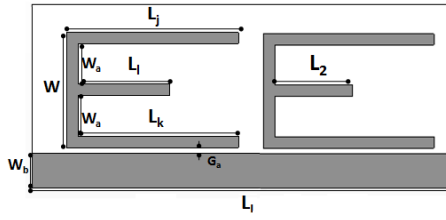


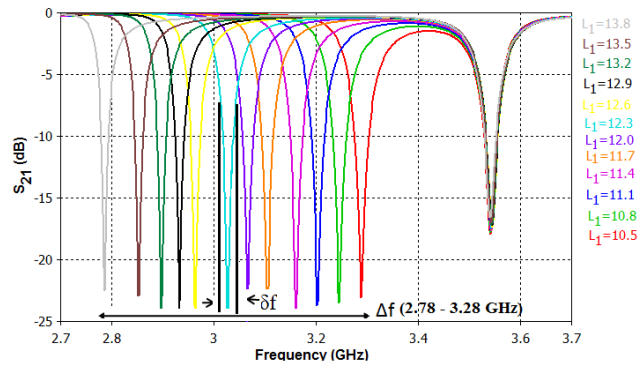
Fig. 5.29: Layout of multiresonator with two E shaped resonators $L_j = 15$, $L_k = 14$, $W = 10$, $L_l = 40$, $W_a = 3.5$, $G_a = 0.5$, $W_b = 3$ (All dimensions in mm), Substrate: loss tangent = 0.0018, $\epsilon_r = 4.3$, $h = 1.6$ mm

5.5.6 Frequency shift coding applied to multiresonator with two E shaped resonators

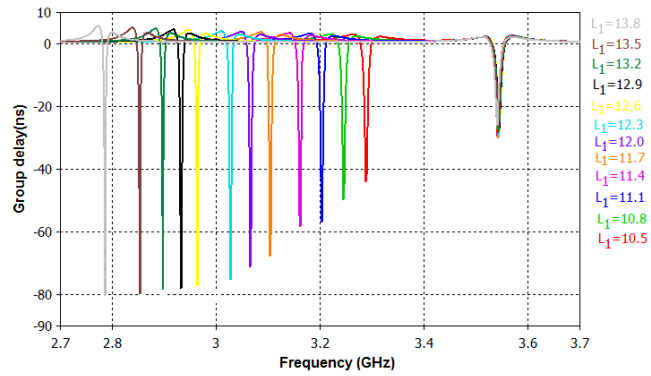
Fig.5.29 shows the layout of multiresonator with two E shaped resonators whose length (L_i) is individually varied for FSC. The frequency band (Δf) and resonant frequency(f) of each resonator are listed in Table 5.5. Variation of the middle arm length of the first resonator, keeping the dimensions of the second resonator constant, results in twelve different resonant frequencies as shown in Fig.5.30. Similarly, variation of the middle arm length of the second resonator, keeping the dimensions of the first resonator constant, results in twelve different resonant frequencies as shown in Fig.5.31. Further increase in the number of resonant frequencies is limited by the presence of higher harmonics. Unique identification code can be assigned to each combination of resonant frequencies. Since twelve different resonant frequencies are possible for each resonator, combining the two, 144 different codes ranging from [0000 0000] to [1000 1111] are possible with two resonators. The measured resonator response and the bistatic response of the multiresonator with two E shaped resonators for three different configurations by varying the length of middle arm of first E shaped resonator and second E shaped resonator are shown in Fig.5.32 and Fig.5.33 respectively. Fig.5.34 shows the photograph of fabricated multiresonator with two E shaped resonators.

Table 5.5: Frequency band (Δf) and resonant frequency (f) of multiresonator with two E shaped resonators (All values in GHz)

	Δf_1 (2.78 -3.28)	Δf_2 (3.3 - 3.85)
f_1	2.78	3.3
f_2	2.85	3.35
f_3	2.89	3.40
f_4	2.93	3.45
f_5	2.96	3.51
f_6	3.02	3.56
f_7	3.06	3.60
f_8	3.10	3.66
f_9	3.16	3.71
f_{10}	3.20	3.75
f_{11}	3.24	3.80
f_{12}	3.28	3.85

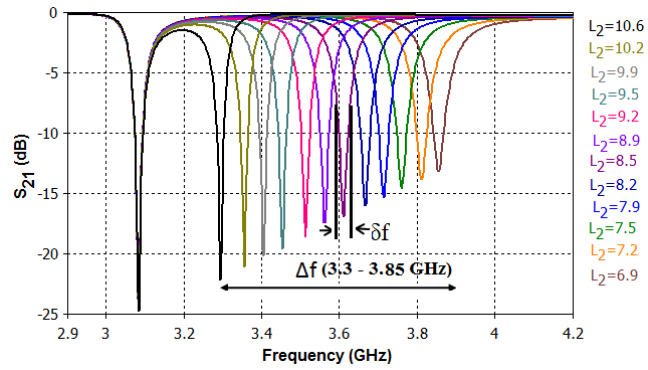


(a) S_{21}

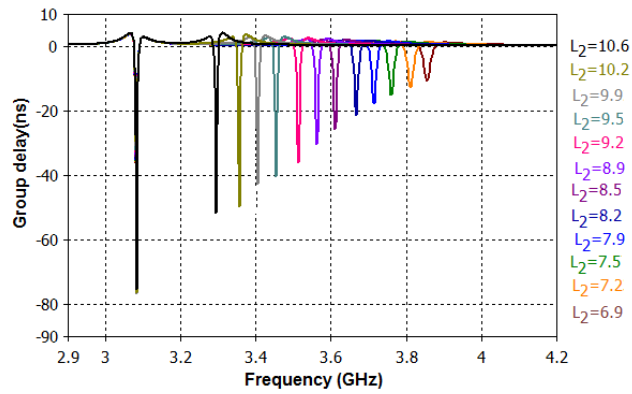


(b) Group delay

Fig. 5.30: Simulated transmission characteristics of tuning the first E shaped resonator in multiresonator with two E shaped resonators shown in Fig.5.29 ($L_2 = 9$ mm, L_1 in mm)



(a) S_{21}



(b) Group delay

Fig. 5.31: Simulated transmission characteristics of tuning the second E shaped resonator in multiresonator with two E shaped resonators shown in Fig.5.29 ($L_1 = 12$ mm, L_2 in mm)

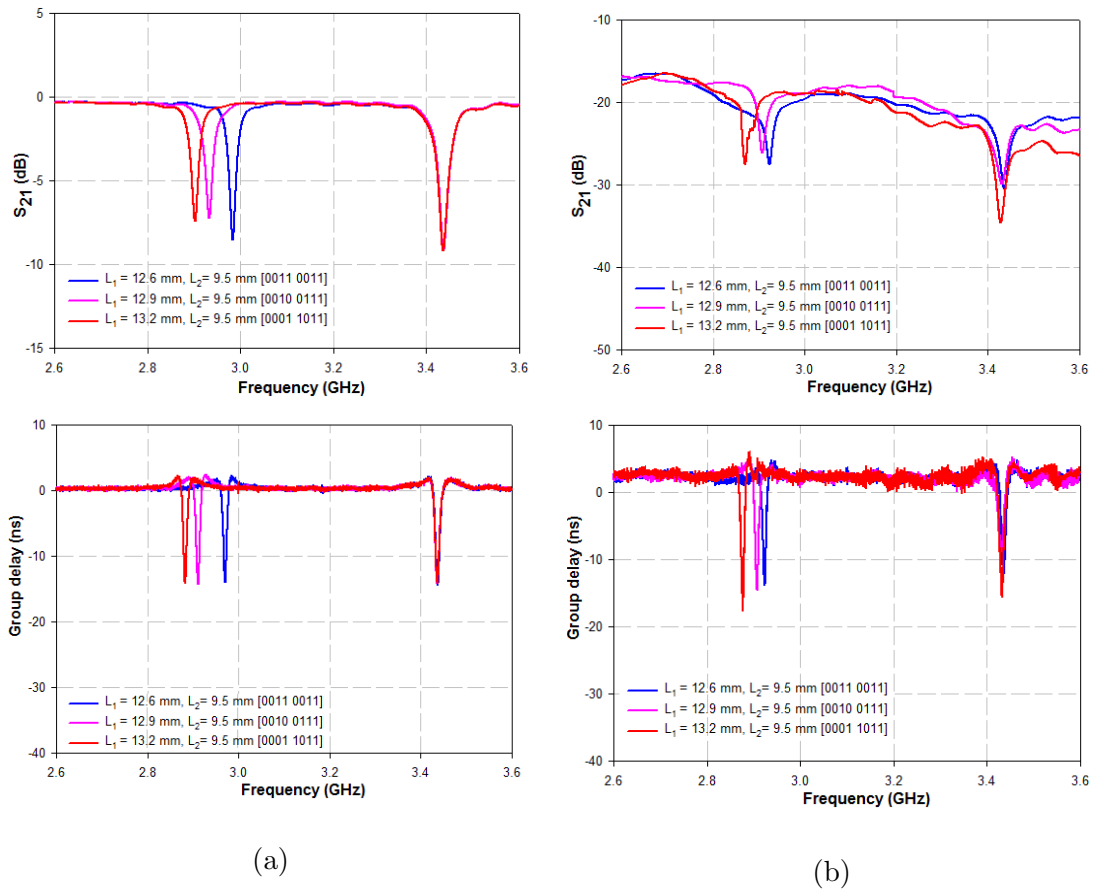


Fig. 5.32: Measured response of the multiresonator with two E shaped resonators for two different configurations by varying the length of middle arm of first E
 (a) Transmission characteristics of the resonator (b) Bistatic response

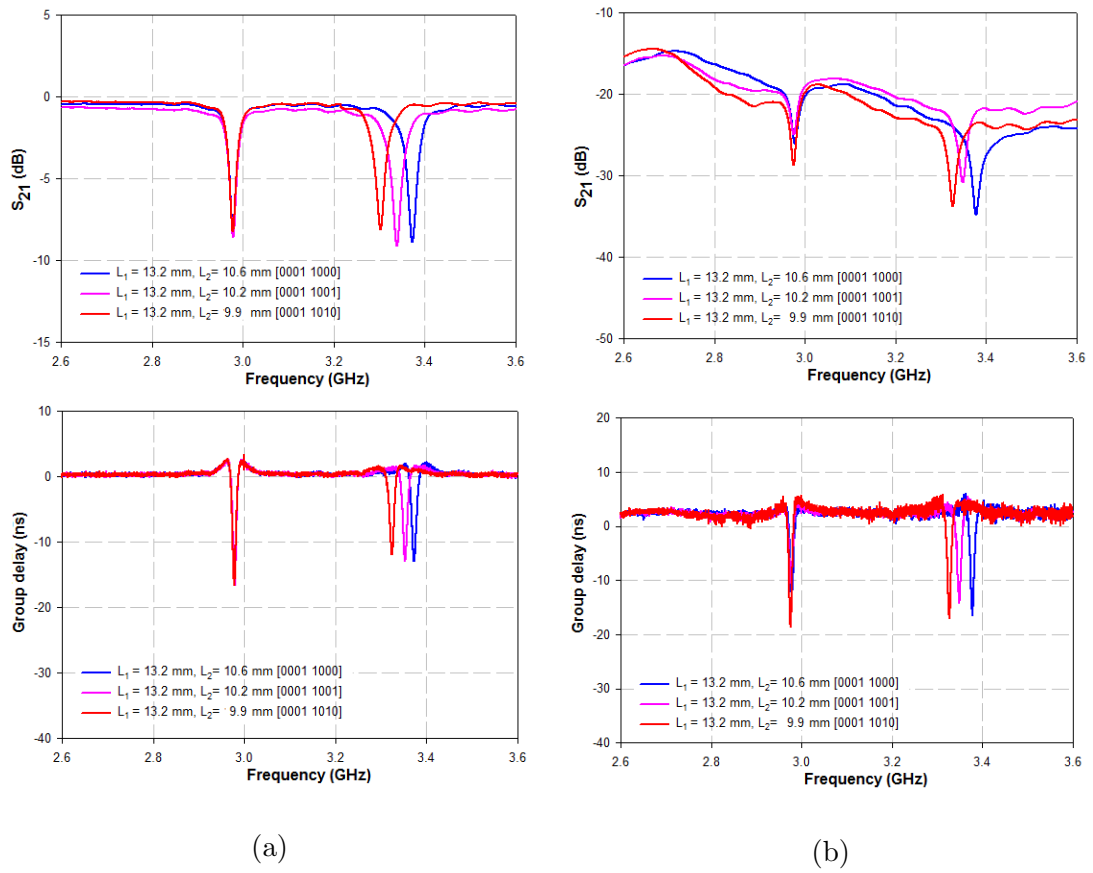


Fig. 5.33: Measured response of the multiresonator with two E shaped resonators for two different configurations by varying the length of middle arm of second E (a) Transmission characteristics of the resonator (b) Bistatic response

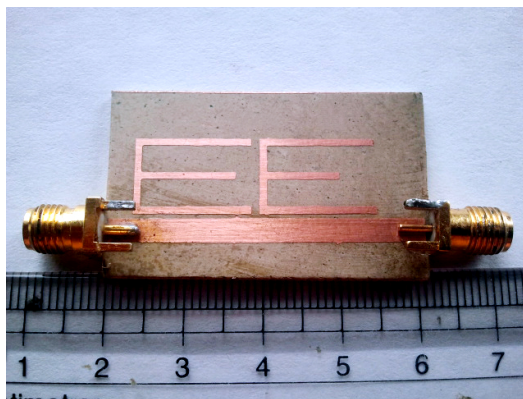


Fig. 5.34: Photograph of fabricated multiresonator with two E shaped resonators

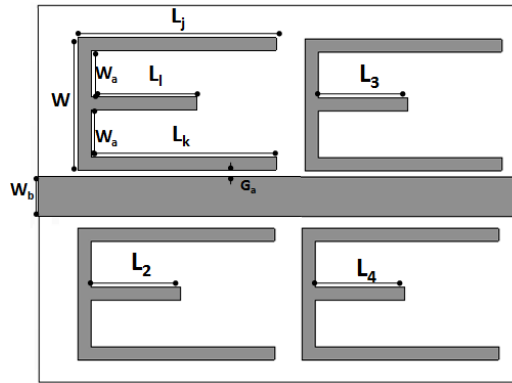


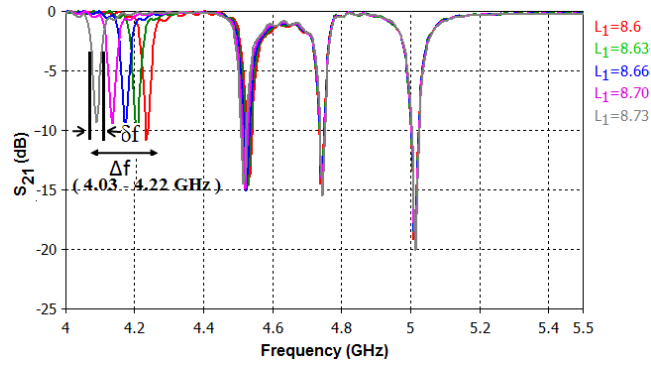
Fig. 5.35: Layout of multiresonator with four E shaped resonators $L_j = 15$, $L_k = 14$, $W = 10$, $L_l = 40$, $W_a = 3.5$, $G_a = 0.5$, $W_b = 3$ (All dimensions in mm), Substrate: loss tangent = 0.0018, $\epsilon_r = 4.3$, $h = 1.6$ mm

5.5.7 Frequency shift coding applied to multiresonator with four E shaped resonators

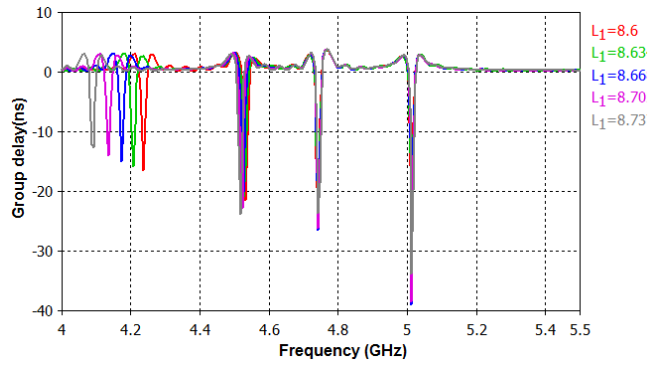
Fig.5.35 shows the layout of multiresonator with four E shaped resonators whose middle arm length (L_i) is individually varied for FSC. The frequency band (Δf) and resonant frequency (f) of each resonator is listed in Table 5.6. Variation of the length of one resonator, keeping the dimensions of other resonators constant, results in five different resonant frequencies. Fig.5.36 to Fig.5.39 show the results obtained by individually varying the length of each resonator. While varying the length of each resonator care must be taken that the resonance due to other resonators remain unaffected. In FSC for bit encoding, precautions must also be taken so that merging of resonant bands (Δf) does not occur and harmonics of the lower frequency resonators do not interfere with the resonance of higher frequency resonators. Unique identification code can be assigned to each combination of resonant frequencies. Since five different resonant frequencies are possible for each resonator, combining the four, 625 (5^4) different codes are possible with four resonators.

Table 5.6: Frequency band (Δf) and resonant frequency (f) of multiresonator with with four E shaped resonators (All values in GHz)

Resonator	Δf	f_1	f_2	f_3	f_4	f_5
1	4.03 - 4.2	4.03	4.07	4.10	4.14	4.2
2	4.31 - 4.49	4.31	4.37	4.39	4.44	4.49
3	4.59 - 4.80	4.59	4.64	4.70	4.75	4.80
4	5.13 - 5.32	5.13	5.20	5.24	5.28	5.32

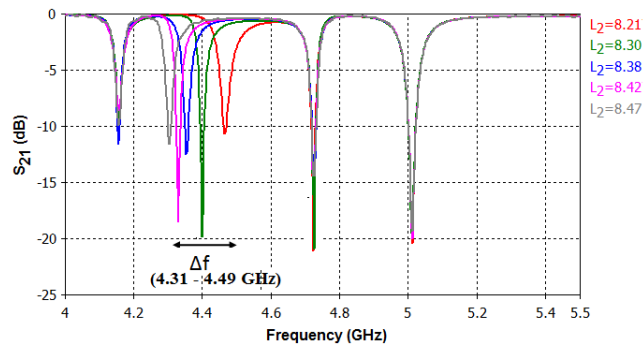


(a) S_{21}

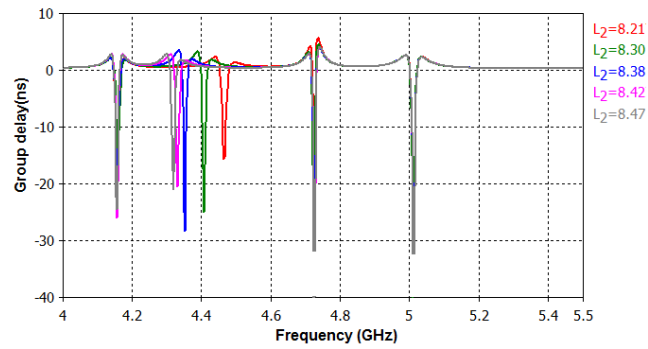


(b) Group delay

Fig. 5.36: Simulated transmission characteristics of tuning the first E shaped resonator in multiresonator with four E shaped resonators shown in Fig.5.35 ($L_2 = 8.2$ mm, $L_3 = 7.4$ mm, $L_4 = 6.5$ mm, L_1 in mm)

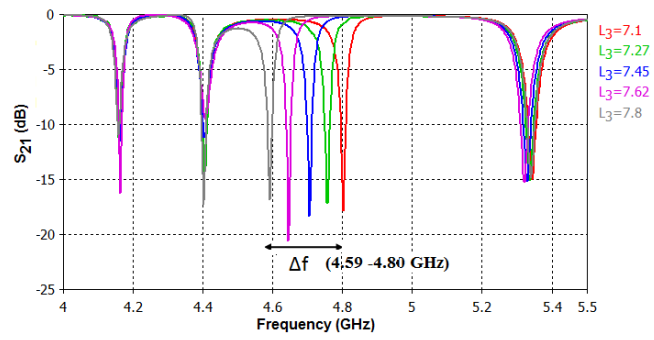


(a) S_{21}

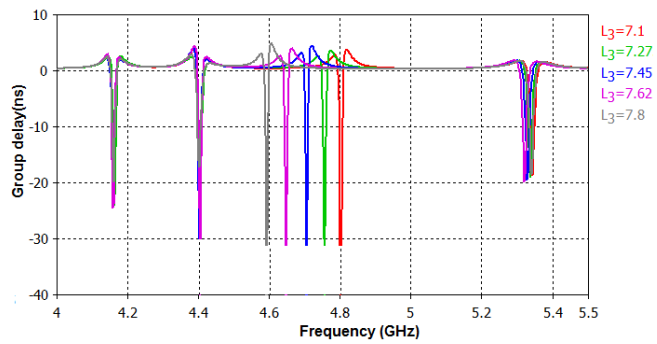


(b) Group delay

Fig. 5.37: Simulated transmission characteristics of tuning the second E shaped resonator in multiresonator with four E shaped resonators shown in Fig.5.35 ($L_1 = 8.66$ mm, $L_3 = 7.4$ mm, $L_4 = 6.5$ mm, L_2 in mm)

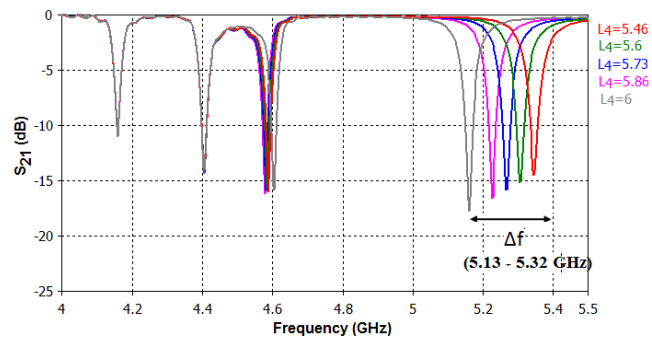


(a) S_{21}

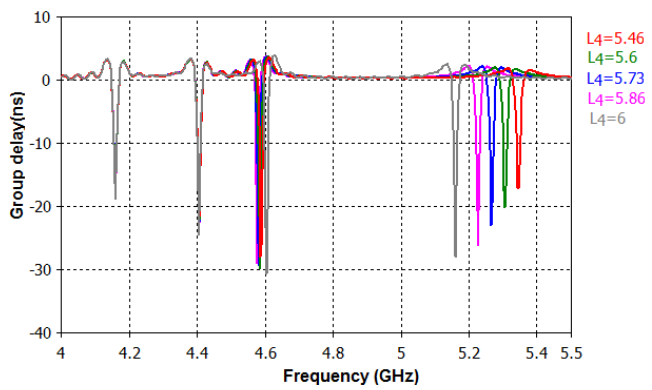


(b) Group delay

Fig. 5.38: Simulated transmission characteristics of tuning the third E shaped resonator in multiresonator with four E shaped resonators shown in Fig.5.35 ($L_1 = 8.66$ mm, $L_2 = 8.3$ mm, $L_4 = 5.4$ mm, L_3 in mm)



(a) S_{21}



(b) Group delay

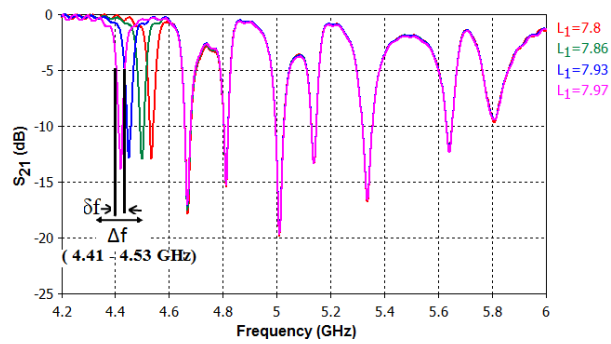
Fig. 5.39: Simulated transmission characteristics of tuning the fourth E shaped resonator in multiresonator with four E shaped resonators shown in Fig.5.35 ($L_1 = 8.66$ mm, $L_2 = 8.3$ mm, $L_3 = 7.4$ mm, L_4 in mm)

5.5.8 Frequency shift coding applied to multiresonator with eight E shaped resonators

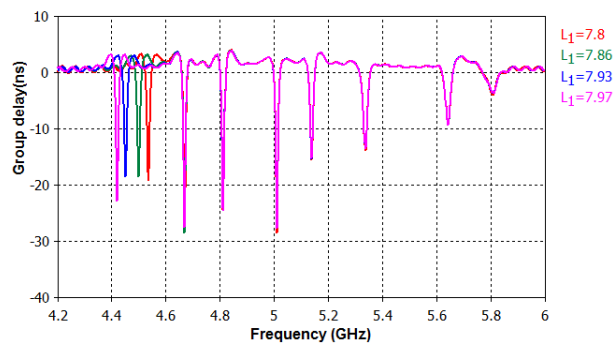
When the concept of FSC is applied to multiresonator with eight E shaped resonators, eight different frequency bands (Δf) occur as detailed in Table 5.7. Variation of the length of one resonator, keeping the dimensions of other resonators constant, results in four different resonant frequencies. Fig.5.40 to Fig.5.47 show the results obtained by individually varying the length of each resonator. Since four different resonant frequencies are exhibited each resonator, combining the eight, 65536 (4^8) different codes are possible with eight resonators. Fig.5.48 shows the measured resonator response and bistatic response for varying dimensions of the eighth resonator (L_8).

Table 5.7: Frequency band (Δf) and resonant frequency (f) of multiresonator with eight E shaped resonators (All values in GHz)

Resonator	Δf	f_1	f_2	f_3	f_4
1	4.41 - 4.53	4.41	4.44	4.49	4.53
2	4.59 - 4.71	4.59	4.63	4.66	4.71
3	4.75 - 4.85	4.75	4.91	4.96	4.85
4	4.87 - 4.97	4.87	4.91	4.94	4.97
5	5.04 - 5.15	5.04	5.07	5.1	5.15
6	5.22 - 5.36	5.22	5.27	5.30	5.36
7	5.49 - 5.61	5.49	5.10	5.55	5.61
8	5.70 - 5.91	5.69	5.76	5.85	5.91

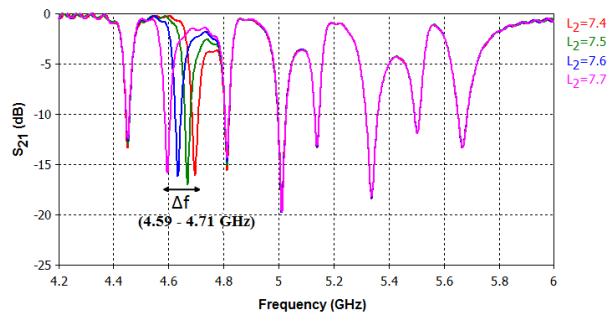


(a) S_{21}

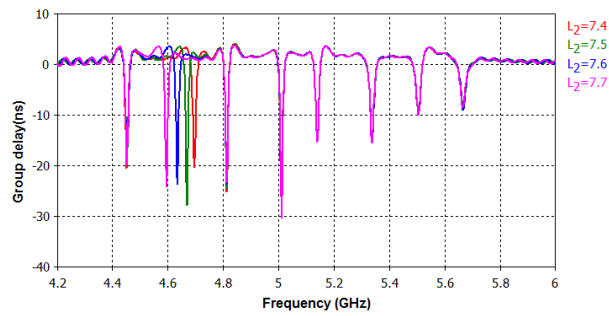


(b) Group delay

Fig. 5.40: Simulated transmission characteristics of tuning the first E shaped resonator in multiresonator with eight E shaped resonators shown in Fig.5.1 ($L_2 = 7.6$ mm, $L_3 = 6.9$ mm, $L_4 = 6.52$ mm, $L_5 = 6.1$ mm, $L_6 = 5.4$ mm, $L_7 = 5$ mm, $L_8 = 4.3$ mm, L_1 in mm)

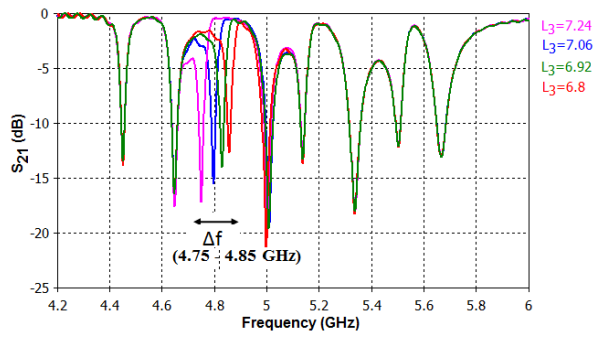


(a) S_{21} Magnitude

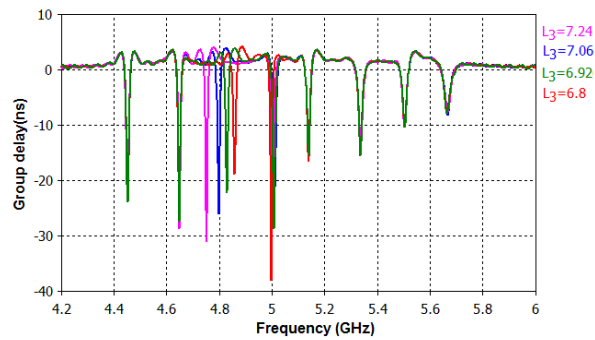


(b) Group delay

Fig. 5.41: Simulated transmission characteristics of tuning the second E shaped resonator in multiresonator with eight E shaped resonators shown in Fig.5.1 ($L_1 = 7.93$ mm, $L_3 = 6.9$ mm, $L_4 = 6.52$ mm, $L_5 = 6.1$ mm, $L_6 = 5.4$ mm, $L_7 = 5$ mm, $L_8 = 4.3$ mm, L_2 in mm)

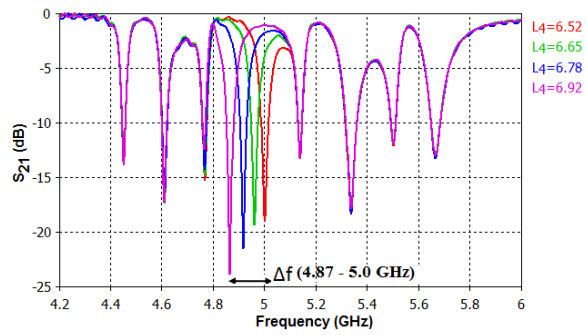


(a) S_{21}

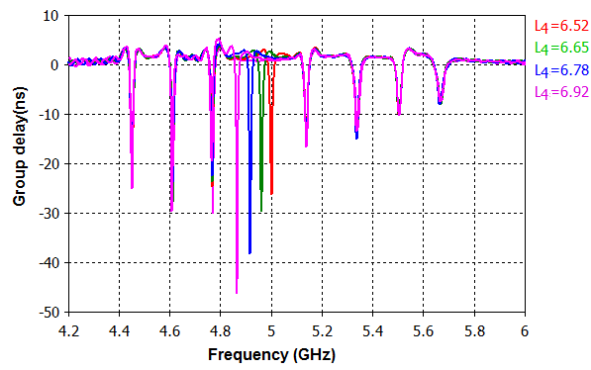


(b) Group delay

Fig. 5.42: Simulated transmission characteristics of tuning the third E shaped resonator in multiresonator with eight E shaped resonators shown in Fig.5.1 ($L_1 = 7.93$ mm, $L_2 = 7.6$ mm, $L_4 = 6.52$ mm, $L_5 = 6.1$ mm, $L_6 = 5.4$ mm, $L_7 = 5$ mm, $L_8 = 4.3$ mm, L_3 in mm)

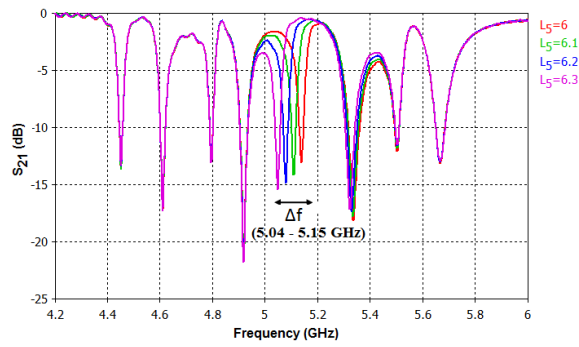


(a) S_{21}

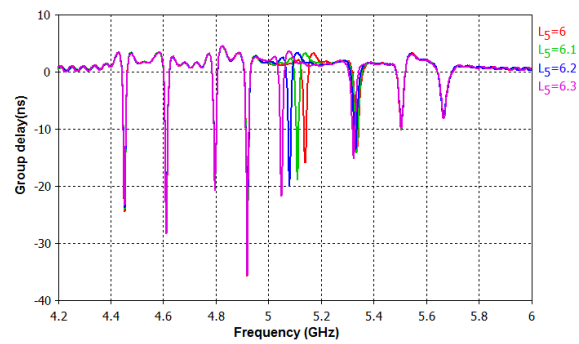


(b) Group delay

Fig. 5.43: Simulated transmission characteristics of tuning the fourth E shaped resonator in multiresonator with eight E shaped resonators shown in Fig.5.1 ($L_1 = 7.93$ mm, $L_2 = 7.6$ mm, $L_3 = 6.9$ mm, $L_5 = 6.1$ mm, $L_6 = 5.4$ mm, $L_7 = 5$ mm, $L_8 = 4.3$ mm, L_4 in mm)

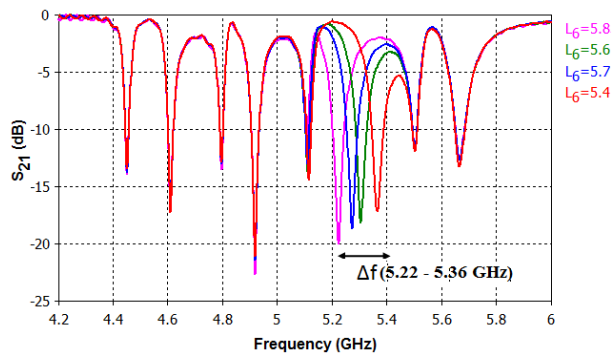


(a) S_{21}

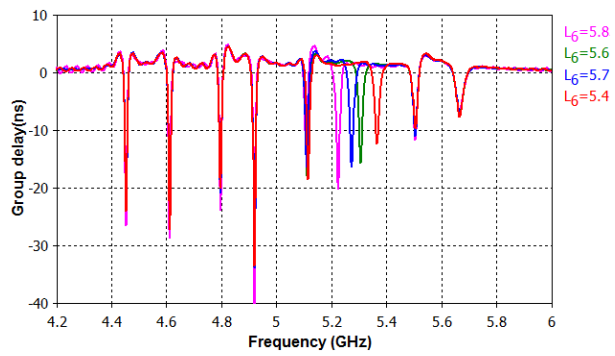


(b) Group delay

Fig. 5.44: Simulated transmission characteristics of tuning the fifth E shaped resonator in multiresonator with eight E shaped resonators shown in Fig.5.1 ($L_1 = 7.93$ mm, $L_2 = 7.6$ mm, $L_3 = 6.9$ mm, $L_4 = 6.52$ mm, $L_6 = 5.4$ mm, $L_7 = 5$ mm, $L_8 = 4.3$ mm, L_5 in mm)

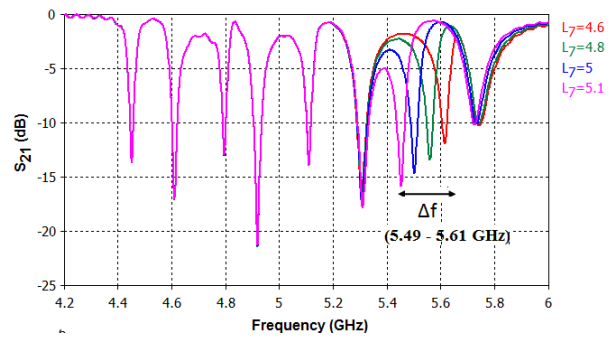


(a) S_{21}

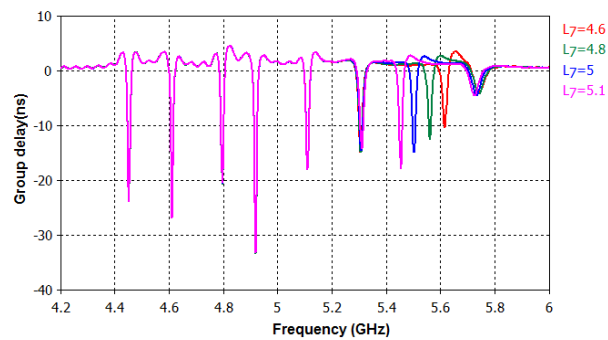


(b) Group delay

Fig. 5.45: Simulated transmission characteristics of tuning the sixth E shaped resonator in multiresonator with eight E shaped resonators shown in Fig.5.1 ($L_1 = 7.93$ mm, $L_2 = 7.6$ mm, $L_3 = 6.9$ mm, $L_4 = 6.52$ mm, $L_5 = 6.1$ mm, $L_7 = 5$ mm, $L_8 = 4.3$ mm, L_6 in mm)

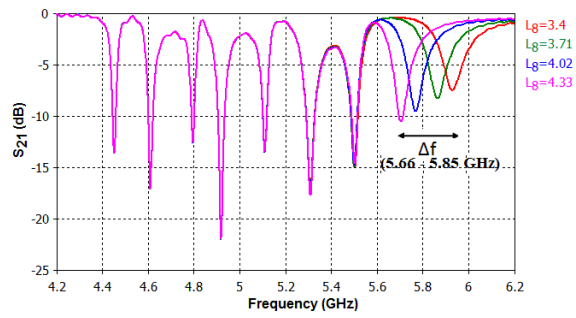


(a) S_{21}

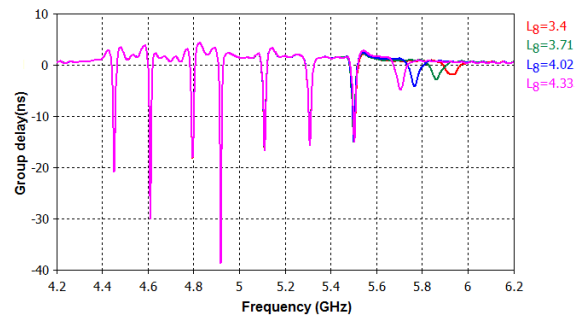


(b) Group delay

Fig. 5.46: Simulated transmission characteristics of tuning the seventh E shaped resonator in multiresonator with eight E shaped resonators shown in Fig.5.1 ($L_1 = 7.93$ mm, $L_2 = 7.6$ mm, $L_3 = 6.9$ mm, $L_4 = 6.52$ mm, $L_5 = 6.1$ mm, $L_6 = 5.4$ mm, $L_8 = 4.3$ mm, L_7 in mm)



(a) S_{21}



(b) Group delay

Fig. 5.47: Simulated transmission characteristics of tuning the eighth E shaped resonator in multiresonator with eight E shaped resonators shown in Fig.5.1 ($L_1 = 7.93$ mm, $L_2 = 7.6$ mm, $L_3 = 6.9$ mm, $L_4 = 6.52$ mm, $L_5 = 6.1$ mm, $L_6 = 5.4$ mm, $L_7 = 5$ mm, L_8 in mm)

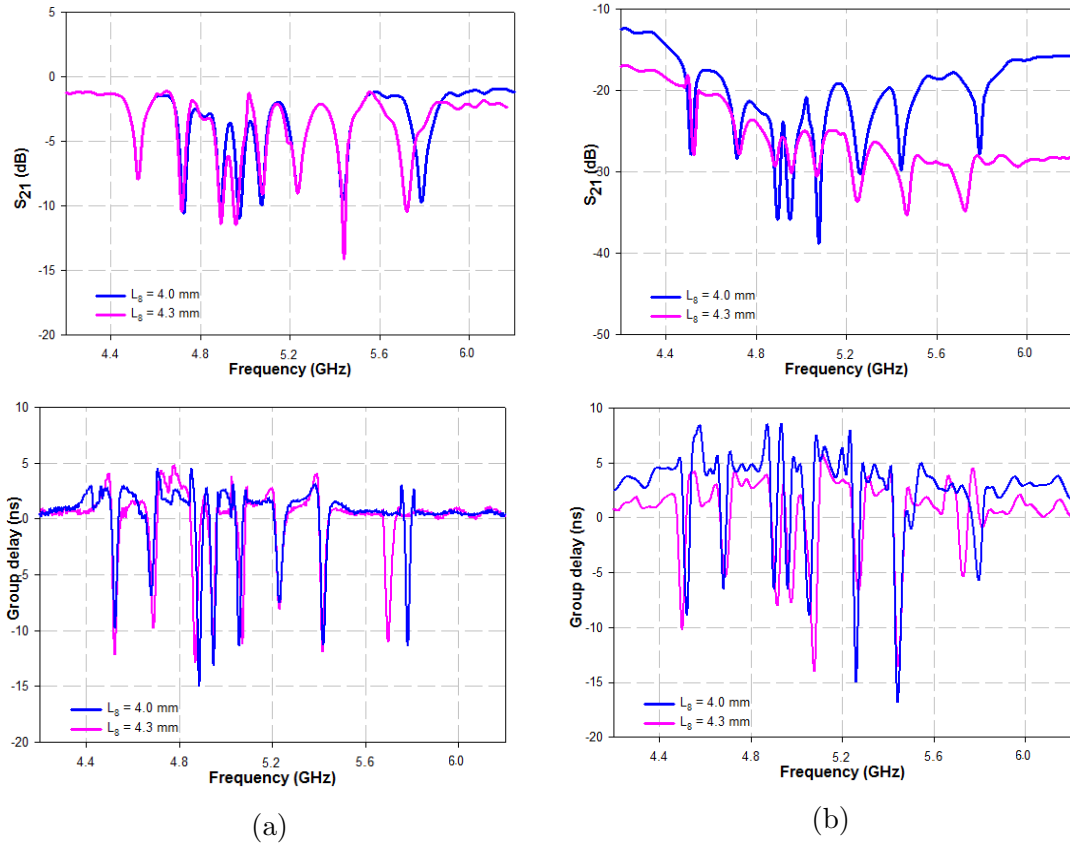


Fig. 5.48: Measured response of multiresonator with eight E shaped resonators for two different configurations ($L_1 = 7.86$ mm, $L_2 = 7.5$ mm, $L_3 = 6.8$ mm, $L_4 = 6.5$ mm, $L_5 = 6$ mm, $L_6 = 5.4$ mm, $L_7 = 5.1$ mm) (a) Transmission characteristics of the resonator (b) Bistatic response

All the above results reveal the design flexibility and high data encoding capacity of the proposed E shaped multiresonator for chipless RFID applications.

5.6 Chapter Summary

This chapter explains the implementation of chipless RFID tag using E-shaped multiresonator. The multiresonator consisting of eight E shaped resonators is developed by varying the length of the middle arm (L_i). The novelty of the resonator lies in its simplicity to generate different set of resonant frequencies by altering the values for L_i with all other parameters remaining the same. Equiv-

alent circuit model of the resonator is designed and validated with Agilent ADS. Design equation of the resonator is developed using multiple regression analysis. Orthogonally polarized circular monopole antennas are integrated to the multiresonator for range enhancement. The concept is validated using bistatic measurement for an eight bit prototype. The tag can encode data in magnitude and group delay. Various bit combinations for the absence or presence method of encoding the tag identity is generated, either by removing the corresponding E resonator or by decoupling the corresponding resonator from the transmission line. In this method, maximum bits that can be represented by an RFID tag is equal to the number of resonators. The bit coding capacity of the tag can be enhanced using FSC technique. It is found that using eight resonators, the number of code words in FSC increases to 65536 (4^8) compared to 256 (2^8) in the case of absence or presence method. Table 5.8 gives a comparison of the proposed chipless RFID tags with other reported tag designs. The comparison is done based on absence or presence coding technique. The proposed tag requires only less bandwidth (620 MHz) to encode 2^8 code words compared to other designs.

Table 5.8: Performance comparison of different chipless RFID tag

Parameters	(Zainud Deen <i>et al.</i> , 2013)	(Ashraf <i>et al.</i> , 2015)	(Preradovi <i>et al.</i> , 2008b)	(Nijas <i>et al.</i> , 2012)	Proposed tag
RFID operating band (GHz)	3.5 - 4.3	6.13 - 7.81	2 - 2.5	2.08 - 4.03	3.15 - 3.77
Bandwidth required	800 MHz	1.68 GHz	500 MHz	1.95 GHz	620 MHz
Bit states per resonator	2	2	2	2	2
Number of resonators	6	7	6	8	8
Number of code words	2^6	2^7	2^6	2^8	2^8
Bandwidth requirement for each bit (MHz)	< 100	< 100	< 50	< 100	< 80
Surface coding density (bits/cm ²)	0.12	0.818	0.35	0.533	0.452

5.7 Inferences

1. The proposed multiresonator represents 256 (2^8) bit combinations within a narrow band of 620 MHz using absence or presence coding technique.
2. Bit encoding capacity can be enhanced from 2^8 to 4^8 by using FSC technique. 4^8 bit combinations are represented within a frequency band of 1.5 GHz.
3. Different sets of resonant frequencies in 650 MHz band can be derived by choosing a different set of values for middle arm L_i ($i= 1$ to 8), with all other dimensions remaining the same. This feature provides the designer a greater advantage of designing variety of RFID tags with minimal layout modifications.

CHAPTER 6

CONCLUSION

6.1 Thesis highlights

The thesis focuses on the design and development of multiresonators with high data encoding capacity. The four novel multiresonator designs presented here use U slot, shorted stub, spurline and E shaped resonators. Detailed analysis is carried out on all the multiresonators presented. The thesis highlights are as follows.

- Design and analysis of four different types of multiresonators for chipless RFID tag applications.
- Implementation of two data encoding methods namely absence or presence coding technique and frequency shift coding technique.
- Development of equivalent circuit of resonators.
- Formulation of design equations using multiple regression analysis.
- Experimental validation of results in both the data encoding methods.

An introduction to RFID technology and its evolution is presented in Chapter 1. Motivation for the present work, methodology and the outline of the thesis is also discussed. Different types of multiresonators designed for chipless RFID tag application are explained in Chapter 2 to Chapter 5.

The U slot multiresonator consists of a 50Ω transmission line running on the top layer of the substrate CMET/LK 4.3 and six U slot resonators of varying dimensions etched on the bottom layer. Each resonator is excited when the slot dimension is equal to $\lambda_g/2$. Six resonators are designed to resonate in a band of 1.91 GHz ranging from 1.99 GHz to 3.9 GHz. 64 different code words can be generated using absence or presence coding technique. The number of code words increases to 729 using frequency shift coding technique.

The shorted stub multiresonator consists of eight half wavelength long stubs, connected to transmission line at one end and shorted to ground through via at the other end. Eight bits are encoded in a band of 1.81 GHz ranging from 1.93 GHz to 3.74 GHz. 256 different code words can be generated using absence or presence coding technique. The number of code words increases to 6561 using frequency shift coding technique.

The spurline multiresonator consists of eight spurlines of varying length engraved in a transmission line. Each resonator is excited at the resonant frequency corresponding to a length $\lambda_g/4$. Eight bits are encoded in a band of 1.8 GHz ranging from 2.39 GHz to 4.19 GHz. 256 different code words can be generated using absence or presence coding technique. The number of code words increases to 6561 using frequency shift coding technique.

The E shaped multiresonator consisting of eight E shaped resonators is developed by varying the length of the middle arm of each E shaped resonator. Eight bits are encoded in a narrow band of 620 MHz from 3.15 GHz to 3.77 GHz. 256 different code words can be generated using absence or presence coding technique. The number of code words increases to 65536 using frequency shift coding technique. Compared to other multiresonators, E shaped multiresonator has higher data encoding capacity.

The multiresonators discussed above can be used as RFID tags for access control applications where the tag is in close proximity of the reader. However, for increasing the read range, two cross polarized disc monopole antennas are integrated to the multiresonator. Bistatic measurements validate the functionality of the tag. The U slot multiresonator having relatively low data encoding capacity can be used for sensing applications. Shorted stub and spurline multiresonators with higher data encoding capacity can be used for conveyor belt applications. E shaped multiresonator can be used in asset tracking applications that demand a still higher data encoding capacity. Using FSC coding technique, all the proposed multiresonators can be used for the design of high security tags.

A comparison of the features of the designed multiresonators based on absence or presence coding technique and frequency shift coding technique is presented in Table 6.1 and Table 6.2 respectively. Dimensions of the multiresonators are expressed in wavelength corresponding to the center frequency of band of operation. The maximum read range obtained mentioned in Table 6.1 is for a transmitted power of 1 mW (0 dBm). However, read range can be increased by simply increasing the transmitted power.

6.2 Suggestions for future Work

The compactness of the tag is limited by the dimensions of transmitting and receiving antennas connected to it. So new RFID tags can be designed which can successfully operate without antennas. Further, new reading technique can be found so that the reader system is made simple. The feasibility of multiresonators fabricated on flexible substrates can be studied for applications such as wearable health monitoring tags for patients, monitoring of civil structures

Table 6.1: Comparison of proposed multiresonators based on absence or presence coding technique

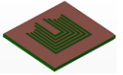
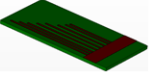
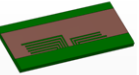
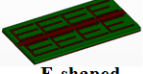
Proposed multiresonator configurations	Absence or presence coding						
	Band of operation (GHz)	Bandwidth required	Bandwidth requirement for each bit (MHz)	No of code words	Surface coding density (bits/cm ²)	Maximum read range (cm)	Dimensions of the multiresonator
 U slot multiresonator	1.99 – 3.9 GHz	1.91 GHz	< 100	64	0.55	25	0.39 λ x 0.27 λ
 Shorted stub multiresonator	1.93 – 3.74GHz	1.81GHz	< 100	256	0.416	30	0.31 λ x 0.57 λ
 Spurline multiresonator	2.39 – 4.19 GHz	1.8 GHz	< 100	256	0.987	25	0.49 λ x 0.19 λ
 E-shaped multiresonator	3.15 - 3.77 GHz	620 MHz	< 80	256	0.452	30	0.68 λ x 0.35 λ

Table 6.2: Comparison of proposed multiresonators based on frequency shift coding technique

Proposed multiresonator configurations	Frequency shift coding			
	Number of code words			
	One resonator	Two resonators	Four resonators	Eight resonators
U slot multiresonator	16	100	625	729 (Six resonators)
Shorted stub multiresonator	12	100	625	6561
Spurline multiresonator	16	144	625	6561
E shaped multiresonator	17	144	625	65536

etc. The use of nano-materials for printing RFID tags with sensors will find numerous real world applications. The suitability of materials like silicone based electrically conductive adhesives for RFID applications can also be explored.

APPENDIX A

CHIPLESS RFID TAG WITH INTEGRATED ANTENNAS

A.1 Introduction

This appendix describes the integration of two microstrip fed folded monopole antennas to the spurline resonator. Similar folded monopole antennas with optimized dimensions are used at the reader for transmission and reception purpose. The aim is to reduce the size of the tag and simplify the reader setup. The operating band of the antenna should cater to the resonant frequencies of the spurline resonators.

Spurline is a L shaped slot etched in a microstrip transmission line. The slot is quarter wavelength long at the resonant frequency. A detailed explanation of spurline resonator was presented in chapter 4. Microstrip fed folded monopole antennas (A_{t1} , A_{t2}) integrated to the tag act as transmit and receive antennas. Folded monopole antenna is chosen due to its simple structure and compactness (Suma *et al.*, 2006). Fig.A.1 shows the proposed chipless RFID tag with integrated folded monopole antenna. The dimension of the ground plane (lg_1 x Wg_1) is 11.7 mm X 23.4 mm.

Two microstrip fed folded monopole antennas with similar geometry and optimised dimensions (A_{r1} , A_{r2}) are used as reader antennas for transmission and reception purpose at the reader end. Fig.A.2 shows the proposed structure of the reader antenna.

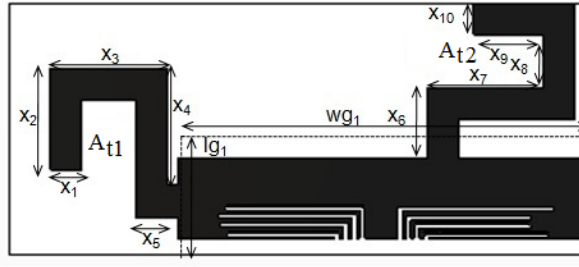


Fig. A.1: Chipless RFID tag with integrated folded monopole antenna [$x_1 = 3$, $x_2 = 9.6$, $x_3 = 11$, $x_4 = 11$, $x_5 = 4$, $x_6 = 6.6$, $x_7 = 11$, $x_8 = 5$, $x_9 = 6.6$, $x_{10} = 3$, $lg_1 = 11.7$ and $Wg_1 = 23.4$ (All dimensions in mm), Substrate: loss tangent = 0.003, $\epsilon_r = 3.7$, $h = 1.6$ mm]

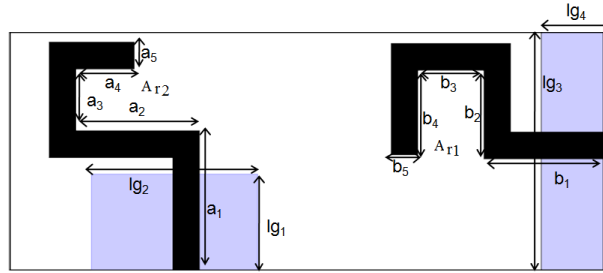
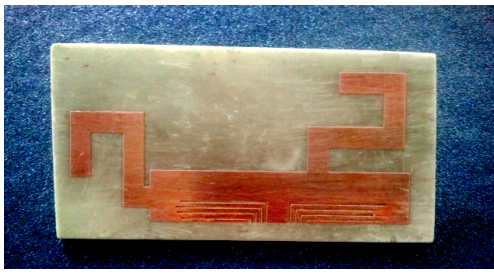


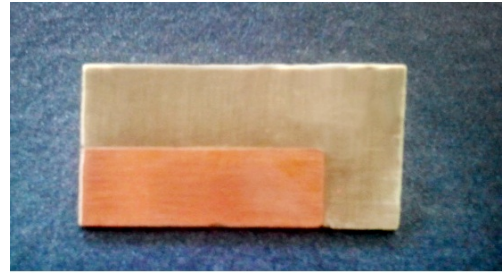
Fig. A.2: Proposed microstrip fed folded monopole reader antennas [$a_1 = 15.7$, $a_2 = 14$, $a_3 = 7$, $a_4 = 6.6$, $a_5 = 3$, $b_1 = 13.6$, $b_2 = 10$, $b_3 = 7.5$, $b_4 = 9.5$, $b_5 = 3$, $lg_1 = 10.8$, $lg_2 = 18.8$, $lg_3 = 26.8$, $lg_4 = 7$ (All dimensions in mm) Substrate: loss tangent = 0.02, $\epsilon_r = 4.3$, $h = 1.6$ mm]

A.2 Experimental results

Fig.A.3 shows the photographs of the top layer and the bottom layer of the proposed chipless RFID tag with integrated antennas. The photographs of the top layer and bottom layer of the reader antenna is shown in Fig.A.4 and the photograph of the measurement setup is shown in Fig.A.5. The tag is kept three cm away from the reader antenna. Measurements are carried out using PNA E8362B vector network analyser. Measured response of the RFID tag for the bit combinations [1111 1111] is shown in Fig.A.6(a). The resonant frequencies are 2.38 GHz, 2.5 GHz, 2.75 GHz, 2.98 GHz, 3.44 GHz, 3.79 GHz, 3.85 GHz and 4.04 GHz. Absence or presence coding technique is used to encode the tag identity. Various bit combinations can be generated either by removing the corresponding spurline or by simply shorting the spurline as explained in



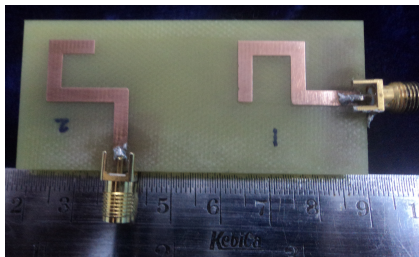
(a)



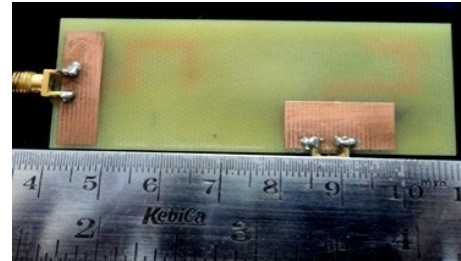
(b)

Fig. A.3: Chipless RFID tag with integrated antennas (a)Top layer (b)Bottom layer

Section 4.5.1. Measured response of the RFID tag for the bit combination [0111 1111] is shown in Fig.A.6(b).



(a)



(b)

Fig. A.4: Reader antenna (a) Top layer (b) Bottom layer

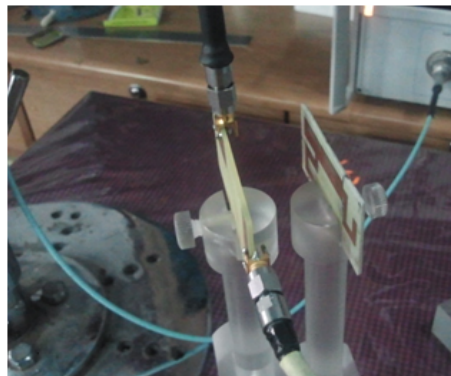


Fig. A.5: Measurement setup

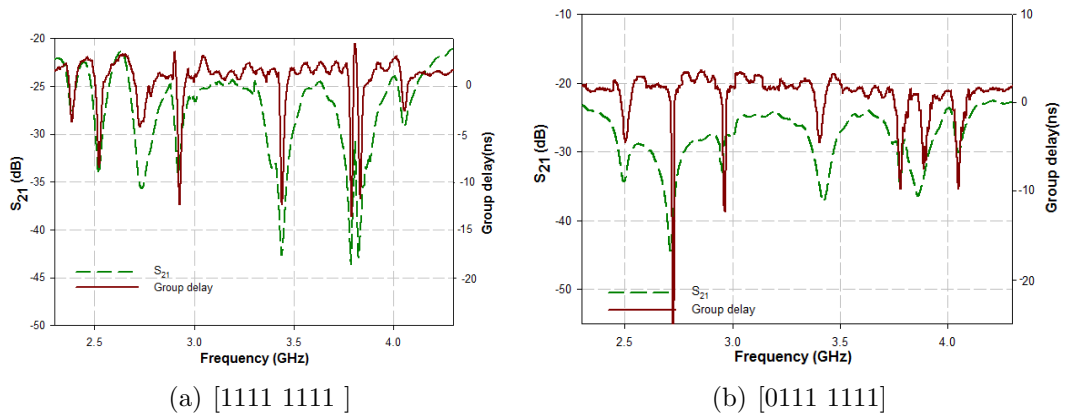


Fig. A.6: Measured response of the tag for different bit combinations

A.3 Inference

The aim of integrating folded monopole antenna is to design a compact RFID tag and to simplify the reader setup. However experimental studies reveal the limited read range with respect to the conventional bistatic setup.

APPENDIX B

CHIPLESS RFID TAG USING COPLANAR SPURLINE MULTIRESONATOR

B.1 Introduction

Chipless RFID tags discussed so far used microstrip resonators. This appendix presents the development of a six bit chipless RFID tag on coplanar waveguide(CPW). In a coplanar waveguide all conducting elements, including the ground planes, are on the same side of the dielectric substrate (Lin *et al.*, 2010). The aim is to develop a prototype suitable for circuit integration.

The multiresonator has evolved from a coplanar spurline resonator shown in Fig.B.1(a). The slot is quarter wavelength ($\lambda_g/4$) long at the resonant frequency. The spurline and the ground are etched on same side of the substrate. From the simulated transmission characteristics shown in Fig.B.1(b), it is clear that a band stop centered at 3.92 GHz is obtained.

A six bit coplanar spurline multiresonator is shown in Fig.B.2(a). The resonant frequency can be tuned by varying the length (L) of the spurline. Individual resonators operates at frequencies 2.35 GHz, 2.75 GHz, 3.30 GHz, 3.6 GHz, 3.9 GHz and 4.1 GHz. Fig.B.2(b) shows the simulated transmission characteristics of the multiresonator. Various bit combinations can be generated either by removing the corresponding spurline or by simply shorting the spurline as explained in Section 4.5.1.

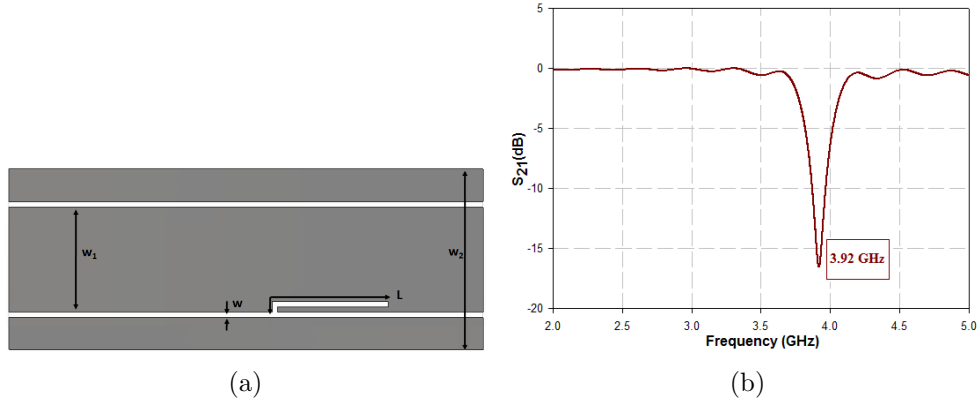


Fig. B.1: (a) Coplanar spurline resonator [$L = 12$, $W = 0.5$, $W_1 = 10.7$, $W_2 = 21.7$ (All dimensions in mm), Substrate: loss tangent = 0.0018, $\epsilon_r = 4.3$, $h = 1.6$ mm] (b) Simulated transmission characteristics of coplanar spurline resonator

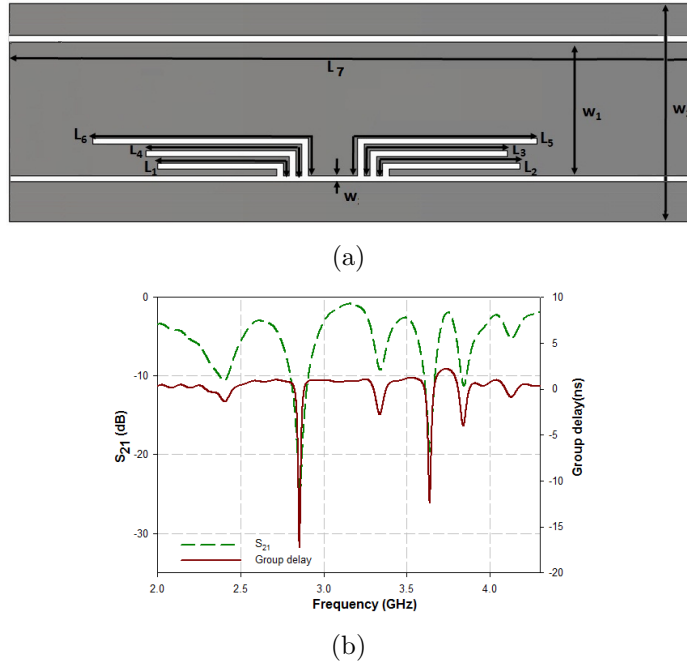


Fig. B.2: (a) Proposed six bit coplanar multiresonator [$W=0.5$, $W_1 = 10.7$, $W_2 = 21.7$, $L_1 = 11$, $L_2 = 12$, $L_3 = 13$, $L_4 = 14$, $L_5 = 18$, $L_6 = 21$, $L_7 = 45$ (All dimensions in mm), Substrate: loss tangent = 0.0018, $\epsilon_r = 4.3$, $h = 1.6$ mm] (b) Simulated transmission characteristics of multiresonator



Fig. B.3: Photograph of the fabricated multiresonator

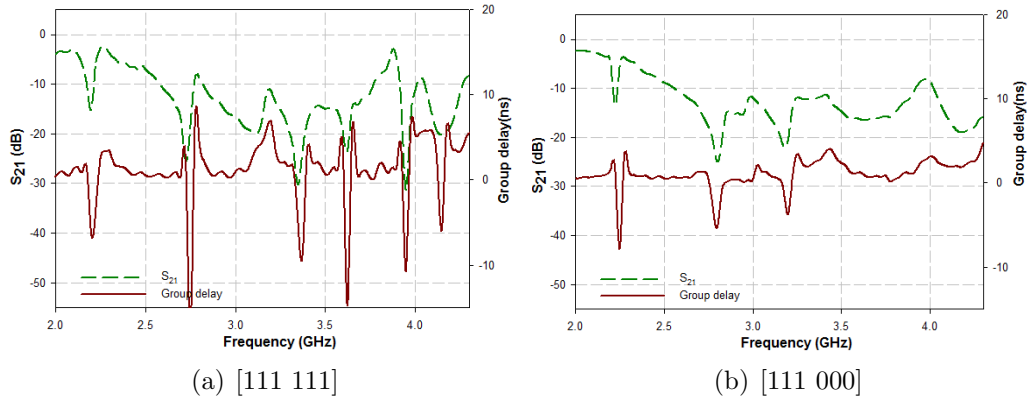


Fig. B.4: Measured transmission characteristics of the multiresonator for different bit combinations

B.2 Experimental results

Fig.B.3 shows the photograph of the fabricated multiresonator. Measurements are conducted using the PNA E8362B vector network analyser. Fig.B.4(a) and Fig.B.4(b) show the measured transmission characteristics for the bit combination [111 111] and [111 000]. The shift in resonant frequency may be due to the mutual coupling between the resonators.

Absence or presence coding technique discussed in Section 4.5.1 is used to generate various bit combinations. Bistatic measurement as explained in Section 4.4 is used to validate the tag. The tag is kept five cm away from horn antennas. Fig.B.5(a) and Fig.B.5(b) show the measured bistatic response for bit combinations [111 111] and [111 000].

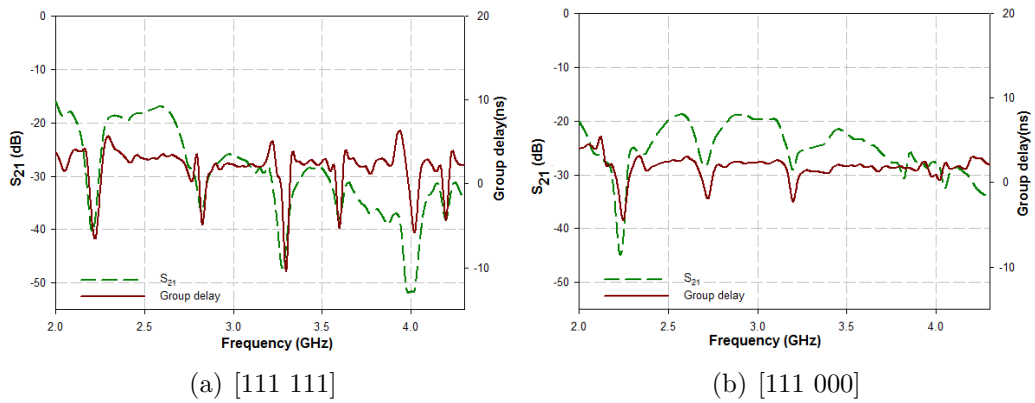


Fig. B.5: Measured bistatic response of the tag for different bit combinations

B.3 Inference

The aim of designing coplanar spurline is to design a RFID tag suitable for circuit integration. However experimental studies reveal the limited read range with respect to microstrip equivalent.

REFERENCES

1. **Amin, E. M., R. Bhattacharyya, S. Sarma, and N. C. Karmakar**, Chipless rfid tag for light sensing. *In IEEE Antennas and Propagation Society International Symposium (APSURSI), Memphis, USA.* 2014.
2. **Amin, E. M. and N. Karmakar**, Development of a chipless rfid temperature sensor using cascaded spiral resonators. *In IEEE SENSORS, Limerick.* 2011.
3. **Amin, E. M., N. Karmakar, and S. Preradovic**, Towards an intelligent em barcode. *In 7th International Conference on Electrical and Computer Engineering (ICECE), Bangladesh.* 2012.
4. **Amin, E. M. and N. C. Karmakar**, Development of a low cost printable humidity sensor for chipless rfid technology. *In IEEE International Conference on RFID-Technologies and Applications (RFID-TA), France.* 2012.
5. **Aruna, S., M. Nandi, and G. G. Vani** (2014). A preliminary study on rfid library management system. *Automation and Autonomous System*, **6**(3), 98–101.
6. **Ashraf, M. A., O. M. Haraz, M. R. AlShareef, H. M. Behairy, and S. Alshebeili**, Design of a chipless uwb rfid tag using cpw circular monopole antennas and multi-resonators. *In 2015 IEEE International Conference on Ubiquitous Wireless Broadband (ICUWB), Canada.* 2015.
7. **Balbin, I. and N. Karmakar**, Novel chipless rfid tag for conveyor belt tracking using multi-resonant dipole antenna. *In IEEE European Microwave Conference (EuMC), Europe.* 2009a.

8. **Balbin, I.** and **N. C. Karmakar** (2009*b*). Phase-encoded chipless rfid transponder for large-scale low-cost applications. *IEEE Microwave and Wireless Components Letters*, **19**(8), 509–511.
9. **Bates, R.** (1977). Design of microstrip spur-line band-stop filters. *IEE Journal on Microwaves, Optics and Acoustics*, **1**(6), 209–214.
10. **Bhuiyan, M. S., A. Azad,** and **N. Karmakar**, Dual-band modified complementary split ring resonator (mcsrr) based multi-resonator circuit for chipless rfid tag. In *IEEE Eighth International Conference on Intelligent Sensors, Sensor Networks and Information Processing, Australia*. 2013.
11. **Bindu, C. J.** (2015). *Design and development of compact planar filters for ultrawide band applications*. Ph.D. thesis, Cochin University of Science and Technology.
12. **Bolic, M., M. Rostamian,** and **P. M. Djuric** (2015). Proximity detection with rfid: A step toward the internet of things. *IEEE Pervasive Computing*, **14**(2), 70–76.
13. **Borriello, G.** (2005). Rfid: Tagging the world. *Communications of the ACM*, **48**(9), 34–37.
14. **Bowden, L.** (1985). The story of iff (identification friend or foe). *IEE Proceedings A-Physical Science, Measurement and Instrumentation, Management and Education-Reviews*, **132**(6), 435–437.
15. **Butters, A. et al.** (2006). Radio frequency identification: An introduction for library professionals. *Australasian Public Libraries and Information Services*, **19**(4), 164.

16. **Casula, P. M., Giovanni Andrea** (2014). A narrowband chipless multiresonator tag for uhf rfid. *Journal of Electromagnetic Waves and Applications*, **28**(2), 214–227.
17. **Chakraborty, G.**, Keynote lecture: A novel paradigm of chipless rfid using metal patches. *In International Conference on Communication and Industrial Application (ICCIA), Kolkata*. 2011.
18. **Chamarti, A. and K. Varahramyan** (2006). Transmission delay line based id generation circuit for rfid applications. *IEEE Microwave and Wireless Components Letters*, **16**(11), 588–590.
19. **Chen, Y. Y., T. T. Wu, and K. T. Chang**, P5h-3 a com analysis of saw tags operating at harmonic frequencies. *In IEEE Ultrasonics Symposium, Newyork*. 2007.
20. **Cho, H. and Y. Baek**, Design and implementation of an active rfid system platform. *In IEEE International Symposium on Applications and the Internet Workshops (SAINTW'06), Arizona, USA*. 2006.
21. **Cho, S. i. and N. Y. Kim** (2011). A novel spiral meander spurline resonator and its implementation to a low-phase noise oscillator. *Microwave and Optical Technology Letters*, **53**(10), 2258–2262.
22. **Chongcheawchamnan, R.** (2011). Miniaturisation and electronic tuning techniques for microstrip spurline filters. *IET Microwaves, Antennas and Propagation*, **5**(1), 1–9.
23. **Chuang, M. L. and W. H. Shaw** (2007). Rfid: integration stages in supply chain management. *IEEE Engineering Management Review*, **35**(2), 80–87.
24. **Cisco** (May 2008). Wi-fi location-based services 4.1 design guide.

25. **Costa, F., S. Genovesi, and A. Monorchio** (2013). A chipless rfid based on multiresonant high-impedance surfaces. *IEEE Transactions on Microwave Theory and Techniques*, **61**(1), 146–153.
26. **CST** (2009). Users manual. cst - microwave studio.
27. **Dey, S., P. Kalansuriya, and N. C. Karmakar**, Chipless rfid based high resolution crack sensing through swb technology. *In IEEE International Microwave and RF Conference (IMaRC), Bangalore*. 2014.
28. **Elena de la, V. M. P., Elena Lozano** (2013). Interacting with objects in games through rfid technology. *Radio Frequency Identification from System to Applications*, 326 – 340.
29. **Finkenzeller** (2003). Rfid handbook: Fundamentals and applications in contactless smart cards and identification.
30. **Finkenzeller, K.**, *RFID Handbook: Radio-frequency identification fundamentals and applications*. Wiley, 1999.
31. **Fisher, J. A. and T. Monahan** (2008). Tracking the social dimensions of rfid systems in hospitals. *International Journal of Medical Informatics*, **77**(3), 176–183.
32. **Girbau, D., J. Lorenzo, A. Lazaro, C. Ferrater, and Villarino** (2012a). Frequency-coded chipless rfid tag based on dual-band resonators. *IEEE Antennas and Wireless Propagation Letters*, **11**, 126–128.
33. **Girbau, D., A. Ramos, Lazaro, S. Rima, and Villarino** (2012b). Passive wireless temperature sensor based on time-coded uwb chipless rfid tags. *IEEE Transactions on Microwave Theory and Techniques*, **60**(11), 3623–3632.

34. **Gupta, S.** and **L. J. Jiang**, Chipless rfid tags based on multiple band-rejected planar log-periodic antennas. *In IEEE Antennas and Propagation Society International Symposium (APSURSI), Orlando.* 2013.
35. **Han, T., H. Wang,** and **S. Yongan** (2008). Reflection and scattering characteristics of reflectors in saw tags. *IEEE Transactions on Ultrasonics, Ferroelectrics, and Frequency Control*, **55**(6), 1387–1390.
36. **Harma, S., W. G. Arthur, C. S. Hartmann, R. G. Maev,** and **V. P. Plessky** (2008). Inline saw rfid tag using time position and phase encoding. *IEEE Transactions on Ultrasonics, Ferroelectrics, and Frequency Control*, **55**(8), 1840–1846.
37. **Harma, S., V. Plessky, C. Hartmann,** and **W. Steichen**, Saw rfid tag with reduced size. *In 2006 IEEE Ultrasonics Symposium, Vancouver, Canada.* 2006.
38. **Hartmann, C. S.**, A global saw id tag with large data capacity. *In IEEE Ultrasonics Symposium, Munich, Germany.* 2002.
39. **Herrojo, C., J. Naqui, F. Paredes,** and **F. Martyn**, Spectral signature barcodes implemented by multi-state multi-resonator circuits for chipless rfid tags. *In IEEE MTT-S International Microwave Symposium (IMS), California.* 2016.
40. **Jalaly, I.** and **I. Robertson**, Capacitively tuned split microstrip resonators for RFID barcodes, Paris. 2005a.
41. **Jalaly, I.** and **I. Robertson**, Rf barcodes using multiple frequency bands. *In IEEE MTT-S International Microwave Symposium Digest.* 2005b.

42. **Jalil, K. A. D., Rahim**, Chipless rfid tag based on meandered line resonator. *In IEEE Asia-Pacific Conference on Applied Electromagnetics (APACE), Malaysia*. 2014.
43. **Jalil, M., N. A. Samsuri, M. K. A. Rahim, and R. Dewan**, Compact chipless rfid metamaterial based structure using textile material. *In International Symposium on Antennas and Propagation (ISAP), Australia*. 2015.
44. **Jang, H. S., W. G. Lim, K. S. Oh, S. M. Moon, and J. W. Yu** (2010). Design of low-cost chipless system using printable chipless tag with electromagnetic code. *IEEE Microwave and Wireless Components Letters*, **20**(11), 640–642.
45. **Jones, E. C., S. Gupta, et al.** (2015). Hospital supply chain management by implementing rfid. *International Journal of Supply Chain Management*, **4**(3), 1–6.
46. **Kalansuriya, P., R. Bhattacharyya, S. Sarma, and N. Karmakar**, Towards chipless rfid-based sensing for pervasive surface crack detection. *In IEEE International Conference on RFID-Technologies and Applications (RFID-TA), France*. 2012.
47. **Kim, T., U. Kim, J. Kwon, and J. Choi**, Design of a novel chipless rfid tag using a simple bandstop resonator. *In IEEE Asia-Pacific Microwave Conference Proceedings (APMC), Japan*. 2010.
48. **Klaus, F.** (2003). Rfid handbook. *Jone Willey & Sons*, 61–110.
49. **Konkel, M., V. Leung, B. Ullmer, and C. Hu** (2004). Tagaboo: a collaborative childrens game based upon wearable rfid technology. *Personal and Ubiquitous Computing*, **8**(5), 382–384.

50. **Kumar, A.** and **A. Verma**, Control of stop band using spur line resonators of dgs based low pass filter. *In IEEE Students' Technology Symposium (TechSym), Kharagpur.* 2011.
51. **Landt, J.** (2005). The history of rfid. *IEEE Potentials*, **24**(4), 8–11.
52. **Le, T., R. A. Bahr, M. M. Tentzeris, B. Song,** and **C. P. Wong**, A novel chipless rfid-based stretchable and wearable hand gesture sensor. *In European Microwave Conference (EuMC), Paris.* 2015.
53. **Lee, S. J., J. Lim, D. Ahn,** and **S. M. Han**, Flexible microwave chipless tag system based on dgs resonators. *In IEEE 14th Annual Wireless and Microwave Technology Conference (WAMICON), Florida.* 2013.
54. **Lehpamer, H.,** *RFID design principles.* Artech House, 2012.
55. **Lin, H. J., X. Q. Chen, X. W. Shi, L. Chen,** and **Y. F. Bai**, A wide stopband cpw low pass filter using quarter wavelength stepped impedance resonators. *In International Conference on Microwave and Millimeter Wave Technology (ICMMT), China.* 2010.
56. **Liu, H., L. Sun,** and **Z. Shi** (2007). Dual-bandgap characteristics of spurline filters and its circuit modeling. *Microwave and Optical Technology Letters*, **49**(11), 2805–2807.
57. **Liu, H., Z. Zhang, S. Wang, J. Wan, Y. Jiang,** and **L. Zhu**, Transmission characteristic control of dual-mode filter using spurline technique. *In IEEE International Conference on Microwave and Millimeter Wave Technology (ICMMT), Chengdu, China.* 2010.
58. **Liu, H. W., Z. Shi, A. Boutejdar, R. H. Knoechel,** and **K. F. Schuene-mann** (2008). Harmonics suppression of wilkinson power divider using spurlines

- with adjustable rejection bands. *Microwave and Optical Technology Letters*, **50**(3), 601–604.
59. **Liu, J.** and **J. Yao** (2008). Wireless rf identification system based on saw. *IEEE Transactions on Industrial Electronics*, **55**(2), 958–961.
 60. **Liu, Y., H. Zheng,** and **C. Sun**, A tunable compact bandstop filter using meander spurline and folding open stubs. *In 2nd International Conference on Consumer Electronics, Communications and Networks (CECNet), China.* 2012.
 61. **Mahajan, K. D., P. Pandey,** and **B. K. Pandher**, Application of rfid technology in libraries and role of librarian. *In 12th MANLIBNET Convention, Jaipur.* 2010.
 62. **Malherbe, J.** (1979). Microwave transmission line filters. *Dedham, Mass., Artech House.*
 63. **McVay, J., A. Hoorfar,** and **N. Engheta**, Space-filling curve rfid tags. *In IEEE Radio and Wireless Symposium, Sandiego.* 2006.
 64. **Moscato, S., R. Moro, M. Bozzi, L. Perregrini, S. Sakouhi, F. Dhawadi, A. Gharsallah, P. Savazzi, A. Vizziello,** and **P. Gamba**, Chipless rfid for space applications. *In IEEE International Conference on Wireless for Space and Extreme Environments (WiSEE), Netherland.* 2014.
 65. **Mukherjee, S.**, Chipless radio frequency identification by remote measurement of complex impedance. *In IEEE European Conference on Wireless Technologies, Paris.* 2007.
 66. **Mun, I. K., A. B. Kantrowitz, P. W. Carmel, K. P. Mason,** and **D. W. Engels**, Active rfid system augmented with 2d barcode for asset management

- in a hospital setting. *In IEEE International Conference on RFID, Texas, USA.* 2007.
67. **Nair, R., E. Perret, and S. Tedjini**, Chipless rfid based on group delay encoding. *In IEEE International Conference on RFID-Technologies and Applications (RFID-TA), Spain.* 2011.
 68. **Nair Sreejith, M., V. Shameena, M. Nijas, and P. Mohanan** (2012). Novel chipless rf identification technology for on-touch data transfer applications. *Microwave and Optical Technology Letters*, **54**(10), 2325–2327.
 69. **Narkcharoen, P. and S. Pranonsatit**, The applications of fill until full (fuf) for multiresonator-based chipless rfid system. *In 8th International Conference on Electrical Engineering/Electronics, Computer, Telecommunications and Information Technology (ECTI-CON), Thailand.* 2011.
 70. **Nguyen, C., Cam**, Millimeter wave printed circuit spurline filters. *In IEEE MTT-S International Microwave Symposium Digest, Boston.* 1983.
 71. **Nijas, C., U. Deepak, P. Vinesh, R. Sujith, S. Mridula, K. Vasudevan, and P. Mohanan** (2014). Low-cost multiple-bit encoded chipless rfid tag using stepped impedance resonator. *IEEE Transactions on Antennas and Propagation*, **62**(9), 4762–4770.
 72. **Nijas, C., R. Dinesh, U. Deepak, A. Rasheed, S. Mridula, K. Vasudevan, and P. Mohanan** (2012). Chipless rfid tag using multiple microstrip open stub resonators. *IEEE Transactions on Antennas and Propagation*, **60**(9), 4429–4432.
 73. **Nijas, C., P. Vinesh, V. Sajitha, P. Anila, and P. Mohanan**, Optimisation of quarter wave microstrip open stub resonators for chipless rfid applications. *In IEEE Antennas and Propagation Society International Symposium (APSURSI), Orlando.* 2013.

74. **Noor, T., A. Habib, Y. Amin, J. Loo, and H. Tenhunen** (2016). High-density chipless rfid tag for temperature sensing. *Electronics Letters*, **52**(8), 620–622.
75. **Pavlina, J. and D. Malocha**, Chipless rfid saw sensor system-level simulator. *In IEEE International Conference on RFID (IEEE RFID 2010), Orlando*. 2010.
76. **Perret, E., R. S. Nair, E. B. Kamel, A. Vena, and S. Tedjini**, Chipless rfid tags for passive wireless sensor grids. *In XXXIth URSI General Assembly and Scientific Symposium (URSI GASS), China*. 2014.
77. **Plessky, V., S. Kondratiev, R. Stierlin, and F. Nyffeler**, Saw tags: new ideas. *In Proceedings of IEEE Ultrasonics Symposium, USA*. 1995.
78. **Pozar, D. M.**, *Microwave engineering*. John Wiley & Sons, 2009.
79. **Preradovic, S., I. Balbin, and N. Karmakar**, The development and design of a novel chipless rfid system for low-cost item tracking. *In Asia-Pacific Microwave Conference, Hongkong*. 2008a.
80. **Preradovic, S., I. Balbin, N. C. Karmakar, and G. Swiegers**, A novel chipless rfid system based on planar multiresonators for barcode replacement. *In IEEE International Conference on RFID, Lasvegas*. 2008b.
81. **Preradovic, S. and N. Karmakar**, Chipless rfid for intelligent traffic information system. *In IEEE International Symposium on Antennas and Propagation (APSURSI), Washington*. 2011.
82. **Preradovic, S. and N. C. Karmakar**, Design of fully printable planar chipless rfid transponder with 35-bit data capacity. *In European Microwave Conference, Rome*. 2009.
83. **Preradovic, S. and N. C. Karmakar** (2010). Chipless rfid: Bar code of the future. *IEEE Microwave Magazine*, **11**(7), 87–97.

84. **Preradovic, S.** and **A. Menicanin**, Chipless wireless sensor node. *In International Convention on Information and Communication Technology, Electronics and Microelectronics (MIPRO), Croatia.* 2012.
85. **Preradovic, S., S. Roy,** and **N. Karmakar**, Fully printable multi-bit chipless rfid transponder on flexible laminate. *In IEEE Asia Pacific Microwave Conference, APMC, Singapore.* 2009.
86. **Ramirez, R. A., E. A. R. Nastrucci,** and **T. M. Weller**, 3d tag with improved read range for uhf rfid applications using additive manufacturing. *In IEEE 16th Annual Wireless and Microwave Technology Conference (WAMI-CON), Florida.* 2015.
87. **Reichardt, L., G. Adamiuk,** and **G. Jereczek**, Car-to-infrastructure communication using chipless, passive rfid tags. *In IEEE Antennas and Propagation Society International Symposium, Toronto.* 2010.
88. **Remenyi, D., G. Onofrei,** and **J. English**, An introduction to statistics using microsoft excel. Academic Conferences Limited, 2011.
89. **Rezaiesarlak, R.** and **M. Manteghi**, *Chipless RFID: Design Procedure and Detection Techniques.* Springer, 2014.
90. **Roberti, M.** (2005). The history of rfid technology. *RFID Journal*, **16**(01).
91. **Rodrigues, R. A. A., E. C. Gurjao, F. M. de Assis, V. Palazzi, F. Alimenti, L. Roselli, P. Mezzanotte,** and **S. Tedjini**, Design of planar resonators on flexible substrate for chipless tags intended for crack sensing. *In IEEE 15th Mediterranean Microwave Symposium (MMS), Italy.* 2015.
92. **S Harma, S., V. P. Plessky,** and **P. Li** (2009). Feasibility of ultra-wideband saw rfid tags meeting fcc rules. *IEEE Transactions on, Ultrasonics, Ferroelectrics, and Frequency Control*, **56**(4), 812–820.

93. **Sakouhi, S., R. Hedi, R. Bedira, and A. Gharsallah**, A novel meander complementary split ring resonator-based rfid chipless tag. *In Proceedings of 2014 Mediterranean Microwave Symposium (MMS2014), Morocco*. 2014.
94. **Sarhadi, A., A. Hashemi, and H. Emami**, Optimization of q factor in complementary spiral resonator for rfid application. *In 21st Telecommunications Forum (TELFOR), Belgrade*. 2013.
95. **Schiffman, B. and G. Matthaei** (1964). Exact design of band-stop microwave filters. *IEEE Transactions on Microwave Theory and Techniques*, **12**(1), 6–15.
96. **Schuster, S., S. Scheiblhofer, A. Stelzer, and A. Springer**, Model based wireless saw tag temperature measurement. *In Proceedings of Asia Pacific Microwave Conference, Suzhou*. 2005.
97. **Shrestha, S., J. Vemagiri, M. Agarwal, and K. Varahramyan** (2007). Transmission line reflection and delay-based id generation scheme for rfid and other applications. *International Journal of Radio Frequency Identification Technology and Applications*, **1**(4), 401–416.
98. **Shutzberg, L.** (2004). Radio frequency identification (rfid) in the consumer goods supply chain: Mandated compliance or remarkable innovation. *An Industry Whitepaper, Rock-Teen Company*.
99. **Slack, C. et al.** (2013). Impact of radio-frequency identification (rfid) technologies on the hospital supply chain: a literature review. *Perspectives in Health Information Management*, 1–5.
100. **Stockman, H.** (1948). Communication by means of reflected power. *Proceedings of the IRE*, **36**(10), 1196–1204.
101. **Suma, M., R. K. Raj, M. Joseph, P. Bybi, and P. Mohanan** (2006). A compact dual band planar branched monopole antenna for dcs/2.4-ghz wlan

- applications. *IEEE Microwave and Wireless Components Letters*, **16**(5), 275–277.
102. **Tedjini, S., N. Karmakar, E. Perret, and A. Vena** (2013). Hold the chips: Chipless technology, an alternative technique for rfid. *IEEE Microwave Magazine*, **14**(5), 56–65.
 103. **Tikhov, Y. and Y. h. Min** (2008). Rfid barcode and rfid barcode reading system. US Patent 7,353,997.
 104. **Vemagiri, J., A. Chamarti, M. Agarwal, and K. Varahramyan** (2007). Transmission line delay based radio frequency identification (rfid) tag. *Microwave and Optical Technology Letters*, **49**(8), 1900–1904.
 105. **Vena, A., E. Perret, and S. Tedjini**, Novel compact rfid chipless tag. *In PIERS Proceedings, Morocco*. 2011a.
 106. **Vena, A., E. Perret, and S. Tedjini**, Rfid chipless tag based on multiple phase shifters. *In IEEE MTT-S International Microwave Symposium Digest (MTT), Baltimore*. 2011b.
 107. **Vena, A., E. Perret, and S. Tedjini** (2012a). Design of compact and auto-compensated single-layer chipless rfid tag. *IEEE Transactions on Microwave Theory and Techniques*, **60**(9), 2913–2924.
 108. **Vena, A., E. Perret, S. Tedjini, D. Kaddour, A. Potie, and T. Barron**, A compact chipless rfid tag with environment sensing capability. *In IEEE MTT-S International Microwave Symposium Digest (MTT), Montreal*. 2012b.
 109. **Vena, A., E. Perret, S. Tedjini, G. E. P. Tourtollet, A. Delattre, F. Garet, and Y. Boutant** (2013a). Design of chipless rfid tags printed on paper by flexography. *IEEE Transactions on Antennas and Propagation*, **61**(12), 5868–5877.

110. **Vena, A., E. Perret, and S. Tedjni** (2013b). A depolarizing chipless rfid tag for robust detection and its fcc compliant uwb reading system. *IEEE Transactions on Microwave Theory and Techniques*, **61**(8), 2982–2994.
111. **Voulodimos, A. S., C. Z. Patrikakis, A. B. Sideridis, V. A. Ntafis, and E. M. Xylouri** (2010). A complete farm management system based on animal identification using rfid technology. *Computers and Electronics in Agriculture*, **70**(2), 380–388.
112. **Wang, Y. Y., F. Wei, H. Xu, B. Liu, and X. W. Shi**, A tunable dual-stop-band filter using spurlines. *In International Conference on Microwave and Millimeter Wave Technology (ICMMT), shenzhen*. 2012.
113. **Want, R.** (2004a). Enabling ubiquitous sensing with rfid. *Computer*, **37**(4), 84–86.
114. **Want, R.** (2004b). The magic of rfid. *Queue*, **2**(7), 40–48.
115. **Weng, Y., S. Cheung, T. Yuk, and L. Liu** (2013). Design of chipless uwb rfid system using a cpw multi-resonator. *IEEE Antennas and Propagation Magazine*, **55**(1), 13–31.
116. **Whitmore, A., Andrew Agarwal and D. Xui** (2015). The internet of things- a survey of topics and trends. *Information Systems Frontiers*, **17**(2), 261–274.
117. **Yang, L., R. Zhang, D. Staiculescu, C. P. Wong, and M. M. Tentzeris** (2009). A novel conformal rfid-enabled module utilizing inkjet-printed antennas and carbon nanotubes for gas-detection applications. *IEEE Antennas and Wireless Propagation Letters*, **8**, 653–656.

118. **Zainud Deen, S., M. A. Hassan, H. Malhai, and K. Awadalla**, Simple microstrip bandstop resonators for chipless rfid tag. *In IEEE 30th National Radio Science Conference (NRSC), Cairo*. 2013.
119. **Zainud Deen, S., M. A. Hassan, H. Malhet, and K. Awadalla**, Novel chipless tag with electromagnetic code. *In Middle East Conference on Antennas and Propagation (MECAP), Cairo*. 2012.
120. **Zhu, X., S. K. Mukhopadhyay, and H. Kurata** (2012). A review of rfid technology and its managerial applications in different industries. *Journal of Engineering and Technology Management*, **29**(1), 152–167.

LIST OF PAPERS BASED ON THESIS

International Journals

1. **Sumi M**, Dinesh R, Nijas C M, S. Mridula and P. Mohanan (2014). Frequency coded chipless RFID tag using spurline resonators. *Radio Engineering*, **23**, 203 - 208.
2. **Sumi M**, Dinesh R, Nijas C M, S. Mridula and P. Mohanan (2014). Spectral signature-encoded chipless RFID tag with planar multiresonators. *Journal of Electromagnetic Waves and Applications*, **28(18)**, 2266 - 2275.
3. **Sumi M**, Dinesh R, Nijas C M, S. Mridula and P. Mohanan (2014). High Bit Encoding Chipless RFID Tag Using Multiple E-Shaped Microstrip Resonators. *Progress In Electromagnetics Research B*, **61**, 185 - 196.

International Conferences

1. **Sumi M**, Dinesh R, Nijas C M, S. Mridula and P. Mohanan. Frequency signature based Chipless RFID tag using shorted stub resonators. *IEEE Asia Pacific conference on Antennas and Propagation*, Bali, Indonesia, July 2015.
2. **Sumi M**, Dinesh R, Nijas C M, S. Mridula and P. Mohanan. U slot multiresonator RFID tag with enhanced bit encoding capacity. *IEEE TENCON 2016 - Technologies for Smart Nation*, Singapore, November 2016.

National Conferences

1. **Sumi M**, Dinesh R, Nijas C M, S. Mridula. Chipless RFID tag based on Spurline resonators. *Proceedings of the National Symposium on Microwave Antennas and Propagation (APSYM-12)*, Cochin, December 2012.
2. **Sumi M**, Dinesh R, Nijas C M, S. Mridula and P. Mohanan. Compact chipless RFID tag using coplanar multiresonators. *Proceedings of Fourth National Technological Congress (NATCON 2014)*, Wayanad, February 2014.

CURRICULUM VITAE

SUMI M

ASSISTANT PROFESSOR

DEPT. OF ELECTRONICS AND COMMUNICATION

N S S COLLEGE OF ENGINEERING

PALAKKAD 678008, KERALA.



Education

Degree	Institution	Period	Remarks
SSLC	St. Joseph's Higher Secondary School, Cochin	1996 -1997	First class with distinction, 93.3%
HSE	Model Technical Higher Secondary School, Cochin	1997 -1999	First class with distinction, 84.1%
B.Tech	Model Engineering College, Cochin	1999 - 2003	First class with distinction, 80.3%
M.Tech	Indian Institute of Science (IISc), Bangalore	2007 - 2009	First class (CGPA 6.6 out of 8)
Ph.D	Cochin University of Science and Technology, Cochin	Registered on 11.10.2010	

Fields of research interest

Development of chipless RFID tags, Active RFID tags, Implementation of wireless sensor networks.

Publications

International Journal	3
International Conference	2
National Conference	2

Software skill set

Languages : C-programming, VHDL

Software packages and platforms: CST Microwave Studio, ModelSim, Xilinx Foundation Series ISE, Electric, LTSpice, Corel draw, Latex

Operating system: Windows, Linux

Personal details

Age and date of birth	35 Years, 26/11/1981
Gender	Female
Nationality	Indian
Religion	Hindu
Languages	English, Malayalam, Hindi
e-mail	sumi.harikrishnan@gmail.com
Permanent Address	Shreyadeep, Vakipotta, Akathethara, Palakkad 678008, Kerala.

